UNIVERSITY OF SOUTHAMPTON

FACULTY OF ENGINEERING AND THE ENVIRONMENT
AIRBUS NOISE TECHNOLOGY CENTRE

The noise generation by a main landing gear door

by

Ryu J. Fattah

Thesis for the degree of Doctor of Philosophy

March 2016

UNIVERSITY OF SOUTHAMPTON

ABSTRACT

FACULTY OF ENGINEERING AND THE ENVIRONMENT
AIRBUS NOISE TECHNOLOGY CENTRE

Doctor of Philosophy

THE NOISE GENERATION BY A MAIN LANDING GEAR DOOR

by Ryu J. Fattah

Experimental measurements and numerical simulations were conducted on a simplified main landing gear model that consists of a leg-door, and a main strut in a parallel configuration. The effects of varying the leg-door angle of attack, and the gap distance between the two elements, were initially studied by two-dimensional and low-order numerical simulations, using the unsteady Reynolds-Averaged Navier-Stokes equations. The strut diameter was specified to the same diameter as a full-scale main landing gear, and simulated under a free-stream Mach number of 0.2, and a Reynolds number based on the cylinder diameter of 1.7×10^6.

Further three-dimensional and high-order numerical simulations were conducted on models with a constant gap distance of 8.7% of the cylinder diameter. The high-order solver evaluates the three-dimensional Navier-Stokes equations in the full-conservation form, with the Zonal Detached-Eddy Simulation model. The fidelity of the numerical solver was improved in two parts. Firstly, an Eigenvalue analysis for a multiple-block environment was developed to optimise the combination of spatial and filtering schemes for maximum grid resolution that is numerically stable. Secondly, a grid quality metric, which correlates strongly to the solution accuracy, was developed.

A validation database of experimental measurements on a tripped 26% scale interaction model, at a free-stream Mach number of 0.09, and a Reynolds number based on the cylinder diameter of 2×10^5, was developed at the 2.1 m ×1.5 m wind tunnel at the University of Southampton. The experimental and numerical results show that the wake generated by the interaction model is dominated by low frequencies that correspond to the vortex shedding modes of the cylinder, and the door. As the door angle is increased from 0 to 10.7 degrees, the intensity of the cylinder shedding mode decreased. The sound pressure levels of the radiated noise were calculated using the FW-H method. The dominant noise source is a compact dipole, which reduced in strength as the door angle was increased.

Contents

Acknowledgements xvii

1 Introduction 1
- 1.1 Research objectives . . . 3
- 1.2 Original contributions . . . 3
- 1.3 Thesis outline . . . 5

2 Review of previous works 7
- 2.1 Principles of aerodynamic sound . . . 7
- 2.2 Bluff body flows . . . 10
- 2.3 The main landing gear . . . 14
- 2.4 Leg-door and cylinder flows . . . 25
- 2.5 Summary . . . 29

3 Research methodology 31
- 3.1 Experimental methods . . . 31
- 3.2 Numerical methods . . . 36
- 3.3 Geometry definition . . . 50
- 3.4 Technical approach . . . 53

4 Numerical methods development 55
- 4.1 Original spatial scheme . . . 56
- 4.2 Penta-diagonal spatial scheme . . . 59
- 4.3 Impact of the changes . . . 63
- 4.4 Numerical stability of spatial schemes . . . 65
- 4.5 Grid quality assessment . . . 72
- 4.6 Summary . . . 96

5 Experimental work 97
- 5.1 Introduction and aim . . . 97
- 5.2 Experimental model . . . 97
- 5.3 Results . . . 99
- 5.4 Summary . . . 119

6 High-order simulations 123
- 6.1 Grid development . . . 124
- 6.2 Validation of the numerical predictions . . . 130
- 6.3 Aerodynamic effects of the interaction . . . 134

6.4 Far-field noise calculations . . . 144
6.5 Summary . . . 153

7 Conclusions and recommendations 157
7.1 Summary of the work . . . 157
7.2 Conclusions . . . 159
7.3 Future work . . . 161

A Low-order Simulations 165
A.1 Input parameters for the OpenFOAM solver . . . 168

B Temporal Scheme Error Analysis 173

C High-order code validation and verification 177
C.1 Boundary layer and SA model validation . . . 177
C.2 Overview of validation cases for the high-order code . . . 179

D Grid Quality Example 181

E Surface pressure spectra comparison 183

List of Figures

1.1 Contour map of the equivalent continuous noise level (Leq) for day operations at Heathrow airport, London, United Kingdom [2] for the year 2013. 1

2.1 The laminar flow around a circular cylinder. 11
2.2 The Von-Kármán vortex street flow visualisation around a circular cylinder at $Re = 140$ [27]. 11
2.3 Flow around a circular cylinder at $Re = 2000$ [27]. Shear layers (—), vortex core (—), and entrainment paths (—). 12
2.4 Dominant Strouhal number variation with Reynolds number [29]. 13
2.5 The effect of bluff body geometry on the dominant Strouhal number variation with Reynolds number [29]. 14
2.6 Main landing gear key components. 15
2.7 Effect of the leg-door on the directivity patterns from a 6.3% scale MLG model[12] at two frequencies. 19
2.8 A simplified hierarchy of noise prediction methods. 20
2.9 Influential parameters that affect the flow around a cylinder placed near a flat plane boundary. 28

3.1 Convergence of PIV residuals for the stream-wise (+) and transverse (×) velocity statistics with increasing sample size N. 34
3.2 An example of a grid metric discontinuity. 45
3.3 Simplified Airbus landing gear model including the leg-door. 50
3.4 Simplified 2-D door-strut interaction model. Dimensions are highlighted in blue, and the influential design parameters are given in red. 51
3.5 The effect of G and α_D on the force fluctuations along the cylinder and door elements. 52

4.1 The effect of the sixth-order explicit filters on the dispersion relation for interior and boundary schemes of the 8/4 method. Curves for the exact solution —, interior scheme -▲-, boundary scheme at $i = [1, N-1]$ -○-, and the boundary scheme at $i = [0, N]$ - - -. Filter transfer function is highlighted in grey. 58
4.2 Fourier analysis of errors on the penta-diagonal scheme with fully-biased boundary schemes[100]. Curves for the exact solution —, interior scheme - - -, boundary schemes at $i = [0, N]$ -○-, at $i = [1, N-1]$ -▲-, and at $i = [2, N-2]$ -□-, ... 61
4.3 Fourier analysis of errors on the penta-diagonal scheme with ghost point boundary schemes [51]. Curves for the exact solution —, interior scheme - - -, boundary schemes at $i = [0, N]$ -○-, and at $i = [1, N-1]$ -▲- . . . 62

4.4 Implicit filter transfer function for the interior points, with $k_c = 0.9$ ─□─, $k_c = 0.8$ ─▽─, $k_c = 0.7$ ─△─, and $k_c = 0.6$ ─○─. 62
4.5 Implicit filter transfer function for the boundary points $i = \{2, N-2\}$, with $k_c = 0.9$ ─□─, $k_c = 0.8$ ─▽─, $k_c = 0.7$ ─△─, $k_c = 0.6$ ─○─. 63
4.6 The flow features behind a cylinder at $Re_D = 1.7 \times 10^6$ predicted by the original and new versions of the code. Turbulent are illustrated by a surface contour of $Q = 1$ and coloured by the velocity magnitude. 64
4.7 The flow features behind an interaction case at $Re_D = 1.7 \times 10^6$ predicted by the original and new versions of the code. Turbulent features are illustrated by a surface contour of $Q = 1$ and coloured by the velocity magnitude. 65
4.8 The surface pressure spectra on a circular cylinder at $\theta = 0$ predicted by the old (——) and new (——) version of the code 65
4.9 The field of $\overline{v'v'}$ around an interaction model at $\alpha_D = 10.7$ degrees predicted by the old and new versions of the code. The block edges are highlighted in red. 66
4.10 Eigenvalue analysis for a 51-node on a single block domain using two different spatial schemes, with (•) and without (•) the penta-diagonal filters ($k_c = 0.85\pi$) [101]. 68
4.11 A nine point grid cluster divided into a left and right blocks. The interface and boundary zones are highlighted by the red dashed line. 69
4.12 Two block system Eigenvalues using 8/4 fully-biased schemes at interface boundaries with the CIC. 70
4.13 Two block system Eigenvalues using the 8/4 central schemes at block interfaces with the GP method. 71
4.14 Two block system Eigenvalues using the penta-diagonal fully-biased schemes at block interfaces with the CIC. 71
4.15 Two block system Eigenvalues using the penta-diagonal central schemes at block interfaces with the GP method. 72
4.16 Dispersion error for explicit central spatial schemes of 2^{nd} - - -, 4^{th} ─×─, 6^{th} -×-, 8^{th} ─■─ and 10^{th} ─■─ order. Exact solution is given by ——. . . . 76
4.17 Filtering transfer function for explicit central schemes of 4^{th} ─×─, 6^{th} -×-, and 8^{th} ─■─ order. With no filtering $T(k) = 1$ ——. 78
4.18 Generalisation of the changes to the grid coordinates induced by spatial filters, on to a two-dimensional curvilinear mesh. Original grid points are highlighted by ■, and the modified coordinate due to the filtering is highlighted by ▲. 80
4.19 Four block uniform grid. (a) Pressure disturbance field over-set with every fifth grid line, (b) Density error field at $t = t_{\text{final}}$. 82
4.20 The effect of an abrupt change in the grid spacing at $x = 0$ on the mesh quality. (a) $A_x = 1.25$, (b) $A_x = 2$. 83
4.21 The effect of an abrupt change in the grid spacing at $x = 0$ on the solution error at $t = t_{\text{final}}$. (a) $A_x = 1.25$, (b) $A_x = 2$. 84
4.22 Effect of abrupt changes in the grid spacing at $x = 0$ on the grid quality and on the solution error. (a) The effect of A_x on the grid quality, (b) the effect of grid quality on the solution error at $t = t_{\text{final}}$. 84
4.23 The effect of an abrupt change in the grid spacing at $x = 0$ on the mesh quality. (a) $A_y = 0.25$ (b), $A_y = 0.875$. 85

4.24 The effect of an abrupt change in the grid spacing at $x = 0$ on the solution error at $t = t_{\text{final}}$. (a) $A_y = 0.25$, (b) $A_y = 0.875$. 85

4.25 Effect of abrupt changes in the grid line direction at $x = 0$ on the grid quality and the solution error. (a) The effect of A_y on the grid quality, (b) the effect of grid quality on the solution error at $t = t_{\text{final}}$. 86

4.26 The effect of uniform skewness in the grid on the solution error at $t = t_{\text{final}}$. Block edges for $A_s = 0.25$ and $A_s = 1$ are shown in thick and thin black lines, respectively. 87

4.27 The effect of uniform skew on the grid quality metric and the solution error. (a) The effect of A_s on the grid quality, (b) the effect of the grid quality on the solution error at $t = t_{\text{final}}$. 87

4.28 Mesh for $A_t = 1.5$ showing every fifth grid line. 88

4.29 The effect of non-uniform skewness on the mesh quality. (a) $A_t = 0.5$, (b) $A_t = 1.5$ 89

4.30 The effect of non-uniform skew on the grid quality metric and the solution error. (a) The effect of A_t on the grid quality, (b) the effect of grid quality on the solution error at $t = t_{\text{final}}$. 89

4.31 The effect of grid scale and grid orientation on the grid quality metric Q for a uniform grid morphed by Equation 4.44 with $A = 1.5$. (a) Original grid (b) original grid scaled by 0.1, (b) original grid scaled by 0.1 and rotated by 45 degrees. 91

4.32 Effect of grid filtering on the grid lines. Original grid — and filtered grid after one iteration - - - 92

4.33 Measures of the grid quality on the unfiltered grid (a) and (b), and on the filtered grid after one iteration (c) and (d). 93

4.34 Effect of grid filtering on the solution error. (a) Original grid, (b) Filtered grid after one iteration. 94

4.35 The effect of filtering the grid recursively on (a) the integral grid quality metric Q_I, and on (b) the integral solution error E_I 94

5.1 Side view illustration of the model set-up. 98

5.2 Downstream view of the model set-up in the test section. 98

5.3 Upstream view of the model set-up in the test section. 99

5.4 Aerodynamic loads on an isolated door at varying angle of attack. C_D (clean) - □, C_D (tripped) - +, C_L (clean) - ○, C_L (tripped) - ×. Loads are normalised by the reference area based on the span and chord of the door element. 102

5.5 Oil flow patterns on the lower surface of an isolated door model at $\alpha_D = 0°$. Position of the frame is highlighted by the red line. 103

5.6 Oil flow patterns along the upper surface of an isolated door at $\alpha_D = 0°$. Position of the frame is highlighted by the red line. 103

5.7 Comparison of the oil flow features along the end plates for $\alpha_D = 10.7°$ under an isolated door configuration at two speeds $U_\infty = 24, 34$ m/s. . . . 103

5.8 Aerodynamic loads on the door-cylinder model at varying angle of attack. C_D (clean) - □, C_D (tripped) - +, C_L (clean) - ○, C_L (tripped) - ×. Loads are normalised by the reference area based on the span and chord of the door element only. 105

5.9 Illustration of the major flow features identified around the leg-door and cylinder model. 106

5.10 Oil flow features on the lower surface of the door with the cylinder interaction at $\alpha_D = 0°$. Position of the frame is highlighted by the red line. 106
5.11 Velocity magnitude, and 2-D TKE fields at $\alpha_D = 0°$ at various speeds. 108
5.12 Z-Vorticity field and stream line plots for $\alpha_D = 0°$ at various speeds. 109
5.13 Velocity magnitude, and 2-D TKE fields at $\alpha_D = 5°$ at various speeds. 110
5.14 Z-Vorticity field and stream line plots for $\alpha_D = 5°$ at various speeds. 111
5.15 Velocity magnitude, and 2-D TKE fields at $\alpha_D = 10.7$ at various speeds. 112
5.16 Z-Vorticity field and stream line plots for $\alpha_D = 10.7°$ at various speeds. 113
5.17 TKE production term for $\alpha_D = 0°$ at various speeds. 114
5.18 TKE production term for various α_D°. 114
5.19 Effect of the door angle on the velocity profiles at $x/D = 2$ downstream in the wake of the model. 115
5.20 Effect of the door angle in the energy profiles at $x/D = 2$ downstream in the wake of the model. 116
5.21 Surface pressure spectra at two free-stream speeds for an isolated cylinder: —, $\alpha_D = 0°$: —, $\alpha_D = 5°$: - - -, $\alpha_D = 10.7°$: ······. 118
5.22 Differences in the surface pressure spectra compared to the isolated cylinder data. Data from $\alpha_D = 0°$: —, $\alpha_D = 5°$: - - -, $\alpha_D = 10.7°$: —. 119

6.1 Computational grid for the isolated cylinder model. The block edges are highlighted in red, the boundary condition edges are highlighted in black, and the grid lines are highlighted in grey. 126
6.2 Computational grid for the isolated door model with an angle of attack. The block edges are highlighted in red, the boundary condition edges are highlighted in black, and the grid lines are highlighted in grey. 127
6.3 Computational grid designed for the intercase case *Case_0*. Block edges are highlighted in red, boundary conditions are applied along the edges highlighted in black. Mesh lines are highlighted in grey. 128
6.4 Instantaneous surface plot of constant Q-criterion $Q = 0.1$ coloured by the local Mach number and over set by the velocity divergence field in the range of $-0.01 < \nabla \cdot \vec{u} < 0.01$ in grey scale. 129
6.5 The mean pressure distribution along an isolated cylinder from the numerical simulation at $Re = 1.6 \times 10^6$ (red cross), and from experiments by Roshko [116] at $Re = 8.4 \times 10^6$ (black square) and by Flachsbart [116] at 6.7×10^5 (black cross). 130
6.6 The mean velocity field behind an interaction model with $\alpha_D = 0°$, according to simulation and experiment. 131
6.7 The mean velocity profiles across the wake region from the simulation (—) and experiments (•). 132
6.8 The 2-D TKE profiles across the wake region from the simulation (—) and experiments (•). 133
6.9 Comparison of the stream-wise velocity fluctuation profiles across the wake region between simulation (—) and experiments (•). 135
6.10 Comparison of the transverse velocity fluctuation profiles across the wake region between simulation (—) and experiments (•). 136
6.11 The distribution of mean pressure along the cylinder surface, from an interaction model with varying door angle. Data from the interaction case (black cross), and the isolated cylinder simulation (red cross). 137

6.12 The distribution of SPL along the cylinder surface, from an interaction model with varying door angle. Data from the interaction case (black cross), and the isolated cylinder simulation (red cross). 138

6.13 The distribution of mean pressure along the leg-door surface, from an isolated, and interaction model with varying door angle. Data along the upper surface (red) and along the lower surface (black). 139

6.14 Effect of door angle on the door surface distribution of the variance of pressure. Data along the upper surface (red) and along the lower surface (black). 143

6.15 Far-field acoustic signal prediction at an observer angle of $\theta = 90^\circ$. 144

6.16 Integration surfaces for the FW-H calculations overset by contours of $|\lambda| = |\vec{\omega} \times \vec{u}|$. The surface zone names are US (blue), DS1 (red), DS2 (black), WZC (cylinder), and WZD (door) surface. 146

6.17 Far-field sound directivity plots from three FW-H calculations. Wall zone only (······), US and DS1 zones (——), US and DS2 zones (- - -). 146

6.18 Far-field noise spectra at observer angles of $\theta = 90^\circ$ (——), and at $\theta = 270^\circ$ (——). 147

6.19 Far-field sound directivity plots for the interaction cases as predicted from three FW-H calculations. Wall zone only (······), US and DS1 zones (——), US and DS2 zones (- - -). 149

6.20 Far-field OASPL directivity computed from the on-surface FW-H integration surface (WZC and WZD zones) for the interaction cases at door angles of $\alpha_D = 0^\circ$ (——), $\alpha_D = 2.5^\circ$ (- - -), $\alpha_D = 5^\circ$ (——), $\alpha_D = 7.5^\circ$ (- - -), and $\alpha_D = 10.7^\circ$ (——). 150

6.21 Far-field noise spectra computed from the on-body FW-H surfaces (WZC and WZD zones) for door angles of $\alpha_D = 0^\circ$ (——), and $\alpha_D = 10.7^\circ$ (——). 150

6.22 Cylinder surface SPL at varying Strouhal number and along varying azimuthal angles. 151

6.23 Door upper surface noise maps highlighted in SPL [dB]. 154

6.24 Door lower surface noise maps highlighted in SPL [dB]. 155

A.1 Instantaneous field of pressure coefficient computed by 2-D URANS with the $k - \omega$ SST model, for an interaction model configured to $G = 0.087$ and $\alpha_D = 7.5^\circ$. 166

A.2 Power spectral density of the lift force fluctuation recorded on the door surface for a grid with a span-wise grid resolution of 20 (red) and 35 (black) points per cylinder diameter. 166

A.3 Instantaneous iso-contour plot of constant Q-criterion at $Q = 100000$ s^{-1} coloured by the local Mach number (assuming $c_\infty = 340$ m/s). 167

A.4 OpenFOAM system file for the finite volume schemes (part 1 of 4). 168

A.5 OpenFOAM system file for the finite volume schemes (part 2 of 4). 169

A.6 OpenFOAM system file for the finite volume schemes (part 3 of 4). 170

A.7 OpenFOAM system file for the finite volume schemes (part 4 of 4). 171

B.1 Numerical errors from a second order implicit time integration scheme on the one-dimensional wave equation. 175

C.1 Comparison of the velocity and turbulent viscosity profiles between the high-order code (- - -) and CFL-3D (——). 178

D.1 The mesh quality for two grids developed for the interaction model with a door angle of $\alpha_D = 10.7°$. 181

E.1 Surface pressure spectra comparisons between experiments and simulation for an on-surface microphone located along the cylinder model at $\theta = 0°$. Data for an isolated cylinder: ——, $\alpha_D = 0°$: ——, $\alpha_D = 5°$: - - -, $\alpha_D = 10.7°$: ······. 184

List of Tables

2.1 Table of experimental works on LG geometries. Measurement key: PMA - Phased Microphone Array, MA - Microphone array, FFM - Far-field Microphone, NS - Noise spectra, DP - Directivity Profile, MP - Mean Pressure, UP - Unsteady Pressure, PIV - Particle Image Velocimetry, HW - Hot Wire Anemometry, LDV - Laser Doppler Velocimetry, ML-Mean Loads. . . . 18

4.1 Correlation coefficient between the grid quality metric and the solution error. . . . 90

5.1 Key dimensions of the experimental model. . . . 99
5.2 Test matrix of the experiments. ML - Mean loads, OF - Oil flow, PIV - Particle Image Velocimetry, M - Microphone. . . . 101

6.1 Case descriptions for the high-order numerical simulations. . . . 124

C.1 Validation and verification cases for the high-order CAA solver listed in chronological order. . . . 180

DECLARATION OF AUTHORSHIP

I, Ryu J. Fattah , declare that the thesis entitled "*The noise generation by a main landing gear door*", and the work presented in the thesis are both my own, and have been generated by me as the result of my own original research. I confirm that:

- This work was done wholly or mainly while in candidature for a research degree at this University;
- Where any part of this thesis has previously been submitted for a degree or any other qualification at this University or any other institution, this has been clearly stated;
- Where I have consulted the published work of others, this is always clearly attributed;
- Where I have quoted the work of others, the source is always given. With the exception of such quotations, this thesis is entirely my own work;
- I have acknowledged all main sources of help;
- Where the thesis is based on work done by myself jointly with others, I have made clear what was done by others and what I have contributed myself;
- Parts of this work have been published by the author, as listed in Section 1.2.

Signed: ....

Date: ....

Acknowledgements

I would like to thank my supervisors Doctor Zhiwei Hu, and Doctor David Angland for providing support, guidance, and patience throughout the course of my PhD. Thanks must also go to Professor Xin Zhang, for further supporting my project.

I would like to acknowledge the Engineering and Physical Sciences Research Council (EPSRC), and Airbus, who provided and supported this project through the Airbus Noise Technology Centre (ANTC). The use of the IRIDIS High Performance Computing Facility, and associated support services at the University of Southampton, is also acknowleged in the completion of this work.

I would like to thank my colleagues at the University of Southampton for their invaluable support. Thanks go to James Gill, Chris Tyson, Michael Sanderson, Nicolas Renard, and Meng Wang.

I would also like to thank members of the Southampton University Mountaineering Club for giving me experiences that I will never forget. Thanks also go to my climbing parnters BL, AW, DA, LS, and RK. Thanks also go to many other members of the club who helped in making it an incredible society to be part of.

Finally, I would like to thank my family for everything else.

Nomenclature

Roman

C_D	Coefficient of drag	
C_L	Coefficient of lift	
C_p	Coefficient of pressure	
c_p	Specific heat at constant pressure	J/(kg K)
c_v	Specific heat at constant pressure	J/(kg K)
D	Cylinder diameter	m
e	Gap width	m
e_t	Total energy	N m
f	Frequency	Hz
G	Gap width ratio, $G = e/D$	
$H()$	Heaviside function	
I	Identity matrix	
J	Jacobian of the grid coordinate transformation	
L	Reference length	m
L_{eq}	Equivalent continuous sound level	dB
M	Mach number	
P	Pressure	Pa
P_{ij}	Compressible stress tensor	
Pr	Prandtl number	

Q	Second invariant of the velocity gradient tensor	1/s
Re	Reynolds number	
S_{ij}	Symmetric strain rate tensor	1/s
St	Strouhal number	
T	Temperature	K
t	Time	s
T_{ij}	Lighthill stress tensor	
u_i, u, v, w	Cartesian velocity components	m/s
x_i, x, y, z	Cartesian coordinates	m
y^+	Normalised wall distance	

Greek

α_D	Door angle of attack	degree
δ	Boundary layer thickness	m
δ_{ij}	Dirac delta function	
ϵ	Turbulent dissipation rate	$\mathrm{m^2/s^{-3}}$
η	Kolmogorov length scale	m
γ	Ratio of specific heats (c_p/c_v)	
λ	Cross product of velocity and vorticity	
μ	Dynamic viscosity	Ns/m
ν	Kinematic viscosity	$\mathrm{m^2/s}$
ν_T	Turbulent eddy viscosity	$\mathrm{m^2/s}$
ρ	Density	$\mathrm{kg/m^3}$
τ	Psudeo-time	
τ_{ij}	Shear stress tensor	$\mathrm{N/m^2}$
θ	Observer angle	degree
$\tilde{\nu}$	Modified eddy viscosity	$\mathrm{m^2/s}$

ξ, η, ζ	Generalised coordinates

Subscripts

$()_0$	Reference quantity
$()_\infty$	Free-stream quantity
$()_{RMS}$	Root mean square
$()_T$	Turbulent quantity

Superscripts

$()'$	Perturbation quantity
$\langle\rangle$	Ensemble averaged quantity
$\overline{()}$	Time averaged quantity

Abbreviations

2-D	Two-dimensional
3-D	Three-dimensional
ANTC	Airbus Noise Technology Centre
APG	Adverse pressure gradient
CAA	Computational aeroacoustics
CFD	Computational fluid dynamics
CFL	Courant-Friedrichs-Lewy
CIC	Characteristic interface condition
CLG	Centre landing gear
DES	Detached-eddy simulation
DNS	Direct numerical simulation
FD	Finite difference
FV	Finite volume
FW-H	Ffowcs Williams and Hawkings

LES	Large-eddy simulation
LG	Landing gear
MLG	Main landing gear
NASA	National Aeronautics and Space Administration
OASPL	Over-all sound pressure level
PIV	Particle image velocimetry
PSD	Power spectral density (re $p_{\mathrm{ref}} = 2 \times 10^{-5}$Pa)
SA	Spalart-Allmaras
SGS	Sub-grid scale
SPL	Sound pressure level (re $p_{\mathrm{ref}} = 2 \times 10^{-5}$Pa)
SST	Shear stress transport
TBL	Turbulent boundary layer
URANS	Unsteady Reynolds-Averaged Navier-Stokes

Chapter 1

Introduction

The noise generated from an aircraft during its near-airport operation can have an environmental impact on the surrounding areas that are typically residential. The extent of aircraft noise pollution is shown by Figure 1.1, which illustrates the equivalent continuous sound levels (Leq) surrounding the area around Heathrow airport. The aforementioned sound level unit (Leq) is a time-averaged measure of the fluctuating acoustic pressure energy that is expressed in a logarithmic decibel unit (dB). According to Parliament in the United Kingdom, residential areas exposed to more than 69 dB Leq over a 16 hour period should receive assistance or compensation by the airport [1]. The impact of aviation noise on personal health and quality of life is recognised as an issue, and further details to this subject can be found in the report published by the House of Commons [1].

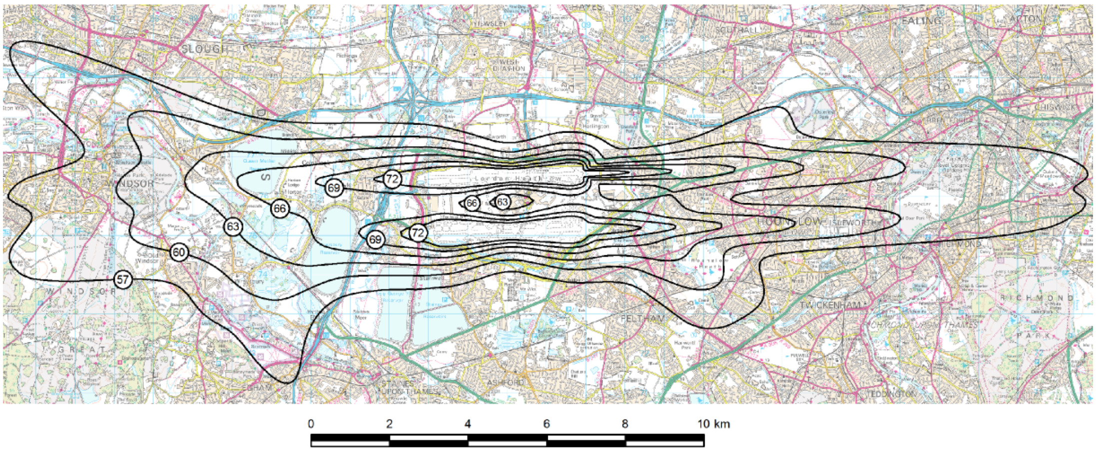

Figure 1.1: Contour map of the equivalent continuous noise level (Leq) for day operations at Heathrow airport, London, United Kingdom [2] for the year 2013.

The International Civil Aviation Organization (ICAO) acts through the United Nations to propose noise certification standards known as Chapters, proposing the allowable noise emissions of an aircraft during take-off and landing. Once new Chapters are established each ICAO member applies these standards to its own country. The progressive Chapters dictate stricter noise levels. In 2002, Chapter 3 was introduced and in the same year aircraft falling under Chapter 2 were banned from operating in the European Union. More recently, in 2006 Chapter 4 was introduced requiring that all future aircraft be 10 dB quieter with respect to the standards of Chapter 3. The next Chapter is expected for 2017 and will demand a 7 dB reduction compared to Chapter 4 standards [1]. In the United Kingdom laws have been introduced to permit an airport authority to charge aircraft operators for the use of the airport based on noise and emissions [3]. These incentives from international and local government bodies drive the development of quieter and cleaner aircraft.

During the take-off phase the majority of aircraft noise is radiated by the engines. However, on approach and landing, the airframe noise can dominate [4, 5]. The landing gear has been identified as a major source for airframe noise. The landing gear is a system of multiple bluff bodies with a large range of scales that are closely spaced. This design induces a highly separated and unsteady flow field, which can be extremely complex and leads to broadband noise characteristics.

Noise reduction strategies apply modifications to current landing gear designs based on the understanding of the noise generation mechanisms. Many studies have identified that the noise generation of the major sources are sensitive to the Reynolds number [6] and the upstream flow conditions [7, 8]. Noise reduction methods have been proposed by means of a drastic re-design of the landing gear components [9, 10]. Additionally, less drastic changes have also been suggested, by modifying the bogie toe angle [11] or by adopting a fairing [12], for example.

Experimental measurements and numerical simulations of main landing gear (MLG) models typically include the largest components to ensure that a similar flow field to that of a full-scale aircraft can be obtained. The leg-door of a MLG is one of the larger components of the assembly, with dimensions that are comparable to the length of the main strut. Some experimental studies suggest that the additional noise due to the presence of a MLG leg-door is small [12, 13]. However, these studies considered a single leg-door design. The noise radiated by the MLG components is sensitive to the local flow conditions, which may be affected by changes in the MLG design [9, 10, 12]. Therefore, the close proximity of the leg-door to neighbouring bluff-body components, together with its relatively large scale, suggests that variations in the leg-door design may significantly effect the properties of surrounding noise sources. Studies of the MLG leg-door interactions may provide a more clear understanding to the noise generation mechanisms, and thereby provide additional means of noise reduction.

1.1 Research objectives

The objective of this Ph.D project is to study the aerodynamic interactions between a landing gear leg-door and the main strut, and to determine the subsequent impact on the radiated sound. The effect of the proximity between these two components has briefly been studied in the past [8]. However, the effect of the leg-door angle of attack has never been studied. The tools available for the investigation are: low-order computational fluid dynamic (CFD) solvers, an in-house high-order computational aeroacoustic (CAA) solver, and the 2.1 m ×1.5 m wind tunnel facility, at the University of Southampton.

To achieve the goals of this project, the work is divided in the following manner.

1. **Experimental measurements**
   Experiments are conducted on a leg-door and strut model in a side-by-side configuration to provide initial diagnostics on the effect of the leg-door angle of attack. An experimental database consisting of velocity field, surface pressure, oil flow and mean loads is also developed for validating the numerical predicitons. The experimental work focuses on the aerodynamic quantities and does not include acoustic measurements.
2. **High-order numerical simulations**
   High-order simulations are conducted with an in-house CAA solver. A high quality grid is developed to solve the flow field around a leg-door and strut model at various door angles. The numerical predictions are compared to the experimental measurements for validation. Aeroacoustic predictions of the radiated far-field noise is obtained by the hybrid CAA method, where an acoustic analogy (FW-H equation) is used.
3. **Development of the CAA tools**
   The fidelity of the high-order CAA solver is enhanced to improve the computational efficiency. This is achieved by:
   (a) Improving the accuracy of the numerical solution from structured meshes by deriving and applying an effective grid quality metric.
   (b) Reducing the level of spatial filtering required to ensure the numerical stability.
   (c) Developing an efficient non-reflective outflow boundary condition.

1.2 Original contributions

Some parts of the work in this thesis have been published in conferences, and some are also intended for journal publications. These are:

- **Hybrid finite-difference and finite-volume solver for CAA**
  A hybrid finite-difference and finite-volume solver was developed. The novel solver is more robust to conventional high-order finite-difference solvers, and it has validated on a single cylinder flow, a tandem cylinder benchmark, and an isolated complex wheel.

  M. Wang, R. Fattah, D. Angland, and X. Zhang, "High-order hybrid cell-centered method for computational aeroacoustics," in *21st AIAA/CEAS Aeroacoustics Conference*, no. AIAA 2015-3279, 2015

- **Non-reflective outflow boundary conditions for CAA**
  The performance of several non-reflective boundary conditions were evaluated using a simplified test case. From this study, the characteristic boundary conditions were identified as the most effective. A novel boundary condition, based on the characteristic method, was developed for computational aeroacoustic simulations. This boundary condition provides significant improvements in the performance compared to existing boundary conditions.

  J. Gill, R. Fattah, and X. Zhang, "Evaluation and development of non-reflective boundary conditions for aeroacoustic simulations," in *21st AIAA/CEAS Aeroacoustics Conference*, no. AIAA 2015-2677, 2015

- **The effect of the door angle on the interaction between a MLG leg-door and the main strut in a side-by-side configuration**
  The aerodynamic interaction between a landing gear door and a cylinder element in a side by side configuration was studied by experiments and numerical simulations. The numerical results were validated by the experimental measurements. The variation of the door angle was found to modify the aerodynamic interaction between the two components. The effect of these changes to the noise radiated to the far-field was determined by using an acoustic analogy.

  R. Fattah, Z. Hu, and D. Angland, "Aeroacoustics of a landing gear door," in *19th AIAA/CEAS Aeroacoustics Conference*, no. AIAA 2013-2259, 2013

- **An effective grid quality measure for structured grids**
  A high grid quality is required for high-order simulations. High-order methods provide a high fidelity solution, if the use spatial filtering and artificial dissipation, which ensures numerical stability, is minimised. The grid quality for high-order solvers may contain geometric features that induce numerical instabilities. A grid quality metric that correlates strongly to the solution accuracy is derived. The correlation between the grid quality metric and the solution accuracy was measured

using a vortex convection benchmark case. Finally, a grid optimisation procedure was outlined and demonstrated using the vortex convection benchmark.

R. Fattah, D. Angland, and X. Zhang, "A priori grid quality estimation for high-order finite differencing," *Journal of Computational Physics (Article under preparation)*, 2016

1.3 Thesis outline

This thesis is organised as follows. Firstly, in Chapter 2 the literature of recent, and significant, works related to the Ph.D project are reviewed. This literature review is concluded by an overview of the current state of landing gear noise research. In Chapter 3 the experimental and numerical methods used for the project are detailed. An evaluation of these methods is also provided, highlighting any limitations or drawbacks of the methods. At the end of Chapter 3, the interaction model consisting only of the leg-door and the main strut is defined, that has dimensions that are representative of a full-scale MLG. Influential design parameters that may affect the landing gear leg-door and main strut interaction are discussed, with the aid of 2-D low-order URANS predictions. The experimental measurements conducted on a 26% scaled interaction model are detailed in Chapter 5. In Chapter 6 the experimental database is compared to the high-order numerical predictions for validation. The effect of the leg-door angle on the far-field noise radiation is also described in Chapter 6, where the FW-H equation is solved using the numerical data. A detailed summary of the work is provided at the end of each Chapter, and a summary of the entire project is also provided in Chapter 7. Further work is also discussed in this final chapter.

Chapter 2

Review of previous works

The aim of the current project is to determine the aerodynamic and aeroacoustic effects of varying the landing gear leg-door angle, on a simplified MLG model that consists of the leg-door and the main strut only.

In this section a review of the literature on the subject of airframe and landing gear noise is divided in the following manner. First the principles of aerodynamic sound generation and bluff body flows are outlined. This is followed by a review of recent works on the experimental measurements and numerical simulations of MLG. The current state of MLG noise research is then overviewed, and the novelty of the current project is discussed. Finally, the literature on the subject of cylinders and inclined rectangular plates in isolation and in interaction, are reviewed as these areas relate more specifically to the current work.

2.1 Principles of aerodynamic sound

The mechanisms of aerodynamic sound generation, according to density-based acoustic analogies, are outlined in this section. Noise sources can be described by the use of acoustic analogies that are derived as a rearrangement of the continuity and momentum conservation equations, which are

$$\frac{\partial \rho}{\partial t} + \frac{\partial \rho u_i}{\partial x_i} = 0, \tag{2.1}$$

$$\frac{\partial \rho u_i}{\partial t} + \frac{\partial \rho u_i u_j}{\partial x_j} = -\frac{\partial p}{\partial x_i} + \frac{\partial \tau_{ij}}{\partial x_j}, \tag{2.2}$$

where ρ is the density, t is the time, p is the static pressure, u_i and x_i are the velocity and the axis coordinate in the i^{th}-direction, respectively. The shear stress term τ_{ij} can be expanded as

$$\tau_{ij} = 2\mu\left(S_{ij} - \frac{1}{3}S_{kk}\delta_{ij}\right), \tag{2.3}$$

where μ is the dynamic viscosity, δ_{ij} is the Kronecker delta function, and S_{ij} is the strain rate tensor defined as,

$$S_{ij} = \frac{1}{2}\left(\frac{\partial u_i}{\partial x_j} + \frac{\partial u_j}{\partial x_i}\right). \tag{2.4}$$

By manipulating these conservation equations, an acoustic analogy can be obtained. An acoustic analogy is an inhomogeneous wave equation with source terms on the right hand side that describe the sound generation mechanism. Outside the source region, the source terms go to zero, and the homogeneous wave equation is recovered. Acoustic analogies can be categorised into density-based, Π-based[1] and enthalpy-based formulations [18]. These variants differ in their arguments of which terms belong on the left and right hand sides of an analogy, and by their level of complexity. The majority of airframe noise calculations apply density-based analogies. Therefore, only this category is discussed. However, a full review of these analogies can be found in [18].

2.1.1 Aerodynamic sound from unbounded flows

Lighthill's description of aerodynamic sound [19] is derived by considering an unbounded fluid with no external forces. By taking the difference between the time derivative of the continuity equation and divergence of the momentum equation, we obtain

$$\frac{\partial^2 \rho}{\partial t^2} = \frac{\partial^2}{\partial x_i x_j}\left(\rho u_i u_j + p\delta_{ij} - \tau_{ij}\right), \tag{2.5}$$

where ρ is the density, t is the time, x_i is the spatial coordinate tensor, u_i is the velocity tensor, p is the static pressure and τ_{ij} is the stress tensor. The wave operator on the left hand side of Equation 2.5 can be obtained by applying the term $-c_0^2\nabla^2\rho$ to both sides. To ensure that the wave operator applies to an acoustic field, the density field is decomposed as the sum of the time-averaged $\overline{\rho}$, and the disturbance ρ' quantities . This yields Lighthill's acoustic analogy

$$\frac{\partial^2 \rho'}{\partial t^2} - c_0^2\frac{\partial^2 \rho'}{\partial x_i^2} = \frac{\partial^2}{\partial x_i \partial x_j}\left[\rho u_i u_j + (p - c_0^2\rho')\delta_{ij} - \tau_{ij}\right] = \frac{\partial^2 T_{ij}}{\partial x_i x_j}, \tag{2.6}$$

---

[1] a logarithmically scaled pressure field defined by $\Pi = \frac{1}{\gamma}\ln(\frac{P}{P_0})$

where T_{ij} is the Lighthill stress tensor that describes the sound generation by the distributions of the Reynolds stresses, the entropy variations, and the viscous stresses. The disturbance density ρ' tends to an acoustic quantity towards the limit of very small perturbations (i.e., $\rho'/\overline{\rho} << 1$). This is due to the implicit definition of the disturbance density, which does not explicitly differentiate between acoustic, vortical or entropy disturbances. The strength of the quadrupole source, per unit of volume, is specified by the Lighthill stress tensor, T_{ij}.

An approximation of Lighhill's equation is given by Powell's analogy [20]. By assuming that the conditions inside the source region are incompressible, and that viscous and entropy terms do not contribute, Lighthill's analogy may be rewritten in vector notation as

$$\frac{\partial^2 \rho'}{\partial t^2} - c_0^2 \frac{\partial^2 \rho'}{\partial x_i^2} = \nabla \cdot \left[\rho \left(\vec{\omega} \times \vec{u} \right) + \frac{1}{2} \nabla \left(\rho \vec{u} \cdot \vec{u} \right) \right], \tag{2.7}$$

where $\vec{\omega} = \nabla \times \vec{u}$ is the vorticity vector, $\vec{u}$ is the velocity vector, and ρ is the density. In Powell's analogy, the sources are dipole, and the role of vorticity is explicit.

2.1.2 Effect of solid boundaries and source motion

Lighthill's analogy is limited to an unbounded medium, which is applicable to jet flows. Curle [21] extended Lighthill's analogy to account for the presence of solid boundaries. However, the most general acoustic analogy is provided by the Ffowcs-Williams and Hawkings (FW-H) [22] equation, which additionally includes the effect of source motion. The FW-H equation is

$$\left(\frac{\partial^2}{\partial t^2} - c_0^2 \frac{\partial^2}{\partial x_i^2} \right) \left(H(f) \rho' \right) = \frac{\partial^2}{\partial x_i x_j} \left[T_{ij} H(f) \right] - \frac{\partial}{\partial x_i} \left[L_i \delta(f) \right] + \frac{\partial}{\partial t} \left[Q \delta \left(f \right) \right], \tag{2.8}$$

where T_{ij} is Lighthill's stress tensor, and f is a scalar field such that $f = 0$ defines the boundary of a moving surface, and the regions inside and outside that moving surface are specified by $f < 0$ and $f > 0$, respectively. This bound is applied to the governing equations by a Heaviside function $H(f)$, which takes the value of zero when $f < 0$ and a value of 1 when $f \geq 0$. By following the same procedure in the derivation of Lighthill's analogy, the FW-H equation is obtained. The FW-H equation contains additional dipole and monopole sources terms that are due to the additional effects of a moving boundary. The dipole source term can be expanded as

$$L_{ij} = P_{ij} n_j + \rho u_i \left(u_n - v_n \right), \tag{2.9}$$

where $P_{ij} = p\delta_{ij} - \tau_{ij}$ is the compressive stress tensor, u is the fluid velocity, v is the surface velocity, and the subscripts i and n denote the components in the i^{th} and surface-normal direction, respectively. The monopole term can be expanded as

$$Q = \rho_0 v_n + \rho \left(u_n - v_n\right), \tag{2.10}$$

which accounts for the presence of an unsteady mass addition, and surface boundary movement. The absence of a solid boundary simplifies the FW-H equation to Lighthill's analogy.

2.1.3 Summary

An acoustic analogy is an inhomogeneous wave equation with source terms on the right hand side, which is derived from the continuity and momentum conservation equations. The aerodynamic noise by an unbounded medium is classified as a quadrupole source, and is due to the distributions of entropy fluctuations, the Reynold's stresses, and the viscous stresses. Source regions that contain a stationary and solid boundary additionally contain a dipole term, which is dominantly due to the boundary pressure distribution. Finally, the effects of solid boundaries in motion are accounted for by an additional monopole source term. Away from the source region, the right hand side terms tend towards zero, and the homogeneous wave equation is recovered. By applying dimensional analysis with a free-space Green's function, the far-field sound intensity due to the quadrupole sources can be shown to scale with the 8th power of the flow speed [23, 24]. By a similar analysis, the far-field sound intensities of the dipole and monopole sources scale with the 6th and 4th power of the flow speed, respectively [24]. These application of acoustic analogies to airframe noise calculations are be discussed further in Section 2.3.2.

2.2 Bluff body flows

The landing gear is an assembly of multiple components of varying size. Many of the components may be classified as bluff bodies. Bluff bodies are unstreamlined geometries that generate a relatively large low-pressure wake. This is generated by the early separation of the boundary layer, and this separation is caused by the presence of a strong adverse pressure gradient. The properties of the wake can vary with the flow Reynolds number.

The near-wake formation of vortices behind a smooth cylinder at very low Reynolds numbers $5 < Re < 40$ is illustrated in Figure 2.1. Many of the initial studies into bluff body flows relied on qualitative analysis of photographs obtained experimentally [25, 26].

These include the data from phase-averaged streamline and streakline images. Streamline patterns are derived from an instantaneous velocity field, and streaklines outline the path of a fluid particle across time. These lines are equivalent for steady flows. The streamline patterns in Figure 2.1 resemble a closed cavity flow in which two symmetric and opposing vortices reside. The symmetric feature of the steady state restricts any streaklines crossing the stream-wise symmetry plane of the cylinder. At higher Reynolds numbers, $Re > 40$, laminar vortex shedding is present and the previously closed cavity becomes open. An *alleway*, as described by Perry *et al.* [25], forms across the open cavity, which allows some fluid to entrain across the symmetry plane to the other side. This entrainment is key to the interaction of the shear layers on opposite sides of the bluff body, and leads to the formation of a periodic and unsteady pattern, shown in Figure 2.2, which is known as the Von-Kármán vortex street.

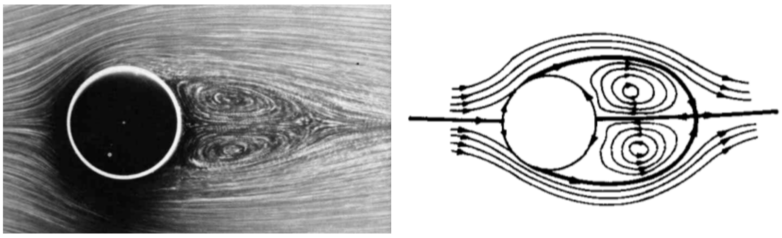
(a) $Re = 26$ [27]   (b) Streamlines by Perry *et al.* [25]

Figure 2.1: The laminar flow around a circular cylinder.

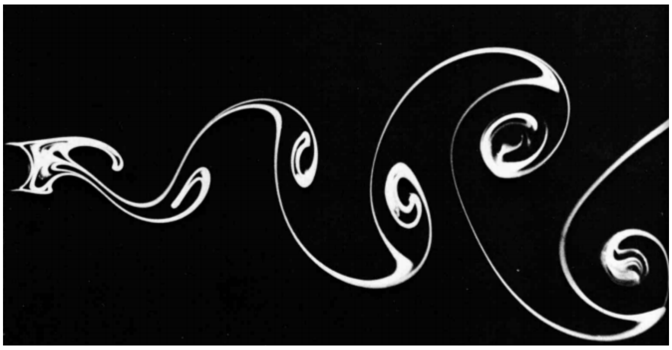

Figure 2.2: The Von-Kármán vortex street flow visualisation around a circular cylinder at $Re = 140$ [27].

A theory to the mechanisms forming of the Von-Kármán vortex street was proposed by Gerrard [26] and is explained using Figure 2.3. The mechanism is driven by the entrainment of fluid from the shear layer (SL_2) associated with the weaker vortex (V_2), to the larger vortex (V_1). The entrainment of this fluid diverges into three paths labelled A, B, and C. The vortex shedding mechanism is described by three key stages:

1. **Entrainment path formation**

   The wake region becomes asymmetric as one vortex becomes larger than the other.

An entrainment path forms where the vorticity generated by the shear layer, associated with the smaller vortex, is transported across the wake to the other side. In Figure 2.3, the entrainment of fluid is from the shear layer (SL_2) towards the upper shear layer (SL_1).

2. **Vortex growth**
   The vorticity generated by the shear layer (SL_1), and the fluid entrained by path A, contributes to growing the vortex (V_1).

3. **Vortex detachment**
   The entrainment path B provides vorticity of opposite sign to the shear layer that is key to the growth of the primary vortex. This cuts the supply of vorticity and detaches the vortex which is then convected by the mean flow. After detachment, the asymmetry of the vortices switches and an opposite entrainment path is formed, where by the process of vortex growth and detachment repeats itself.

This entrainment process repeats in a periodic manner and at a particular frequency. This mechanism describes the coherent patterns that are found in vortex shedding. The key feature in the mechanism is the interaction between the opposite shear layers, which is due to the presence of an entrainment path.

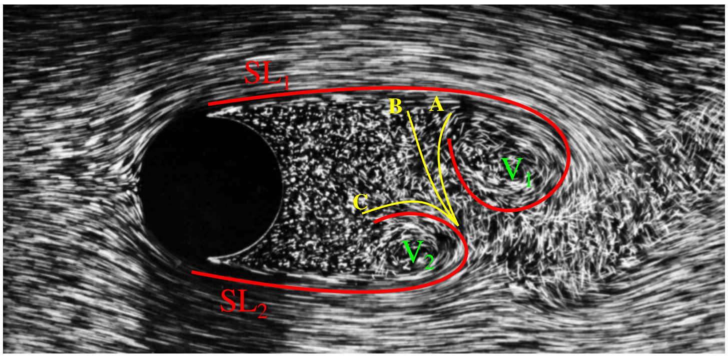

Figure 2.3: Flow around a circular cylinder at $Re = 2000$ [27]. Shear layers (——), vortex core (——), and entrainment paths (——).

The unsteady flow behind a cylinder changes with Reynolds number (Re). These changes are characterised by the base pressure coefficient ($C_{p,b}$) and additionally by the Strouhal number (St). The St is a frequency measure, which is normalised by a reference length, and a reference velocity. The velocity spectra measured in the wake of a cylinder flow contains a dominant tone at a particular Strouhal number. The variation of the St with Reynolds number is illustrated in Figure 2.4. Flow regimes are defined across the Re, across which major changes in the boundary layer properties occur. The three primary flow regimes are the sub-critical, critical, and the post-critical regime [28].

The sub-critical range is for $40 < Re < 1.3\times10^5$ where laminar boundary layer separation occurs. Upon separation the shear layer instabilities trip the flow to a turbulent state.

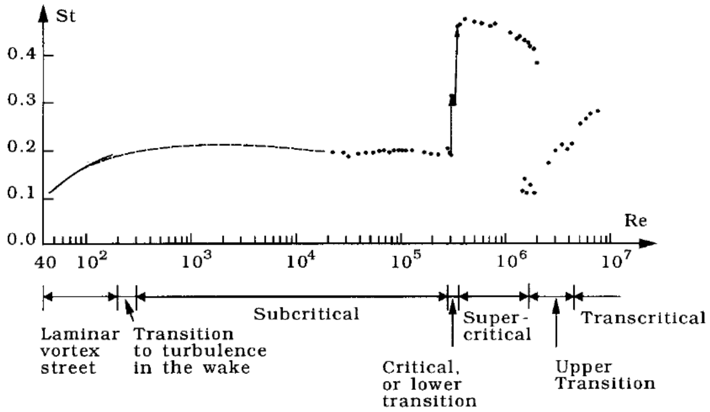

Figure 2.4: Dominant Strouhal number variation with Reynolds number [29].

However, no flow reattachment occurs and the early flow separation induces a wide wake. This induces a low-frequency vortex shedding at $St = 0.2$. In the post-critical regime $Re > 1.9 \times 10^6$ the separation points are shifted due to a fully turbulent boundary layer on both sides, which mixes high momentum fluid towards the wall. A turbulent boundary layer delays the separation point, which generates a narrower wake. For a narrower wake, the shear layers are positioned closer to each other, resulting in a higher frequency vortex shedding. The Strouhal number of the dominant tone can range in this regime between $0.25 < St < 0.3$ [29]. Between these flow regimes lies a critical regime at $Re \approx 1.5 \times 10^6$ [29] where the boundary layer transition occurs near the separation point. This generates lee-wake vortices which form irregular and disorderly shedding [29].

A Narrower wake generates smaller vortices that induce smaller fluctuating loads, as well as a lower pressure drag. The thresholds between the flow regimes are sensitive to the free-stream turbulence and surface roughness, as they can influence the boundary layer separation position along geometries with a continuous and smooth cross-section [28, 29].

The vortex shedding behind other bluff bodies, such as rectangular plates and wedges, follows a similar mechanism as described by Gerrard [26] and Perry *et al.* [25] . However, the effect of Re on the dominant St, shown by Figure 2.5, is different for the various cross-sections. The lack of dramatic changes between flow regimes for particular geometries may be due to the presence of sharp features that induce flow separation by a highly adverse pressure gradient, which is less sensitive to the boundary layer state. The three-dimensionality of the flow along the span of a two-dimensional cross-section is affected by the Re [28, 30]. Confinement of the span-wise flow can induce an increased span-wise coherence and reduce the dominant Strouhal number [28].

This outlines a general description of bluff body flows. A more detailed description, particularly on rectangular plates and the of cylinders near flat plane boundaries, is provided in a later section. Prior to that, in the following sections the components of

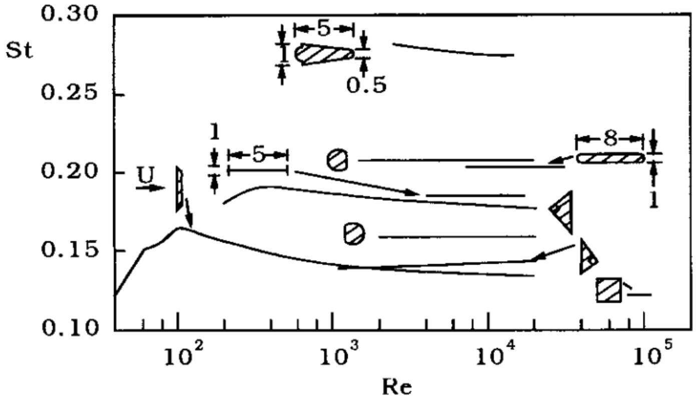

Figure 2.5: The effect of bluff body geometry on the dominant Strouhal number variation with Reynolds number [29].

interest from a main landing gear are identified and a general overview of the state of landing gear noise research is outlined.

2.3 The main landing gear

The landing gear (LG) is the undercarriage assembly that supports an aircraft when it is on the ground. A conventional landing gear configuration consists of a nose landing gear (NLG), which provides the steering capability, and the main landing gear (MLG) that provides most of the support. On large commercial aircraft the MLG design is consistently similar between models and is composed of several major components. These major components are illustrated in Figure 2.6, which also highlights the design similarities between a Boeing and Airbus model.

The noise generated by the MLG is more significant for wide-body aircraft [11]. The far-field noise spectra from a MLG varies with the observer position, but it consists primarily of a broadband characteristic with a maximum amplitude towards lower frequencies, which is associated with the larger components such as the bogie section. This aerodynamic noise is generated by the largely separated and unsteady flow around an assembly of multi-scaled bluff bodies. Simple bluff bodies in isolation induce aeolian tones, however bluff bodies placed in close proximity, or in tandem to other components, generates a more broadband spectra that is also more intense. This is due to additional noise generated by the impingement of upstream vortices on downstream components. The following sections of LG studies are divided into experimental measurements and numerical simulations.

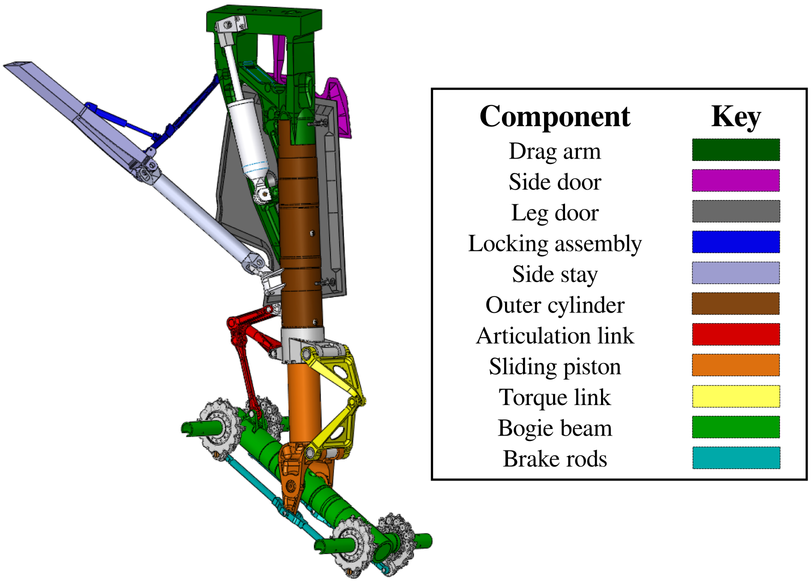

(a) A340 MLG CAD courtesy of Airbus

(b) B777 MLG [31]

Figure 2.6: Main landing gear key components.

2.3.1 Experiments on landing gears

Experimental measurements provide realistic data that can be used for validating computational methods. They are also useful in studying complex geometries where computational studies would otherwise be too costly. Airframe noise experiments can be conducted either by full-scale flyover measurements, or by using scaled wind tunnel models. Table 2.1 outlines the works that are discussed in this section to provide an overview on the range of model scale, *Re* and database measurements that are present in MLG experiments.

Flyover measurements are acquired from a microphone array placed on the ground that records data whilst the aircraft passes over it. This information can be used to compute noise source maps using techniques such as beam-forming, which help in identifying the location of noise sources at particular frequencies [12, 13, 31]. Fly-over tests also give an insight into the characteristic contributions of isolated components, such as flaps and landing gears. This is done by calculating the differences in the measurements recorded with a selective deployment of aircraft components [4, 31]. Finally fly-over tests also provide validation databases to compare against wind tunnel data [12] and empirical predictions [32, 33] as the measurements are obtained under realistic flow and flight conditions.

Wind tunnel experiments are conducted on scaled-down models to ensure an acceptable blockage ratio. Some data, acquired from larger facilities, have tested on larger, or full scale models [9, 34]. The variations between a full-scale fly-over test, to a wind tunnel test, may be due to the following:

- **Effects of the model scale and details**
  The disparity in the model scale and level of details can cause significant differences between the measurements recorded on scaled and full-scale models. This effect is due to the Reynolds number sensitivity of the major flow features [6]. Model detail can also affect the recorded noise measurements. Guo *et al.* [33] found that various components of the LG contribute to a band of low, medium or high frequency noise. Additionally, the different frequency components have different dependencies on the flow parameters. Finally, the scale of the model affects the blockage ratio in the test section, which can affect the aerodynamics. The model fidelity and scale is mostly determined by the resources of time and finance [35].

- **Effects of the model configuration**
  In full-scale fly-over tests the approach angle of the aircraft may vary and this influences the effective inflow conditions upstream of the LG geometry [7]. The changes to the inflow conditions for a wing-mounted LG are affected by the circulation induced by the high-lift devices (HLD) [7]. In several studies this induced circulation is ignored, and the LG assembly is simply mounted along a wall [9, 36], or beneath a flat plate [12, 33]. In some works, the approach angle is modelled [9, 13] to a 6 degree angle of attack, by inclining the LG model relative to the plane boundary [9].

- **Effects of large scale interactions**
  Large scale interactions may exist between different airframe components. Guo [7] studied the potential impact of the flow variations due to the circulation induced by a HLD for a wing-mounted LG. The circulation reduces the effective inflow velocity to the bluff body assemblies, and thereby reduces the acoustic intensity of the source. Horne *et al.* [13] conducted a 26% scale semi-span aircraft model with the HLD and LG assemblies and observed a small impact of increasing angle of attack on the noise levels. They also observed changes to the flap noise at 1.4 kHz and attributed it to the MLG interaction. Large scale interactions can

also exist between neighbouring LG. Close placement of multiple LG is present for large wide-body aircraft such as the Boeing 747, and the Airbus A-340 and A-380. Dobrzynski *et al.* [37] studied noise generated by a centre landing gear (CLG) and MLG in various span-wise and stream-wise separation distances. The measurements show that the maximal excess interaction noise of 6 dB occurs for in-line gear arrangements for $f < 30$ Hz (full-scale), and a broadband noise reduction above $f > 100$ Hz (full-scale).

The leg-door of a MLG system is quite large and is included in some high-fidelity models to provide more realistic flow conditions around potential noise sources. The leg-door is inclined to the flow at an angle of approximately 8 degrees [36], to help with its deployment in the event of hydraulic power loss [13]. Horne *et al.* compared the noise spectra from a traversing array on three MLG configurations deployed on a 26% scale, full-aircraft semi-span model. The first configuration consisted of a high-fidelity LG model with the leg-door door, and the other two configurations were of simplified models with and without doors. They concluded that no consistent effect of the doors was present. However, Humphreys and Brooks [12] observed changes to the noise spectra from their 6.3% scale isolated MLG model, which is similar in design to the 26% MLG model. Humphreys and Brooks investigated the changes to the noise directivity pattern at various frequencies from four MLG configurations, to evaluate the effects of the leg-door, and additionally the effects of a bogie fairing. The measured data ranges for a full-scale frequency of $125 < f < 6000$ Hz. Differences in the directivity pattern, of up to 5 dB, were observed along side-line and overhead observer positions due to the presence of the leg-door. The most significant changes due to the leg door are illustrated in Figure 2.7 at a full-scale frequency of $f = 200$ Hz and $f = 6300$ Hz. Some acoustic shielding seems to be present at the higher frequency. In the lower frequency plot, the differences are likely due to the aerodynamic interactions between the leg-door and nearby components, which affects the SPL along the fly-over axis. The potential additional noise sources due to the leg-door include the door tip vortex, and the noise generated around the attachment braces [13]. Furthermore, the close-proximity of the leg-door to nearby components may induce aerodynamic interactions which may affect the noise generated from nearby components. Finally, an outline of recent experimental works on MLG noise is listed in Table 2.1.

Year	Author	Re_D (M)	Measurement	Comments
2002	Dobrzynski et al.	(0.2)	FFM	FS 2-wheel NLG, 4 & 6-wheel MLG
2002	Lazos	6×10^5	PIV, MP	31% 4-wheel simplified MLG
2005	Horne et al.	(0.12-0.24)	PMA	26% scale MLG on a semi-span model
2006	Guo	(0.18-0.24)	MA,FFM	FS 2-wheel NLG
2007	Remillieux	(0.118-0.169)	PMA. DP.	26% scale 6 Wheel MLG
2009	Manoha *et al.*	(0.18-0.23)	MP,UP,MA	40% scale 2-wheel NLG (Lagoon)
2009	Neuhart *et al*	7.3×10^4(0.166)	MP,UP,PIV	25% scale 2-wheel NLG (G550)
2009	Humphreys and Brooks	$2.1 - 3.3 \times 10^5$(0.11-0.17)	NS, DP	6.3% scale 6 Wheel MLG
2011	Spalart and Mejia	$10^6(< 0.2)$	OF,MP,UP,ML	28% scale 4-wheel MLG

Table 2.1: Table of experimental works on LG geometries. Measurement key: PMA - Phased Microphone Array, MA - Microphone array, FFM - Far-field Microphone, NS - Noise spectra, DP - Directivity Profile, MP - Mean Pressure, UP - Unsteady Pressure, PIV - Particle Image Velocimetry, HW - Hot Wire Anemometry, LDV - Laser Doppler Velocimetry, ML- Mean Loads.

(a) Model variations: with the leg-door (left), and without the leg-door (right).

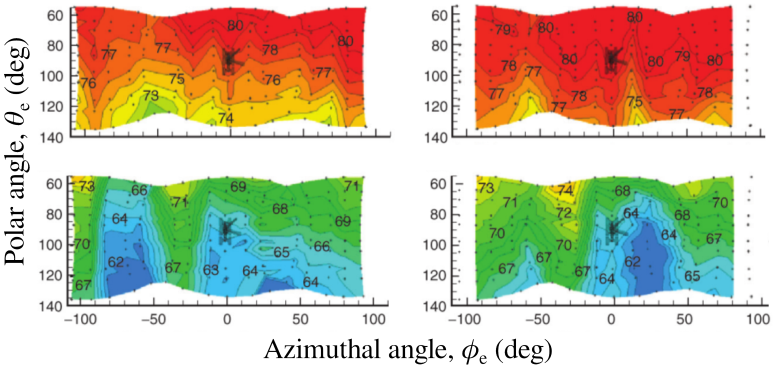

(b) Directivity variations at full-scale frequencies of $f \approx 200$ Hz (top) and at $f \approx 6300$ Hz (bottom). Data with the leg-door (left), and without the leg-door (right).

Figure 2.7: Effect of the leg-door on the directivity patterns from a 6.3% scale MLG model[12] at two frequencies.

2.3.2 Numerical simulations of landing gear

Computational aeroacoustic (CAA) simulations employ numerical methods to solve governing equations that describe the fluid dynamics in a discretised space. The strategy that is typically applied to airframe noise studies is outlined in Figure 2.8. There are four aspects to noise calculations; the problem description, the noise source definition, the noise propagation modelling, and far-field sound prediction. The problem description and the available computational resource determines the likely strategies applied to a particular study. However, the two key areas for an accurate CAA simulations lies in a well defined noise source and correct sound propagation. Studies focusing only on the propagation phenomena may employ simplified models, such as the linearised Euler Equations (LEE). However, studies on MLG apply a hybrid CAA method, where the noise generation and propagation effects are evaluated in the near-field region, and the far-field acoustics are obtained by the use of an acoustic analogy (e.g., the FW-H equation). Therefore, the subject of noise propagation modelling is included in Figure 2.8 to outline the general CAA methods, but further discussions about this subject are not included.

The effects of the near field sources on the far-field radiation are evaluated by the application of a free-space Green's function and a description of the near field source

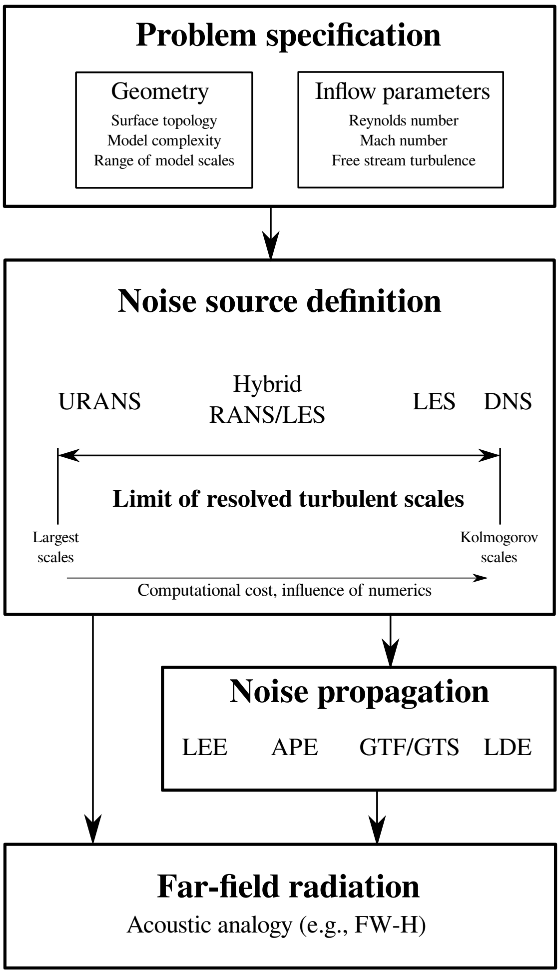

Figure 2.8: A simplified hierarchy of noise prediction methods.

terms. Early applications of the FW-H equation utilised a solid integration surface, which was placed along a physical surface. This confines all the flow non-linearities to the volume integral [38] in Lighthill's stress tensor. The volume integral extends away from the integration surface and early solutions ignored its contribution to save in computational effort. This approximation is valid at low Mach numbers [38]. The volumetric source term effects can be contained within the surface integration terms when the FW-H surface is placed away from the source region. This requires the use of a penetrable, or permeable, integration surface such as the Kirchhoff formulation. The Kirchhoff method is limited by the requirement that the integration surface must be placed in the region of the flow that is governed only by linear effects [39]. A permeable formulation of the FW-H equation was described by Ffowcs-Williams and Hawkings [22] and allows for some of the quadrupole source effects to be accounted for by the surface terms [38]. Singer *et al.* [40] evaluated the permeable FW-H method, and showed that accurate predictions from non-compact sources could be obtained. However, differences are consistently found between varying off-body surfaces, that cross through areas of strong vorticity. The convection of non-acoustic sources through the integration surface was tested on the flow around a smooth cylinder [40], and found to have small effects on the far-field directivity. Lockard [41] estimated that the non-acoustic source contributions along an integration surface are important for $M > 0.5$. However airframe studies at lower Mach number [42, 43, 44] suggest that there is a noticeable impact of these non-acoustic sources. The acoustic analogies are derived by decomposing the fluid flow into a time averaged and a disturbance quantity which are independent of each other. The lack of an explicit differentiation between acoustic, vortex or entropy disturbances means that the formulation provides a description of acoustic waves at the limit of extremely small perturbations, i.e., $\rho'/\overline{\rho} << 1$. This limitation may be the cause of the discrepancies observed in the far-field signals computed by different permeable surfaces. Methods to minimise the effect of non-acoustic sources, convecting through an integration surface, employ open-ended integration regions [42, 43], or by attempting to isolate non-acoustic sources. The latter can be achieved by a correction equation [41], or by post-processing the FW-H data from multiple outflow faces [42]. Overall differences to the far-field sound predicted by off-body and on-body surfaces are consistent in the over prediction due to the vorticity disturbances across the outflow face. Spalart *et al.* [42] observed differences that exceeded 5 dB from a the MLG calculation, and similar differences were also observed by Lockard [45].

The solution to the FW-H equation can be obtained by the retarded-time method, or with the advanced-time formulation. Farassat's Formulation 1A [46] employs the retarded-time method. In this method, a summation of all the perturbations reaching the observer at a specific time provides the acoustic far-field signal at the specified reception time. Depending on the velocity and location of the observer and the source, the aforementioned perturbations may be emitted at different retarded times. This method requires the source information to be defined at each point along the the integration surface with a sufficiently long time signal and therefore requires a large amount of computer memory. Casalino [38] proposed the advanced-time formulation, which reduces the computational memory required. However, the most common method is the Farassat Formulation 1A. These methods require an accurate description of the near-field flow field, which determines the noise source properties. For airframe CAA calculations, the description of the noise sources is determined by the turbulence modelling strategy.

2.3.3 Noise source modelling

Chu and Kovansznay [47] showed that the Navier-Stokes equations are a composition and interaction of acoustic, vorticity, and entropy fluctuations. Part of these fluctuations describe the aerodynamic noise sources. For airframe studies, such as on MLG containing largely separated flows, the turbulent flow is the primary mechanism for noise generation. The ratio between the largest and smallest scales in a turbulent flow, as described by the Kolmogorov hypothesis, scales with $Re^{9/4}$ [48]. The computational cost of numerical simulations is measured by the number of grid points, and an estimate of 10^{16} grid points [49] is required for a direct numerical simulation (DNS) of an airframe calculation at realistic *Re*. Furthermore, the accuracy of numerical methods becomes more important for DNS calculations, and so it tends to be applied for simple geometries such as jet flows [50, 51]. The methods employed on airframe noise calculations use the following turbulence modelling strategies:

- **Reynolds Averaged Navier-Stokes (RANS)**
  The RANS equations show that the mean velocity field is affected by the Reynolds stresses [40, 48]. These stresses have a wide range of scales and the entire range is modelled by additional transport equations that describe the production, destruction and diffusion of the Reynold's stresses. Alternatively, the turbulent viscosity hypothesis can be applied [40, 48], which models the Reynolds stress terms in an isotropic manner by adding viscosity. This method models the entire range of scales of the turbulent field and resolves primarily the largest structures. Due to the large levels of dissipation added by the turbulence model, a weak dependency of the results on the numerics is present.

- **Large Eddy Simulation (LES)**
  The LES strategy is based on the Kolmogorov theory of self-similarity. In LES the governing equations are divided into a resolvable and unresolvable spatial scale. The threshold between the two ranges is determined by the local grid spacing and the energy containing range of turbulent scales are resolved by the Navier-Stokes equations. The smaller, unresolvable scales are filtered from the solution and their effects are modelled by a sub-grid scale model. The sub-grid scale model predicts the energy dissipation at the smaller length scales where viscous diffusion becomes significant. LES computations require a very fine grid in the near wall region to ensure an accurate prediction of the boundary layer properties. This makes LES impractical for high *Re* problems. The computational cost required for LES calculations is estimated at a grid count in the order of 10^{11} for an airframe simulation at high *Re* [49]. Imamura *et al.* [43] conducted LES of a 40% scale two wheel MLG and found that the mean surface pressure profile compared poorly against experimental measurements recorded along the wheel centreline. This may be due to a poor wall resolution or a highly anisotropic near-wall mesh. The grid resolution requirement in the near-wall region can be reduced by applying a wall model. A strong dependency of the solution to the numerics is present for LES simulations [50].

- **Hybrid RANS/LES**
  The hybrid method employs RANS models in the near-wall regions and switches to an LES model in the regions dominated by large-scale structures. Detached-Eddy Simulation (DES) is an example of a hybrid RANS/LES method. In DES

> the blending of RANS and LES is achieved by modifying the length scale in the turbulence model. The length scale is unmodified in the near wall region, which enables the RANS mode, and switches to the local grid scale, which enables the LES mode [49]. Further extensions to the DES model have been derived to improve its robustness, such as delayed DES (DDES) and improved DDES (IDDES) [52]. Another extension of DDES, developed by Deck [53], employs a zonal (Z-DES) approach where various DES modes are explicitly defined by the user depending on the expected flow behaviour. The Z-DES method can overcome an identified issue in DES where the natural growth of non-linear instabilities in an LES region may be reduced by the wall functions in the RANS model [54].

The selection of the turbulence modelling has a significant impact on the noise source definition. Lockard *et al.*[44] compared URANS and DES simulations of the flow around a MLG model and found significant differences to the FW-H source strengths at higher frequencies. The FW-H inputs are usually defined by the range of resolved turbulent scales, which is much narrower in RANS compared to DES. The effect of the turbulence model on the mean flow features around bluff bodies has also been noticed [44, 53, 54]. These sensitivities highlight the need for further assessment of the results, and comparisons to experimental data for validation.

The accuracy of the noise source region is additionally affected by the numerical methods. High-order schemes are favoured in CAA applications as they provide a wider spectral range of resolvable scales compared to low-order schemes, for a given grid density. The order of the scheme, derived from a truncated Taylor series, refers to the decay rate of the truncation errors with increased resolution. A scheme can be evaluated by Fourier analysis [55] and can be optimised to minimise the global errors [56]. Higher-order schemes contain desirable properties for efficient CAA simulations. However, high-order schemes also provide low artificial dissipation [55] and thereby become highly sensitive to inaccurate boundary conditions. For instance, outflow boundary conditions are prone to undesirable acoustic reflections that may remain in the domain due to the low levels of artificial dissipation. Any generation or growth of inaccuracies formed within the computation can be treated by artificial viscosity, artificial dissipation, or by a numerical filter [50]. Each of these methods has an impact on the wave properties within a particular range, and is applied with the minimal amount in order to preserve the properties of the waves. The application of artificial viscosity or dissipation in non-linear problems is equivalent to a turbulence model, which may have an impact on the range of scales and thereby affect the accuracy of the description of the noise sources [50]. High-order schemes also conserve the properties of sound propagation, such as the group velocity. Inaccuracies in the sound speed from interacting sources will affect the interference pattern. The requirement for an accurate description of the noise source and propagation phenomena in CAA studies requires for the use of high-order schemes. However, its application is more commonly applied to simplified geometries. CAA studies on more complicated geometries tend to employ low-order schemes [44, 57].

2.3.4 Summary

Fly-over experiments remain an expensive method of investigating aircraft noise, and the majority of knowledge is acquired from wind tunnel experiments and numerical simulations. The major features that affect the overhead noise are the cluster of components within the bogie region [13]. The intensity of the interaction noise emanating from clustered regions can be altered by affecting the upstream conditions, such as the flow velocity and the free-stream turbulent kinetic energy [33]. These variables can be affected by larger scale aerodynamic interactions between other MLG or with the HLD.

Noise predictions by hybrid RANS/LES methods for MLG simulations [42, 58] are favourable as they provide a noticeable improvement to the spectral resolution of the resolved turbulent flow in comparison to URANS simulations [44]. The extended resolution of the noise source spectra improves the frequency resolution of the far-field predictions. Further improvements to the spectral characteristic of the wake region can be achieved by the Zonal DES method [53].

Numerical simulations conducted on complex LG geometries which include, for example, the side brace [59], or the leg-door [44, 57], are evaluated using low-order schemes. However, the use of high-order schemes on LG simulations for effective CAA studies is becoming more common [42, 43, 60]. The numerical models that have greater geometric complexity improve the fidelity of the noise source description, as it includes the interaction effects between the larger components. The addition of components, such as the side brace [59] or the leg-door [57], generates an asymmetry to the geometry and the MLG wake, that affects the far-field directivity pattern [57, 59]. This effect of geometric asymmetry was also observed by experiments [12].

In contrast to the aeroacoustic studies of large complex LG models, isolated studies on individual components on highly simplified geometries have been conducted to assess the potential impact of particular LG design features. For instance, Windiate [61] investigated the effect of the landing gear torque link configuration using a cylinder and torque-link model. Another example is by Van Mierlo *et al.* [62], who studied the effects of the bogie toe angle on a highly simplified MLG. Another example is by Aubert *et al.* [63], who conducted numerical simulations on a simplified cylinder and drag-stay model. Finally, several examples of simplified interaction studies by experiments were conducted by Hutcheson and Brookes [8].

A large component of aircraft MLG that has seen significant differences between model designs, is the landing gear leg-door. Between models, changes to the proximity and incident angle can be observed. The effect, of what is essentially a large flat plate, on the overall noise is not well understood. Currently, empirical noise models assume the acoustic source of the LG leg-door as a trailing edge source [32, 64]. To understand the noise generation mechanisms by a main landing gear door, a simplified model is proposed. This simplified model focuses on the aerodynamic and aeroacoustic interactions between the leg-door and the main strut. The simplified study also makes high-order numerical simulations a viable option due its geometric simplicity. In the following section, the literature specific to leg-door and cylinder flows is reviewed.

2.4 Leg-door and cylinder flows

There are three key areas of further literature to be reviewed. These consider the flows around an isolated cylinder, an isolated door-like geometry and the effect of varying the angle of attack, and on the interaction between a cylinder and door-like geometry. The review of the following works consists of experimental measurements and numerical simulations.

2.4.1 Isolated cylinders at high Reynolds numbers

As previously discussed in Section 2.2, the Strouhal number of the wake generated by a cylinder is sensitive to the boundary layer properties. A potential sources of error in the numerical modelling of cylinder flows can come from the turbulence modelling. Orselli *et al.* [65], and Cox *et al.* [66] investigated various RANS turbulence models on the two-dimensional flow around a cylinder at various Re. They found that different models predicted different energy levels for the vortex shedding, and that the largest differences occurred towards the lower Re range. This difference diminishes as the flow Re exceeds the super-critical threshold. Schewe [30] observed that inherently 2-D geometries consist of 3-D aerodynamic effects, which may partly explain the improvement in the flow field predictions observed by Cox *et al.* [66] when conducting 3-D simulations.

Hybrid RANS/LES, DES simulations have been applied to cylinder flows over a range of Re by Travin *et al.* [67]. Methods that resolve turbulence require the use of a 3-D geometry. In their tests, a span-wise length of two cylinder diameters $2D$ was used. With turbulence models, a set of auxiliary partial differential equations are solved in tandem to the governing equations. These additional equations model the transport of the turbulent viscosity, and are bounded by initial and boundary conditions. In DES simulations, the Spalart-Allmaras (S-A) [68] turbulence model is applied. Travin *et al.* applied different free-stream conditions to the modelled eddy-viscosity ratio. For laminar and turbulent separation cases the free-stream condition was respectively set to $\tilde{\nu} = 0$, and $\tilde{\nu} = 5\nu_\infty$. The skin friction profile for cylinder flows with a laminar separation are predicted well with the DES model. However, at higher Re, the simulations at

$Re > 3 \times 10^6$ over-predict in the skin friction profile significantly. The over-prediction is likely due to the assumption in the RANS model that the boundary layer is completely turbulent, which may induce larger skin friction compared to a laminar boundary layer [67]. Squires *et al.* [69] also observed this over-prediction in the skin friction profile when applying Delayed-DES (DDES) on a cylinder flow at $Re_D = 8 \times 10^6$.

2.4.2 Isolated plates and the effect of angle of attack

The flow field around rectangular shaped bodies has been previously studied. Three key areas of literature are reviewed on this subject. These areas are on the effects of the aspect ratio, the inclination angle, and the leading and trailing edge features. Edge features may be circular (rounded), or bevelled (ramped) to to a sharp edge.

Stokes and Welsh [70] studied the flow around a rectangular bluff body with square edges at low Re and divided into flow regimes depending on its aspect ratio (AR). The rectangular plate induces separated shear layers from the leading edges, which interact with the trailing edge differently depending on the aspect ratio of the plate. For small aspect ratio plates ($AR < 3.2$) the leading edge shear layers do not reattach, and they interact with each other to form a vortex street, similar to the flow around a cylinder. For rectangular plates with an aspect ratio of $3.2 < AR < 7.6$ the shear layers reattach to the trailing edge in a periodic manner, and a coherent wake is formed. On plates with even larger aspect ratios $7.6 < AR < 16$ the leading edge separated flow reattaches upstream of the trailing edge. This difference forms a time-varying separation bubble that generates and detaches packets of vorticity. If significant diffusion of these packets does not occur before reaching the trailing edge, an irregular shedding pattern is generated. Rectangular plates with $AR > 16$ have a large enough length between the separation bubble and the trailing edge to ensure sufficient diffusion of these vortices, and recover the coherent vortex shedding, which is driven by the paring of opposite shear layers. The flow regime confined to an aspect ratio of $3 < AR < 16$ is also influenced by the impingement of the leading edge shear layers. Nakamura *et al.* [71] found that when the vortex shedding wavelength is just beyond the chord length, the vortex shedding mode becomes locked. This first instance occurs when $AR \approx 3$. Higher mode numbers (n) are triggered when the aspect ratio changes with $AR \approx 3n$. This behaviour is referred to as the impinging-shear-layer instability [71] and is due to the interaction of upstream vortices with the trailing edge, and is strongest with the presence of sharp trailing edges. This phenomena was also found when applying the method to rectangular plates with rounded edges [71].

Chen and Fang [72] investigated the flow around a rectangular plate ($AR \approx 7.6$) with three different leading and trailing edges, across a range of angle of attack (AoA), and a Reynolds number range of $(0.35 - 3.2) \times 10^4$. The edges were bevelled at angles of 30, 45 and 60 degrees and induce similar flow features at high AoA. Beyond an AoA of

10 degrees, the bevelled edges and flow Re have little influence to the boundary layer separation point, and a fully detached flow occurs. With larger AoA, the projected height of the plate increases, and therefore larger vortices with lower Strouhal number are generated. The shedding frequency of rectangular plates beyond an inclination angle of 10 degrees scales with the projected height to form a wake region with $St \approx 0.16$. In their experiment, the bevelled features are along the suction surface of the angled plates. Therefore, at lower AoA, the possibility of delayed separation, or reattachment, along the surface is present. This makes the St more sensitive to the AoA and flow Re. At higher Reynolds number the velocity spectra of the wake region becomes broadband [72], which implies that the coherency of the wake diminishes.

Breuer *et al.* [54] conducted numerical simulations of an inclined flat plate at an AoA of 18 degrees and a $Re_c = 2 \times 10^4$. Differences in the mean and unsteady statistics in the near-wake of the separated region were compared between RANS-SA, DES and LES. The mean flow features from the DES were in closer agreement to the LES simulations, while the RANS-SA predictions of the unsteady flow (using URANS) were poor. Further analysis of the DES results showed a lack of breakdown of the leading edge shear layer due to overproduction of the eddy viscosity. One of the reasons for this overproduction in the DES strategy is due to the inclusion of near-wall functions applied to the LES region. A modified model was tested and showed improved predictions. This modified model holds similarities to the Z-DES variant Mode I developed by Deck [53].

2.4.3 Cylinder flows near a plane boundary

Figure 2.9 shows the influential parameters that affect the near-wake behind a smooth cylinder placed near a plane boundary. Price *et al.* [73] conducted experiments at $1200 < Re_D < 4960$ and determined four distinct regions identified across a range of gap distances, described by a normalised parameter $G = e/D$. For narrow gaps ($0 < G < 0.125$) the gap flow is weak and no regular vortex shedding occurs downstream. For gaps in the range of $0.25 < G < 0.375$ the shear layers from the cylinder interacts with the shear layer formed along the plane boundary, within the gap region. For gaps with $G < 0.75$, vortex shedding occurs and there is a reduction in the upstream separated flow, and for $G > 1$ the cylinder flow seems unaffected by the plane boundary. Other experiments show that the boundary layer properties have an impact on the predicted critical gap (G_{crit}) at which regular vortex shedding ceases to exist.

As a cylinder is brought closer to the plane boundary, the stagnation point shifts towards the wall side and induces a steady mean force on the cylinder that is directed away from the wall [74]. The critical gap for suppressed vortex shedding is in the range of $0.2 < G_{crit} < 0.4$. The St measured in the wake is unaffected by G outside the critical regime. The theory to the vortex shedding suppression at small gaps is linked to the cancellation of vorticity due to the interaction of the shear-layers from the wall,

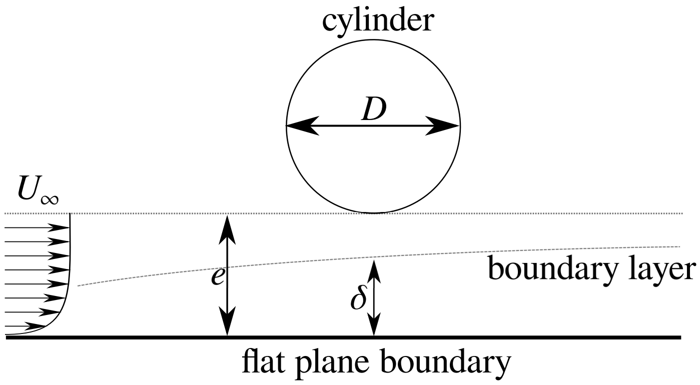

Figure 2.9: Influential parameters that affect the flow around a cylinder placed near a flat plane boundary.

and on the side of the cylinder closest to the wall [73]. Later experiments conducted using a towing tank or a moving ground [75] effectively eliminated the boundary layer along the ground side, however the vortex shedding suppression is still observed. As explained in Section 2.2, vortex shedding mechanisms is driven by the entrainment of fluid across the wake by the interaction of the opposite shear layers along the cylinder. A weak entrainment may suppress the vortex detachment and result in a stable near-wake region. Furthermore, at small gap ratios the outer shear layer does not roll up to form a vortex. At small gap ratios, the vorticity production in the shear layer on the ground side may be reduced due to the favourable pressure gradient induced by the plane boundary. The resulting difference in the shear layer intensity on both sides of the cylinder may result in one vortex overwhelming the other, resulting in a weak pairing and thus a stable near-wake region.

Nishino *et al.* [76] conducted numerical simulations using RANS and DES methods and verified the superiority of DES in predicting the mean velocity field compared against experimental data. This comparison against the experimental data was not included for the Reynolds stresses, which were found to contain discrepancies as shown by Breuer *et al.* [54], due to the over-production of eddy viscosity in the shear layer around the separation region.

Aeroacoustic tests were conducted on a flat plate and rod configuration as part of a wider study of noise generation mechanisms by Hutcheson and Brooks [8]. Their experiment compared the far-field noise induced by door and a rod in a side-by-side configuration with a gap ratio (G) of 0 and 0.133 and at a $Re_D = 4.8 \times 10^4$ ($M = 0.13$). The door element consisted of 30 degree bevels across the leading and trailing edges, and the aspect ratio was 20. The far-field spectra for an observer at 90 degrees, overhead of the model along the door-free side, was compared between two configurations of G and two configurations of free-stream turbulence. Significant changes to the spectra between the two gap configurations were observed within the range of $0.075 < St < 0.379$. In the no-gap configuration, a primary tone forms at a frequency that is much lower than the expected shedding frequency from the rod alone. It may be that under a no-gap configuration, the rod and door act as a single bluff body, which induces a larger characteristic length, and thus a lower shedding frequency. With a gap, the amplitude of the far-field fundamental tone reduces and shifts to a lower frequency. Additionally, a secondary peak forms at the vortex shedding tone of an isolated rod. The noise spectra from a model immersed in a free-stream flow, with a higher turbulent intensity that is generated by a turbulence grid, is broader. Additionally, a significantly weaker tone is generated with the turbulent free-stream flow. The noise generated by the model with a finite gap is weaker than the model that has no gap. This difference is 20-25 dB for the free-stream with a low free-stream turbulent intensity, and 3 dB for grid induced turbulent free-stream flow. The noise scaling of this model is proportional to the 6^{th} power of free-stream velocity, and the directivity pattern closely follows a dipole behaviour, with a maximum deviation of 2.5 dB from a theoretical dipole directivity.

2.5 Summary

Experimental measurements on the MLG have identified the major noise sources. The effect of changes to the local flow conditions upstream of major noise sources, due to large and small scale interactions, has an impact on the noise radiated. Changes to the MLG design, either by modifying the bogie toe angle, or by fitting a fairing, attempt to change the local flow conditions to reduce the noise generated. Wing mounted MLG contain a leg-door that is commonly angled to aid in its deployment in the case of hydraulic failure. The designs of the Boeing 757 MLG, Boeing 777 MLG, and the Airbus A340 MLG, contain variations in the leg-door shape, and the leg-door angle. Differences in the leg-door configuration may affect the local flow conditions of neighbouring noise sources. Therefore, simplified studies are beneficial in understanding the noise generation of a MLG door alone. However, the only simplified study conducted to date has investigated the effect of two gap distances, and there is a need to investigate the effect of the door angle. A simplified model will additionally provide a more fundamental understanding of the aerodynamic interaction. Finally, simplified models can be applied to high-order CAA solvers. The geometric complexity of a simplified model is smaller. Therefore, a high grid quality should be possible.

Chapter 3

Research methodology

In this chapter, the experimental and numerical methods are outlined, when applied to study the effects of the door angle on the interaction between a leg-door and a circular cylinder. In Section 3.1 the experimental methods are given, that are used to acquire steady and unsteady aerodynamic data from the interaction model. In Section 3.2 a detailed overview of the numerical methods applied in the high-order CAA solver are given. In Section 3.3 the leg-door and strut interaction model is defined, and the influential design parameters are discussed. The effects of two design parameters are evaluated by 2-D URANS simulations using a low-order CFD tool. Finally, an overview of the technical approach is provided.

3.1 Experimental methods

The methods outlined in this section were applied in the 7' × 5' wind tunnel at the University of Southampton. The high-speed test section has dimensions of $4.4 \times 2.1 \times 1.5$ $(L \times W \times H)$ metres, with a contraction ratio of 5:1. The wind speed can range from 4 to 45 m/s and a period of one week of was available for model set-up, measurements and disassembly.

3.1.1 Oil flow visualisation

A mixture of luminous particles immersed in a liquid with a high rate of evaporation is applied to the model surface in a homogeneous manner. Once applied, the solution begins to dry and during this time the wind tunnel is operating. The aerodynamic shear stresses, induced by the flow, act on the drying paint which forms patterns. These patterns visualise the skin friction distribution [77] and can highlight particular flow features such as vortices, separation and reattachment points, bifurcation lines, and saddles. The majority of oil flow measurements are qualitative. However, some quantities, such as the separation point, can be measured.

3.1.2 Mean loads measurement

The aerodynamic loads induced on the model are transferred into a load cell placed above the wind tunnel. The measurements are recorded using a three-component weight beam balance. The time averaged loads on the model are measured by collecting two sets of ten readings, which are recorded on separate days to confirm the repeatability of the experiment. Each reading consists of a six second time average which is acquired at a sampling frequency of approximately 25 Hz. The forces are normalised by the free-stream dynamic pressure and a reference area. The experimental measurements for the mean loads on a bluff body flow are recorded across a range of Re, to ensure that the primary observations are made in the desired flow-regime.

3.1.3 Particle image velocimetry

The velocity field is measured by a non-intrusive method of Particle Image Velocimetry (PIV). This system consists of four components: the laser, the camera, the synchronizer, and the smoke generator. The smoke generator seeds the working fluid with particles. Some of these particles are illuminated by a 2-D laser sheet approximately 2-3 mm in thickness. The laser system consists of two Gemini Nd:YAG lasers that run at 4 Hz, emitting 120 mJ pulses at 532 nm. The position of the illuminated particles are recorded on a Charge-Coupled Device (CCD) by a high resolution TSI PowerView 4M Plus digital camera with a 64 bit frame grabber.

The monochromatic 4.2 Megapixel square images record the particle positions on two frames with a discrete time interval that is of the order of microseconds. The timing of the camera shutter and the laser pulse is controlled by the synchroniser and ensures that the two frames have similar exposure levels. The instantaneous velocity field is finally acquired by post-processing the two frames. A PIV data sample consists of an image pair, or two snapshots of the particle position, which is then post-processed to provide an instantaneous velocity field. By collecting multiple samples the statistical mean and variance of the velocity field can be obtained.

Each 2048×2048 pixel frame of an image pair, is divided into interrogation regions of 32×32 pixels, and then into regions of 16×16 pixels. The particle distribution pattern in an interrogation region is expressed by the image intensity field, and the pattern is cross-correlated between the frames recorded at two separate instances. The average particle displacement is predicted for each interrogation region. The size of the interrogation region determines the velocity field resolution as well as the cross-correlation strength [78]. The following considerations should be taken into account for the PIV method:

1. **The particle feedback to the working fluid**
   The influence of the seeded particles on the working fluid should be neglegible and this is ensured by the use of small particles of $1\,\mu$m to $5\,\mu$m in size.

2. **Homogeneous distribution of particles**
   This condition ensures a consistent and uniform image intensity of the reflected laser light, as well as ensuring that a sufficient particle density of at least 10 particles [78] exists within the interrogation region, across the entire frame.

3. **Fine image resolution**
   The detection of valid particle displacements can be affected by the presence of strong velocity gradients [78]. These gradients can be reduced by recording the flow field with a finer image resolution. The image resolution is determined by a number of variables including the selection of the lens, and the physical distance between the camera and the target plane.

4. **Appropriate time delay**
   To ensure that the interrogation regions between image pairs are correlated, an appropriate time delay is chosen. The maximum particle displacement along the target plane should be less than one-quarter of the interrogation region size. The presence of a strong cross-flow normal to the target plane may cause particles to shift out of the target plane [78] between frames. This causes a different set of particles being recorded between the image pairs, leading to a poorly correlated image pair. The choice of the time delay between the image pair should be optimized to the satisfy these requirements, which will be unique to the experiment.

Derived quantities

By obtaining a large sample of instantaneous velocity fields, the following quantities can be derived. The mean velocity field, normalised by the free-stream velocity, is defined by

$$\overline{u_i}^* = \frac{1}{U_\infty}\left(\sum_i^N \frac{u_i}{N}\right), \tag{3.1}$$

where u_i is the instantaneous velocity field at the i^{th} sample, and N is the total number of samples. Two of the three components of the velocity vector are measured by the 2-D PIV recording. The convergence of the mean velocity with increasing number of samples can be defined by

$$\Delta\overline{u_i}^*(N) = \frac{1}{U_\infty}\left(\sum_i^{N+1} \frac{u_i}{N+1} - \sum_i^N \frac{u_i}{N}\right), \tag{3.2}$$

which is the difference in the mean using $N+1$ and N samples. The variance in the velocity field is defined by

$$\overline{u_i'u_i'}^* = \overline{u_i u_i} - \overline{\overline{u_i}\,\overline{u_i}}. \tag{3.3}$$

Four of the nine components, of the velocity variance tensor, are measured by the 2-D PIV system. The normalised velocity variance is defined by

$$\overline{u_i'u_i'}^* = \frac{1}{U_\infty^2}\left(\sum_i^N \frac{u_i^2}{N} - \left(\sum_i^N \frac{u_i}{N}\right)^2\right). \tag{3.4}$$

Similarly, the difference in the variance between $N+1$ and N samples is

$$\Delta\overline{u_i'u_i'}^*(N) = \frac{1}{U_\infty^2}\left(\sum_i^{N+1} \frac{u_i^2}{N+1} - \sum_i^N \frac{u_i^2}{N} - \left(\sum_i^{N+1} \frac{u_i}{N+1}\right)^2 + \left(\sum_i^N \frac{u_i}{N}\right)^2\right). \tag{3.5}$$

The convergence with sample size is plotted in Figure 3.1 and shows a $1/N$ relation. The residual levels in Figure 3.1 are normalised quantities. Therefore, these plots show that residuals in the mean and the variance for a sample of $N = 500$ is of the order of $1 \times 10^{-3.5}\%$. This corresponds to the difference in the quantity of velocity mean and variance. Therefore, a PIV sample of 1000 images should be more than sufficient to obtain statistically converged results.

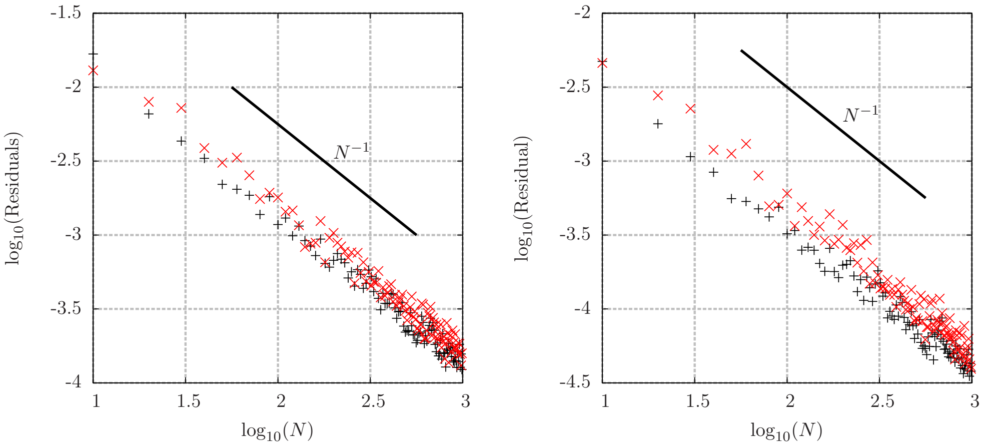

(a) Residual $\overline{u}^*$ and $\overline{v}^*$

(b) Residual $\overline{u'u'}^*$ and $\overline{v'v'}^*$

Figure 3.1: Convergence of PIV residuals for the stream-wise (+) and transverse (×) velocity statistics with increasing sample size N.

Additional sources of errors

The errors in the velocity variance field are greater compared to the mean flow. If the errors are generalised into systematic and random errors, then the instantaneous velocity field can be expressed as,

$$u = u_E + \epsilon_r + \epsilon_s, \tag{3.6}$$

where u_E is the exact velocity and ϵ_r and ϵ_s are the time-varying random and time-independent systematic errors, respectively. By taking the time average of Equation 3.6 the mean velocity can be expressed as,

$$\overline{u} = \overline{u}_E + \overline{\epsilon}_s, \tag{3.7}$$

and the expression for the velocity fluctuations is,

$$\overline{u'u'} = \overline{u'_E u'_E} - \left(2\overline{\epsilon_s \epsilon_s} + \overline{\epsilon_r \epsilon_r} + 2\overline{u'\epsilon_r}\right). \tag{3.8}$$

These expressions show that the velocity variance is more prone to the influence of errors than the mean statistics. This explains why, for instance, the 2-D TKE fields tend to be more noisy in comparison to the mean velocity field. The following are potential sources of additional errors:

1. **Signal to noise ratio**
   This can be caused by a large displacement between the target field and the camera. This requires the optical data to be recorded through a thicker layer of smoke, induced by the seeded particles from the smoke generator.

2. **Synchroniser error**
   A laser misfiring or an error with the synchronisation of the camera and laser may occur. This tends to occur when very small timings are specified. This causes the two images to be completely uncorrelated, resulting in a poor data set.

3. **Laser light reflection**
   The recorded data from the PIV system should only consist of the smoke particles. Any residual light scattered by reflective surfaces on the model, or wind tunnel walls can result in areas of overexposure. This error may degrade the correlation of the particles between recorded frames.

To overcome most of the errors, the correlation intensity from the post-processing is used to verify the validity of the predicted velocity vectors. The output from a single post-processed PIV image pair, contains the 2-D spatial coordinates, the instantaneous velocity field, and a scalar indicating the validity of the vector. Invalid vectors are automatically detected and replaced by interpolated data using neighbouring valid information.

3.1.4 On surface microphone

On surface time-traces of the pressures are recorded by a flush mounted microphone. The data is acquired using National instruments PXI-4472 data acquisition card. The frequency range of the microphone is 20 Hz to 20 kHz, and it has a nominal sensitivity of -35 dB ± 4 dB (re $p_{\text{ref}} = 2 \times 10^{-5}$ Pa). The data is recorded at a sampling frequency of 48 kHz for 8 seconds.

Modal analysis of the signal is conducted by using a Fast Fourier Transform (FFT) along 60 segments of 8192 samples with zero overlapping. The signal is also processed by zero-padding (by one quarter of the segment length) and a Hanning window.

3.2 Numerical methods

Two high-performance facilities were available during the course of the project. *Iridis 3* was operational from 2010 to 2013, which consisted of 924 nodes. Each node was fitted with a Westmere 12-core system and operated at 2.4 GHz with 22 GB of memory. These resources were shared between 1552 users. In 2014 the University of Southampton opened the *Iridis 4* cluster, which is currently shared between 1173 users. This cluster consists of 750 nodes. Each node is a Sandybridge 16-core system which operates at 2.6 GHz with 62 GB of memory.

In this section the numerical methods used to model the fluid dynamics are detailed. Three solvers were used throughout the duration of the project: FLUENT, OpenFOAM and SotonCAA. The first two are CFD packages, and the latter is an in-house high-order code developed within the Airbus Noise Technology Centre (ANTC) for the purpose of CAA research. In this section the numerical methods employed in the high-order code is outlined.

3.2.1 Governing equations

The governing equations are the compressible, three-dimensional, Navier-Stokes equations, which conserve the mass, momentum and energy in a continuum fluid in a small control volume. The variables in the governing equations are made non-dimensional by reference quantities, and defined by the asterisk as follows,

$$\begin{aligned} x_i^* &= x_i/L_0, \qquad u_i^* = u_i/c_0, \qquad t^* = tc_0/L_0, \\ p^* &= p/\left(\rho_0 c_0^2\right), \qquad \rho^* = \rho/\rho_0, \qquad \mu^* = \mu/\mu_0. \end{aligned} \tag{3.9}$$

where the u_i and x_i are the velocity and coordinate in the i-direction, respectively, t is the time, and p, ρ and μ are the pressure, density and viscosity scalars, respectively. The reference variables are indicated by the subscript 0 that are typically chosen as free-stream quantities in external flows [51]. The ideal gas law provides the following relationship for the non-dimensional temperature

$$T^* = \gamma p^*/\rho^*. \tag{3.10}$$

In the remaining sections, the asterisk will be ignored for brevity, and all variables will refer to a non-dimensional quantity unless stated otherwise. The non-dimensional Navier-Stokes equations are,

$$\frac{\partial \mathbf{Q}}{\partial t} + \frac{\partial \mathbf{E} - \mathbf{E}_v}{\partial x} + \frac{\partial \mathbf{F} - \mathbf{F}_v}{\partial y} + \frac{\partial \mathbf{G} - \mathbf{G}_v}{\partial z} = 0, \tag{3.11}$$

where the conserved variable vector is defined as

$$\mathbf{Q} = [\rho, \rho u, \rho v, \rho w, \rho e_T]^T. \tag{3.12}$$

The inviscid flux vectors are defined as

$$\mathbf{E} = [\rho u, \rho uu + p, \rho uv, \rho uw, (\rho e_T + p)u], \tag{3.13a}$$

$$\mathbf{F} = [\rho u, \rho uv, \rho vv + p, \rho vw, (\rho e_T + p)v], \tag{3.13b}$$

$$\mathbf{G} = [\rho u, \rho uw, \rho vw, \rho ww + p, (\rho e_T + p)w]. \tag{3.13c}$$

$$\tag{3.13d}$$

The total energy per unit mass e_T is defined as the sum of the internal and kinetic energy per unit mass

$$e_T = c_v T + \frac{1}{2}\left(u_i u_i\right). \tag{3.14}$$

The viscous flux vectors are

$$\mathbf{E}_v = [0, \tau_{xx}, \tau_{xy}, \tau_{xz}, b_x + u\tau_{xx} + v\tau_{xy} + w\tau_{xz}], \tag{3.15a}$$

$$\mathbf{F}_v = [0, \tau_{xy}, \tau_{yy}, \tau_{xz}, b_y + u\tau_{yx} + v\tau_{yy} + w\tau_{yz}], \tag{3.15b}$$

$$\mathbf{G}_v = [0, \tau_{zx}, \tau_{zy}, \tau_{zz}, b_z + u\tau_{zx} + v\tau_{zy} + w\tau_{zz}]. \tag{3.15c}$$

$$\tag{3.15d}$$

The shear stress tensor is given by

$$\tau_{ij} = 2\mu \left(S_{ij} - \frac{1}{3} S_{kk} \delta_{ij} \right) \frac{M}{Re}, \tag{3.16}$$

where M is the Mach number, Re is the Reynolds number and S_{ij} is the symmetric strain rate tensor, which is defined as

$$S_{ij} = \frac{1}{2} \left(\frac{\partial u_i}{\partial x_j} + \frac{\partial u_j}{\partial x_i} \right). \tag{3.17}$$

The Mach number and Reynolds number are defined in terms of the reference quantities in Equation 3.9 and are expressed by

$$M = \frac{u_0}{c_0}, \qquad Re = \frac{\rho_0 u_0 L_0}{\mu_0}. \tag{3.18}$$

The heat fluxes in Equation 3.15 are based on Fourier's law and are defined by

$$b_i = \frac{M}{Re\,(\gamma - 1)\,Pr} \frac{\partial T}{\partial x_i}, \tag{3.19}$$

where Pr is the Prandtl number defined as the ratio of the rate of viscous diffusion to thermal diffusion, and γ is the ratio of the specific heat capacities at constant pressure and constant volume. The viscosity scalar field is defined by Sutherland's law

$$\mu = (T)^{3/2} \frac{1 - S}{T - S}, \tag{3.20}$$

where S is a reference temperature normalised by the free-stream temperature and taken as $S = 110.4[\mathrm{K}]/T_\infty$ [79].

3.2.2 Transformation to computational space

High-order spatial schemes using finite difference methods require a uniform grid spacing across the computational stencil. This condition cannot always be satisfied in the physical space, referred to in Cartesian coordinates by (x, y, z). By employing a structured grid, the high-order schemes can be applied along a generalised coordinate system (ξ, η, ζ), often referred to as the computational space, where the grid spacing is uniform. The governing equations in the curvilinear coordinate system is

$$\frac{\partial \hat{\mathbf{Q}}}{\partial t} + \frac{\partial \hat{\mathbf{E}}}{\partial \xi} + \frac{\partial \hat{\mathbf{F}}}{\partial \eta} + \frac{\partial \hat{\mathbf{G}}}{\partial \zeta} = J\left(\frac{\partial \mathbf{E}_v}{\partial x} + \frac{\partial \mathbf{F}_v}{\partial y} + \frac{\partial \mathbf{G}_v}{\partial z}\right), \tag{3.21}$$

with,

$$\hat{\mathbf{Q}} = J\mathbf{Q}, \tag{3.22a}$$

$$\hat{\mathbf{E}} = J\left(\tilde{\xi}_x \mathbf{E} + \tilde{\xi}_y \mathbf{F} + \tilde{\xi}_z \mathbf{G}\right), \tag{3.22b}$$

$$\hat{\mathbf{F}} = J\left(\tilde{\eta}_x \mathbf{E} + \tilde{\eta}_y \mathbf{F} + \tilde{\eta}_z \mathbf{G}\right), \tag{3.22c}$$

$$\hat{\mathbf{G}} = J\left(\tilde{\zeta}_x \mathbf{E} + \tilde{\zeta}_y \mathbf{F} + \tilde{\zeta}_z \mathbf{G}\right). \tag{3.22d}$$

The Jacobian J of the grid transformation is

$$J^{-1} = \begin{vmatrix} x_\xi & x_\eta & x_\zeta \\ y_\xi & y_\eta & y_\zeta \\ z_\xi & z_\eta & z_\zeta \end{vmatrix}, \tag{3.23}$$

and the standard metrics of the grid transformation are

$$\begin{aligned}
\tilde{\xi}_x &= (y_\eta z_\zeta - z_\eta y_\zeta), & \tilde{\xi}_y &= (z_\eta x_\zeta - x_\eta z_\zeta), & \tilde{\xi}_z &= (x_\eta y_\zeta - y_\eta x_\zeta), \\
\tilde{\eta}_x &= (y_\zeta z_\xi - z_\zeta y_\xi), & \tilde{\eta}_y &= (z_\zeta x_\xi - x_\zeta z_\xi), & \tilde{\eta}_z &= (x_\zeta y_\xi - y_\zeta x_\xi), \\
\tilde{\zeta}_x &= (y_\xi z_\eta - z_\xi y_\eta), & \tilde{\zeta}_y &= (z_\xi x_\eta - x_\xi z_\eta), & \tilde{\zeta}_z &= (x_\xi y_\eta - y_\xi x_\eta).
\end{aligned} \tag{3.24}$$

The right hand side viscous terms in Equation 3.21 are evaluated using spatial derivatives taken along the curvilinear coordinates and are expressed in the physical coordinate system via the chain rule

$$\frac{\partial f}{\partial x_i} = \frac{\partial f}{\partial \xi}\frac{\partial \xi}{\partial x_i} + \frac{\partial f}{\partial \eta}\frac{\partial \eta}{\partial x_i} + \frac{\partial f}{\partial \zeta}\frac{\partial \zeta}{\partial x_i}. \tag{3.25}$$

The precise computation of the Jacobian and the metrics of the grid transformation is vital for stable and accurate CAA computations. These terms are evaluated by numerical schemes, which may contain errors. This subject was discussed in part by Deng *et al.* [80], and a strong conservation form of Equation 4.30 was proposed to reduce grid transformation errors and to preserve the grid conservation laws (GCL). The GCL metrics are defined as

$$\begin{aligned}
\tilde{\xi}_x &= (y_\eta z)_\zeta - (y_\zeta z)_\eta, & \tilde{\xi}_y &= (z_\eta x)_\zeta - (z_\zeta x)_\eta, & \tilde{\xi}_z &= (x_\eta y)_\zeta - (x_\zeta y)_\eta, \\
\tilde{\eta}_x &= (y_\zeta z)_\xi - (y_\xi z)_\zeta, & \tilde{\eta}_y &= (z_\zeta x)_\xi - (z_\xi x)_\zeta, & \tilde{\eta}_z &= (x_\zeta y)_\xi - (x_\xi y)_\zeta, \\
\tilde{\zeta}_x &= (y_\xi z)_\eta - (y_\eta z)_\xi, & \tilde{\zeta}_y &= (z_\xi x)_\eta - (z_\eta x)_\xi, & \tilde{\zeta}_z &= (x_\xi y)_\eta - (x_\eta y)_\xi.
\end{aligned} \tag{3.26}$$

The GCL metrics are applicable only for three-dimensional problems. Therefore a more effective means of reducing the grid-induced numerical errors, for two-dimensional problems, is required. This subject is discussed further in Section 4.5 where a grid quality assessment tool for two- and three-dimensional cases is outlined. All three-dimensional high-order simulations were conducted using the GCL metrics.

3.2.3 Turbulence modelling

The CAA solver is implemented with the Spalart-Almaras (S-A) turbulence model. This model provides a transport equation for an eddy viscosity (μ_t), which is used to model the Reynolds stress via the Boussinesq approximation. Its application to the compressible RANS equations [81] is given by

$$\overline{-\rho u_i'' u_j''} = 2\hat{\mu}_t \left(\hat{S_{ij}} - \frac{1}{3}\frac{\partial \hat{u}_k}{\partial x_k}\delta_{ij} \right) - \frac{2}{3}\overline{\rho} k \delta_{ij}, \tag{3.27}$$

where k is the local turbulent kinetic energy, and the variables containing a hat represent Favre-averaged quantities $f = \hat{f} + f''$. A Reynolds analogy is also used to model the turbulent heat flux, which requires a turbulent Prandlt number (Pr_t), the local eddy viscosity, and the local temperature gradient. The eddy viscosity in the S-A model is given by [68],

$$\hat{\mu}_t = \rho \hat{\nu} f_{v1}, \tag{3.28}$$

where $\hat{\nu}$ is defined by the following transport equation,

$$
\begin{aligned}
\frac{\partial \hat{\nu}}{\partial t} + u_j \frac{\partial \hat{\nu}}{\partial x_j} = c_{b1}(1 - f_{t2})\hat{S}\hat{\nu} \\
- \left[c_{w1} f_w - \frac{c_{b1}}{\kappa^2} f_{t2} \right] \left(\frac{\hat{\nu}}{d} \right)^2 \\
+ \frac{1}{\sigma} \left[\frac{\partial}{\partial x_j} \left((\nu + \hat{\nu}) \frac{\partial \hat{\nu}}{\partial x_j} \right) + c_{b2} \frac{\partial \hat{\nu}}{\partial x_i} \frac{\partial \hat{\nu}}{\partial x_i} \right].
\end{aligned}
\tag{3.29}
$$

The constants and additional equations required to solve the transport equation are found in [68]. Several versions of the S-A model exist to address various issues of numerical stability (S-A *noft2* and the S-A *neg* models), and physical applications (including a trip term, rotation correction and effects of compressibility) [82]. In the high-order code the S-A *noft2* model is implemented, and its verification case is provided in the Appendix C.1.

Hybrid RANS/LES methods

The Detached-Eddy Simulation (DES) method is a hybrid RANS/LES method. The method modifies the definition of the length scale ($\tilde{d}$) used in the S-A model to be a function of the local grid spacing, $\Delta = \max(\Delta_x.\Delta_y, \Delta_z)$. This modification enables the S-A model to behave as an LES sub-grid scale model [83]. The switch between the RANS and LES regions is defined by a separate function. In the original DES model this function is

$$
\tilde{d} = \min\left(d, C_{DES}\Delta\right), \tag{3.30}
$$

where C_{DES} is a constant. Issues of undesirable switching to the LES mode in the original method, were addressed by Spalart *et al.* and resolved in the Delayed DES (DDES) [52] and Improved-delayed DES (IDDES) models.

The Zonal Detached Eddy Simulation (Z-DES) method is a multi-block approach, which requires engineering judgement. When applied correctly, it enhances the prediction of detached flows compared to the standard DDES model. The Z-DES method defines each of the blocks in a domain with a specific mode. The mode determines the turbulence modelling method to be used. The modes are selected according to the type of flow problem that is expected in each block. In Mode 1, the near-wall functions in the S-A model are removed, which enhances the growth of instabilities in areas where the flow detachment is fixed by the geometry. In the Z-DES Mode 2, the model behaves as the standard DDES model inside the boundary layer but switches to a Z-DES model outside the boundary layer.

3.2.4 Boundary conditions

Accurate solutions to the governing equations are initialised appropriately, and bound by accurate boundary conditions. Boundary conditions are imposed along edges or zones by specifying a state-variable (Dirichlet), or its derivative (Neumann) quantity to satisfy a desired condition [84].

Viscous wall boundary condition

All wall boundaries are assumed to be rigid with an infinite impedance, and a no-slip condition is enforced. The flux of mass, momentum and energy through the wall boundary is set to zero. An adiabatic wall sets a zero temperature gradient normal to the wall. For low Mach numbers an isothermal wall condition is almost equivalent to an adiabatic wall due to the negligible gradients in the temperature field. The isothermal no-slip wall boundary condition is numerically simpler to implement, whereby the temperature and velocity are set to their stagnation quantities. To ensure mass continuity the density is computed via the continuity equation, and this provides a fully bounded condition on the conserved variables along the wall regions.

Pressure far-field

This method is a non-reflective boundary condition based on the Riemann invariants for a one-dimensional and isentropic flow normal to the boundary. The point along the boundary is fixed to the free-stream conditions, and the adjacent node is modified. The Riemann invariants for the incoming and outgoing waves in a subsonic flow are

$$R^{-} = v_{n_\infty} - \frac{2c_\infty}{\gamma - 1}, \tag{3.31}$$

$$R^{+} = v_{n_i} + \frac{2c_i}{\gamma - 1}, \tag{3.32}$$

where v_n is the velocity magnitude normal to the boundary, γ is the ratio of specific heats for an ideal gas, and the subscripts i and ∞ refer to the conditions within the vertex adjacent to the boundary face, and in the free-stream, respectively. The sound speed and the normal velocity at the boundary face is

$$c = \frac{\gamma - 1}{4}\left(R_i - R_\infty\right). \tag{3.33}$$

$$U_f = \frac{1}{2}\left(R_i + R_\infty\right), \tag{3.34}$$

The Cartesian velocity vector is then updated by decomposing the normal and tangential velocities [85] using

$$\begin{aligned} u &= u_{ref} + \frac{\xi_x}{|\nabla\xi|}\left(U_f - u_{ref}\right), \\ v &= v_{ref} + \frac{\xi_y}{|\nabla\xi|}\left(U_f - v_{ref}\right), \\ w &= w_{ref} + \frac{\xi_z}{|\nabla\xi|}\left(U_f - w_{ref}\right), \end{aligned} \tag{3.35}$$

where the sign of U_f determines if an inflow condition ($u_{ref} = u_\infty$) or an outflow condition ($u_{ref} = u_i$) is imposed. The density and pressure are evaluated by solving the following equations simultaneously

$$s = p/\rho^\gamma, \qquad c = \gamma p/\rho, \tag{3.36}$$

where interior conditions for s and c are taken for an outflow condition ($U_f > 0$), and free-stream conditions are taken for an inflow condition. This boundary condition performs well under only under the presence of acoustic waves. From further tests, it was found that vorticity disturbances passing through the boundary condition would generate undesireable acoustic reflections.

Span-wise periodic boundary condition

The periodic boundary condition is applied in order to model the flow across an infinite span. This condition is set by copying the local flow variables on one domain extent, into the ghost points of the other side. This provides a perfect coherency of the flow structures in the wake by the model span L_z. In order to obtain results comparable to experiments, the model span L_z should be larger than the span-wise correlation length L_c for the particular problem. Numerical simulations of a cylinder at high Re have applied a span-wise distance of around $2D < L_z < 4D$ [67, 69].

3.2.5 Characteristic boundary conditions

The following approaches are based on the generalised method proposed by Kim and Lee [86, 87]. By rearranging the Navier-Stokes equations into a quasi-linear characteristic form, the fluxes across cell faces are expressed in terms of incoming and outgoing characteristic waves. The derivation of the characteristic form of the governing equations is detailed in the original references [86, 87], and is only briefly described in this section. The governing equations in Equation 3.21 are rearranged in the following form

$$\frac{\partial \boldsymbol{Q}}{\partial t} + \boldsymbol{A}\frac{\partial \boldsymbol{Q}}{\partial \xi} = -\left(\frac{\partial \hat{\boldsymbol{F}}}{\partial \eta} + \frac{\partial \hat{\boldsymbol{G}}}{\partial \zeta}\right) + \boldsymbol{S}_v, \tag{3.37}$$

where the fluxes along the η and ζ are expressed as source terms, together with the viscous terms that have been collected as $\boldsymbol{S}_v$. By diagonalising the flux Jacobian $\boldsymbol{A}$, Equation 3.37 can be decomposed into its one-dimensional characteristic modes. The diagonal matrix $\boldsymbol{\lambda}$ is related to the flux Jacobian $\boldsymbol{A}$ by the matrix $\boldsymbol{P}$ and its inverse $\boldsymbol{P}^{-1}$

$$\boldsymbol{\lambda} = \boldsymbol{P}^{-1}\boldsymbol{A}\boldsymbol{P}. \tag{3.38}$$

Finally, the characteristic form of the Navier-Stokes equations can be expressed as

$$\frac{\partial \mathbf{R}}{\partial t} + \lambda\frac{\partial \mathbf{R}}{\partial \xi} = \mathbf{S}_c, \qquad \partial \boldsymbol{R} = \boldsymbol{P}^{-1}\boldsymbol{Q}, \tag{3.39}$$

where the left hand side is the quasi-linear scalar-wave convection equation and the right hand side consists of source terms composed of the viscous and transverse fluxes. The implementation of the characteristic boundary conditions in the high-order code follows the procedure outlined by Peers *et al.* [88] where the matrix $\boldsymbol{P}$ is provided. The characteristic differential variables and the corresponding convection speeds are [88],

$$\partial \mathbf{R} = \begin{bmatrix} \tilde{\xi}_x \delta s + \delta \tilde{V}_x \\ \tilde{\xi}_y \delta s + \delta \tilde{V}_y \\ \tilde{\xi}_z \delta s + \delta \tilde{V}_z \\ \frac{\delta p}{\rho c} + \delta \tilde{U} \\ \frac{\delta p}{\rho c} - \delta \tilde{U} \end{bmatrix}, \quad \lambda(diag) = \begin{bmatrix} U \\ U \\ U \\ U + c\sqrt{\xi_x^2 + \xi_y^2 + \xi_z^2} \\ U - c\sqrt{\xi_x^2 + \xi_y^2 + \xi_z^2} \end{bmatrix}, \tag{3.40}$$

$$\delta \tilde{V}_x = \tilde{\xi}_z \delta v - \tilde{\xi}_y \delta w, \quad \delta \tilde{V}_y = \tilde{\xi}_z \delta v - \tilde{\xi}_y \delta w, \tag{3.41}$$

$$\delta \tilde{V}_z = \tilde{\xi}_z \delta v - \tilde{\xi}_y \delta w, \quad \delta s = \delta \rho - \frac{\delta p}{c^2} \tag{3.42}$$

where the tilde indicates quantities normalised by $|\nabla \xi|$, c is the sound speed and U is the contravariant velocity. The first three characteristic waves carry the vorticity and entropy disturbances across a face of constant ξ, and the remaining two characteristics carry the acoustic disturbances. Boundary conditions can be applied in terms of the desired amplitude of characteristic variables, and described as a temporal derivative of the conserve variables ($\partial \boldsymbol{Q}/\partial t$), in the Navier-Stokes equations. This method requires use of the relationships that transform Equation 3.21 into Equation 3.39.

Characteristic interface condition

Areas with discontinuous grid metrics are areas that contain an abrupt change in the grid line direction or grid spacing. An example of this grid feature is shown in Figure 3.2. Along the discontinuities the computed grid metrics will be contaminated by large dispersion errors, formed by the resolution limitations of the spatial schemes. The grid transformation errors may contaminate the results. A strong spatial filter may be applied to correct the result [89] solution. However, stronger filters will effectively reduce the fidelity of the solver, and therefore this alternate method is favoured.

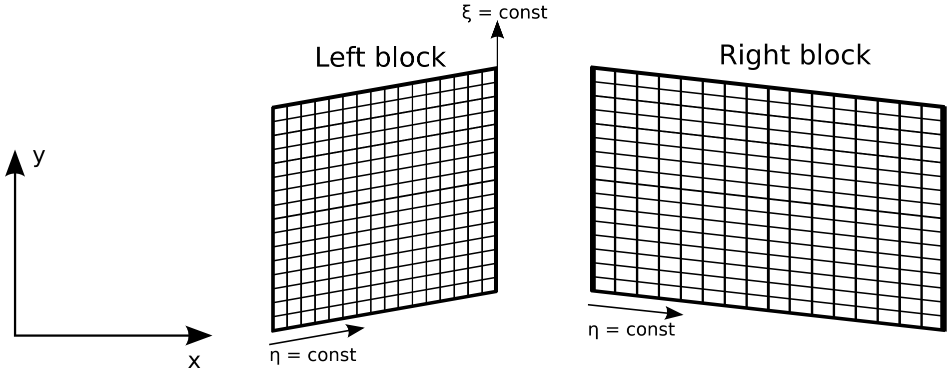

Figure 3.2: An example of a grid metric discontinuity.

A characteristic interface condition (CIC) proposed by Kim and Lee [87] can be applied along such block boundaries. The CIC method is a prediction-correction method which consists of three key steps. Firstly, the flux derivatives are predicted using biased schemes to remove the numerical issues when employing central schemes across discontinuous grid metrics. Secondly, the CIC is imposed where the characteristic waves are up-winded in the direction of the wave propagation, after which the flux derivatives are corrected and matched across an interface boundary. The continuity across the block interface is enforced by

$$\frac{\partial \mathbf{R}^L}{\partial t} = \frac{\partial \mathbf{R}^R}{\partial t}, \tag{3.43}$$

where the superscripts L and R denote the variables on the left and right sides of the interface illustrated in Figure 3.2. If the convective term in Equation 3.39 is simplified as

$$\mathbf{L} = \lambda \frac{\partial \mathbf{R}}{\partial \xi}, \tag{3.44}$$

then the interface condition (Equation 3.43) can be expressed as,

$$\mathbf{L}^L - \mathbf{S}_c^L = \mathbf{L}^R - \mathbf{S}_c^R. \tag{3.45}$$

The numerical implementation of Equation 3.45 is done as follows. The vector $\boldsymbol{L}$ contains the five modes which propagate at speeds defined by $\lambda(diag)$. If $\lambda_i > 0$ the characteristic wave propagates from left to right and therefore $\boldsymbol{L}_i^R$ is corrected by

$$\boldsymbol{L}^R = \boldsymbol{L}^L - \boldsymbol{S}^L + \boldsymbol{S}^R. \tag{3.46}$$

Similarly, a negative propagation speed requires that the opposite characteristic wave is corrected. A secondary treatment is implemented whereby the primitive variables along the interface are averaged, at the end of each time step, to ensure that the flow field solution remains continuous. When the propagation speed through the face is extremely small, the up-winding procedure becomes vague and this has been identified as an issue for the CIC [90].

3.2.6 Non-reflecting boundary conditions

The boundary conditions along the edges of a computational domain must be free of numerical instabilities, and not generate or reflect acoustic waves. The use of low artificial dissipation methods makes the near-field region of interest prone to contamination by reflected or spurious acoustic waves [40, 50]. Non-reflective conditions can be categorised as: (1) Buffer/sponge zone techniques, (2) far-field conditions and (3) characteristic based methods. Some of these methods were evaluated by Richards *et al.* [91], and more recently by Gill *et al.* [15], where the best methods to employ were found to be a combination of the characteristic and buffer-zone methods. For this reason only characteristic and buffer-zone methods will be detailed here.

Characteristic outflow condition

The only characteristic that can propagating back into the domain is modified, and all other modes are left unmodified. The characteristic non-reflecting condition is enforced by setting the amplitude of the reflected acoustic mode to zero. This condition is ideal, but results in an un-bounded outflow pressure that can cause numerical instabilities [86]. Instead the boundary condition is defined such that the outflow pressure is corrected towards the free-stream pressure using

$$L_5 = K_{out}\left[(p - p_\infty)\,\rho c\right], \qquad K_{out} = \sigma\left(1 - M_{max}^2\right)(c/l), \tag{3.47}$$

where K_{out} is a forcing constant based on the local Mach number (M), sound speed (c) and a characteristic length (l) measured as the distance from the near-field region to the outflow boundary. The tuneable parameter is recommended to be within the range of $0.1 < \sigma < 0.4$ [86].

Buffer-zone boundary condition

The buffer-zone method corrects the flow variables gradually towards a target value inside a buffer-region. The explicit buffer-zone formulation modifies the solution vector at the end of each time step $(n+1)$ using

$$\tilde{\mathbf{Q}}^{n+1} = \mathbf{Q}^{n+1} - \sigma\left(\mathbf{Q}^{n+1} - \mathbf{Q}_T\right), \tag{3.48}$$

where $\tilde{\mathbf{Q}}^{n+1}$ and $\mathbf{Q}^{n+1}$ are the solution vectors after and prior to the explicit damping, respectability, and $\mathbf{Q}^T$ is the solution vector containing the target values which are typically set as mean quantities. The explicit damping is controlled by the damping function σ which is defined by

$$\sigma\left(x\right) = \sigma_{max}\left(1 + \frac{x-L}{L}\right)^{\beta}, \tag{3.49}$$

where x is the distance to the buffer zone edge, L is the buffer zone length, and σ_{max} and β are user tuneable parameters that affect the properties of the damping function. Gill *et al.* [15] showed that the performance of explicit buffer-zones is dependant of the time step. This property makes the explicit buffer-zone performance case dependant. Instead an implicit formulation is used, where the damping is part of the governing equations as a sink term. The one-dimensional scalar wave equation with an implicit buffer-zone would be expressed as

$$\frac{\partial f}{\partial t} + c\frac{\partial f}{\partial x} = -\sigma(x)\left(f - f_T\right), \tag{3.50}$$

where f and f_T are the scalar field and target field respectively, t is the time, and c is the propagation speed of the characteristic along the x direction. The damping function of the sink term in the implicit buffer-zone holds the same definition as Equation 3.49. By approximating the temporal derivative as a first-order upwind scheme, the solution at the next time-step can be expressed by

$$f^{n+1} = f^{n} - \Delta t c\frac{\partial f}{\partial x} - \Delta t\sigma(x)\left(f - f_T\right). \tag{3.51}$$

This shows that the implicit buffer-zone is equivalent to the explicit buffer-zone method (Equation 3.48) with a damping term that is weighted by the time step size.

Hybrid radiation conditions

The characteristic and buffer-zone techniques are commonly applied to CAA problems involving strong acoustic and vorticity modes, such as on a landing gear geometry [60], or for jet flow simulations [51]. Each technique holds unique advantages and disadvantages and a hybrid of these boundary conditions was suggested by Sandberg and Sandham [92]. The buffer-zone technique is simple to employ but cannot differentiate between acoustic, vorticity or entropy modes, and therefore all modes are damped regardless of its propagation direction. For sub-sonic flows with a mean-flow directed out of the computational domain, the only up-stream propagating wave mode is the $\boldsymbol{L}_5$ acoustic mode. Therefore a characteristic boundary condition can ensure that only the reflected mode is damped. However, the characteristic outflow condition has multiple tunable parameters. Sandberg and Sandham [92] applied the buffer-zones only on the up-stream travelling acoustic mode. Gill *et al.* [15] enhanced its performance by incorporating the otherwise ignored transverse terms into the characteristic boundary condition.

3.2.7 Temporal scheme

A second-order implicit temporal scheme was chosen instead of a high-order Runga-Kutta scheme [93] to enable a comparatively higher temp step size. The temporal scheme is a fully implicit method by Li *et al.* [94] and is outlined in this section. The governing equation described by Equation 3.13 can be expressed as,

$$\frac{\partial \mathbf{Q}}{\partial t} = -\mathbf{S}(\mathbf{Q}) + \mathbf{S}_v(\mathbf{Q}), \tag{3.52}$$

where the vector $\mathbf{S}$ and $\mathbf{S}_v$ denote the inviscid and viscous flux terms, which are a function of the conserved variables vector $\mathbf{Q}$. The second-order implicit temporal scheme, which evolves at the time level n, is given by

$$\frac{\partial \mathbf{Q}}{\partial t} = \frac{3\mathbf{Q}^{n+1} - 4\mathbf{Q}^{n} + \mathbf{Q}^{n-1}}{2\Delta t} = -\mathbf{S}(\mathbf{Q}^{n+1}) + \mathbf{S}_v(\mathbf{Q}^{n}), \tag{3.53}$$

where the inviscid and viscous fluxes are evaluated implicitly and explicitly, respectively. The solution at the next time step is obtained by a sub-iterative method using a pseudo time τ, which evolves at the time level m. This gives the following expression

$$\frac{\mathbf{Q}^{m+1} - \mathbf{Q}^{m}}{\Delta \tau} + \frac{3\mathbf{Q}^{m+1} - 4\mathbf{Q}^{n} + \mathbf{Q}^{n-1}}{2\Delta t} = -\mathbf{S}(\mathbf{Q}^{m+1}) + \mathbf{S}_v(\mathbf{Q}^{m}). \tag{3.54}$$

Finally by substituting $\mathbf{Q}^{m+1} = \mathbf{Q}^{m} + \Delta\mathbf{Q}$, the implicit inviscid fluxes can be rewritten

$$\mathbf{S}(\mathbf{Q}^{m+1}) = \mathbf{S}(\mathbf{Q}^m) + \frac{\partial \mathbf{S}}{\partial \mathbf{Q}} \Delta \mathbf{Q}^m, \tag{3.55}$$

and substituted into Equation 3.54. By setting $\tau \to \infty$ a Newton-like sub-iteration system is formed, yielding the final expression as,

$$\left[\left(\frac{3}{2\Delta t} \right) I + \frac{\partial \mathbf{S}}{\partial \mathbf{Q}} \right] \Delta \mathbf{Q}^m = -\frac{3\mathbf{Q}^m - 4\mathbf{Q}^n + \mathbf{Q}^{n-1}}{2\Delta t} + \mathbf{S}_v(\mathbf{Q}^m). \tag{3.56}$$

This solution for $\Delta \boldsymbol{Q}^m$ is obtained by an LU decomposition scheme [94]. The vector $\Delta \boldsymbol{Q}^m$ evolves the solution $\boldsymbol{Q}^{m+1}$ towards $\mathbf{Q}^{n+1}$ as the number of sub-iterations increases (the limit where $\tau \to \infty$). Finally the residual of the sub-iterative method is given by $\Delta \boldsymbol{Q}^m$. The CFL requirement for time accurate solutions is CFL < 0.1, and is outlined in Appendix B.

3.2.8 The FW-H solver

In Section 2.1, the FW-H acoustic analogy was introduced. The far-field acoustic signals are calculated by an in-house FW-H solver. This solver applies numerical methods to evaluate the integral representation of the FW-H equation, known as Formulation 1A of Farassat [46]. A time-domain solution to the FW-H equation is obtained by a Green's function. In Formulation 1A, the speed and accuracy of the calculation is improved by converting the spatial derivative into a time derivative, and moving the time derivatives inside the integrals [46]. In this formulation the volume integral outside of the source region is omitted, and the remaining thickness and loading terms are in the following form:

$$4\pi p'(\boldsymbol{x}, t) = \int_{f=0} \left[\frac{Q(\boldsymbol{y}, \tau)}{r|1 - M_r|} \right]_{ret} dS \approx \sum_{i=1}^{N} \left[\frac{Q(\boldsymbol{y}_i, \tau_i)}{r_i|1 - M_r|_i} \right]_{ret} \Delta S_i, \tag{3.57}$$

where Q is the source strength, $\boldsymbol{y}$ is the source position, τ is the source emission time, and M_r is the Mach number in the radiation direction at time τ. The integration is evaluated along N discrete panels of size ΔS_i, along the FW-H surface. The CFD source data on each panel is interpolated to the retarded time. The temporal derivatives, contained within the integrals, are evaluated by a fourth-order central difference scheme. Once the source terms for all panel are defined at the retarded times, a far-field prediction at a fixed time is obtained. This calculation is then repeated for the remaining observer times. The FW-H solver has been validated by Peers [95] for an acoustic monopole radiation benchmark. The validation case is listed as part of the code verification and validation database listed in Appendix C.2.

The FW-H solver requires three inputs to compute the sound at an observer position: (1) the FW-H integration surface grid information, (2) the FW-H integration surface CFD time history of the primitive variables, and (3) the observer position information relative to the source region. The CFD data is interpolated onto the integration surface by a second-order accurate interpolation scheme.

3.2.9 Summary

This section has outlined the numerical methods employed in the high-order solver. The high-order solver has been validated on several test cases on simple and complex geometries. An outline of the validation cases is provided in Appendix C.2.

3.3 Geometry definition

The focus of the project is on the interactions between a MLG leg-door and nearby components. The MLG geometry for the Airbus A-340 model was shown previously in Figure 2.6. A simplified model consisting of only the larger components in the immediate vicinity of the leg-door is shown in Figure 3.3. The proposed simplified model is a two-component study between the leg-door and the main strut. This simplified model is illustrated in Figure 3.4 and highlights two key design parameters; the door angle of attack (α_D) and the gap distance between the two components, which can be expressed in a non dimensional form as the gap ratio, $G = e/D$. Previous studies on the interaction between a cylinder and a plane boundary have considered a plane boundary with a zero degree angle of incidence to the incoming flow. No previous studies have investigated the effect of the door angle of attack on the aerodynamic interactions with a cylinder.

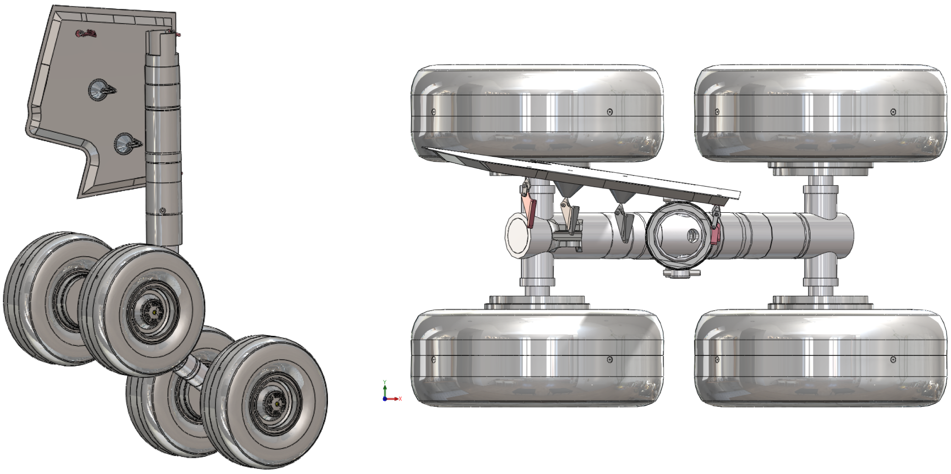

Figure 3.3: Simplified Airbus landing gear model including the leg-door.

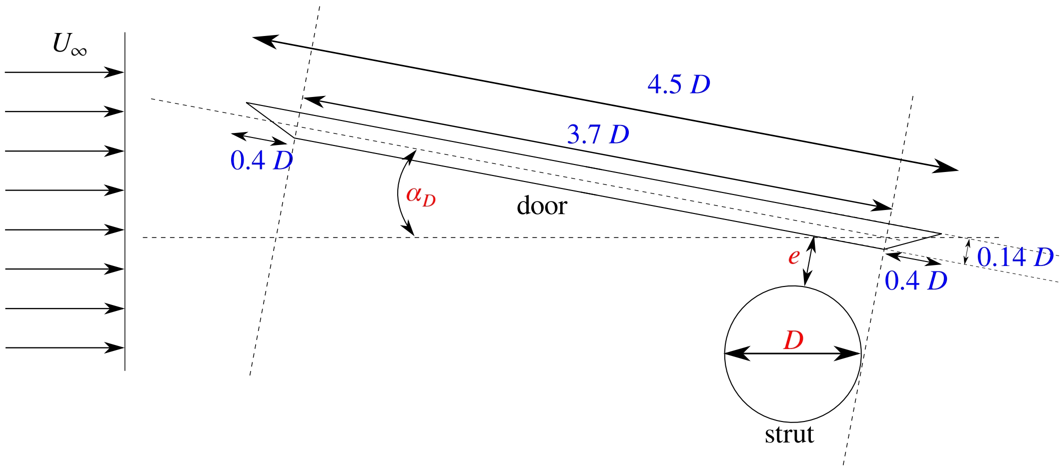

Figure 3.4: Simplified 2-D door-strut interaction model. Dimensions are highlighted in blue, and the influential design parameters are given in red.

3.3.1 Influential parameters

A preliminary CFD study using the incompressible unsteady RANS (URANS) equations was conducted using the software FLUENT. A two-dimensional (2-D) interaction between a leg-door and main strut in side by side configuration was simulated for varying parameters of G and α_D. Further details of the low-order studies are provided in the Appendix A. The aim of the low-order study was to identify the significance of the parameters on the mean and unsteady aerodynamic features. The $k-\omega$ SST turbulence model was applied for these simulations based on the conclusions obtained by Cox *et al.* [66].

The directivity profile of a cylinder and leg-door in a side by side configuration is almost dipole (for $\alpha_D = 0°$) and the majority of the noise source is characterised by low frequencies [8]. The compactness of a source is defined by a small Helmholtz number ($He = l/\lambda$) $<<1$, which is the ratio between the geometric length scale of the source l, to the acoustic wavelength λ. The noise radiation from a cylinder and door interaction is expected to be a compact dipole. For compact sources such as on cylinder flows, the surface pressure fluctuations, are highly correlated with the far-field acoustics.

For all the configurations tested, the lift dipole was significantly larger than the drag dipole. Therefore, the major changes to the far-field acoustics are likely correlated to the changes in the lift dipole strength. Figure 3.5 shows the effect of door angle, and the gap width ratio, on the lift force variance on the cylinder and door. In the Figure, the recorded data points exist along the grid line intersections.

From Figure 3.5 the key observations show the effect of:

1. **The door angle**

   Changing the door angle influences the force fluctuations on the cylinder and the

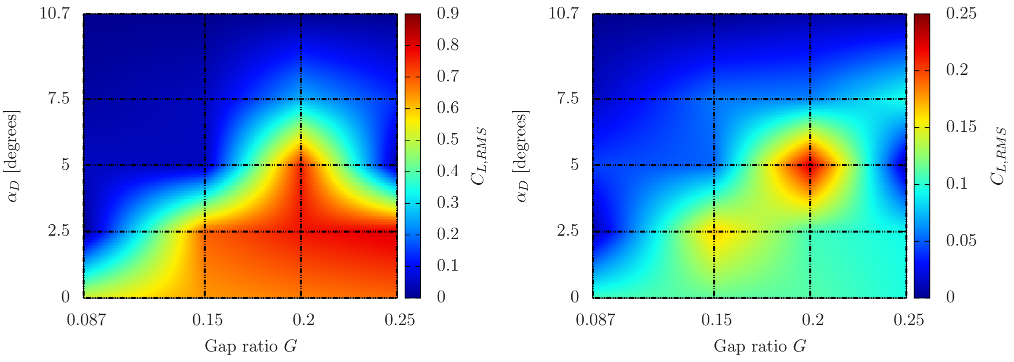

(a) Cylinder loads (b) Door loads

Figure 3.5: The effect of G and α_D on the force fluctuations along the cylinder and door elements.

door. The condition for minimal lift force fluctuations exists in regions of very small gaps $G \to 0$, or at high door angles at larger gaps. The contours suggest that increasing the door angle will eventually result in a reduction in the force fluctuations. For the cases where $G = 0.15$ and $G = 0.2$, increasing the door angle has an initial effect of increasing the fluctuating loads. However, this is followed by a region of a decrease in the variance of the lift force. One might expect that a larger door angle may project a greater frontal area, which makes the geometry less streamlined, and therefore induces a larger wake that generates a more intense unsteadiness. However, these results seem to suggest that a reduction in the wake intensity is expected at larger door angles. This observation may suggest an inherent limitation of the URANS model and a different result may be obtained when running the same case with DES [54, 76].

2. **The gap ratio**
   Smaller gap ratios, G, a weaker wake intensity is induced. The changes in the variance of the lift load as $G \to G_{crit}$ along $\alpha_D = 0°$ agrees with the literature as it is well known that the near wake region behind the cylinder becomes less intense as the gap ratio G is set below the critical threshold $G < G_{crit}$.

The variables that have not been considered as part of this exercise are:

1. **Reynolds number effect**
   This URANS study did not assess the sensitivity of the results to varying Re. However, the separation points on the leg-door surface are most likely fixed due to the presence of the sharp corners.

2. **Varying the strut geometry**
   The strut geometry was fixed as a smooth cylinder. In reality, the main strut contains wiring and details that could mimic the effect of moderate surface roughness.

3. **The lateral positioning of the strut**
   Although it is likely that the lateral positioning of the cylinder along the leg-door may have an affect on the flow dynamics, no tests were conducted to assess its influence.

3.4 Technical approach

The 2-D URANS study along $G = 0.087$ is selected as the primary focus for further investigation via experimental measurements and high-order numerical simulations. The effect of the leg-door angle will be investigated as this will provide a novel insight into the leg-door interaction effects, which have not been previously studied. Experimental measurements will provide a database of forces, surface flow features, the velocity field in the wake, and the surface pressure spectra. This database will be used to validate the numerical simulations. The numerical data will then be used to compute far-field noise via a FW-H solver. These should give insight into the effect of the door angle on the aerodynamic interaction with a circular cylinder in a side by side configuration at a constant gap-proximity. The effect of the changes to the near-field aerodynamics on the far-field acoustics will be investigated.

Chapter 4

Numerical methods development

This section outlines the recent modifications to the high-order CAA solver. Although the code has been validated against analytical solutions for acoustic and vortex wave-propagation problems [88], and applied to a benchmark landing gear problem [60], some numerical issues have since been identified. While two-dimensional Navier-Stokes simulations using RANS turbulence models perform as expected, three-dimensional DES simulations tend to poorly resolve the smaller structures in the wake. The sensitivity of the solution field to the numerics tends to be greater as the spectral range of the resolved turbulence widens. The root cause of this issue was found to be the excessive amount of numerical filtering that is required to ensure numerical stability.

The cause of the numerical instabilities was identified, and the aforementioned numerical issues were overcome by the implementation of alternate spatial and filtering schemes. To outline the steps taken in identifying and resolving these issues, this section is organised in the following manner. Firstly, the numerical methods employed in the original version of the high-order solver are detailed. The applicability of these original methods in solving highly non-linear problems, such as turbulence generation and transport on a complex grid topology, is discussed. The steps taken to overcome the numerical issues are then outlined, and a comparison of the old and updated versions of the solver is provided.

The numerical issues identified affect the fidelity of the solver. The root cause of the numerical issue was the requirement of stronger spatial filters to overcome issues of numerical stability. To improve the fidelity of the solver, a grid assessment method was also developed. This tool removes the need for additional filtering due to poorly defined grids, and its effectiveness is demonstrated with simplified studies.

4.1 Original spatial scheme

The spatial gradient terms in the governing equations are computed using high-order implicit spatial schemes. The spatial scheme for the first derivative of scalar field f with respect to x can be expressed as

$$D_i + \sum_{K=-N}^{M} \left(\alpha_K D_{i+K}\right) = \frac{1}{\Delta x} \sum_{k=-n}^{m} \left(a_k f_{i+k}\right), \tag{4.1}$$

where the index i is point along the grid line, $-N$ and M define the size of the implicit stencil, $-n$ and m define the range of the explicit stencil, and α and a are coefficients that ensure a desired order of accuracy. By setting $M = N = 0$ an explicit scheme is obtained. Hixon and Turkel [96, 97] prefactored the implicit spatial schemes, where the derivative is evaluated as an average of a forward and backward term.

$$D_i = \frac{1}{2}\left(D_i^F + D_i^B\right). \tag{4.2}$$

The forward D_i^F and backward D_i^B operators are defined by a lower-diagonal and upper-diagonal system. Prefactored schemes are advantageous in two ways. Firstly, prefactored schemes can provide a desired order of accuracy with a significantly smaller stencil size. For example, the standard sixth-order compact scheme requires a seven point stencil, whereas the prefactored sixth-order scheme requires only a three point stencil [96]. This is particularly impressive as a second-order explicit central scheme also requires a three point stencil. Secondly, the prefactored schemes are less sensitive to low-order boundary schemes, which makes boundary condition implementations easier. In the original high-order CAA solver the 8/4 prefactored scheme derived by Ashcroft and Zhang [98] was applied. The 8/4 scheme is an optimised fourth-order prefactored scheme based on an eighth-order scheme. The forward D_i^F, and backward D_i^B, operators for the 8/4 scheme are

$$\alpha_F D_{i+1}^F + \beta_F D_i^F = \frac{1}{\Delta x}\left[a_F f_{i+2} + b_F f_{i+1} + c_F f_i + d_F f_{i-1} + e_F f_{i-2}\right], \tag{4.3a}$$

$$\alpha_B D_{i-1}^B + \beta_B D_i^B = \frac{1}{\Delta x}\left[a_B f_{i+2} + b_B f_{i+1} + c_B f_i + d_B f_{i-1} + e_B f_{i-2}\right], \tag{4.3b}$$

where the terms hold their usual meaning, and the coefficients can be found in [98]. If we consider a grid point cluster where information only exists along $i = \{0, N\}$, then Equation 4.3 cannot be applied along $i = \{0, 1, N-1, N\}$. Along these points, one of two schemes can be applied. If neighbouring ghost point information is unavailable, then the following explicit biased boundary schemes are applied [98]

$$D_0 = \frac{1}{\Delta x}\sum_{j=0}^{3} c_j f_j, \qquad D_1 = \frac{1}{\Delta x}\sum_{j=0}^{3} -e_{N+1-j} f_j, \tag{4.4}$$

$$D_N = \frac{1}{\Delta x}\sum_{j=N-3}^{N} -c_{N+1} f_j, \qquad D_{N-1} = \frac{1}{\Delta x}\sum_{j=N-3}^{N} -s_{N+1-j} f_j, \tag{4.5}$$

where the coefficients c_j are obtained by matching the Taylor series of the scheme to third-order. The coefficients for e and s are obtained by matching the Taylor series of the schemes to the Taylor series expansion of the forward and backward schemes given in Equation 4.3. Along boundaries where neighbouring ghost point information is available, the explicit eleven-point fourth-order optimised central scheme is applied [98]. High-order schemes induce low levels of artificial dissipation. Therefore spurious modes are removed by an explicit sixth-order filter, which is applied to the solution field at the end of each time step. An explicit filter applied on a scalar ψ is given by

$$\hat{\psi} = \sum_{i=-M}^{N} a_i \psi, \tag{4.6}$$

where M and N determine the stencil size, and the coefficients a_i are obtained by matching the Taylor series to the desired order for the scheme. The spatial and filtering schemes can be evaluated by their spectral characteristics, which can be obtained by Fourier analysis [55, 99]. The Fourier transformation of Equation 4.1, with the derivative and shifting theorems, gives

$$jk^*\Delta x = \frac{\sum_{z=-n}^{m}\left(a_z e^{jk\Delta x z}\right)}{1+\sum_{Z=-N}^{M}\left(\alpha_Z e^{jk\Delta x Z}\right)}, \tag{4.7}$$

where $j = \sqrt{-1}$, and k and k^* are the original and modified wave number, respectively. The ideal solution $k^*\Delta x = k\Delta x$ is used to assess the performance of the spatial scheme. Equation 4.7 can contain real and imaginary parts, which represent the dispersion and the dissipation errors, respectively. The dispersion relation for the interior and boundary schemes of the 8/4 method are illustrated in Figure 4.1 and it shows that the errors become significant only beyond a threshold wave number $k_c\Delta x$. This threshold varies significantly between the interior and boundary schemes. The term $k\Delta x$ is inversely proportional to the grid resolution for a specific wave number. Therefore, the dispersion errors in Figure 4.1 become larger when the resolution of the wave reduces.

The Fourier transform of the explicit filtering scheme yields its transfer function defined as

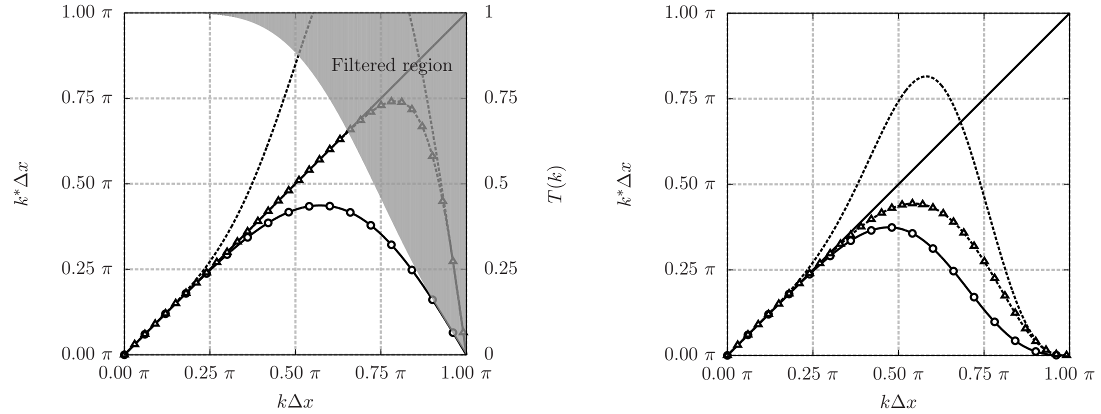

(a) No filter applied

(b) Sixth-order filters applied

Figure 4.1: The effect of the sixth-order explicit filters on the dispersion relation for interior and boundary schemes of the 8/4 method. Curves for the exact solution ——, interior scheme —▵—, boundary scheme at $i = [1, N-1]$ —○—, and the boundary scheme at $i = [0, N]$ - - - . Filter transfer function is highlighted in grey.

$$T(k) = \frac{\hat{\psi}(k)}{\psi(k)} = \sum_{i=-M}^{N} a_i e^{jki}. \tag{4.8}$$

The transfer function $T(k)$ is composed of real and imaginary parts that defines the modulation of an input scalar field along discrete wave numbers. In Figure 4.1 the effect of the filter on the dispersion relation is shown separately. The spatial filters suppress modes that are beyond a threshold wave number. Sixth-order explicit filters have a low threshold wave number, and this results in a significant reduction to the overall resolution capability of the 8/4 schemes. The effect of this excessive filtering is a significant reduction of the resolution in high wave number features, such as the smaller scales of a turbulent wake[1].

Sixth-order filters are not always required for stable computations when using the 8/4 schemes. Figure 4.1 shows that the majority of the dispersion errors are due to the third-order boundary schemes. These boundary schemes are required only in computations that contain a characteristic interface condition (CIC), or a boundary condition with no ghost-point information. For these cases, a high-order, high-pass filter can be applied. However, for the current project all grids require the CIC.

The initial methods to reducing the excessive amounts of spatial filtering were:

---

[1] The lack of small scale structures was also attributed to the deficiency in the non-linear growth of instabilities. Therefore the Z-DES method was also implemented.

- **Weighting the explicit filtering**
  The explicit filters were weighted by a user-defined constant. In this method, only a portion of the filtered solution was applied to the final solution. This method has been applied to high-order jet flow DNS simulations [51]. Although this method provides a simple means of reducing the levels of spatial filtering, the spectral range that is affected by the filters remains unchanged. Furthermore, this method contains a tunable parameter that would be unique for different cases, thereby making it an impractical solution. The source of the instability is due to the large dispersion errors generated by the fully-biased third-order schemes. This strategy does not treat the problem at its source.

- **Improving the boundary scheme**
  The coefficients for the third-order boundary scheme were optimised for maximum dispersion relation preservation. The optimisation process reduces the order of the spatial scheme. The final optimised boundary scheme is first-order accurate and has a dispersion relation profile that is similar to the interior scheme. The application of the first order scheme with the 8/4 interior scheme provides a global accuracy of second-order. Therefore, this method was also decided as infeasible. Alternate implicit boundary formulations were also explored for the prefactored schemes. However, it is desirable to maintain the diagonal form of the prefactored schemes to ensure a low computational cost. An implicit boundary scheme affects this property and would quadruple the computational effort required to evaluating the spatial derivative along a single grid line.

The complex numerical coupling between the spatial and filtering schemes makes the development of newer schemes difficult. Therefore, tested and proven methods were applied instead. In the following section the penta-diagonal implicit spatial schemes [51, 100], and filtering schemes [101] are outlined.

4.2 Penta-diagonal spatial scheme

The spatial derivative D, of a scalar f, along x, at a node indexed by i is given by the following penta-diagonal scheme

$$\beta D_{i-2} + \alpha D_{i-1} + D_i + \alpha D_{i+1} + \beta D_{i+2} = \frac{1}{\Delta x} \sum_{m=1}^{3} a_m \left(f_{i+m} - f_{i-m} \right), \tag{4.9}$$

where all the terms hold their usual meanings. Equation 4.9 requires a five- and seven-point implicit and explicit stencil, respectively. This interior scheme cannot be applied to the nodes at $i = \{0, 1, 2, N-2, N-1, N\}$, for a grid distributed between $i = \{0, N\}$.

Along the block edges, the high dispersion relation preservation provided by the interior scheme is desired. Therefore, the interior scheme is applied towards the block edges, by extrapolating the unknown variables using one of two methods. The extrapolation spline is a fourth-order polynomial and trigonometric function with additional control parameters used for DRP optimization [51, 100].

In a fully biased boundary scheme, the interior grid data is used to extrapolate the field variable, and its spatial derivative, beyond the block edges [100]. The fully biased boundary scheme is applied along the first three, and the final three, grid points i.e., $i = [0, 1, 2, N-2, N-1, N]$. The fully biased boundary schemes are applied along a block edge, where no grid point information is readily available beyond the block edge. However, in a multi-block system, information beyond the block edge is readily available. Therefore, only the spatial derivatives require extrapolation. This forms a separate set of boundary schemes, which are termed herein as ghost point (GP) boundary schemes. Since the implicit stencil is only five points wide, the extrapolation schemes are required only along the first two, and final two, grid points i.e., $i = [0, 1, N-1, N]$.

The dispersion relation for the interior scheme, and for the fully-biased boundary schemes is shown in Figure 4.2, and the dispersion relation for ghost point boundary schemes is shown separately in Figure 4.3. The dispersion relations for the interior and boundary schemes show improvements over the 8/4 method. However, the computational effort required is much greater due to the wider stencil employed by the penta-diagonal schemes.

To provide numerical stability, fully implicit sixth-order filters are applied [101]. The implicit filter is defined in terms of $\Delta\hat{\psi} = \psi + \hat{\psi}$, which is the change induced by the filter, defined as the difference between the unfiltered, and filtered variables. The implicit filters have the following form

$$\beta\Delta\hat{\psi}_{i-2} + \alpha\Delta\hat{\psi}_{i-1} + \Delta\hat{\psi}_{i} + \alpha\Delta\hat{\psi}_{i+1} + \beta\Delta\hat{\psi}_{i+2} = \sum_{m=1}^{3} A_m \left(\psi_{i-m} - 2\psi_i + \psi_{i+m}\right), \quad (4.10)$$

where the coefficients ensure sixth-order grid convergence, and are a function of a user-defined scalar k_c [101]. The performance of the filtering scheme, defined by Equation 4.10, is given by the filter transfer function, which is illustrated in Figure 4.4 for various values of k_c. The parameter k_c controls the cut-off wave number beyond which the filters are effective. Similarly to the penta-diagonal spatial scheme, a fourth-order polynomial extrapolation is applied to the unknown variables that are required when applying Equation 4.10 near the block edges. The extrapolation applied to the nodes at $i = \{0, 1, 2, N-2, N-1, N\}$ generates different sets of filter transfer functions. The transfer functions for the points along $i = \{0, 1, N-1, N\}$ are effectively zero, and the transfer function for $i = \{2, N-2\}$ is shown in Figure 4.5 for various values of k_c.

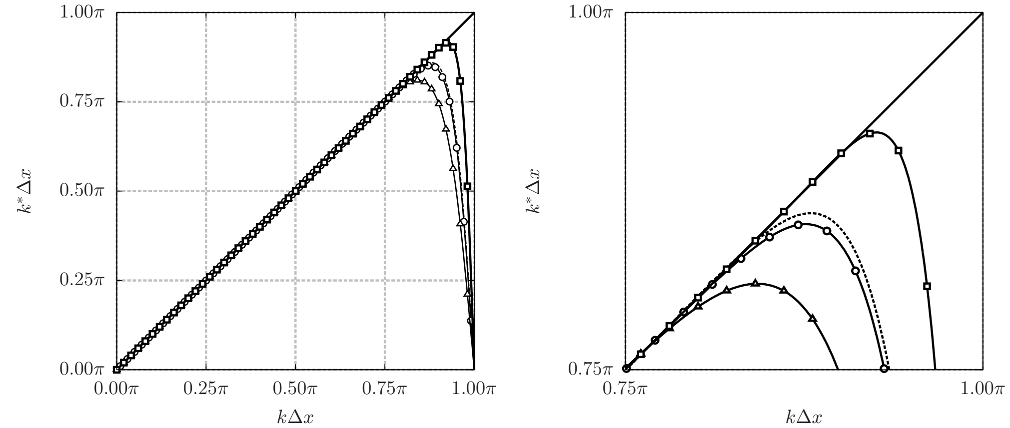

(a) Real part

(b) Close-up of the real part

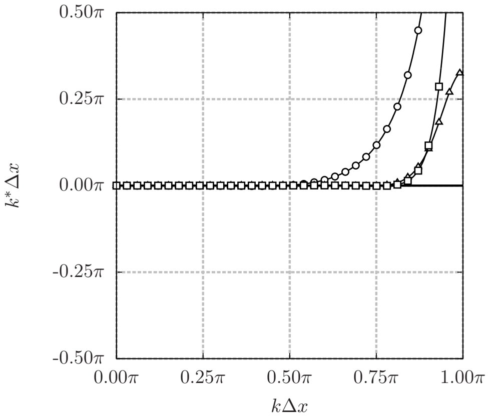

(c) Imaginary part

Figure 4.2: Fourier analysis of errors on the penta-diagonal scheme with fully-biased boundary schemes[100]. Curves for the exact solution ——, interior scheme - - -, boundary schemes at $i = [0, N]$ —○—, at $i = [1, N-1]$ —△—, and at $i = [2, N-2]$ —□—,

The solution to the penta-diagonal system is obtained by decomposing the system into a lower and upper tri-diagonal matrix [102]. The lower and upper diagonal systems are evaluated and stored prior to main simulation.

4.2.1 Summary of the changes

The 8/4 spatial schemes induce large dispersion errors towards block interfaces evaluated using the fully-biased third-order scheme. Fully-biased schemes are required for the CIC method, which is used frequently on structured grids. These dispersion errors generate spurious modes, which remain in the solution field due to the low levels of

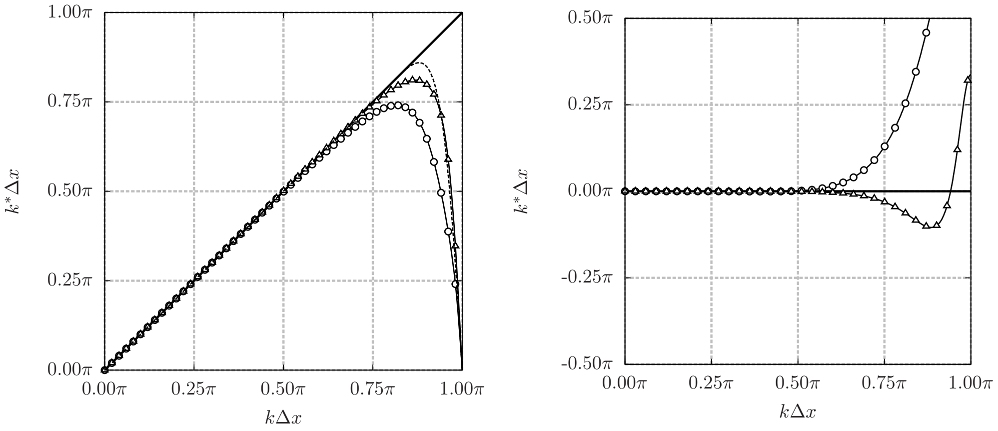

(a) Real part

(b) Imaginary part

Figure 4.3: Fourier analysis of errors on the penta-diagonal scheme with ghost point boundary schemes [51]. Curves for the exact solution ——, interior scheme - - -, boundary schemes at $i = [0, N]$ —○—, and at $i = [1, N-1]$ —△—

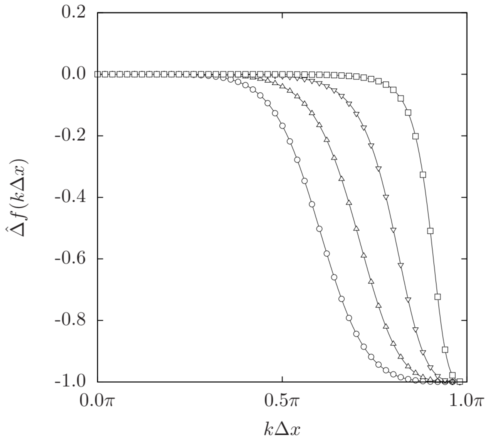

(a) Real part

Figure 4.4: Implicit filter transfer function for the interior points, with $k_c = 0.9$ —□—, $k_c = 0.8$ —▽—, $k_c = 0.7$ —△—, and $k_c = 0.6$ —○—.

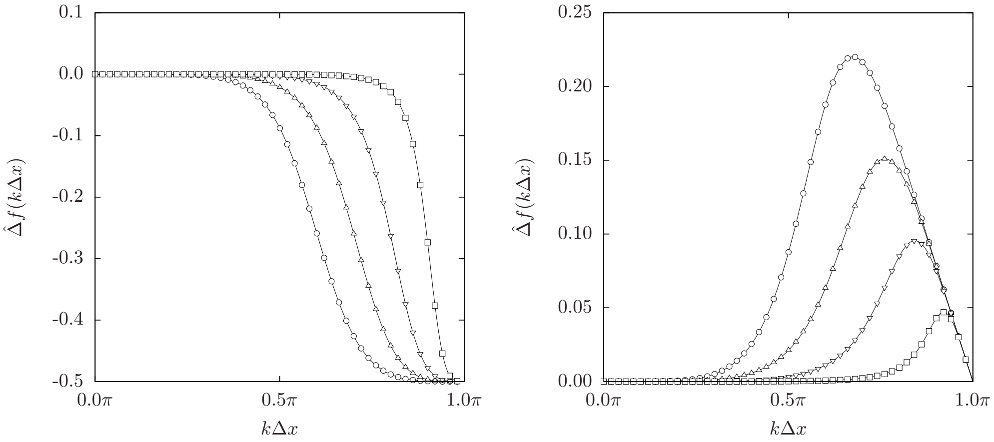

(a) Real part

(b) Imaginary part

Figure 4.5: Implicit filter transfer function for the boundary points $i = \{2, N - 2\}$, with $k_c = 0.9$ −□−, $k_c = 0.8$ −▽−, $k_c = 0.7$ −△−, $k_c = 0.6$ −○−.

artificial dissipation in high-order schemes. Therefore, a sixth-order explicit filter is applied. However, the explicit filters remove small scale features, which are within the resolvable range of the interior scheme. For this reason, the 8/4 schemes may resolve a narrow and small frequency band of turbulent flows, and resemble a highly diffusive and low *Re* turbulent field. An alternate penta-diagonal spatial and filtering schemes were implemented, which have improved dispersion relation preservation characteristics along boundaries that apply the CIC. This enables a reduced level in the global filtering required and improves the fidelity of the solver. In the following section, the impact of these changes is discussed.

4.3 Impact of the changes

Two examples qualitatively illustrate the effects of the changes in the spatial and filtering schemes, on the flow field behind bluff bodies. Figure 4.6 illustrates the resolved flow structures formed in the wake of a circular cylinder at a Reynolds number of $Re_D = 1.7 \times 10^6$ based on the cylinder diameter D, and at a free-stream Mach number of $M = 0.2$. Figure 4.6 highlights how the penta-diagonal schemes improve the range of resolved turbulent scales in the wake region, when compared to the solution field obtained by the 8/4 schemes. For this example, the penta-diagonal filters were set with a cut-off wave number of $k_c = 0.8\pi$, and the Z-DES method was applied.

Another qualitative example is given by Figure 4.7, which illustrates the flow behind an interaction model with a leg-door angle of $\alpha_D = 10.7$ degrees, and under the same Mach number and Reynolds number as the previous example. This result also shows

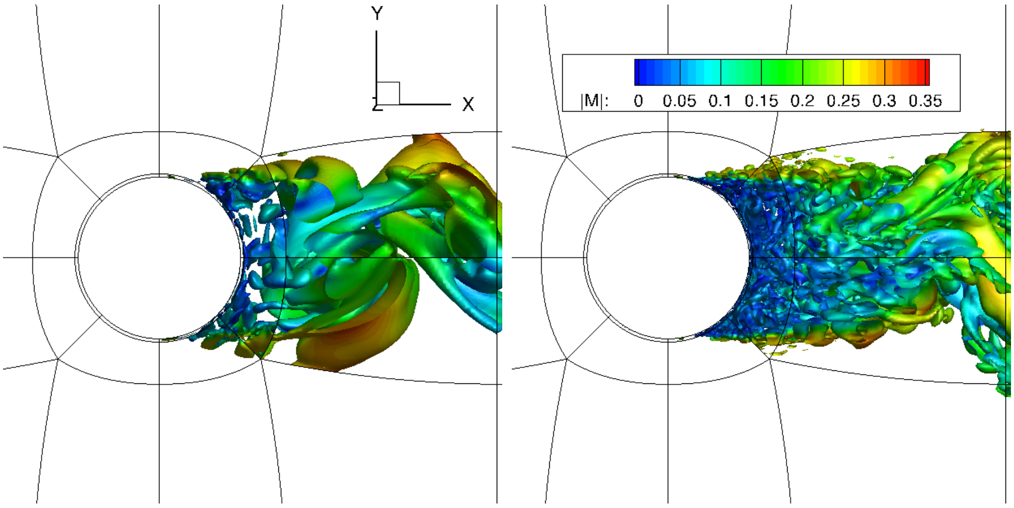

(a) ZDES - 8/4 schemes (b) ZDES - penta-diagonal schemes

Figure 4.6: The flow features behind a cylinder at $Re_D = 1.7 \times 10^6$ predicted by the original and new versions of the code. Turbulent are illustrated by a surface contour of $Q = 1$ and coloured by the velocity magnitude.

the increased fidelity of the solver. The DES modelling was initially hypothesised to be the primary cause of the poor resolution of the wake region. Some of the lack of small scale structures was thought to be due to the suppressed growth of non-linear instabilities. Therefore, the effect of Z-DES modelling was also tested as part of this example. These examples demonstrate that the fidelity of the solver is improved by the changes in the numerical schemes, which allow lower levels of numerical filtering to be applied. The formation of a diffusive wake region was due to the use of low-pass spatial filters. These filters remove the small scale features in a turbulent flow, and this may induce an increase in the vorticity magnitude within the wake region. This increase in vorticity magnitude generates a larger production term in the S-A turbulence model, which increase the viscous diffusion in the wake. The overall effect is a narrow band of large scale and coherent structures formed in the wake of bluff bodies at relatively high Reynolds numbers.

Figure 4.8 compares the power spectral density of a pressure monitor located along the cylinder surface in the most downstream position. The two cases differ only by the spatial and filtering schemes applied. The key changes to the surface spectra are the reduction in the tonal behaviour and the increased energy levels towards higher frequencies. The latter is associated with the reduction in the range of scales that are affected by the implicit filters. The cessation of tonal behaviour signifies a decrease in the coherency of the structure in the wake region, which is attributed to the reduced levels of diffusion in the wake region.

Figure 4.9 illustrates the variance of the mean velocity in the traverse direction, and it shows that the solution obtained with the 8/4 schemes suffers from additional numerical

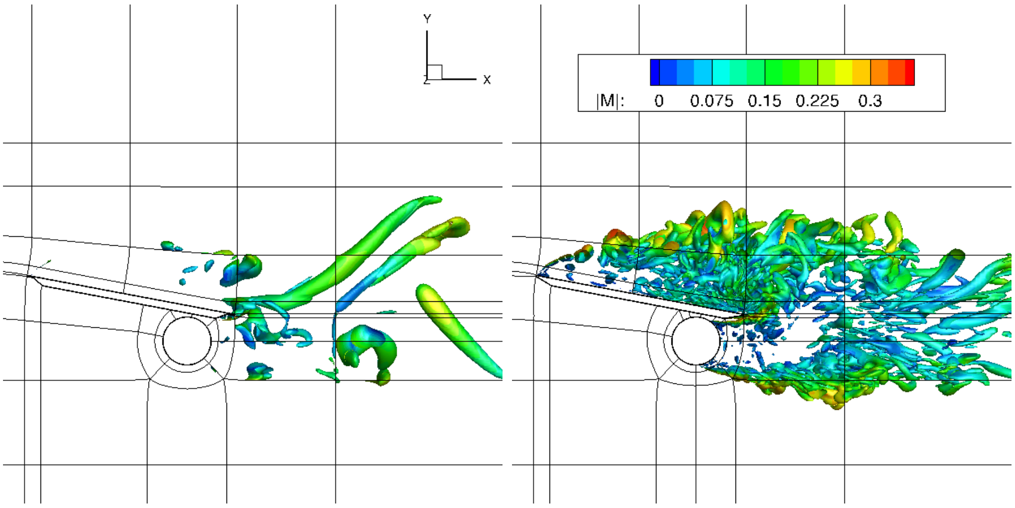

(a) DES97 - 8/4 schemes

(b) ZDES - penta-diagonal schemes

Figure 4.7: The flow features behind an interaction case at $Re_D = 1.7 \times 10^6$ predicted by the original and new versions of the code. Turbulent features are illustrated by a surface contour of $Q = 1$ and coloured by the velocity magnitude.

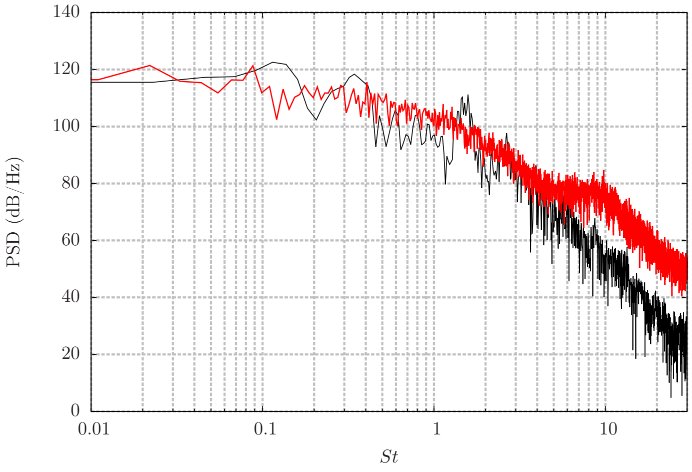

Figure 4.8: The surface pressure spectra on a circular cylinder at $\theta = 0$ predicted by the old (——) and new (——) version of the code

errors along block interfaces. This is due to the low-order biased spatial and filtering schemes applied along the block edges, applied in the original solver. It should be noted that the 8/4 schemes applied with the implicit filters were found to be numerically unstable. This topic is discussed in the next section.

4.4 Numerical stability of spatial schemes

Eigenvalue analysis is performed to verify the asymptotic stability of spatial schemes. The analysis is commonly applied as a single block case [51, 96, 98, 100, 103], which

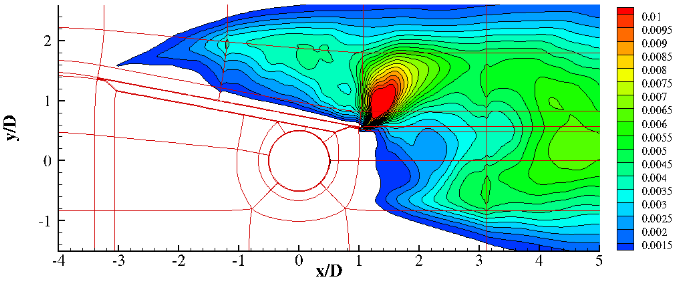

(a) 8/4 schemes

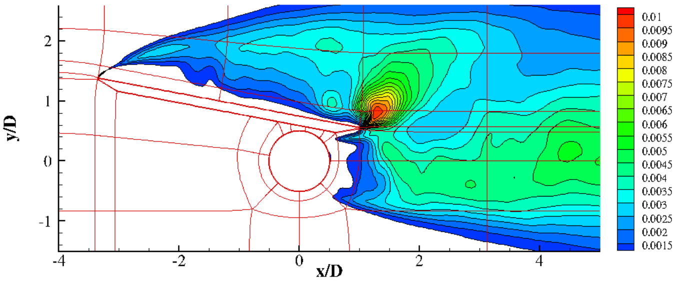

(b) penta-diagonal schemes

Figure 4.9: The field of $\overline{v'v'}$ around an interaction model at $\alpha_D = 10.7$ degrees predicted by the old and new versions of the code. The block edges are highlighted in red.

is suitable for explicit spatial schemes and for cases that do not apply characteristic interface conditions. The analysis on a single block includes the interior and fully-biased boundary schemes. However, the influences of ghost-point implicit boundary schemes and characteristic interfaces cannot be fully considered in a single block environment, therefore an extension to a multi-block environment is proposed. This section is outlined as follows. Firstly, the eigenvalue stability analysis is described for a single block case and is provided for the 8/4 and penta-diagonal schemes. The multi-block extension is then outlined in the second section, and the results from the extended analysis is given.

4.4.1 Eigenvalue Analysis

The method outlined is a brief description of the work by Carpenter *et al.* [103]. The one-dimensional scalar wave equation is given by

$$\frac{\partial u}{\partial t} + c\frac{\partial u}{\partial x} = 0, \tag{4.11}$$

where u is the scalar field, t is the time and c is the propagation speed of the wave. The boundary and initial conditions are defined by

$$u(x=0,t)=g(t), \qquad u(x,t=0)=f(x). \tag{4.12}$$

The spatial derivatives are evaluated along a discretised domain $x \in [0,1]$ with N uniform intervals of width Δx, and the solution is advanced in time by the method-of-lines approach [103]. The spatial derivative operator yields is given by,

$$\mathbf{BD} = \frac{1}{\Delta x}\mathbf{CU}, \tag{4.13}$$

where the matrices $\mathbf{B}$ and $\mathbf{C}$ contain the implicit and explicit scheme coefficients, respectively, and the matrices $\mathbf{U}$ and $\mathbf{D}$ represent the discretised scalar field and its spatial derivative. By substituting Equation 4.13 into 4.11 the following is obtained

$$\frac{d\mathbf{U}}{dt} = -\frac{c}{\Delta x}\mathbf{B}^{-1}\mathbf{CU} + \boldsymbol{B}g(t) = -\frac{c}{\Delta}\mathbf{MU} + \boldsymbol{B}g(t). \tag{4.14}$$

The prefactored schemes, expressed by Equations 4.2, yield the following expression for the matrix [$\mathbf{M}$]

$$\mathbf{M} = \frac{1}{2}\left(\mathbf{B}^{F^{-1}}\mathbf{C}^{F} + \mathbf{B}^{B^{-1}}\mathbf{C}^{B}\right), \tag{4.15}$$

where the spatial derivatives are determined as an average of a forward and backward operator, which are indicated by the superscripts F and B. Setting $g(t)=0$ is convenient with little loss of generality [103], and the exact solution for homogeneous boundary data is

$$u(t) = f(x)e^{Mt}. \tag{4.16}$$

Within the matrix $\boldsymbol{M}$ the boundary condition $u(x=0,t)=0$ is applied and the size of the matrix is reduced by one. The eigenvalues of the $(N-1)$ square matrix $\mathbf{M}$ determines the asymptotic stability of the solution. The system is asymptotically stable if all the eigenvalues lie of the left half of the complex plane. Without the boundary condition $u(0,t)=0$ the analysis will always yield unstable results because the governing equation is not bounded properly. The effect of spatial filtering can be included into the analysis by the following modification to the matrix $\mathbf{M}$ [101],

$$\mathbf{M} = \mathbf{B}^{-1}\mathbf{C}\left(\boldsymbol{I} + \sigma\mathbf{R}^{-1}\mathbf{S}\right), \tag{4.17}$$

where $\boldsymbol{I}$, $\mathbf{R}$ and $\mathbf{S}$ are respectively the identity matrix, and the matrices for the implicit and explicit coefficients for the filtering scheme. The scalar σ acts as a switch to enable, or disable, the effect of the filters into the analysis.

4.4.2 Single block analysis

For a single block environment the only restriction on the matrix $\boldsymbol{M}$ is the boundary condition. The eigenvalues for the 8/4 [98] and penta-diagonal scheme [101] are reproduced in Figure 4.10 to verifty the implementation of the single block analysis against the published results [98, 100]. Figure 4.10 shows the eigenvalues for these schemes with and without the use of the penta-diagonal implicit filters with $k_c = 0.85\pi$[101]. These results show that stable solutions are always expected from either spatial scheme, with the use of a compact filter.

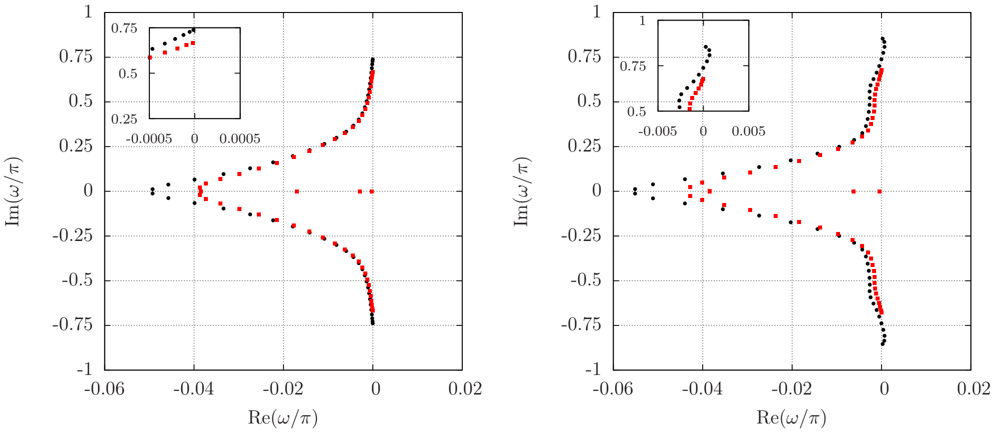

(a) 8/4 Scheme

(b) Penta-diagonal scheme

Figure 4.10: Eigenvalue analysis for a 51-node on a single block domain using two different spatial schemes, with (•) and without (•) the penta-diagonal filters ($k_c = 0.85\pi$) [101].

Early tests showed that the 8/4 scheme does not always provide stable solutions when studying cases containing complex geometries. These complex cases were solved in a multi-block environment and also applied the CIC conditions. The hypothesis is that a single block analysis does not account for the changes to the numerical stability that is due to the use of ghost-point or fully-biased implicit boundary schemes along block interfaces. This is the topic of the following section.

4.4.3 Multiple block analysis

For this section, we consider a multi-block environment illustrated by Figure 4.11. In Figure 4.11, the domain $x \in [0, L]$ is discretised into nine grid points. The domain is divided into a left and right block, which consist of five grid points each. The block interface along the highlighted region is shared between both blocks as an over-set grid point. Although the domain consists of two separate systems, the stability analysis can be applied as a single block by applying the condition $u^L_{i=4} = u^R_{i=0}$, where the superscripts L and R refer to the left and right block, respectively. This condition ensures continuity across the interface, and can be satisfied by two methods.

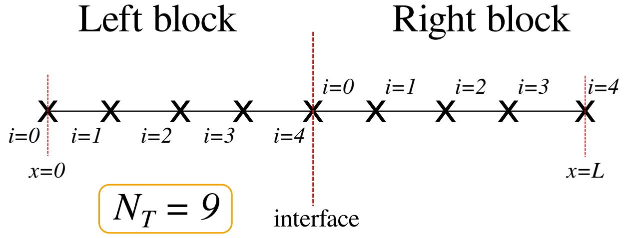

Figure 4.11: A nine point grid cluster divided into a left and right blocks. The interface and boundary zones are highlighted by the red dashed line.

Two interface conditions are tested. The first is a one-to-one boundary condition, whereby neighbouring ghost-point information is used to evaluate the spatial derivatives along the interfaces, and this method will be referred herein as the GP method. For explicit schemes, the single- and multi-block expression for the matrix $\mathbf{M}$ will be equivalent. This is because the spatial schemes employed along the interface and interior points are equivalent. Implicit boundary schemes using ghost-point information are not equivalent to the implicit interior scheme. Therefore, a multi-block expression for a fully implicit spatial scheme will have different characteristics compared to the single block analysis. Due to the bias of the computational stencil, in the implicit GP boundary schemes, the continuity across the interface is not guaranteed. Therefore, an averaging of the spatial derivatives at that point is applied to ensure continuity. This interface averaging is also applied to the implicit filtering scheme as the filters employ fully implicit boundary schemes as well. The averaging for the filters at the interface is expressed by

$$\Delta\tilde{u}^L_{i=4} = \Delta\tilde{u}^R_{i=0} = \frac{1}{2}\left(\Delta\tilde{u}^L_{i=4} + \Delta\tilde{u}^R_{i=0}\right), \tag{4.18}$$

where the superscripts L and R represent the quantities along the left and right sides of the block interface. A multi-block environment is also useful for the prefactored schemes. The spatial schemes employed along block interfaces are also different to the interior schemes. Therefore the stability of a multi-block case is likely to differ from a single-block analysis.

The second interface tested is the characteristic interface condition (CIC), where the spatial derivatives are computed using fully-biased schemes and the fluxes are up-winded in the direction of the wave propagation. The scalar wave equation is already in a characteristic form, therefore the CIC is expressed as

$$\frac{\partial u^R}{\partial x} = \frac{\partial u^L}{\partial x}, \tag{4.19}$$

where the spatial derivative at the interface is up-winded from left to right in the direction of the wave propagation, which is determined by the sign of c in Equation 4.11. By imposing the continuity across the over-set grid points at the interface, the matrix $\mathbf{M}$ for a two-block system, consisting of five points each, can be expressed as a single matrix consisting of nine-points.

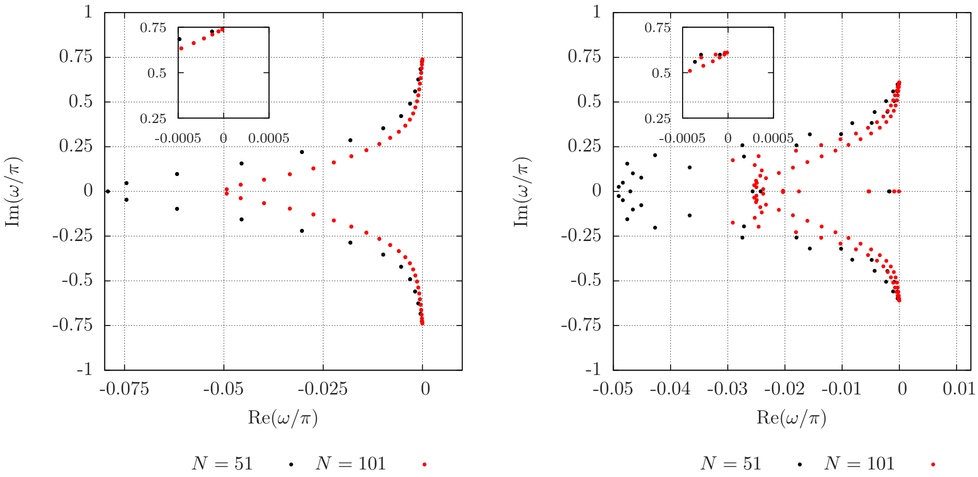

(a) No filters

(b) Implicit filters $k_c = 0.8\pi$

Figure 4.12: Two block system Eigenvalues using 8/4 fully-biased schemes at interface boundaries with the CIC.

Figure 4.12 and 4.13 show the results from the stability analysis for the 8/4 spatial schemes with the GP and CIC interfaces for two examples of a two-block system, with a total of 51 and 101 grid points. These results obtained with the GP interface show that 8/4 schemes do not ensure numerical stability when the implicit filters are applied. Some of the results from this case lie on the right side of the complex plane.

Figure 4.14 and 4.15 show the results for the penta-diagonal schemes using the GP and CIC interfaces under the same conditions are the previous example. These schemes are inherently unstable without the use of numerical filtering. However, with the presence of the implicit filters, the numerical stability is always ensured.

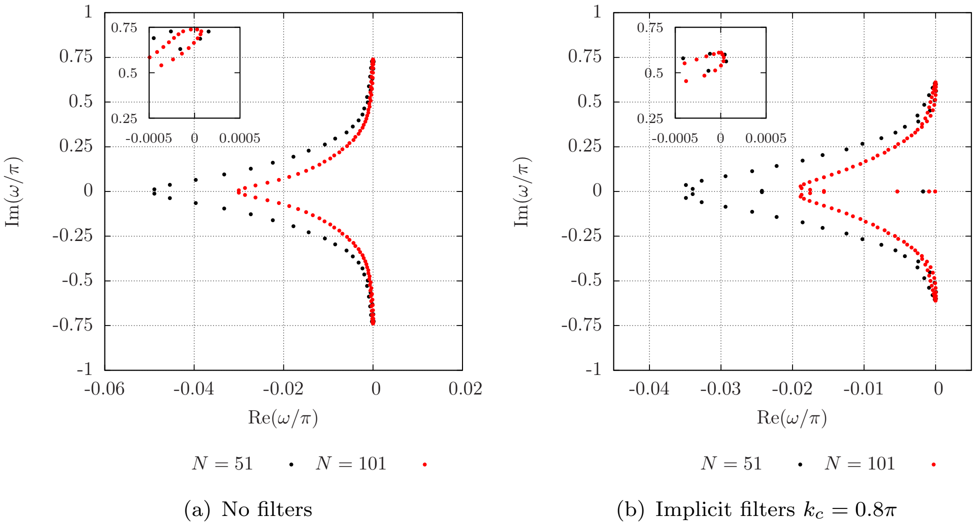

(a) No filters (b) Implicit filters $k_c = 0.8\pi$

Figure 4.13: Two block system Eigenvalues using the 8/4 central schemes at block interfaces with the GP method.

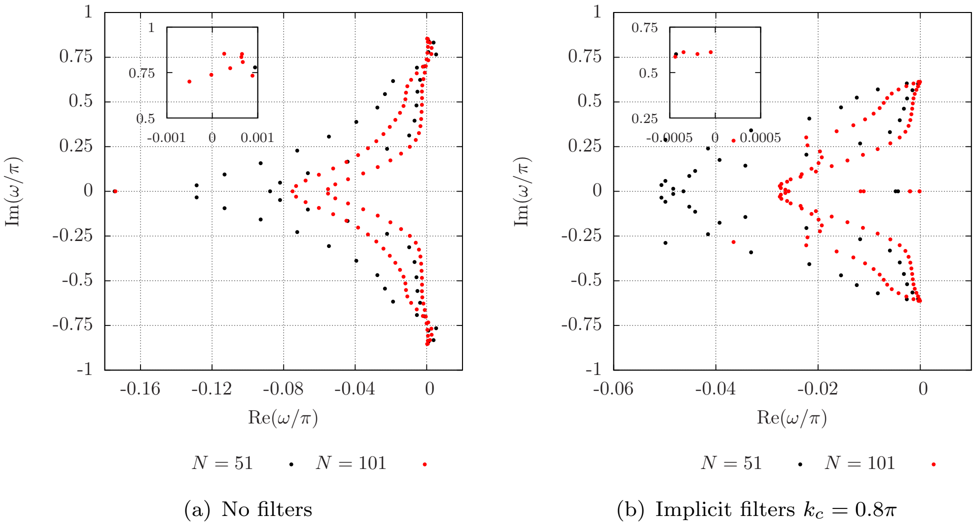

(a) No filters (b) Implicit filters $k_c = 0.8\pi$

Figure 4.14: Two block system Eigenvalues using the penta-diagonal fully-biased schemes at block interfaces with the CIC.

4.4.4 Summary

The minimal use of spatial filtering is paramount for high-fidelity solutions. Spatial filters are required to remove the onset of spurious modes in the solution field that are not treated by high-order spatial schemes due to their low-dissipation properties. The impact of excessive filtering was demonstrated on two examples of bluff body flows.

Reducing the intensity of the spatial filtering is not achieved in a one-step process. The coupled interactions between the spatial, filtering, and boundary, schemes, on the overall numerical stability must be considered by an enhanced multi-block eigenvalue

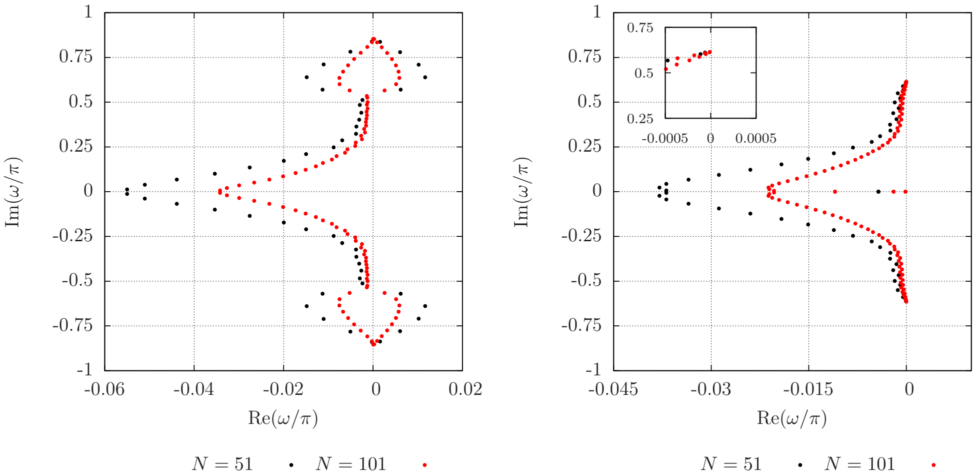

(a) No filters

(b) Implicit filters $k_c = 0.8\pi$

Figure 4.15: Two block system Eigenvalues using the penta-diagonal central schemes at block interfaces with the GP method.

analysis. Multi-block eigenvalue analysis demonstrated the complex coupling of spatial and filtering schemes on realistic block configurations. This enhanced analysis is able to identify unstable combinations of spatial and filtering schemes.

4.5 Grid quality assessment

There is a requirement in computational fluid dynamics (CFD) and computational aeroacoustic (CAA) simulations for low dispersion and low dissipation numerical methods to accurately predict the generation, propagation, and interactions of acoustic, entropic and vortical disturbances. This requirement can be satisfied by using high-order finite differencing (FD) methods, which have been applied in various CFD and CAA studies [51, 60]. Finite-differencing schemes are derived from a Taylor series and contain truncation errors. The amplitude of the truncation error may depend on the solution field and on the grid coordinates. The latter is the source of error that relates to the grid quality. Grids of higher quality generate smaller truncation errors, and contribute less to the total error, thereby providing a more accurate solution.

Inaccuracies in the solution field may be attributed to the properties of a grid, which are defined by the grid point distribution function. Truncation error analysis establishes the relationship between the grid point distribution function and the solution error. The truncation error is an infinite series of increasing higher derivative terms. In this analysis the cumulative truncation error, due to the spatial gradient terms in the governing equations, is estimated by numerically evaluating the leading order terms of the infinite truncation error series. Vinokur [104] investigated the truncation errors generated by different one-dimensional stretching functions, and Mastin [105] applied the method to two-dimensional cases. Lee and Tsuei [106] derived an expression for the truncation errors due to the convective terms in the two-dimensional Navier-Stokes equations, and Sankaranarayanan *et al.* [107] derived a similar equation governed by the linearised two-dimensional shallow water equations. The truncation errors contained in the spatial scheme may be expressed by,

$$T_x = T_{x1} + T_{x2} + T_{x3} + \text{Higher Order Terms}, \tag{4.20}$$

where the right hand side terms can be expanded. In the work by Thompson *et al.* [108] these terms are evaluated by a second order upwind differencing scheme, and the first term, T_{x1}, is defined as,

$$T_{x1} = \frac{1}{3J}\left[\left(y_\eta x_{\xi\xi\xi} - y_\xi x_{\eta\eta\eta}\right) f_x + \left(y_\eta y_{\xi\xi\xi} - y_\xi y_{\eta\eta\eta}\right) f_y\right]. \tag{4.21}$$

The right hand side terms of Equation 4.20 are functions of the Jacobian of the grid metrics (J), in addition to being a function of second and third order derivative terms. This estimation of the grid-induced error is non-trivial to calculate, as the high-order derivative terms must be evaluated by additional spatial schemes.

In the analysis by Lee and Tsuei [106] different spatial schemes were employed for the grid transformation metrics and the convection terms. Deng *et al.* [80] showed, for governing equations expressed in strong conservation form, that this inconsistency of spatial schemes can violate the surface conservation law. This violation may generate artificial and undesirable source and sink terms in the governing equations that result in numerical instabilities, and degrade the robustness of high-order methods.

Abrupt changes in the grid spacing or grid line direction, for example along block interfaces, have been identified as sources of grid-induced errors [87, 89, 105] and can lead to inaccuracies in the solution. Simple grid quality measures based only on local geometric properties have been suggested [109, 110]. However, in these examples a monotonic and strong correlation between the mesh quality metric and the solution accuracy was not obtained. The lack of a strong correlation may be caused by the presence of additional measures to ensure numerical stability. For example, Visbal and Giatonde [89] showed that low-pass filters, which can have similar effects on a numerical solution to artificial dissipation, can provide stable and accurate solutions in areas of the mesh where there are abrupt changes in the grid spacing or grid line direction. Solutions obtained under a strong influence of such additional schemes may reduce the impact of poor grid quality. However, stronger filters remove fine scale features from the solution field, thereby reducing the fidelity of the solution. Some filtering is inherently required for high-order methods to remove spurious modes. However, Colonius and Lele [50] emphasise that the removal of developing spurious waves should be attempted by improving the grid quality and enhancing the boundary condition accuracy rather than by using stronger filters or additional dissipation.

Curvilinear grids may be generated by manual inputs and auxiliary solvers. Typically the profile and the grid point distribution along block edges are defined manually. The interior grid is commonly generated by transfinite interpolation (TFI), or by elliptic solvers. The latter method ensures a smooth grid, and therefore a smooth metric of the grid transformation [111]. These methods involve a level of manual input that may require several iterations until a satisfactory grid is obtained. The number of iterations may be reduced if an effective grid quality measure is developed.

The quality of the mesh is often attributed to specific geometric properties such as the grid non-orthogonality [106, 107], or the aspect ratio [110, 112]. For any structured grid, all geometric features can be expressed by the grid point distribution function. Present grid quality measures, that depend on this function, are based on the work by Mastin [105] and Thompson *et al.* [108]. In these methods, the effects of the grid geometry on the individual terms of the truncation error series, are studied. The results are obtained by evaluating Equation 4.20, which requires a lengthy and non-trivial calculation.

In the current work an alternate approach to truncation error analysis is outlined. The truncation errors for a generic spatial scheme are expressed by Fourier analysis, and are shown to hold similarities to the transfer function of spatial filters. This similarity implies that spatial filters can be used to estimate the truncation errors generated by spatial schemes. A grid quality metric is defined that correlates to the truncation error, which is contained in the metrics of the grid transformation. The grid transformation metrics are dependant on the inverse metrics, which are obtained by applying the spatial schemes to the grid coordinates. Therefore, the truncation errors contained in the inverse metrics, due to the spatial schemes, are quantified by applying a filtering scheme to the grid coordinates. This evaluation is independent of the solution field. The grid quality metric is tested on various meshes containing uniform and non-uniform skewness, and discontinuities in the grid spacing and grid line direction. The purpose of these tests is to show that a clear relationship can be obtained between the solution accuracy and the grid quality measure. Finally a grid optimisation strategy is outlined, which maximises the grid quality by filtering the grid coordinates.

4.5.1 Derivation of the grid quality metric

The methodology to derive the grid quality metric is now described for a 1-D case. The application to higher dimensions is analogous. The 1-D wave equation is given by,

$$\frac{\partial f}{\partial t} + U\frac{\partial f}{\partial x} = 0, \tag{4.22}$$

where f is a scalar variable, t is time, and U is the convection speed in the x-direction. The spatial derivative in Equation 4.22 can be evaluated using a high-order scheme. Higher order spatial schemes may require a larger computational stencil along which the grid spacing is uniform. To apply high-order schemes, Equation 4.22 is transformed into the curvilinear (generalised) coordinate system by,

$$\frac{\partial f}{\partial t} + U\frac{\partial f}{\partial \xi}\frac{\partial \xi}{\partial x} = 0. \tag{4.23}$$

A solution to Equation 4.23 can be obtained by evaluating the spatial derivatives using high-order schemes along the generalised coordinates (ξ), and integrating the solution in time using a temporal scheme, together with accurate boundary conditions. The term $\partial\xi/\partial x$ is the grid transformation metric that is evaluated from the inverse metric, which in turn is evaluated along the generalised coordinate. The first derivative of scalar field f, with respect to ξ, can be evaluated by a generic spatial scheme expressed by,

$$D_i + \sum_{Z=-N}^{M} \left(\alpha_Z D_{i+Z}\right) = \frac{1}{\Delta\xi} \sum_{z=-n}^{m} \left(a_z f_{i+z}\right), \tag{4.24}$$

where the index i is the point on the grid line, $-N$ and M define the size of the implicit stencil, $-n$ and m define the range of the explicit stencil, and α and a are coefficients that ensure a desired order of accuracy. Fourier analysis [55, 99] can be used to obtain,

$$jk^*\Delta\xi = \frac{\sum_{z=-n}^{m}\left(a_z \mathrm{e}^{jk\Delta\xi z}\right)}{1+\sum_{Z=-N}^{M}\left(\alpha_Z \mathrm{e}^{jk\Delta\xi Z}\right)}, \tag{4.25}$$

where $j=\sqrt{-1}$, and k and k^* are the original and modified wave numbers, respectively. This expression decomposes the total truncation error to the contributions at discrete wave numbers. The ideal solution $k^*\Delta\xi = k\Delta\xi$ is used to assess the performance of the spatial scheme. Equation 4.25 may contain real and imaginary parts that represent the dispersion and the dissipation errors, respectively. The dispersion relations for various explicit central schemes are illustrated in Figure 4.16. The term $k\Delta\xi$ is inversely proportional to the grid resolution of a particular wave number. Therefore the truncation errors from a spatial scheme tend to become more significant as the grid resolution of the field, to which it is being applied, is reduced. A threshold wave number can be denoted as $k_c\Delta\xi$, which signifies the point beyond which the errors become significant. Ashcroft and Zhang [98] defined this point as the largest wave number to contain a dispersion error less than 0.5%. Kim [100] defined this point in a similar manner, which required errors less than 0.1%.

In Equation 4.23 a stationary grid is considered, and the numerical errors are due to three different terms. The first term is a temporal derivative, which depends only on

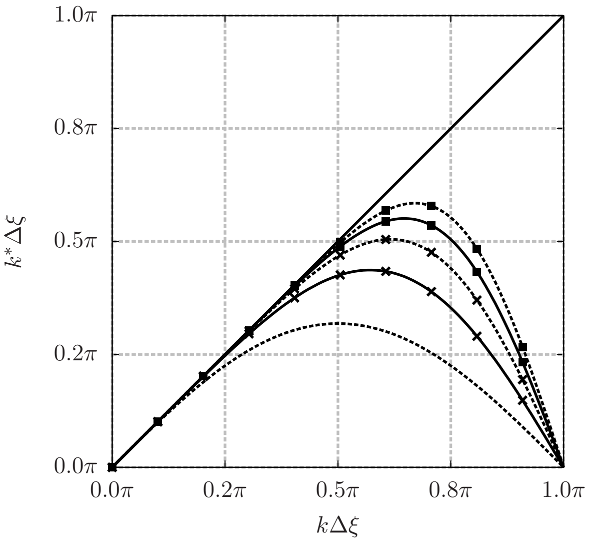

Figure 4.16: Dispersion error for explicit central spatial schemes of 2^{nd} - - -, 4^{th} —×—, 6^{th} -×-, 8^{th} —■— and 10^{th} -■- order. Exact solution is given by ——.

the solution field f. The temporal scheme will generate a truncation error that reduces with a smaller time-step. The remaining terms in Equation 4.23 are approximated using spatial schemes. The first of these terms, $\partial f/\partial\xi$, will generate large truncation errors if the solution field f is resolved poorly along the curvilinear axis ξ. These errors can be reduced by conducting a grid convergence study, where the grid refinement is focused on the areas containing large variations in f. This refinement requires prior knowledge of the solution field. Finally, the term $\partial\xi/\partial x$ is the metric of the grid transformation. Similarly this term will generate large truncation errors if the grid point distribution function ξ is resolved poorly along the physical coordinate x. This source of error can also be reduced by mesh refinement. However, it does not require any prior knowledge of the solution field f. If the solution field is continuous and the time-step is sufficiently small, then the most significant source of error is likely to be the metrics of the grid transformation. Therefore, the focus of this work is the error associated with $\partial\xi/\partial x$.

The discrete frequency Fourier analysis of spatial schemes illustrated by Figure 4.16 describes the mechanism of truncation error generation more clearly in comparison to the alternate, continuous frequency, description given by Equation 4.20. Figure 4.16 also shows that the truncation error profiles vary between different spatial schemes. Therefore, the truncation error estimate, based on the second order schemes, by Thompson *et al.* [108] may not be appropriate for solvers that employ high-order methods.

Truncation error estimation using filtering schemes

The low-dissipation properties of high-order schemes may make the solution vulnerable to spurious modes. Spurious modes are typically of high wave number and may form due to poor boundary conditions, or due to dispersion errors. Spatial filters can be applied, which selectively damp high wave number modes in a solution field [55]. A generalised explicit filtering scheme, derived from a truncated Taylor series, can be expressed by [113],

$$\hat{\psi} = \frac{1}{\Delta\xi} \sum_{i=-M_f}^{N_f} a_i \psi, \tag{4.26}$$

where ψ and $\hat{\psi}$ are the unfiltered and filtered scalars, respectively. The order of the filter is determined by the coefficients a_i and the size of the computational stencil is determined by the constants $-M_f$ and N_f. The filters are applied along the curvilinear coordinates where the grid spacing $(\Delta\xi)$ is uniform. By applying the Fourier analysis [55, 99], a filter transfer function can be defined by

$$T(k) = \frac{\hat{\psi}(k)}{\psi(k)} = \sum_{i=-M_f}^{N_f} a_i \mathrm{e}^{jki}. \tag{4.27}$$

The transfer function defines the modulation to an input scalar field along discrete wave numbers. The transfer functions for several explicit filters are illustrated in Figure 4.17. Low-pass filters have a wave number threshold, denoted by k_f, beyond which the filters damp the wave. This threshold is determined partly by the order of the scheme, and this property bears similarities to the dispersion relation for a spatial scheme, illustrated in Figure 4.16. A filter operator is defined as,

$$\hat{\Delta}\psi_i = \psi_i - \hat{\psi}_i, \tag{4.28}$$

which tends to zero if the scalar ψ is absent of high wave numbers, and tends to larger values as the scalar contains higher wave numbers. By applying a filter that has similarities between the transfer function and the dispersion relation of a spatial scheme, the filter operator output $(\hat{\Delta}\psi)$ can indicate areas of a scalar field (ψ) that are likely to generate large dispersion errors. To enhance the sensitivity of this output, it is recommended that the cut-off wave number of the filtering scheme be lower than the cut-off wave number of the dispersion relation function $(k_f < k_c)$.

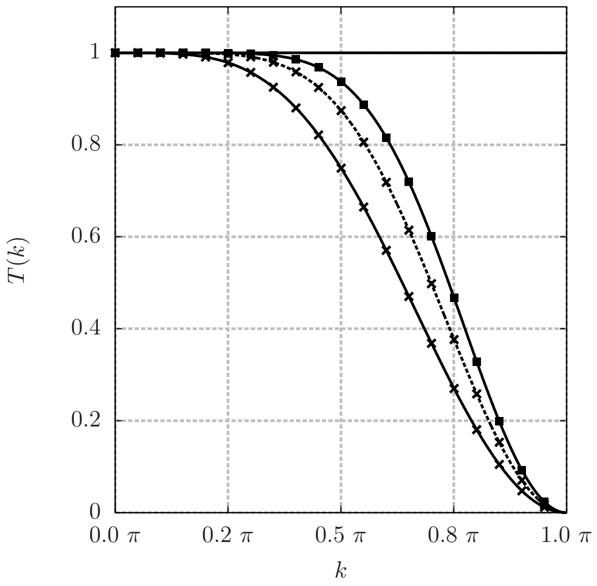

Figure 4.17: Filtering transfer function for explicit central schemes of 4^{th} —×—, 6^{th} - ×- , and 8^{th} —■— order. With no filtering $T(k) = 1$ ——.

Grid quality metric

The solution accuracy for problems evaluated on curvilinear grids, using high-order finite differencing, relies on the accurate measures of the Jacobian (J) and the standard metrics for the grid transformation, which are

$$J^{-1} = \left| \frac{\partial(x,y,z)}{\partial(\xi,\eta,\zeta)} \right|, \tag{4.29}$$

$$\begin{aligned}
\xi_x &= J(y_\eta z_\zeta - z_\eta y_\zeta), & \xi_y &= J(z_\eta x_\zeta - x_\eta z_\zeta), & \xi_z &= J(x_\eta y_\zeta - y_\eta x_\zeta), \\
\eta_x &= J(y_\zeta z_\xi - z_\zeta y_\xi), & \eta_y &= J(z_\zeta x_\xi - x_\zeta z_\xi), & \eta_z &= J(x_\zeta y_\xi - y_\zeta x_\xi), \\
\zeta_x &= J(y_\xi z_\eta - z_\xi y_\eta), & \zeta_y &= J(z_\xi x_\eta - x_\xi z_\eta), & \zeta_z &= J(x_\xi y_\eta - y_\xi x_\eta).
\end{aligned} \tag{4.30}$$

These metrics are calculated from the inverse metrics, which in turn are evaluated by applying spatial schemes to the grid coordinates, defined by the grid point distribution function. The inverse metrics can be expressed as $\partial(x,y,z)/\partial(\xi,\eta,\zeta)$ and will contain a truncation error. A measure of the grid quality will be derived by quantifying these truncation errors via application of the filter operator defined in Equation 4.28, to the physical grid coordinates. In the present work, sixth-order explicit filters [113] are used to estimate the truncation errors generated by the fourth-order compact schemes of Kim and Sandberg [51]. Explicit filters are more favourable as they are simpler to evaluate. Additionally, compact filters, such as the ones used in the main calculations together with the compact spatial schemes [101], require a extrapolation along multi-block interfaces. This extrapolation may yield different results along the over-set edge between neighbouring blocks. Furthermore a more dissipative filter is ideal, as it will highlight the problematic regions more clearly.

The filtering operator for a scalar variable ψ, along a grid line of varying ξ, and at the index i can be expressed as $\hat{\Delta}\psi_i$ in Equation 4.28. Similarly, the filtering operators for ψ along grid lines of varying η and ζ are expressed as $\hat{\Delta}\psi_j$ and $\hat{\Delta}\psi_k$, respectively. By applying the filter operators to the grid points along constant grid lines, the following nine terms are obtained

$$\begin{array}{ccc} \hat{\Delta}x_i, & \hat{\Delta}x_j, & \hat{\Delta}x_k, \\ \hat{\Delta}y_i, & \hat{\Delta}y_j, & \hat{\Delta}y_k, \\ \hat{\Delta}z_i, & \hat{\Delta}z_j, & \hat{\Delta}z_k. \end{array} \tag{4.31}$$

The grid point distribution function for the x-coordinates along a grid line of varying ξ is defined by x_i. The output from the filter operator, $\hat{\Delta}x_i$, will provide a measure of the truncation errors generated by the spatial scheme when evaluating $\partial x/\partial\xi$. Larger values in the terms $\hat{\Delta}x_j$ and $\hat{\Delta}x_k$ will similarly indicate greater truncation errors when the spatial scheme is applied along the η and ζ directions, respectively. The terms in Equation 4.31, relate to the accuracy of the inverse metrics defined by $\partial(x, y, z)/\partial(\xi, \eta, \zeta)$. Any inaccuracies contained in the inverse metrics will affect the accuracy of the Jacobian, and the metrics of the grid transformation.

Therefore, for an ideal grid, each of the nine terms in Equation 4.31 should be zero. A non-dimensional grid quality metric Q is defined, based on these nine terms, and is explained with the aid of Figure 4.18. In Figure 4.18, the unfiltered grid point at (i, j) is shifted to the position (i', j) after applying the filters along the ξ direction. The grid coordinate displacement is defined by,

$$\hat{\Delta}\xi = \sqrt{\hat{\Delta}x_i^2 + \hat{\Delta}y_i^2 + \hat{\Delta}z_i^2}. \tag{4.32}$$

This quantity is normalised by a local length scale ($\Delta\xi$ in Figure 4.18) along the curvilinear axis, and is taken as the average grid spacing between neighbouring vertices, and defined as,

$$\Delta\xi = \sqrt{x_\xi^2 + y_\xi^2 + z_\xi^2}. \tag{4.33}$$

Finally, the grid quality metric for a three-dimensional case can be generalised as,

$$Q = \sqrt{\left(\frac{\hat{\Delta}\xi}{\Delta\xi}\right)^2 + \left(\frac{\hat{\Delta}\eta}{\Delta\eta}\right)^2 + \left(\frac{\hat{\Delta}\zeta}{\Delta\zeta}\right)^2}, \tag{4.34}$$

where larger values of Q indicate larger truncation errors, due to a poorly resolved inverse grid metric and therefore, a lower grid quality. The non-dimensional variable Q is a field quantity that is defined at all grid points.

4.5.2 Correlation between grid quality metric and solution error

The inviscid vortex core convection problem [114] is used to determine the effectiveness of the grid quality metric (Q) as an indicator of the solution accuracy. Initial baseline measures of the grid quality and solution error are obtained for a uniform grid. After the uniform grid, altered versions of the uniform mesh are tested to determine the effects of specific grid features, such as uniform and non-uniform skewness, and abrupt changes to the grid line spacing and direction. Finally, the results from these test cases are used to determine the correlation between the grid quality metric, and the solution accuracy. A strong correlation reflects the effectiveness of the grid quality metric in identifying areas of the grid that are likely to generate large grid-induced errors.

The vortex convection problem is governed by the two-dimensional compressible Euler equations expressed in full conservation form as,

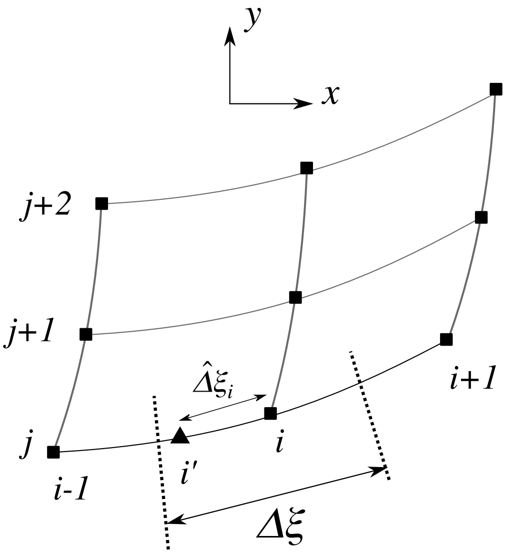

Figure 4.18: Generalisation of the changes to the grid coordinates induced by spatial filters, on to a two-dimensional curvilinear mesh. Original grid points are highlighted by ■, and the modified coordinate due to the filtering is highlighted by ▲.

$$\frac{\partial}{\partial t}\begin{pmatrix}\rho\\ \rho u\\ \rho v\\ \rho e_T\end{pmatrix}+\frac{\partial}{\partial x}\begin{pmatrix}\rho u\\ \rho u^2+p\\ \rho uv\\ \rho(e_T+p)u\end{pmatrix}+\frac{\partial}{\partial y}\begin{pmatrix}\rho v\\ \rho uv\\ \rho v^2+p\\ \rho(e_T+p)v\end{pmatrix}=0, \tag{4.35}$$

where ρ, $\vec{u}=(u,v)$, and p are respectively, the non-dimensional density, velocity, and the static pressure. The free-stream density and speed of sound, are used to normalise these variables. The dimensions of space are normalised by a unit length, and the dimension time is normalised using aforementioned reference quantities. The total energy e_t per unit mass, is defined by,

$$e_T=\frac{p}{\rho(\gamma-1)}+\frac{1}{2}u_iu_i, \tag{4.36}$$

where $\gamma=c_p/c_v$ is the ratio of specific heats. An initialised flow consisting of an inviscid vortex core is marched in time by a fourth-order Runga-Kutta scheme [93], using a Courant number of 0.45. The flux terms are evaluated by fourth-order accurate spatial schemes [51, 100] and the solution is filtered by sixth-order implicit filters [101] at the end of each time-step. The solution is bounded along the edges of the computational domain by a far-field pressure condition, which is evaluated using the Riemann invariants for a one-dimensional flow normal to the boundary. The inviscid vortex [100] is defined by,

$$\begin{aligned}
\rho(x,y,t)&=\rho_\infty\left[1-\frac{\gamma-1}{2}\psi^2(x^*,y)\right]^{1/(\gamma-1)},\\
u(x,y,t)&=u_\infty+a_\infty(y/R)\psi(x^*,y),\\
v(x,y,t)&=-a_\infty(x^*/R)\psi(x^*,y),\\
p(x,y,t)&=p_\infty(\rho/\rho_\infty)^\gamma,\\
\psi(x,y,t)&=\frac{\epsilon}{2\pi}\sqrt{\exp\left[1-\left(x^2+y^2\right)/R^2\right]},\\
x^*&=x-x_0-u_\infty t.
\end{aligned} \tag{4.37}$$

The size and strength of the vortex are controlled by the variables R and ϵ, respectively. For the present study $R=1$ m and $\epsilon=0.05$. The propagation speed of the vortex is set by the free-stream Mach number (M_∞) of 0.5. As shown in Figure 4.19(a), the initial position of the vortex is set to $(x,y)_{t=0}=(-3,0)$ and the final solution is obtained at $t=12$. The error field is defined at every grid point by,

$$E=\frac{(\rho-\rho_{\text{exact}})}{\rho_{\text{exact}}}, \tag{4.38}$$

where ρ and ρ_{exact} are the numerical and analytical solutions, respectively, of the density field at $t = 12$. The integral measures of the solution error and the grid quality are obtained for each case, and are defined by

$$E_I = \iint_{-S}^{S} |E| \; dx \; dy, \tag{4.39}$$

$$Q_I = \iint_{-S}^{S} Q \; dx \; dy, \tag{4.40}$$

where S determines the size of a square integration region. A value of $S = 6$ m was used for all test cases, except for the uniformly skewed grid. For uniformly skewed cases, a smaller value of $S = 3$ m was required to ensure that the integration region is confined to the computational domain.

Uniform mesh

The uniform mesh illustrated in Figure 4.19(a) consists of four square domains. Each domain consists of 101×101 grid points with a uniform grid resolution of 0.01 m $\times 0.01$ m. The half width of the vortex is $R = 1$ m, and the entire width of the vortex is resolved along 20 grid points. The grid quality metric is uniform, and of the order of $Q(x, y) = O(10^{-14})$. The error in the density field, illustrated in Figure 4.19(b), is of the order of $|E(x, y)| = O(10^{-6})$. The uniform test case provides baseline measures for the solution error, and the grid quality metric.

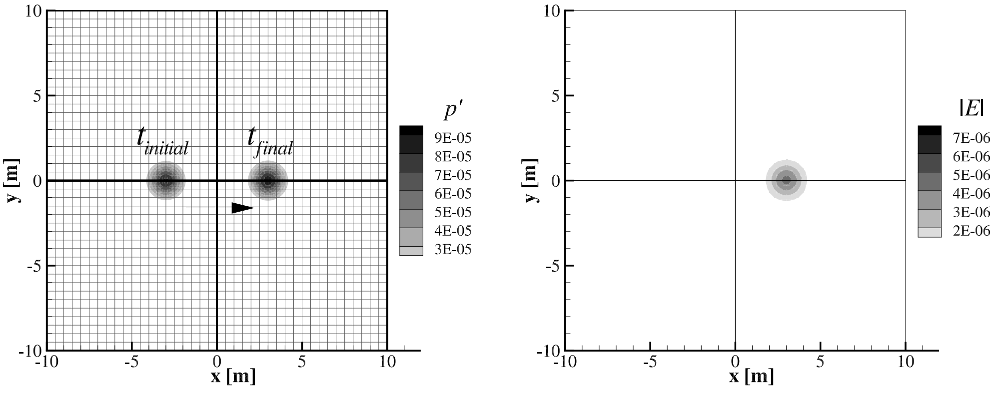

(a) (b)

Figure 4.19: Four block uniform grid. (a) Pressure disturbance field over-set with every fifth grid line, (b) Density error field at $t = t_{\text{final}}$.

Abrupt changes in the grid spacing

Abrupt changes to the grid spacing are imposed by applying the following function to the grid coordinates of the uniform mesh, described in Section 4.5.2

$$x^*(\xi,\eta) = x(\xi,\eta) A_x H(x), \tag{4.41}$$

where (x, y) and (x^*, y^*) are respectively the original, and modified grid coordinates, and $H(x)$ is the Heaviside function. The constant A_x specifies the grid spacing size for all grid points along $x > 0$, relative to the original grid spacing of $\Delta x = 0.01$ m. Figure 4.20 illustrates the grid quality metric field for two examples for $A_x = 1.25$ and 2. As shown in Figure 4.20, the grid quality metric correctly highlights the origin of the grid spacing discontinuity by larger values in the scalar Q. As the constant A_x is increased, the grid spacing discontinuity is enlarged. Therefore, larger values in the scalar Q are obtained, which signifies a lower grid quality.

The impact of sudden changes in the grid spacing on the solution accuracy is demonstrated in Figure 4.21. As the grid spacing discontinuity is enlarged, greater errors in the solution field are obtained due to the increased truncation errors contained in the metrics of the grid transformation. The integral measures of the grid quality Q_I, and the solution error E_I, from seven separate cases, are plotted in Figure 4.22. An abrupt change in the grid spacing with $A_x = 2$, yields a grid quality metric of $Q = O(10^{-2})$, and generates an error field that is two orders of magnitude greater than the baseline uniform case.

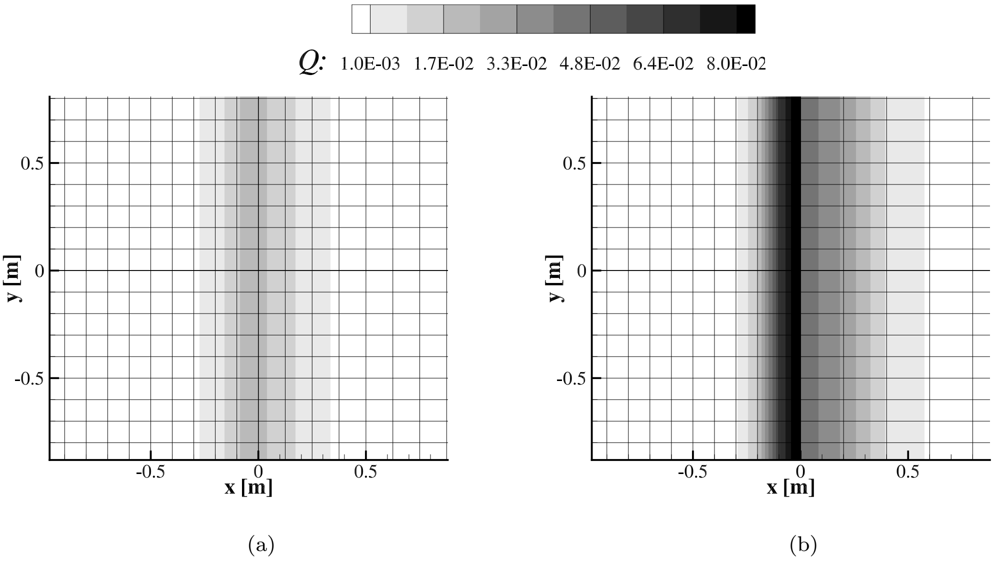

Figure 4.20: The effect of an abrupt change in the grid spacing at $x = 0$ on the mesh quality. (a) $A_x = 1.25$, (b) $A_x = 2$.

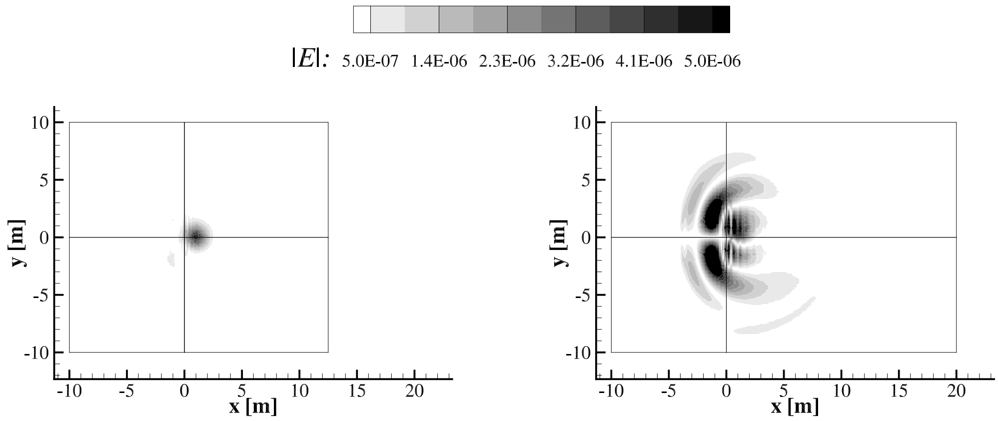

(a)

(b)

Figure 4.21: The effect of an abrupt change in the grid spacing at $x = 0$ on the solution error at $t = t_{\text{final}}$. (a) $A_x = 1.25$, (b) $A_x = 2$.

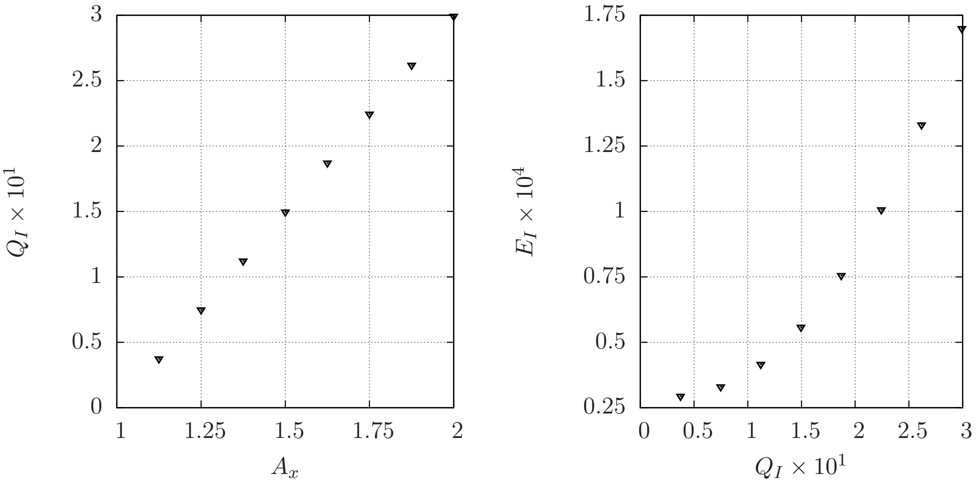

(a)

(b)

Figure 4.22: Effect of abrupt changes in the grid spacing at $x = 0$ on the grid quality and on the solution error. (a) The effect of A_x on the grid quality, (b) the effect of grid quality on the solution error at $t = t_{\text{final}}$.

Discontinuous grid direction

Abrupt changes to the grid line direction are imposed by applying the following function to the grid coordinates of the uniform mesh, described in Section 4.5.2

$$y^*(\xi, \eta) = y(\xi, \eta) + H(x) A_y x(\xi, \eta), \tag{4.42}$$

where (x, y) and (x^*, y^*) are respectively the original, and modified grid coordinates, and $H(x)$ is the Heaviside function. The constant A_y specifies the grid line gradient for $x > 0$. Figures 4.23 and 4.24 respectively show the effect that changes in the grid line direction may have on the local grid quality, and the solution accuracy, for two examples of A_y. The trends illustrated in Figure 4.25 show that as A_y increases, larger truncation errors are contained in the inverse metrics of the grid transformation. Therefore, the solution accuracy is reduced. An abrupt change in the grid line direction with $A_y = 1$ that yields a grid quality measure of $Q = O(10^{-3})$, generates an error field that is one order of magnitude larger, compared to the baseline uniform grid.

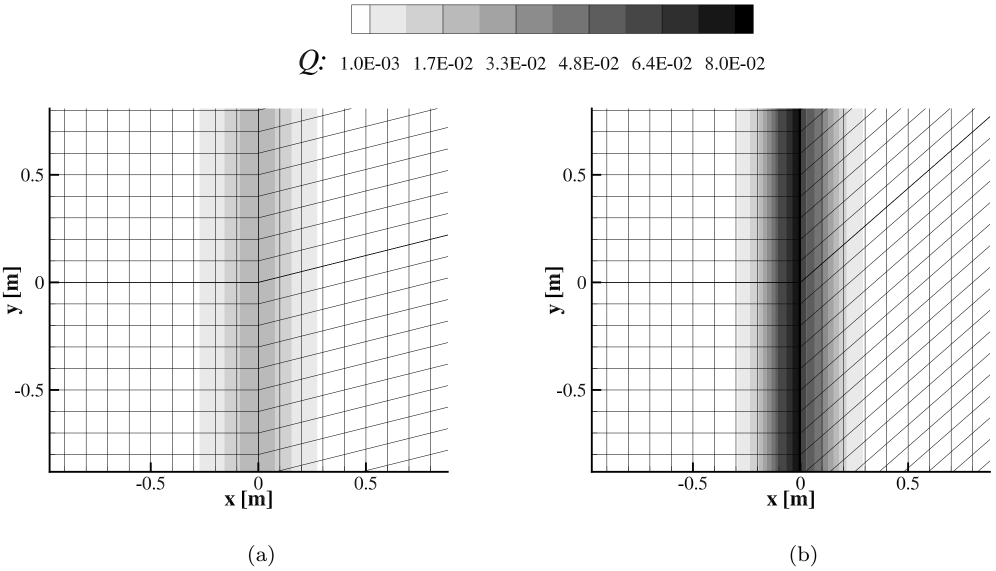

Figure 4.23: The effect of an abrupt change in the grid spacing at $x = 0$ on the mesh quality. (a) $A_y = 0.25$ (b), $A_y = 0.875$.

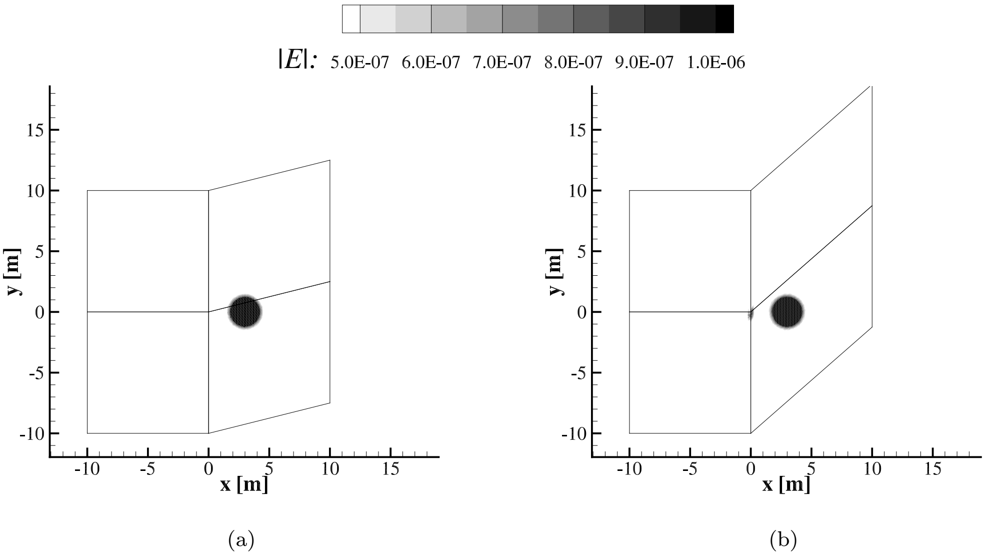

Figure 4.24: The effect of an abrupt change in the grid spacing at $x = 0$ on the solution error at $t = t_{\text{final}}$. (a) $A_y = 0.25$, (b) $A_y = 0.875$.

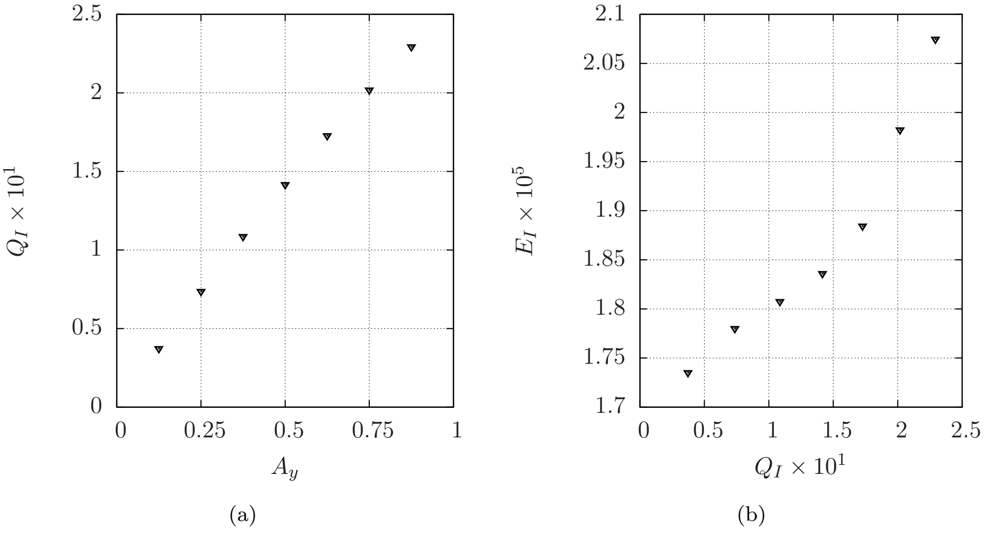

Figure 4.25: Effect of abrupt changes in the grid line direction at $x = 0$ on the grid quality and the solution error. (a) The effect of A_y on the grid quality, (b) the effect of grid quality on the solution error at $t = t_{\text{final}}$.

Uniform skewness

Uniform skewness is introduced by applying the following function to the grid coordinates of the uniform mesh, described in Section 4.5.2

$$x^*(\xi, \eta) = x(\xi, \eta) + A_s y(\xi, \eta), \tag{4.43}$$

where (x, y) and (x^*, y^*) are the original, and modified grid coordinates, respectively, and A_s is a constant that specifies grid line gradient across the entire domain. The angle between grid lines of constant ξ and η are specified by $\arctan(A_s)$. The effect of uniform skewness on the solution accuracy, is shown in Figure 4.26, for two examples of A_s. The integral measures of the grid quality and the solution error are illustrated in Figure 4.27, and are composed from several cases containing uniform skewness.

Uniform skewness does not result in any dispersion errors in the metrics of the grid transformation. Therefore, the level of the grid metric scalar Q is consistently low, at a level of $Q = O(10^{-12})$, and the solution error is of the same order of magnitude as the baseline uniform grid.

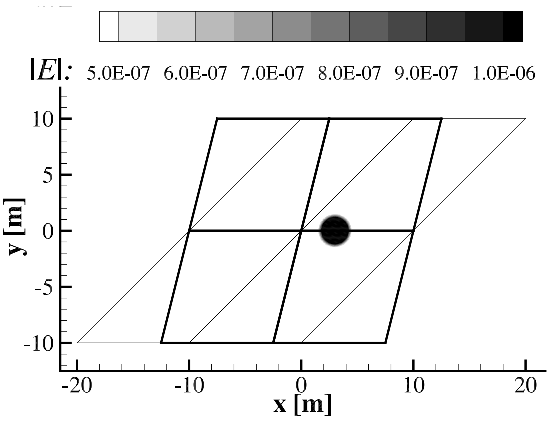

Figure 4.26: The effect of uniform skewness in the grid on the solution error at $t = t_{\text{final}}$. Block edges for $A_s = 0.25$ and $A_s = 1$ are shown in thick and thin black lines, respectively.

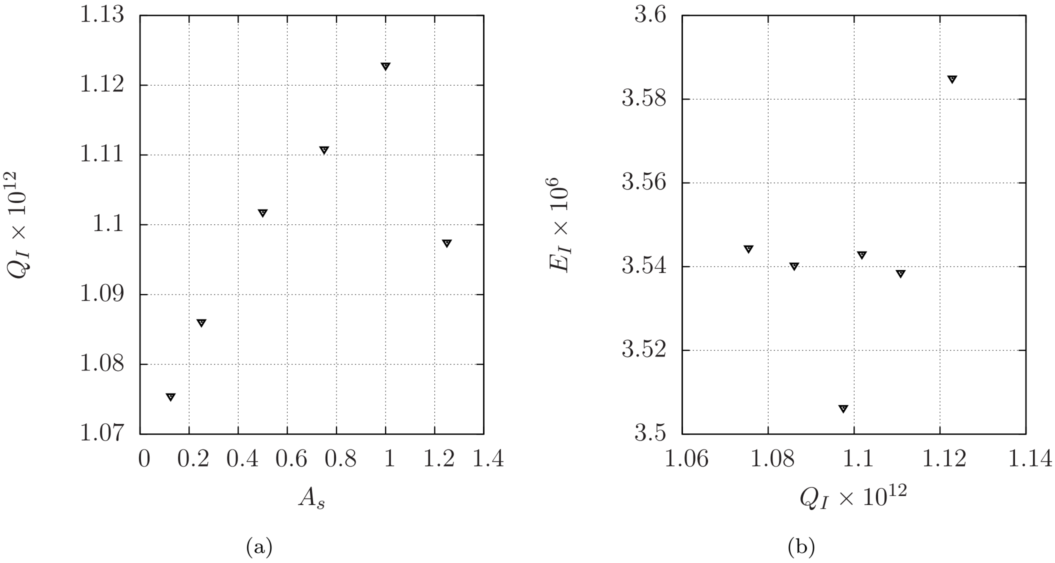

(a)

(b)

Figure 4.27: The effect of uniform skew on the grid quality metric and the solution error. (a) The effect of A_s on the grid quality, (b) the effect of the grid quality on the solution error at $t = t_{\text{final}}$.

Non-uniform skewness

Non-uniform skewness is imposed by applying a trigonometric function to the grid coordinates of the uniform mesh, described in Section 4.5.2

$$\begin{aligned} x^*(\xi,\eta) &= x(\xi,\eta) + A_t \sin\left(\frac{2\pi y(\xi,\eta)}{L}\right), \\ y^*(\xi,\eta) &= y(\xi,\eta) + A_t \sin\left(\frac{2\pi x(\xi,\eta)}{L}\right), \end{aligned} \tag{4.44}$$

where (x, y) and (x^*, y^*) are respectively the original and modified grid coordinates. The variables A_t and L specify the amplitude and wavelength, along which the local skewness will vary. For the following test cases, the wavelength was set to $L = 10$ m, and the amplitude A_t was varied between different grids.

Figure 4.28 illustrates the variations in the local skewness, for a grid with $A_t = 1.5$. Figure 4.29 illustrates the grid quality metric field Q, for two examples of A_t. In these Figures the region of lowest grid quality is focused on the areas where the variations in the grid line direction are greatest, instead of the areas where the local skewness is greatest.

The effect of varying A_t on the integral measures of the grid quality, and the solution error are illustrated in Figure 4.30. The scalar Q is of the order of $Q = O(10^{-7})$, which suggests that the grids are of high quality. This may be due to high resolution of the sinusoidal grid features, by 100 grid points per wavelength, that are illustrated in Figure 4.29. Compared to the baseline uniform case, a grid with $A_t = 1.5$ generates a solution error that is one order of magnitude larger.

In Figure 4.30, there is a significant reduction in the correlation, between the grid quality and the solution error, in the region where $Q_I < 7 \times 10^{-7}$. A threshold may exist beyond which other sources of errors will become more significant when compared to the errors contained in the grid transformation metrics. Examples of other sources of error may include the truncation errors due to the temporal scheme, or possibly by acoustic reflections due to poor boundary conditions.

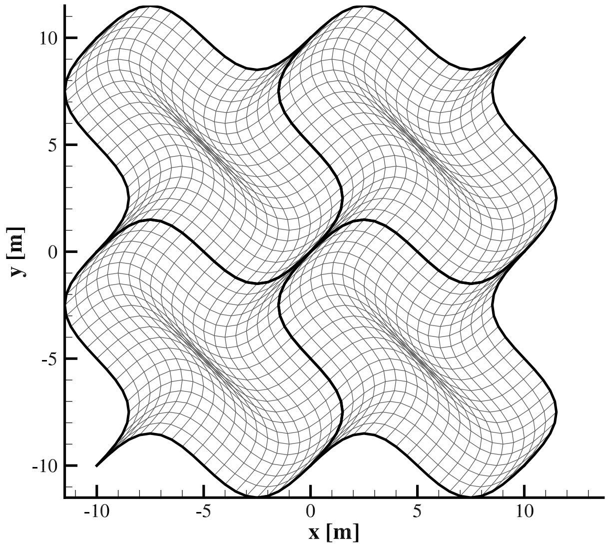

Figure 4.28: Mesh for $A_t = 1.5$ showing every fifth grid line.

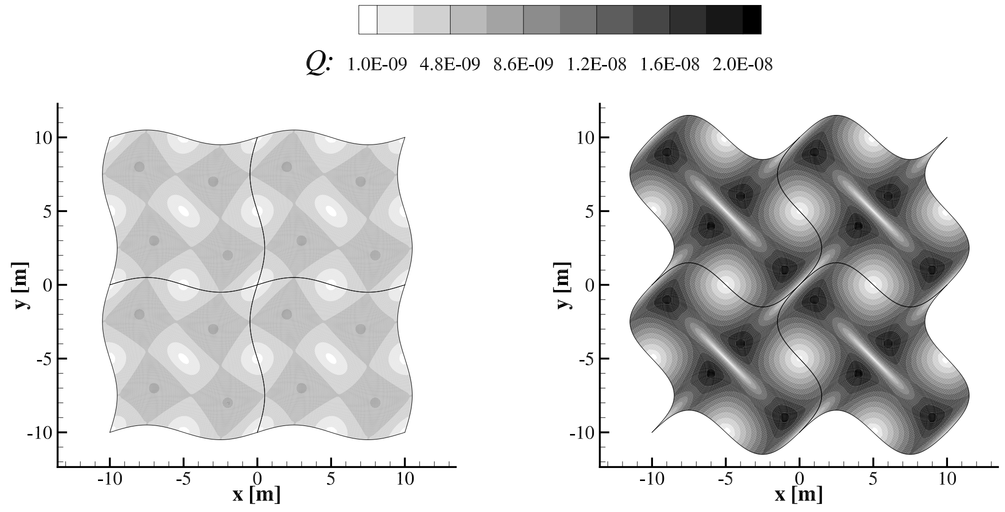

(a)

(b)

Figure 4.29: The effect of non-uniform skewness on the mesh quality. (a) $A_t = 0.5$, (b) $A_t = 1.5$

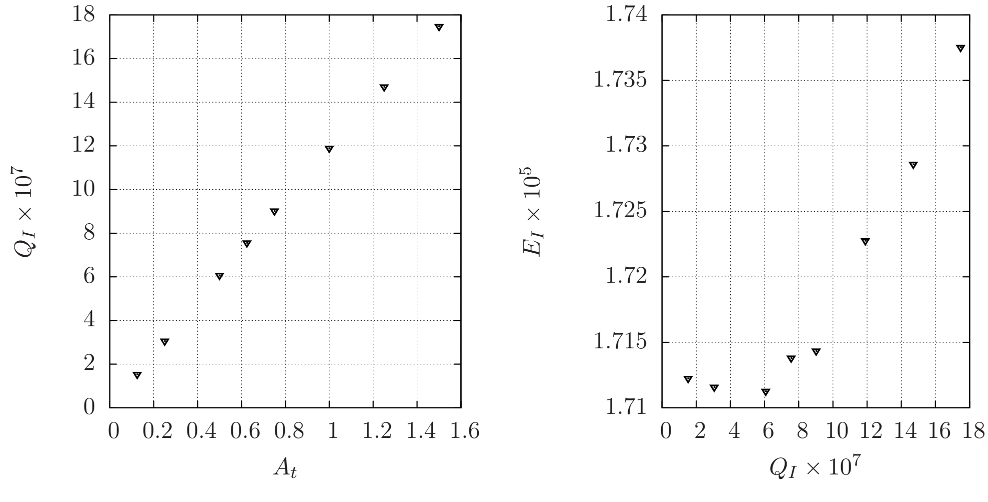

(a)

(b)

Figure 4.30: The effect of non-uniform skew on the grid quality metric and the solution error. (a) The effect of A_t on the grid quality, (b) the effect of grid quality on the solution error at $t = t_{\text{final}}$.

4.5.3 The effectiveness of the grid quality metric

The correlation coefficient (C_{QE}), between the integral measures of the grid quality metric (Q_I) and the solution error (E_I), is calculated using [48],

$$C_{QE} = \frac{\langle Q_I E_I \rangle}{\left[\langle Q_I^2 \rangle \langle E_I^2 \rangle\right]^{1/2}}, \tag{4.45}$$

where $\langle\rangle$ denotes the variance. In Table 4.1 the correlation coefficient is listed, for the test cases containing particular grid features. This is a measure of the ability of the grid quality scalar Q to identify areas of the grid that are likely to generate significant grid-induced errors.

Table 4.1: Correlation coefficient between the grid quality metric and the solution error.

Test case	C_{QE}
Grid spacing discontinuity	0.967
Grid direction discontinuity	0.953
Uniform skewness	0.472
Non-uniform skewness	0.924

Abrupt changes to the grid spacing and grid line direction generate the highest levels in the scalar field Q, which implies the lowest grid qualities. The correlation coefficients for cases containing discontinuous features are very high, with $C_{QE} > 0.95$.

Continuous and non-uniform grid features such as sinusoidal skewness can induce significant truncation errors in the grid metrics if the amplitude of these variations is large. The correlation coefficient for non-uniform skewness is $C_{QE} = 0.924$. However, it was suggested in Section 4.5.2 that cases with an integral grid quality measure of $Q_I < 7 \times 10^{-7}$ may represent a condition where grid induced errors, contained in the grid transformation metrics, are insignificant. It should be noted that the correlation coefficient increases to $C_{QE} = 0.989$, when the data points for $Q_I < 7 \times 10^{-7}$ are disregarded.

Uniform features induce no truncation errors to the metrics of the grid transformation. This explains why the solution error from a uniformly skewed grid is similar to a uniform grid. Due to the lack of significant sources of grid induced errors from uniform features, a poor correlation coefficient of $C_{QE} = 0.47$ is obtained. However, this study suggests that uniform skewness will not affect the solution error. Furthermore, a uniformly skewed grid is rare in practice, and it is therefore not necessary to identify this grid feature.

A grid quality metric that is invariant to the grid scale and grid orientation is useful property, and this is demonstrated for the present method in Figure 4.31. Baseline levels of the desirable grid quality can be established for different solvers by a set of test cases. These levels can be applied to any grid, regardless of its scale or orientation. The threshold between a grid of satisfactory and unsatisfactory quality will vary between solvers, as different methods may be employed. Factors such as the order of the scheme, and the amount of artificial dissipation, affects this threshold level.

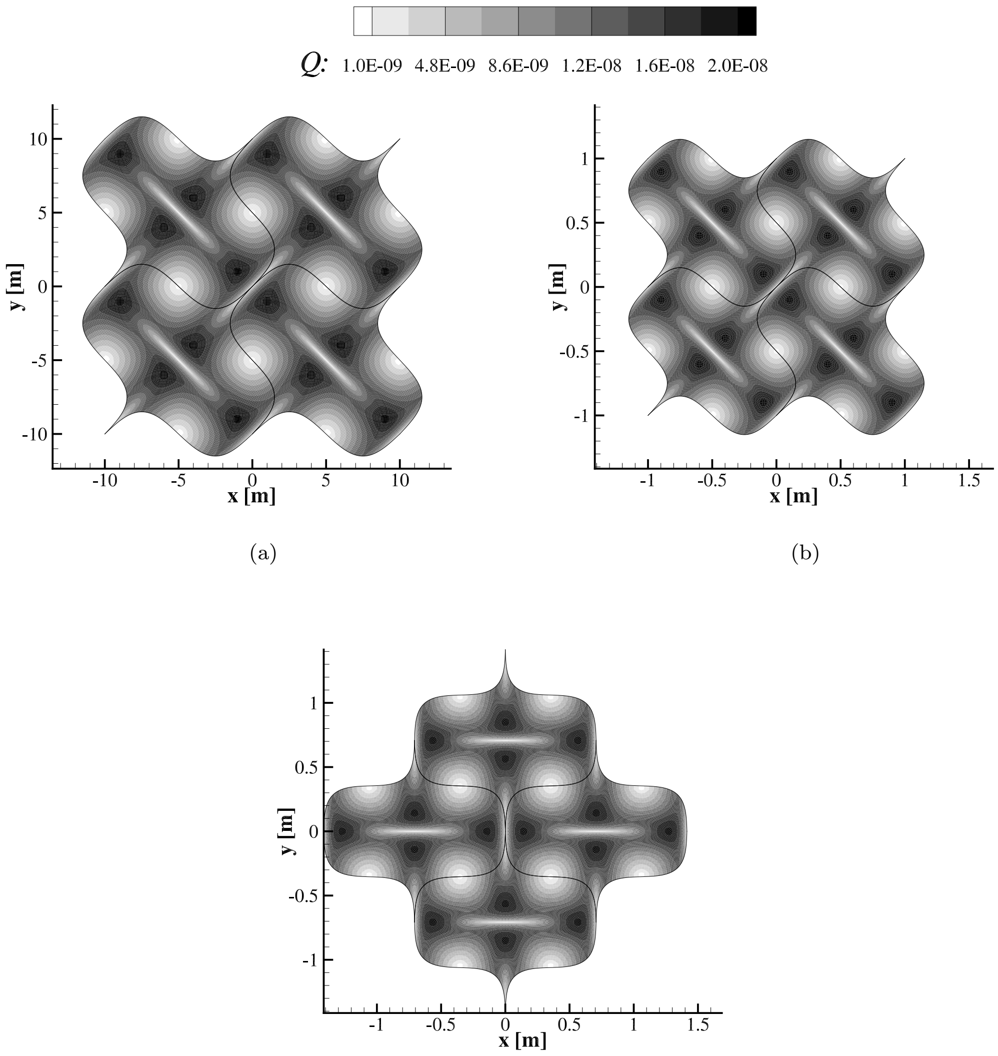

(a)

(b)

(c)

Figure 4.31: The effect of grid scale and grid orientation on the grid quality metric Q for a uniform grid morphed by Equation 4.44 with $A = 1.5$. (a) Original grid (b) original grid scaled by 0.1, (b) original grid scaled by 0.1 and rotated by 45 degrees.

These results show that a strong correlation between the grid quality metric and the solution accuracy is consistently obtained, in the limit that the grid transformation errors are the dominant source of errors. The solution accuracy from preliminary grid designs can be significantly improved, without any knowledge of the solution field. This can be achieved by optimising the grid for minimal levels in the grid quality scalar field, Q.

4.5.4 Grid optimisation using spatial filters

Preliminary grid designs are useful for the development of complex meshes. During this stage, a significant level of manual fine tuning may be involved. This procedure may require several iterations, until a satisfactory grid is obtained. Throughout the iterative process, the mesh may be altered to minimise the effects of the poor grid quality on the solution accuracy.

By filtering the grid coordinates, the grid point distribution function becomes absent of high wave numbers. This procedure will ensure a smooth grid, and therefore a smooth metric in the grid transformation, similar to elliptic grid generation methods. The proposed methodology is unique in that the smoothing of the grid does not require a solution of partial differential equations.

As a demonstration, this procedure is applied recursively to single test case. The initial grid is obtained by modifying the uniform grid in Section 4.5.2 with three features. Firstly, abrupt changes in the grid spacing are imposed by applying Equation 4.41 with $A_x = 1.5$. The modified grid is altered further to include abrupt changes in the grid line direction, as well as non-uniform skewness. These features are imposed on the grid by applying Equation 4.42 with $A_y = 0.625$, and Equation 4.44 with $L = 3$ and $A_s = 0.125$.

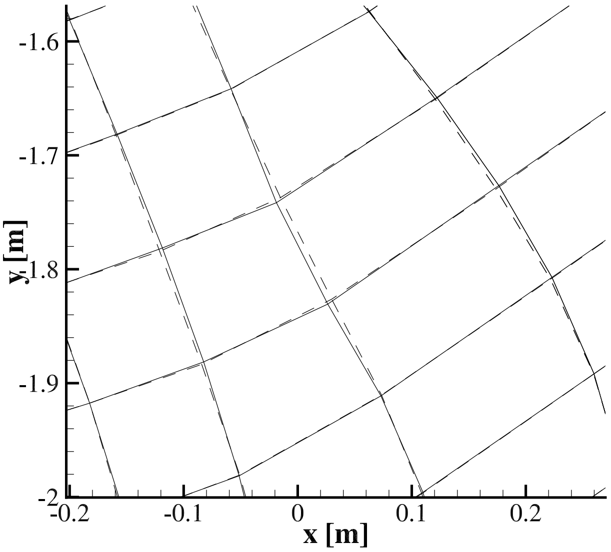

Figure 4.32: Effect of grid filtering on the grid lines. Original grid —— and filtered grid after one iteration - - -

A smoothed grid is obtained by applying the sixth-order filters, directly onto the grid coordinates, and the result after one iteration of filtering is illustrated in Figure 4.32. The changes to the local grid quality metric Q are shown in Figure 4.33, which clearly shows an improvement in the grid quality as a result of the smoothing. Finally, the effectiveness of smoothing the grid is illustrated in Figure 4.34, which demonstrates a clear reduction in the error field.

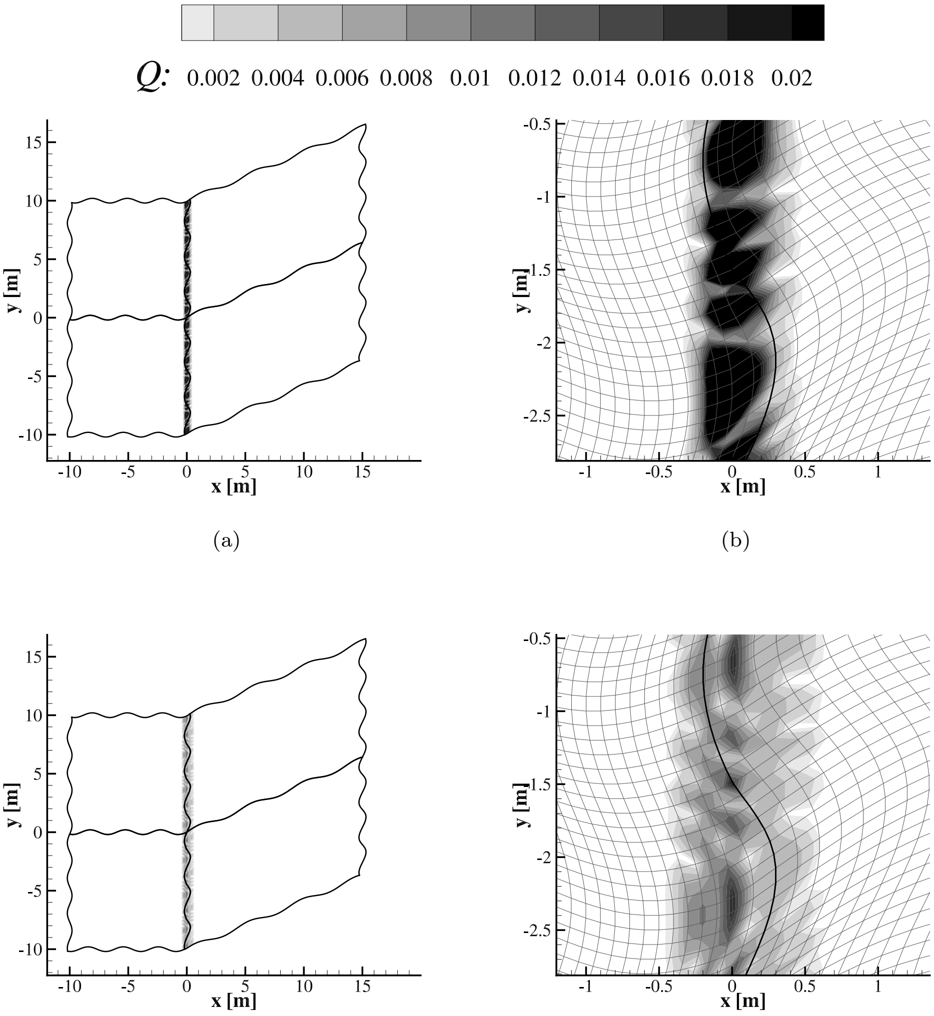

(a) (b)

(c) (d)

Figure 4.33: Measures of the grid quality on the unfiltered grid (a) and (b), and on the filtered grid after one iteration (c) and (d).

Further improvements to the grid quality and the solution error can be obtained by recursively filtering the grid coordinates. The integral measures of the grid quality and solution error are plotted in Figure 4.35 against the number of times the smoothing is applied. These plots show that the recursive filtering converges quickly to a minimal level, which is determined by the contributions of other sources of errors that have not been treated for in this procedure. These sources of errors may be due to the time discretisation, or due to poor boundary conditions.

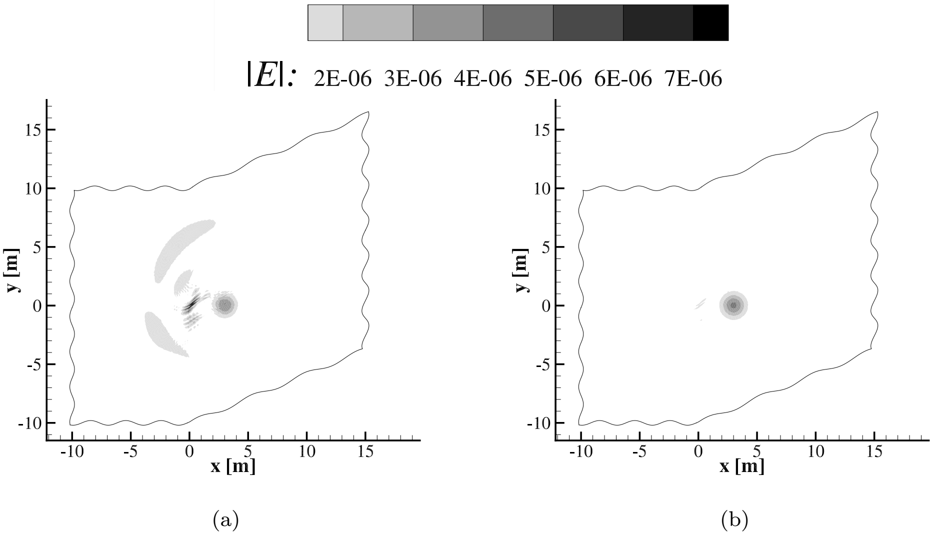

Figure 4.34: Effect of grid filtering on the solution error. (a) Original grid, (b) Filtered grid after one iteration.

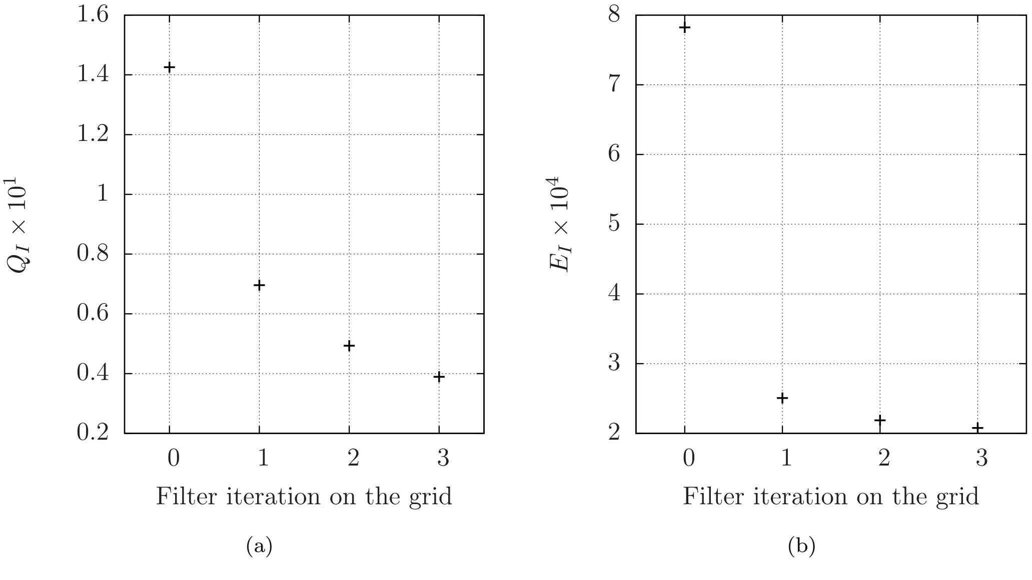

Figure 4.35: The effect of filtering the grid recursively on (a) the integral grid quality metric Q_I, and on (b) the integral solution error E_I

.

4.5.5 Summary of the tool

Grid generation techniques that require manual fine-tuning may contain regions of large grid-induced errors. These regions are typically removed by an iterative and time consuming process, until a satisfactory grid is obtained. Large grid-induced errors may also be suppressed by the use of added artificial dissipation. However, stronger filters will damp fine scale features in the solution field, and therefore degrade the fidelity of the solution.

For time-invariant structured grids employing finite differencing schemes, the grid-induced errors are due to two sources. The first is related to the grid resolution of the solution field, and resolved by a grid convergence study. The second source of error is independent of the solution field and is affected by the accuracy of the grid transformation metrics.

The accuracy of the grid transformation metrics is affected by the inverse metrics, which are measures of the spatial derivatives on the grid along the generalised coordinates. The truncation errors contained in the inverse metrics are generated by the spatial schemes. Fourier analysis shows that the dispersion errors, by spatial schemes, have similarities to the transfer function of spatial filters. This similarity is exploited to define a grid quality metric that can be used to identify areas in the mesh that are likely to generate significant grid-induced errors. These areas can be treated manually, or removed automatically by filtering the grid coordinates.

Several test cases on different grids showed that the grid quality metric is strongly correlated to the solution accuracy, under the condition that the grid induced errors are the most significant sources of error. Therefore improvements in the grid quality metric are very likely to result in an improved solution accuracy. This method improves the fidelity of high-order solvers by minimising the application of additional artificial dissipation that is required to ensure numerical stability, and reduces the amount of computational resources, and time, required for the iterative procedure to obtaining a satisfactory grid.

The grid quality metric proposed is also normalised, which makes the scalar field independent of grid scale or grid orientation. Therefore guidelines on the desired levels of the scalar can be evaluated and applied to any grid. These guidelines will vary between solvers due to the differences in the numerical methods employed. In its current state, only the method has been verified. A practical use of this tool will require a database of test cases. By comparing numerical predictions to experimental measurements a guideline on the desired maximum levels of the grid quality metric can be established. Without this database the grid quality metric may only be used to improve the grid quality, without any indication as to how much of a improvement statistical data will be improved by.

4.6 Summary

In this section changes to the high-order solver have been described. The purpose of the code development was to maximise the fidelity of the simulations. This was achieved by minimising the level of filtering required to ensure numerical stability. Numerical instabilities can be induced by a poor choice of spatial and filtering schemes. Additionally, it may be induced by a poor grid quality. A grid quality assessment tool has been developed that correlates strongly with the solution accuracy, and can ensure the use of high-quality grids by a process of grid optimisation. This tool is independent of the orientation and the scale of the grid. Therefore, it is applicable to any structured grid.

The outcomes within this Chapter are:

1. **Enhanced robustness of the in house code**
   The high-order solver has been updated with more robust schemes following mathematical reasoning on the basis of maximising the fidelity of the simulation.
2. **Multi-block stability analysis**
   Stability analysis is currently limited to a single block case only. A multi-block analysis method has been developed which helps to explain why attempts in running the 8/4 scheme with the implicit filters were found to be unstable. This result cannot be obtained for a single block case and this highlights the importance of studying multi-block cases with different interface treatments.
3. **A priori grid quality assessment**
   A grid quality metric has been developed to minimise the impact of human errors and the presence of grid-induced error sources. These features are identified without requiring any flow simulation to be conducted, and can allow for minimal use of additional filtering or dissipation required to ensure numerical stability.

Chapter 5

Experimental work

5.1 Introduction and aim

The aerodynamic interaction between a leg-door and a circular cylinder in a side by side configuration was studied by experiments at the 2.1×1.5 m ($7' \times 5'$) wind tunnel facility in the University of Southampton. A database constructed of oil flow, mean loads, velocity field, and surface pressure measurements provided a detailed description of the flow around the 26% scale model (based on the Airbus A-340 MLG).

This experiment aims to provide a novel insight into the effects of the leg-door AoA on the aerodynamic interaction with a cylinder. Existing studies on cylinder interactions with a plane, or rectangular, body have been focused primarily on the effects of the gap distance between the two elements [8]. The measurements were primarily obtained at a Reynolds number, based on the cylinder diameter, of $Re_D = 2 \times 10^5$.

The structure of this chapter is as follows. The experimental model and set-up in the test section are detailed. The results are then presented, which are divided into three subsections. Firstly, the aerodynamic features are given on an isolated door model, at varying AoA. The changes to the flow dynamics as a result of interaction with the added cylinder is then discussed, and followed by a discussion on the effect of the door angle on the interaction.

5.2 Experimental model

The experimental model illustrated in Figure 5.1 consists of three elements; the leg-door, the cylinder and the end plates. Figures 5.2 and 5.3 show the set-up of the model in the wind tunnel test section. The model was held in position by the steel struts that connect the end plates to the load balance located above the wind tunnel ceiling. The leg-door and cylinder were screwed into position between the end plates, and the leg-door angle was modified by remounting the door into alternate fixtures on the end plates. The door angle was verified with a digital inclinometer across the four corners, and at the centre, of the door surface. This ensured that the door angle was constant in the span, and removed any twist in the model. The port end plate was fitted with a perspex sheet to provide optical access for the PIV measurements. Key model dimensions are listed in Table 5.1.

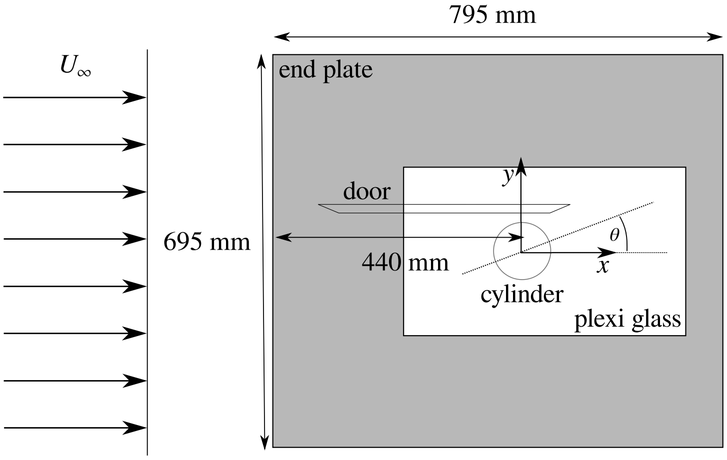

Figure 5.1: Side view illustration of the model set-up.

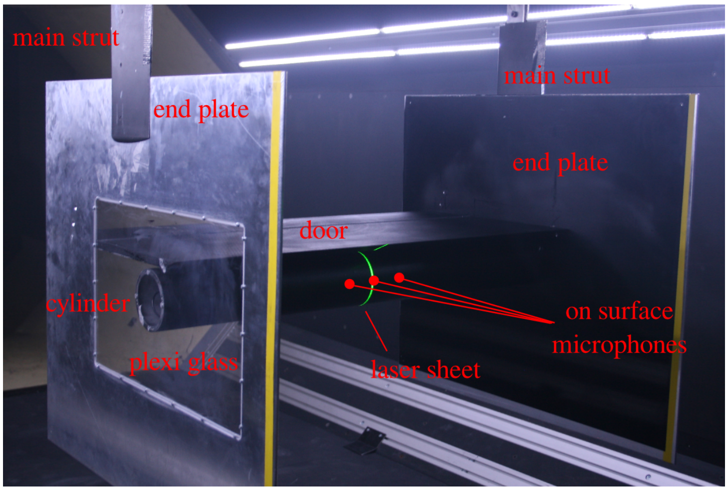

Figure 5.2: Downstream view of the model set-up in the test section.

At the highest door angle of 10.7 degrees, the maximum blockage by the model was 5.3%. The turbulent intensity of the free-stream was less than 0.2% and the maximum flow speed and Mach number were $U_\infty = 45$ m/s and $M_\infty = 0.12$, respectively [115].

To simulate a high Re, roughness strips were applied along the span of the cylinder and door. These strips are constructed of a double-sided tape with a distribution of carborundum grid with an average particle size of 2.7×10^{-4} m^2 (Grit60). The trip strips were applied on the cylinder according to a previous experiment [61], conducted using the same apparatus to study the flow behind a cylinder with a torque link model.

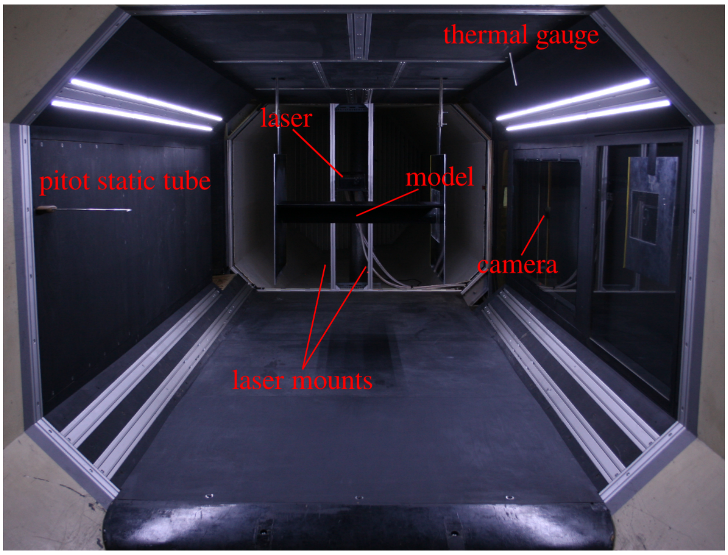

Figure 5.3: Upstream view of the model set-up in the test section.

Parameter	Value
Door long edge	447 mm
Door short edge	374 mm
Door bevel angle	22.62°
Door thickness	15 mm
Door width	900 mm
Cylinder diameter	101 mm
Cylinder width	900 mm
End plate height	695 mm
End plate length	795 mm

Table 5.1: Key dimensions of the experimental model.

The position of the trip strips on the leg-door varied with angle of attack. The positions were determined by oil flow data acquired from clean (un-tripped) configurations. The effectiveness of the boundary layer trip was evaluated by recording the mean loads across a range of *Re*.

The aerodynamic loads induced by the supporting end plate and steel struts are assumed to have a linear effect to the total load. Isolated measurements were recorded across a range of *Re* by Windiate [61] and provide the tare values. The tare loads for the lift and drag coefficients, for a reference area based on the cylinder diameter and the span of the model, converge to $C_{L,\text{tare}} = 0.05$ and $C_{D,\text{tare}} = 0.253$, when the free-stream speed is above $U_\infty > 15$ m/s.

5.3 Results

The test matrix is outlined in Table 5.2, which is listed in chronological order. Initial loads and oil flow measurements were conducted to determine the Re sensitivity for an isolated door model. The isolated door measurements do not include PIV or microphone data and are limited to the mean loads and oil flow visualisation.

The changes to the flow features with the addition of a cylinder are then discussed, which includes PIV and microphone data. As the data sets are quite large, a brief discussion of the measurements is provided after their presentation. Finally, an overview of the results is provided in a summary.

5.3.1 Isolated door at varying angle of attack

The loads measurements across a range of free-stream speeds are given for three door angles α_D in Figure 5.4. The aerodynamic loads were measured for a tripped and untripped configuration of the door model, and there is no noticeable change due to the trip devices. An exception to this is for the isolated door at 0 degrees, at low speeds of $U_\infty < 15$ m/s, where the Reynolds number sensitivity is higher.

The boundary layer trip was designed as a thin strip of double sided tape with Grit60, and it was applied along the top and bottom surfaces of the door model. Oil flow visualisations applied to clean configurations were used to identify the ideal location of the trip strips. The sharp leading edges generate an adverse pressure gradient, which induces boundary layer separation. Figures 5.5 and 5.6 show this recirculating flow along the lower and upper surfaces along the leading edge of the isolated door model at $\alpha_D = 0°$. Figure 5.6 additionally highlights flow features due to end-plate interaction effects. The scale of the end plate features is small compared to the span of the model. It is therefore assumed that this end-plate feature has small effects at low angles.

The separation points along a door without trip devices were measured at a free-stream speed of $U_\infty = 30$ m/s. Due to the inherent flow separation from the leading edge at all angles, the earliest position of a trip device that has a maximal effect, is downstream of the reattachment point, if a reattachment point is present. For all cases, flow reattachment was found along the upper surface of the door. These positions were measured to be at 6.7%, 33.6%, and 95% of the chord length for α_D of 0, 5, and 10.7 degrees, respectively.

From the mean loads data in Figure 5.4, two main observations can be made. Firstly, the mean loads for an isolated door model are almost unaffected by the trip devices. Boundary layer separation points along smooth geometries, such as cylinders, are more sensitive to the boundary layer state, compared to geometries with sharp edges. Therefore the insensitivity in Figure 5.4 may be due to the influence of the sharp edges along the leading and trailing edges. Secondly, the upstream flow separation occurs immediately at the door leading edges. Separation bubbles can induce a transition of the

Measurement	Free-stream speed U_∞ [m/s]	Door angle of attack α_D [degree]	Gap width ratio G	Comments
ML 1	$10 < U_\infty < 34$	0, 5, 10.7	N/A	Clean configuration.
OF 1	30	0, 5, 10.7	N/A	
OF 2	24, 34	10.7	N/A	End plate effect.
ML 2	$10 < U_\infty < 34$	0, 5, 10.7	N/A	Tripped configuration.
ML 3	$10 < U_\infty < 34$	0, 5, 10.7	0.087	Clean leg-door, cylinder tripped.
OF 3	30	0, 5, 10.7	0.087	Clean leg-door, cylinder tripped.
ML 4	$10 < U_\infty < 34$	0, 5, 10.7	0.087	Leg-door and cylinder tripped.
ML 5	$10 < U_\infty < 34$	0	0.087	Alternate leg-door trips.
PIV 1	25, 28, 34	0	0.087	
PIV 2	30, 34	5	0.087	
PIV 3	25, 30, 32	10.7	0.087	Model vibration at 34 m/s.
M 1	0	N/A	N/A	Background noise
M 2	20, 30	N/A	N/A	Isolated tripped cylinder
M 3	0	0, 5, 10.7	0.087	Background noise
M 4	20, 30	0, 5, 10.7	0.087	Tripped interaction model.

Table 5.2: Test matrix of the experiments. ML - Mean loads, OF - Oil flow, PIV - Particle Image Velocimetry, M - Microphone.

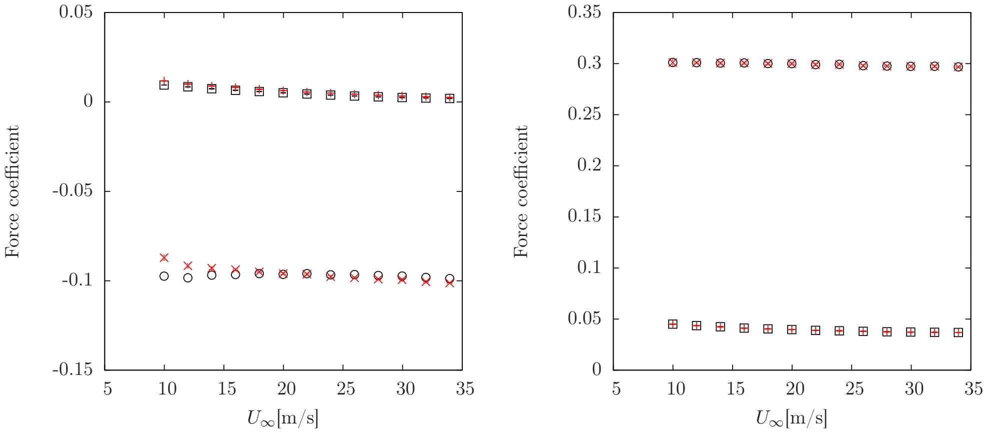

(a) $\alpha_D = 0°$ (b) $\alpha_D = 5°$

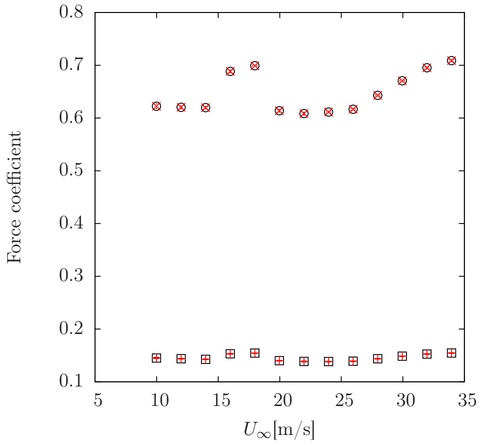

(c) $\alpha_D = 10.7°$

Figure 5.4: Aerodynamic loads on an isolated door at varying angle of attack. C_D (clean) - □, C_D (tripped) - +, C_L (clean) - ○, C_L (tripped) - ×. Loads are normalised by the reference area based on the span and chord of the door element.

boundary layer to a turbulent state, and this may explain the insensitivity of the mean loads to the trip devices.

The loads at 0 and 5 degrees show little influence from changes in the *Re*, but at 10.7 degrees, two regions at $16 < U_\infty < 18$ m/s and at $U_\infty > 26$ m/s show significant changes to the lift coefficient. No significant changes to the oil flow features were identified on the door between $U_\infty = 24$ m/s and 34 m/s. The *Re* sensitivity is likely due to end plate interactions that are illustrated in Figure 5.7. At $U_\infty = 34$ m/s, a coherent vortex structure is formed on the upper surface of the door, near the end plates, which is absent at lower speeds. This vortex structure may induce similar effects as an aircraft strake, and may be the cause of the increase in the lift generated by the isolated door.

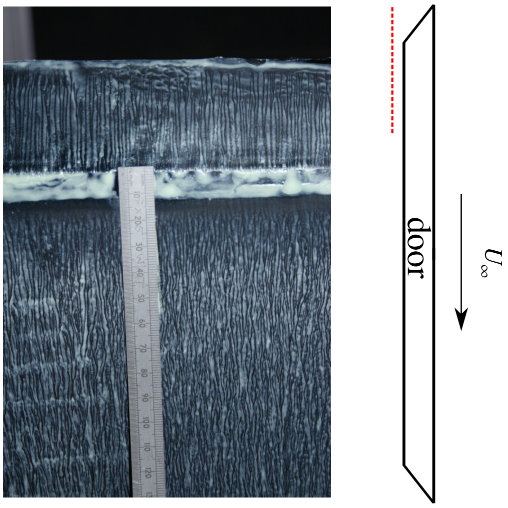

Figure 5.5: Oil flow patterns on the lower surface of an isolated door model at $\alpha_D = 0°$. Position of the frame is highlighted by the red line.

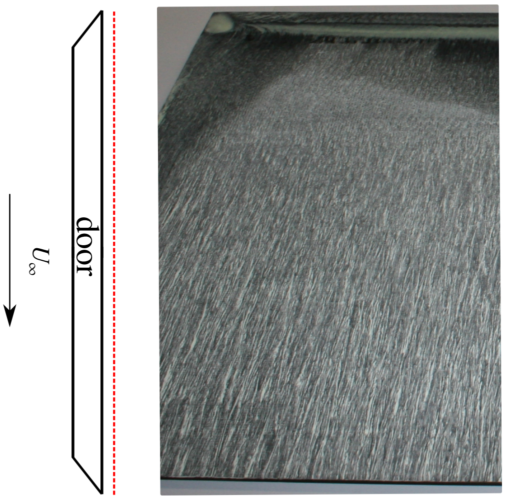

Figure 5.6: Oil flow patterns along the upper surface of an isolated door at $\alpha_D = 0°$. Position of the frame is highlighted by the red line.

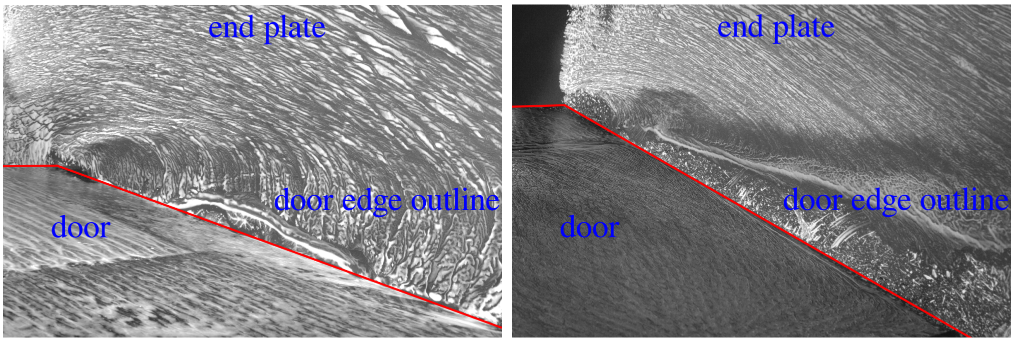

(a) $U_\infty = 24$

(b) $U_\infty = 34$

Figure 5.7: Comparison of the oil flow features along the end plates for $\alpha_D = 10.7°$ under an isolated door configuration at two speeds $U_\infty = 24, 34$ m/s.

At $\alpha_D = 0°$, the lift coefficient is negative as the mean camber line of the door model points downwards. As the door angle is increased from 0 to 5 degrees, the average lift coefficient (across the entire range of Re) increases with a gradient of 4.58 per radian. Similarly, a gradient of 3.52 ± 0.5 per radian is measured between 5 and 10.7 degrees. The reduced gradient at higher door angles implies a greater influence of the flow separation along the upper surface. No PIV data was acquired for the isolated door model as the optical access was focused to the wake of the cylinder only.

5.3.2 Interaction with the cylinder

The effect of the leg-door interaction with a cylinder in a side by side configuration is described by the oil flow, mean loads, PIV and microphone measurements. Firstly the loads data are outlined, followed by PIV and the microphone data. The observations form each measurement techniques are briefly reviewed and later collected to highlight the effects of the cylinder and leg-door interaction, and the effects of varying the leg-door AoA.

Mean Loads and oil flow

Figure 5.8 illustrates the effect of Reynolds number on the mean loads generated by the interaction model, for clean and tripped configurations. The clean configuration refers to a model without trip devices on the door or the cylinder. The location of the trip devices along the cylinder was determined by a separate set of experiments conducted by Windiate [61] using the same apparatus. The location of the trip strips along the door model was determined by the oil flow visualisation, and the trip devices were applied as far upstream as possible in the region of attached boundary layer flow. As the door angle was changed, the trip strip positions were altered due to the changes in the separated flow along the upper section of the door model. However, the trip strip positions along the cylinder element were kept at $\theta = \pm 60$ degrees.

The mean loads data in Figure 5.8 shows that the trip devices have a small influence at door angles of 5 and 10.7 degrees. At $\alpha_D = 0°$, a stronger influence of the trip devices is seen, and a large change to the loads is observed at $U_\infty = 28$ m/s. At this speed, there is an increase in the lift coefficient, and a decrease in the drag coefficient. This change is explained in greater detail with the PIV data. At $\alpha_D = 5°$, there is a large variation to the loads at $U_\infty < 20$ m/s. However, at higher speeds, the aerodynamic loads converge.

Using oil flow visualisation, the major flow features around the leg-door with the cylinder interaction were identified and are generalised in Figure 5.9. The key differences to the surface flow features in Figure 5.9 between an isolated and interacting leg-door model, are the lack of flow separation in the regions: (1) behind the cylinder, (2) at the trailing

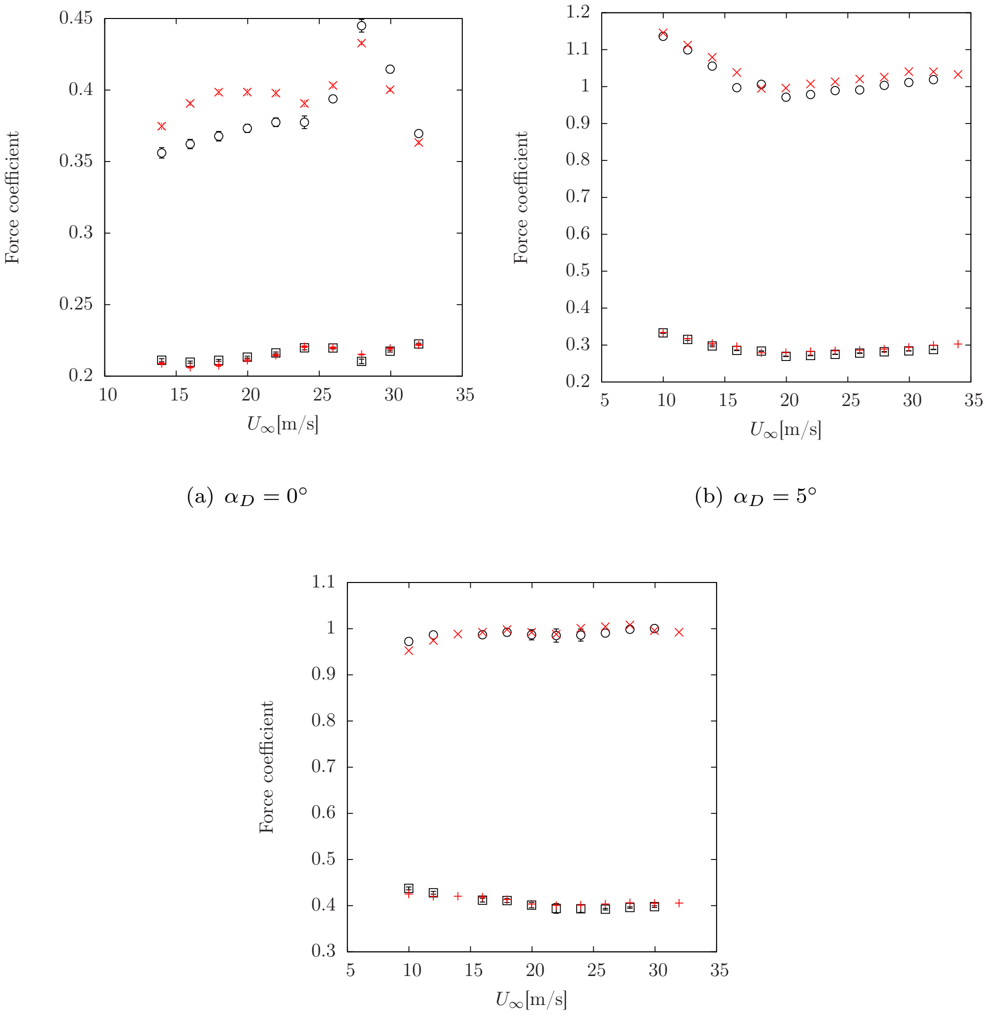

(a) $\alpha_D = 0°$

(b) $\alpha_D = 5°$

(c) $\alpha_D = 10.7°$

Figure 5.8: Aerodynamic loads on the door-cylinder model at varying angle of attack. C_D (clean) - □, C_D (tripped) - +, C_L (clean) - ○, C_L (tripped) - ×. Loads are normalised by the reference area based on the span and chord of the door element only.

edge on the upper surface of the leg-door, and (3) upstream of the cylinder along the lower surface of the leg door. The latter feature is due to the adverse pressure gradient generated by the stagnated flow on the cylinder, which causes the boundary layer to separate along the lower surface of the door. Figure 5.10 illustrates the oil flow features on the lower surface of the leg-door under the influence of a cylinder. The collection and the lack of oil flow sheared beyond the mid-chord region verifies the aforementioned adverse pressure gradient. It should be noted that at higher door angles, this additional flow feature was not present as the positive inclination of the door provides a favourable pressure gradient. The formation of (1) is likely due to the separated boundary layers behind the cylinder, which is commonly observed on isolated cylinders [29, 67], and cylinders near a flat plane boundary [75]. Finally, the recirculation region (2) is generated by the interaction of the flow exhausted through the gap between the cylinder and the door, and the low pressure region generated along the upper surface of the leg-door. Observations from the PIV data at high door angles, which are shown next, clearly indicate that this jet flow is skewed towards the upper surface of the door, thereby generating the reversed flow along the door trailing edge as illustrated in Figure 5.9.

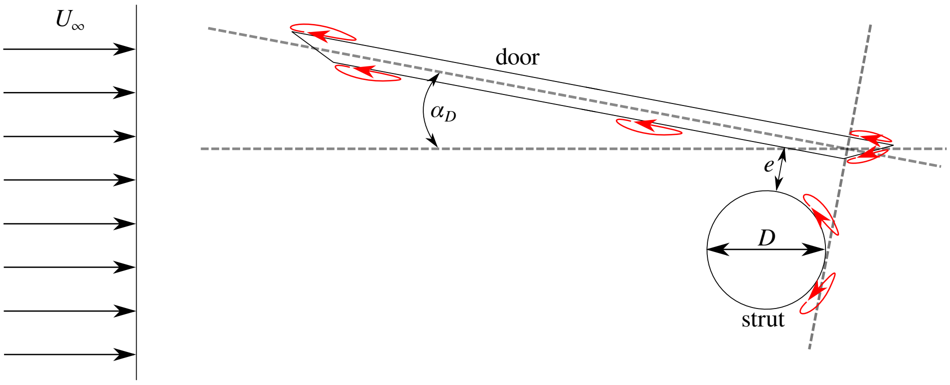

Figure 5.9: Illustration of the major flow features identified around the leg-door and cylinder model.

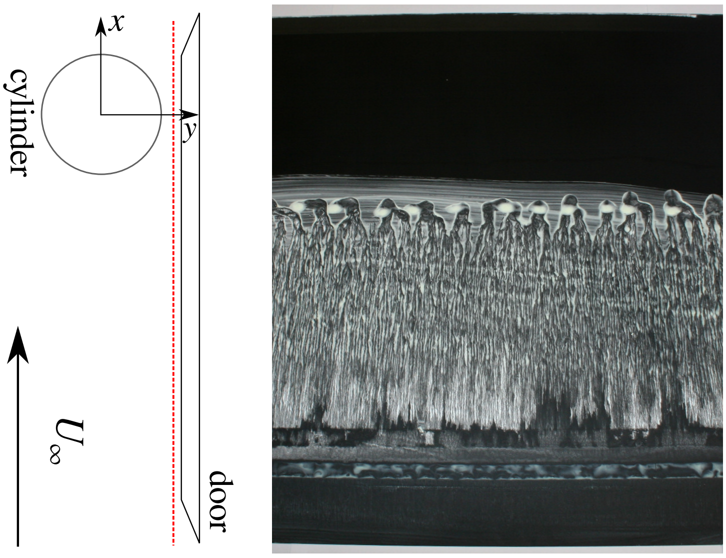

(a) $\alpha_D = 0°$

Figure 5.10: Oil flow features on the lower surface of the door with the cylinder interaction at $\alpha_D = 0°$. Position of the frame is highlighted by the red line.

By comparing the force variation with the door angle between the isolated and interaction cases, the following differences are observed. At $\alpha_D = 0°$, the interaction model generates a positive lift force, unlike the isolated door. This implies that the cylinder interaction generates a positive circulation that may be due to the additional blockage that is induced along the lower surface of the door.

At door angles of 5 and 10.7 degrees, both isolated and interaction cases generate a positive lift force, however the gradient of the lift with respect to angle of attack is noticeably lower for the interaction model. For the interaction case, the lift coefficient remains almost unchanged between 5 and 10.7 degrees. The additional circulation induced by the placement of the cylinder may increase the effective angle of attack of the door. Therefore, the stall angle of the model would decrease, which may explain this reduced lift gradient between 5 and 10.7 degrees, for the interaction model.

Particle Image Velocimetry

The raw PIV data consists of instantaneous velocity fields with a sample size of 1000 images. The PIV data is presented for all door angles, followed by a discussion of the results. The fields derived from this sample that are presented in this section are the mean velocity, the 2-D Turbulent Kinetic Energy (TKE), and the vorticity. Additionally, the streamline patterns derived from the mean velocity field are also illustrated.

The TKE transport equation [48], derived by a rearrangement of the Reynolds stress transport equation, contains a production term scalar P_{TKE} that is defined as

$$P_{TKE} = -\overline{u_i' u_j'} \frac{\partial \overline{u_i}}{\partial x_j}, \tag{5.1}$$

which is a function of the Reynolds stress tensor and the mean flow gradient. The production scalar can be simplified to four terms by assuming $\partial \overline{u_i} / \partial z = 0$ and $\partial \overline{w} / \partial x_i = 0$. These assumptions are true if the model induces a mean flow that is symmetric along the mid-span of the model, and if the symmetry plane is aligned with the PIV measurement plane. The production term field is illustrated by Figures 5.17, and 5.18 for various cases.

Quantitative comparisons are also obtained by extracting the velocity and 2-D TKE data at a downstream position $x/D = 2$ along a vertical line that crosses the wake ($-1.2 < (y/D) < 1.2$). The distributions of mean velocity and 2-D TKE, for varying free-stream speeds and door angles, are shown in Figures 5.19 and 5.20. The profiles at different speeds illustrate the sensitivity of the mean flow features to the Reynolds number.

Using the complete set of PIV data, the following observations can be made. At $\alpha_D = 0°$, Figures 5.11, 5.19, and 5.20 show a velocity deficit located behind the cylinder. The profile of this deficit is wider compared to the one from an isolated cylinder. The velocity magnitude profile towards the edges of the wake is also different compared to an isolated cylinder. An isolated cylinder flow generates regions of accelerated flow around its sides. However, the presence of the leg-door may be confining this process. The confinement effect induces an asymmetry in the wake, which has also been observed by Bearman

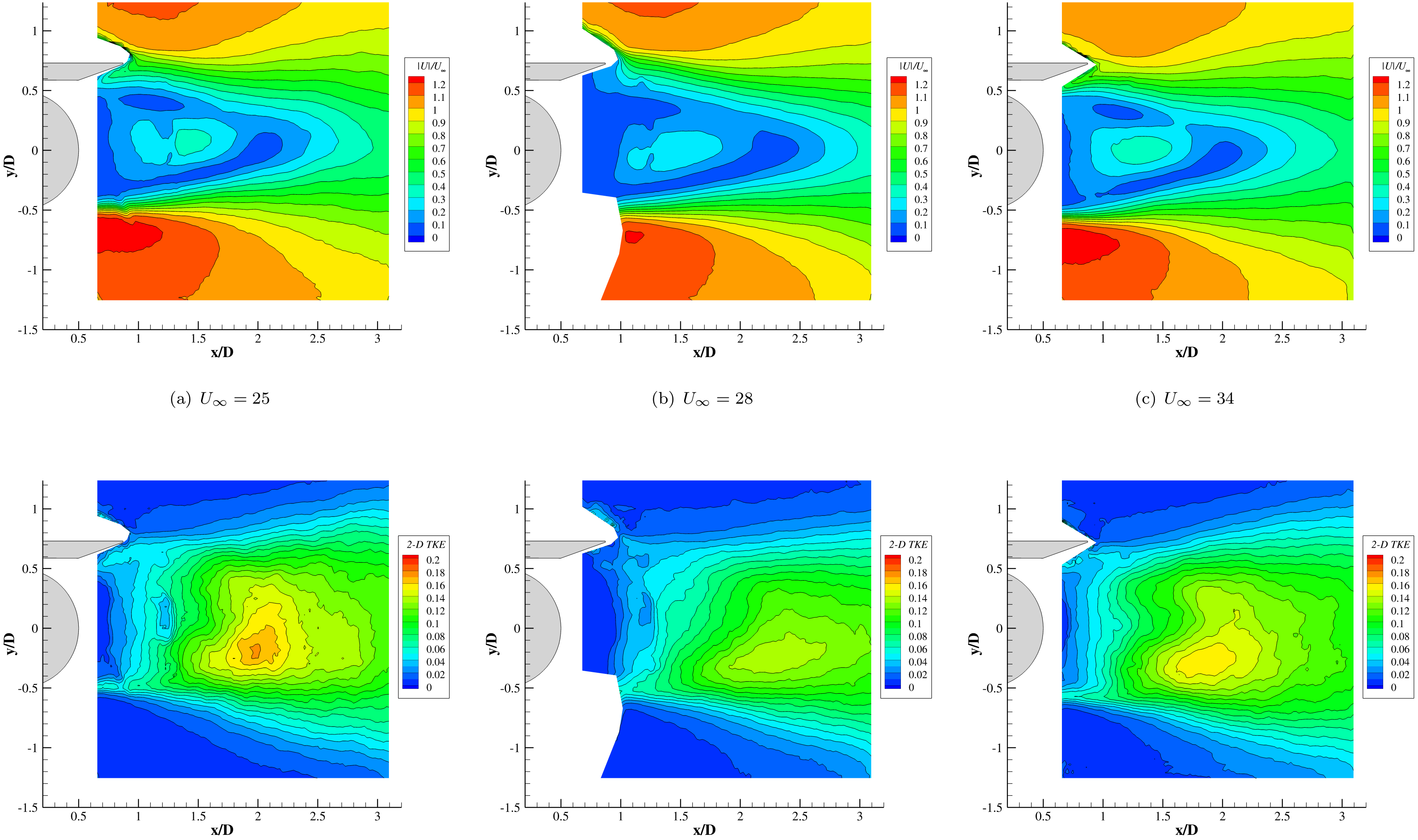

(a) $U_\infty = 25$

(b) $U_\infty = 28$

(c) $U_\infty = 34$

(d) $U_\infty = 25$

(e) $U_\infty = 28$

(f) $U_\infty = 34$

Figure 5.11: Velocity magnitude, and 2-D TKE fields at $\alpha_D = 0°$ at various speeds.

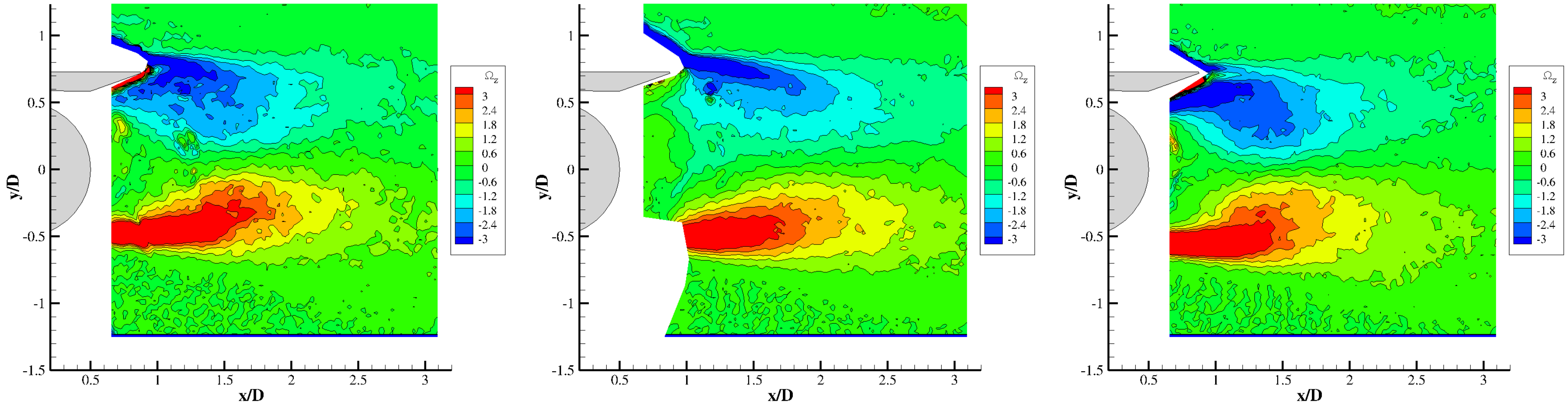

(a) $U_\infty = 25$ (b) $U_\infty = 28$ (c) $U_\infty = 34$

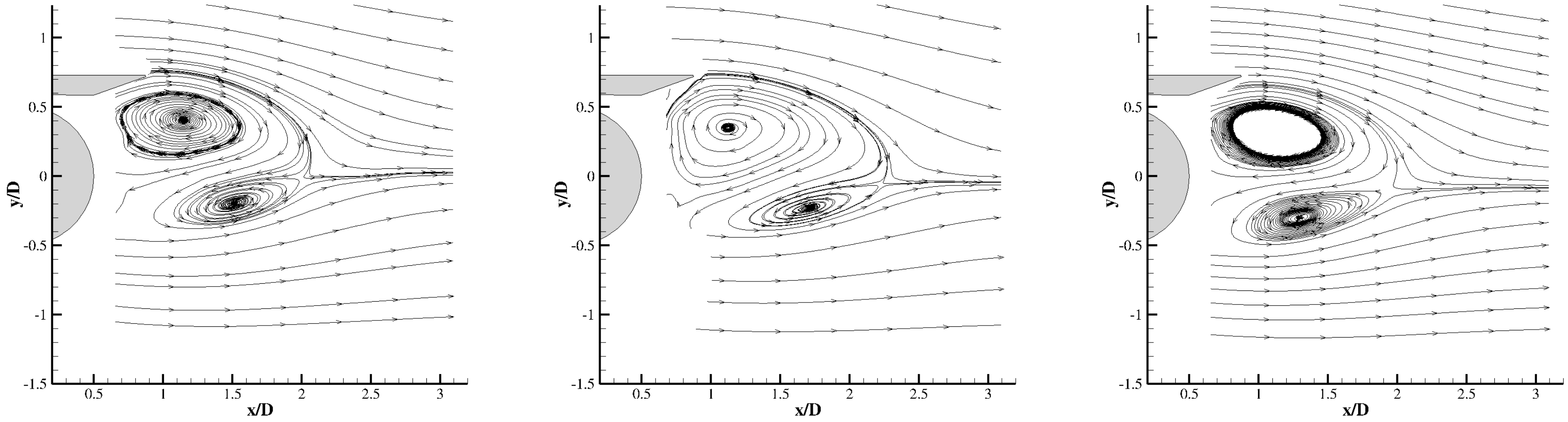

(d) $U_\infty = 25$ (e) $U_\infty = 28$ (f) $U_\infty = 34$

Figure 5.12: Z-Vorticity field and stream line plots for $\alpha_D = 0°$ at various speeds.

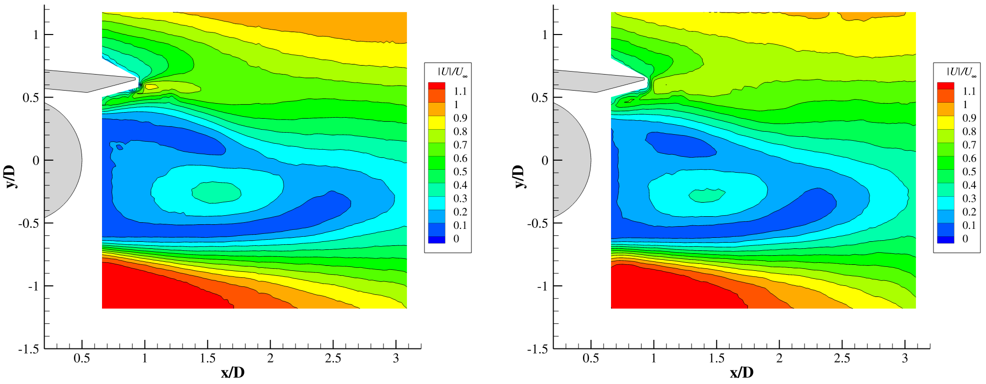

(a) $U_\infty = 30$

(b) $U_\infty = 34$

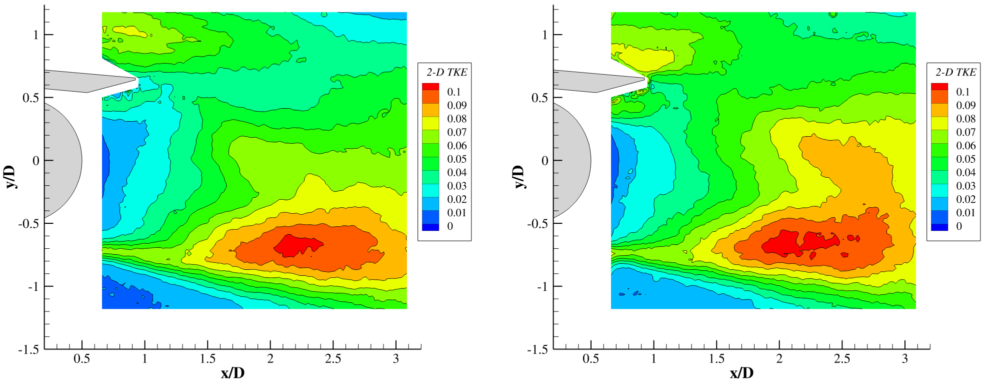

(c) $U_\infty = 30$

(d) $U_\infty = 34$

Figure 5.13: Velocity magnitude, and 2-D TKE fields at $\alpha_D = 5°$ at various speeds.

and Zdravkovich [74] for a cylinder interacting with a flat plane boundary. The velocity deficit in the wake is slightly asymmetric where the maximum deficit is skewed towards the lower, door-free side. The vorticity field in Figure 5.12 shows four sources of vorticity, two of which are due to the separated boundary layers along the cylinder element. The other two sources are from the upper and lower surfaces of the door. Along the lower surface of the door trailing edge, a region of positive vorticity is generated due to the separated flow around the sharp corner. On the upper surface of the door, a source of negative vorticity is formed, which may be due to the high velocity flow interacting with the low velocity formed in the wake region, which resembles a common profile observed along the outer shear layers of jet flows. The slight asymmetry of the wake is also shown in the vorticity and 2-D TKE contours. The TKE is produced in the wake region, as in Figure 5.18, and it is concentrated in the cylinder shear layer on the door-free side.

For $\alpha_D = 0°$ at the intermediate speed of $U_\infty = 28$ m/s, the vorticity magnitude in the gap region is smaller. A difference in the mean streamline patterns near the door

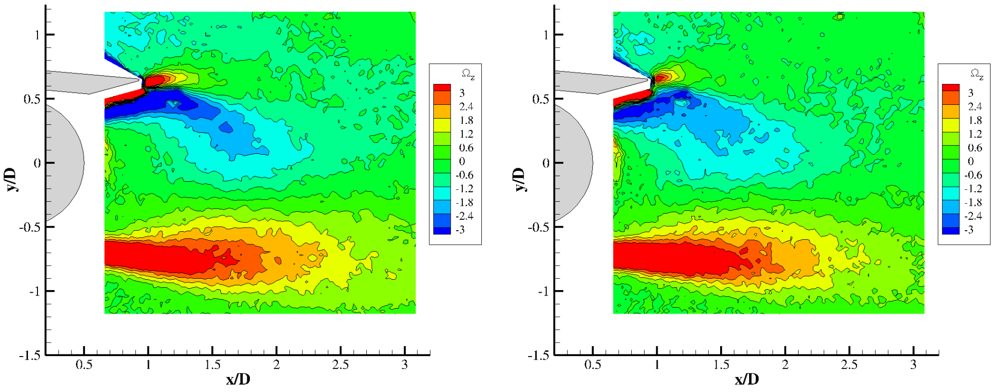

(a) $U_\infty = 30$ (b) $U_\infty = 34$

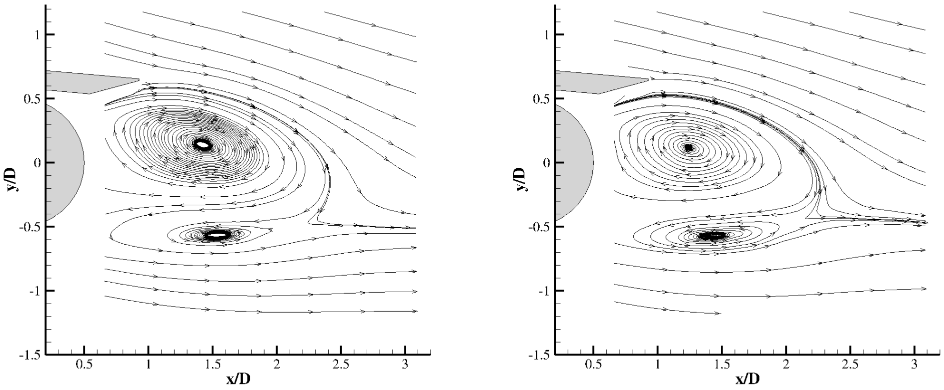

(c) $U_\infty = 30$ (d) $U_\infty = 34$

Figure 5.14: Z-Vorticity field and stream line plots for $\alpha_D = 5°$ at various speeds.

trailing edge is also present at this speed. These differences occur only at $U_\infty = 28$ m/s and may explain the changes to the mean loads that also occur around this speed in Figure 5.8. Lower levels in the 2-D TKE are also present at the intermediate speed, which verifies the reduced drag coefficient in Figure 5.8. The differences may be caused by changes to the flow dynamics in the gap region and at the door trailing edge, which may be due to differences formed upstream of the PIV window.

As the door angle is increased from 0 to 5 degrees, Figures 5.13, 5.19, and 5.20 show that the velocity deficit becomes wider and more asymmetric. The width and the asymmetry of the velocity profile is affected by the increase in the projected height, and the reduced geometric symmetry along the free-stream direction, that occurs at higher door angles. The width of the wake is increased towards $y/D > 0.5$ due to the additional wake generated by the inclined door. The wake formed along the upper surface of the door generates larger levels of 2-D TKE, shown in Figure 5.13. The wider wake formed by

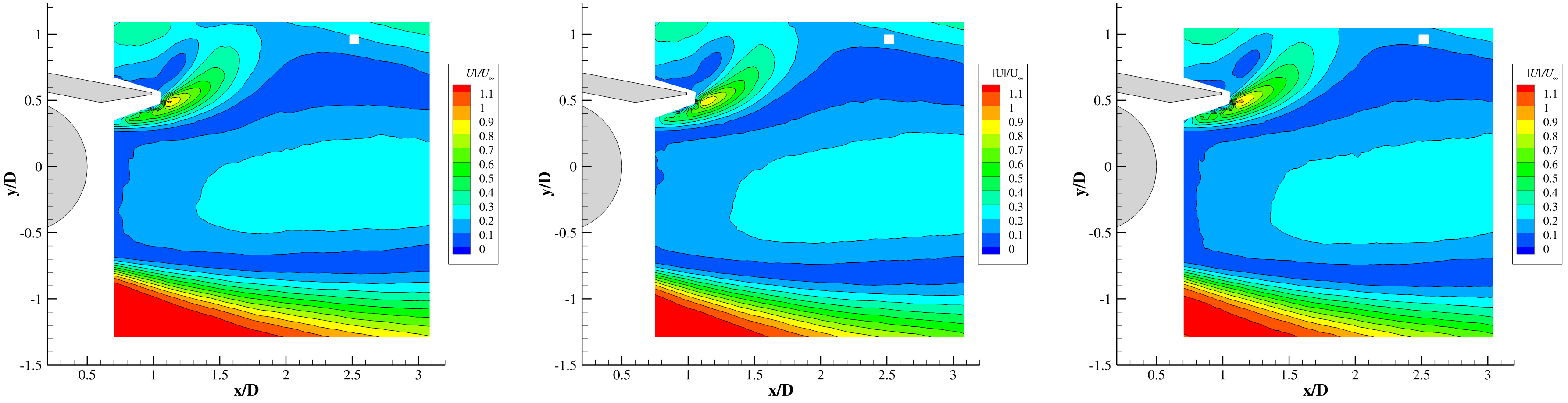

(a) $U_\infty = 25$ (b) $U_\infty = 30$ (c) $U_\infty = 32$

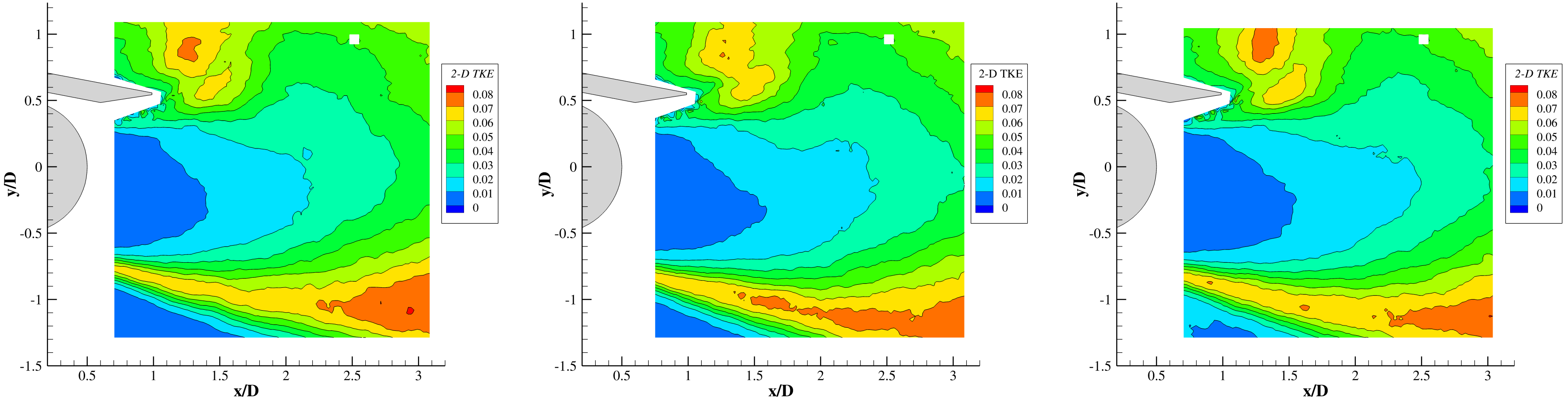

(d) $U_\infty = 25$ (e) $U_\infty = 30$ (f) $U_\infty = 32$

Figure 5.15: Velocity magnitude, and 2-D TKE fields at $\alpha_D = 10.7$ at various speeds.

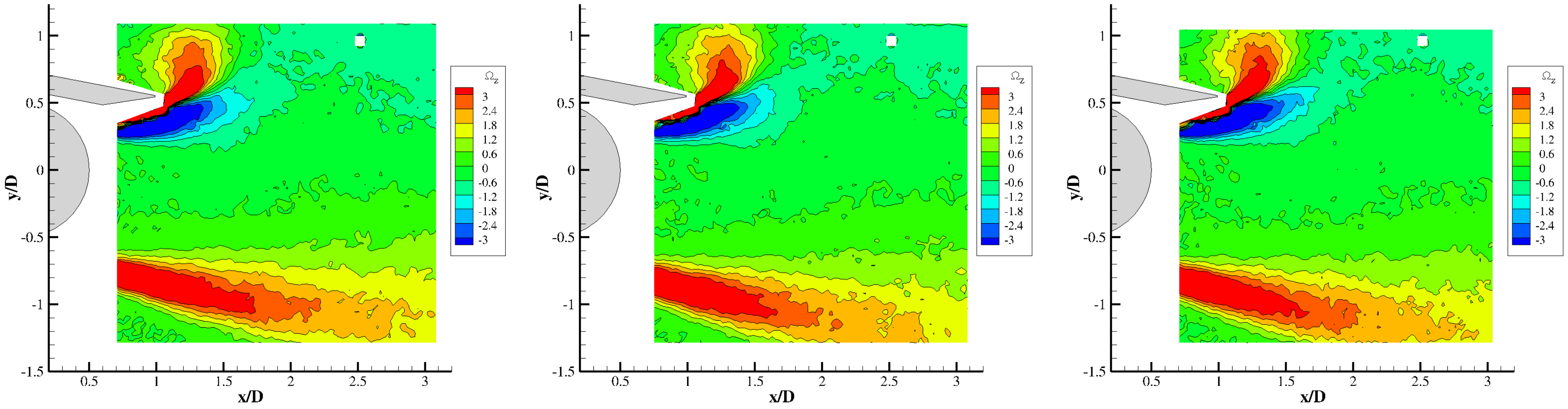

(a) $U_\infty = 25$ (b) $U_\infty = 30$ (c) $U_\infty = 32$

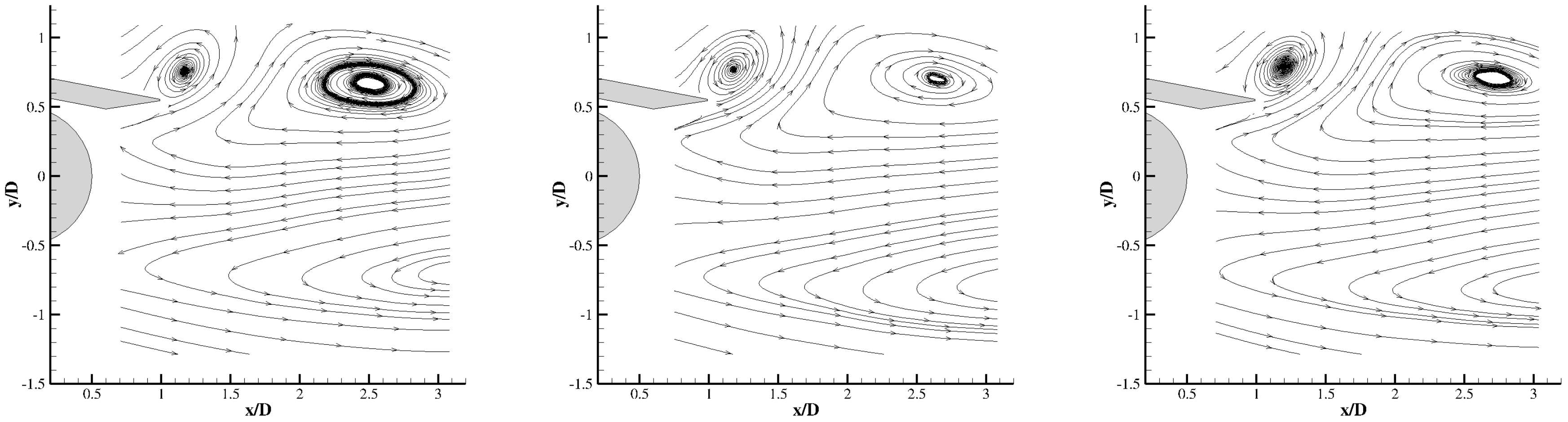

(d) $U_\infty = 25$ (e) $U_\infty = 30$ (f) $U_\infty = 32$

Figure 5.16: Z-Vorticity field and stream line plots for $\alpha_D = 10.7°$ at various speeds.

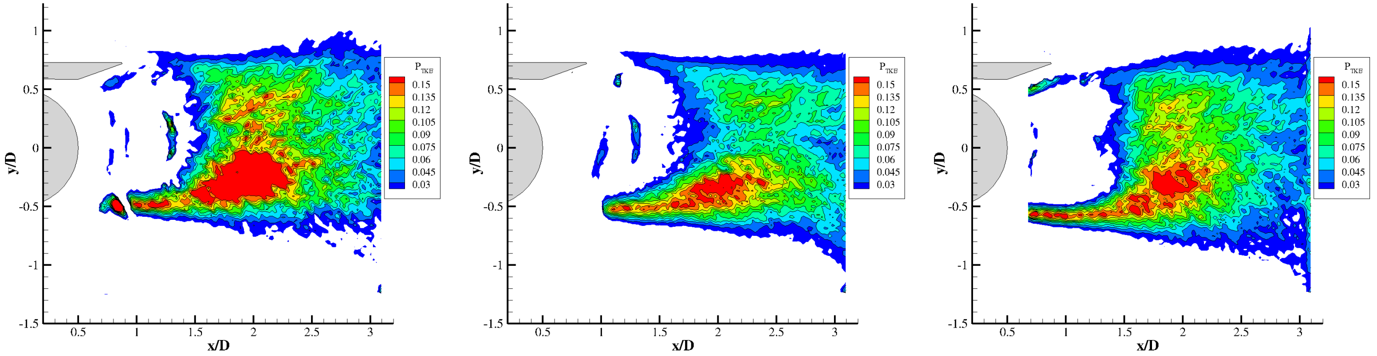

(a) $U_\infty = 25$ (b) $U_\infty = 28$ (c) $U_\infty = 34$

Figure 5.17: TKE production term for $\alpha_D = 0°$ at various speeds.

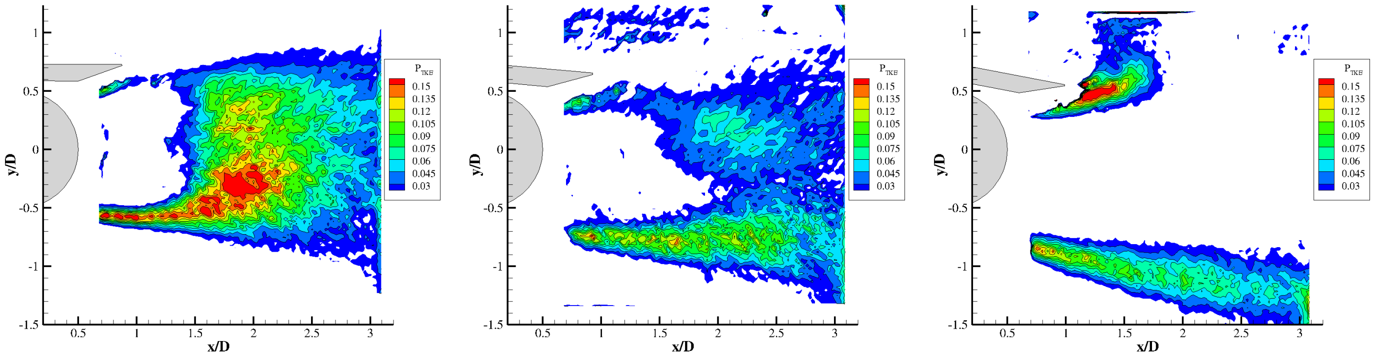

(a) $\alpha_D = 0°$, $U_\infty = 34$ (b) $\alpha_D = 5°$, $U_\infty = 34$ (c) $\alpha_D = 10.7°$, $U_\infty = 32$

Figure 5.18: TKE production term for various α_D°.

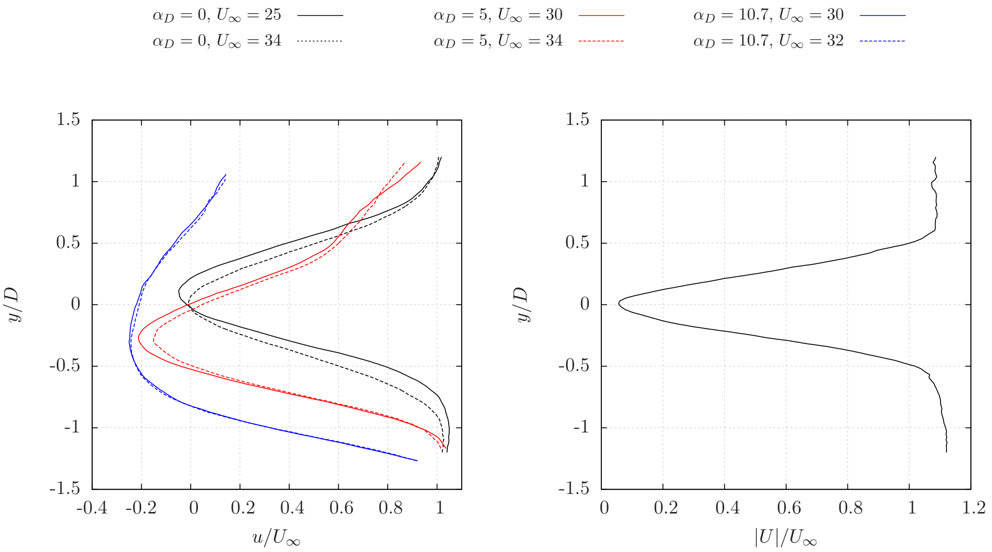

(a) Velocity magnitude

(b) Reference data for an isolated cylinder [61]

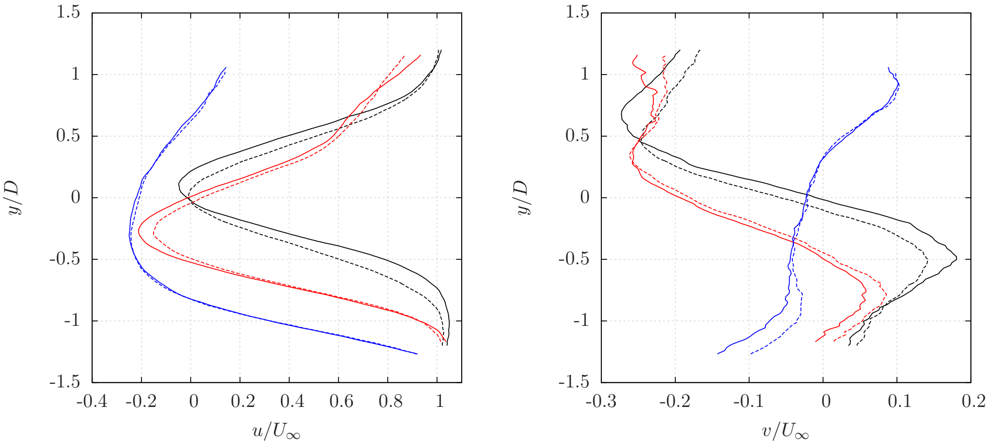

(c) Stream-wise velocity

(d) Transverse velocity

Figure 5.19: Effect of the door angle on the velocity profiles at $x/D = 2$ downstream in the wake of the model.

the angled door also reduces the velocity gradient in the transverse direction, thereby lowering the vorticity magnitude shown in Figure 5.14.

The downwash generated by the door shifts the position of the minimum velocity magnitude in Figure 5.19 to $y/D = -0.3$. It should be noted that the extracted data in Figure 5.19 is taken along a line perpendicular to the free-stream direction. Therefore, the observed wider wake may be partly due to the down wash of the wake region projecting itself across a wider area of the sampled region. The concentration of highest 2-D TKE is along the lower section of the cylinder, and the production field shown in Figure 5.18, verifies that this is due to the shear layer along the door-free side of the cylinder. Figures

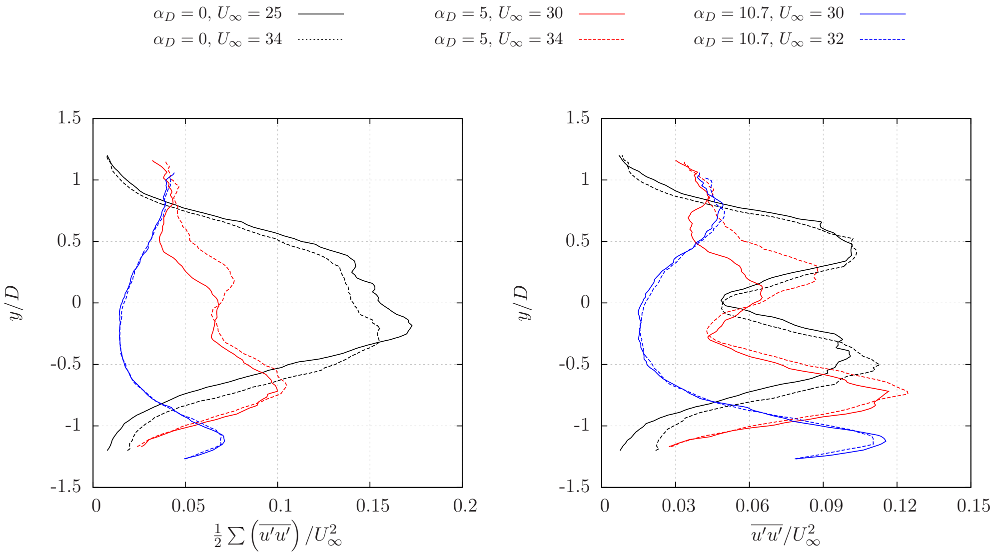

(a) 2-D TKE

(b) Stream-wise component

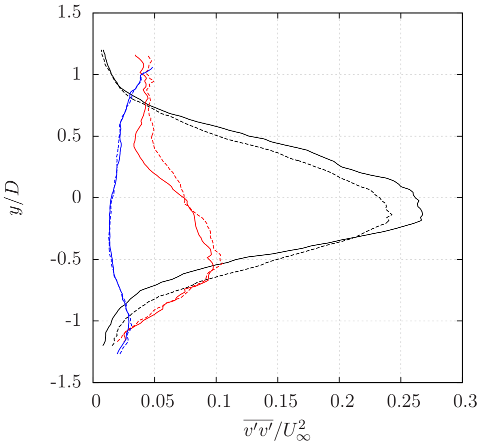

(c) Transverse component

Figure 5.20: Effect of the door angle in the energy profiles at $x/D = 2$ downstream in the wake of the model.

5.20 and 5.18 also show that the amplitude of the production term, and the magnitude of the 2-D TKE, are lower at 5 degrees compared to 0 degrees. The 2-D TKE profiles in Figure 5.20 peak at 0.16 and 0.1 for a door at 0 and 5 degrees, respectively. This reduction is mostly due to the changes in the transverse component. The stream-wise component of TKE remains similar in its peak intensity. The vorticity and stream line patterns for $\alpha_D = 5°$ given in Figure 5.14, which are similar to the patterns shown for $\alpha_D = 0°$.

Figures 5.15 and 5.20 show as the door angle is increased further to 10.7 degrees, the profile of the wake changes further. The wake width is significantly larger, beyond the size of the PIV frame. The transverse velocity profile in Figure 5.19 shows a completely different behaviour compared to lower door angles. For leg-door angles of 0 and 5 degrees, an almost opposite transverse velocity profile is observed. At $\alpha_D = 10.7°$, a significant up-wash of the flow entrained through the gap region occurs towards the upper surface of the door. The streamline patterns of the mean flow in Figure 5.16 show that this mechanism induces a recirculation region towards the upper section of the door trailing edge. Towards the trailing edge, two sources of opposing vorticity are also found. This is likely due to the shear layers formed within the gap region, from the cylinder flow and the leg-door boundary layer. These features are skewed towards the low pressure region generated along the upper surface of the leg-door. The strong upwash formed, only at this door angle, is the source of the differences in the velocity profile in Figure 5.19 in the region of $y/D > 0.5$. At $y/D < 0.5$, the transverse velocity profile is similar to other door angles. However, the increased magnitude of the transverse velocity is likely due to the change in the separation point along the lower section of the cylinder, causing the shear layer to be projected downwards more. Compared to other door angles, a strong production region of TKE is formed towards the door trailing edge. However, the overall levels of TKE, shown in Figure 5.20, are significantly lower than for any other configuration.

The TKE along the wake of a body peaks at a particular location based on an equilibrium between the various terms in the TKE transport equation. The location of the peak can be based on a characteristic length scale. The TKE contours provided by the PIV do not contain the entire width of the wake, and more importantly, do not contain a large amount of downstream content. The PIV field of TKE for 0 and 5 degrees shows that the wake width grows, and a peak level of TKE is contained within the frame. However, a peak level of TKE is not observed in the frame for a door at 10.7 degrees. Therefore it is uncertain that the peak intensity is captured within the frame. However, it can be concluded that the near wake region of the cylinder does indeed experience a significant reduction in the TKE. Finally, it should be noted that the PIV data is limited to the flow behind the cylinder element. The separated flow along the upper surface of the door was not recorded due to the design of the end plates.

Surface pressure data

The surface pressure time-signal was recorded at $\theta = 0$ degrees along the cylinder, positioned in the wake and directed downstream. The pressure signals were recorded at free-stream speeds of 20 and 30 m/s and the comparative changes in the PSD across a range of Strouhal numbers, due to the changes in the door angle, are shown in Figure 5.21. The frequency axis is made expressed as the Strouhal number using the free-stream speed, and a reference length, which was taken for all cases as the cylinder diameter. In Figure 5.21 changes to the tonal behaviour, and a broadband shift in the spectra, are found between the measurements taken from an isolated cylinder with no door interaction, and the three interaction cases at varying α_D°.

At both speeds, the isolated cylinder data contains a peak at a Strouhal number of $St = 0.53$, which corresponds to the drag dipole related to the vortex shedding. Since the drag dipole is at twice the frequency of a lift dipole, this measurement implies a vortex shedding at $St = 0.265$. As the leg-door model at $\alpha_D = 0^\circ$ is included in the model, the tonal peak shifts to lower frequencies, and instead two tonal peaks are identified. The dominant tone is at $St \approx 0.2$ with a second peak at the next harmonic, $St = 0.4$. The shift to lower St is likely due to the widening of the wake. This effect is also observed for isolated cylinders shifting from sub-critical to super-critical flow regimes [29, 67]. The detection of the primary shedding mode at $St \approx 0.2$ is likely due to the induced circulation from the model. The loads data in Figure 5.8 shows that a positive lift force is generated, which implies that the microphone position is no longer in line with the centreline axis of the mean flow in the wake. Therefore, a rotational shift in the lift-dipole is likely to be the source of the lower tone at $St = 0.2$. As the door angle is increased, the tonal behaviour ceases and the overall levels of energy density reduce.

At a free-stream speed of 30 m/s, an additional tone at $St = 4$ is generated. This is not observed at any other speed, is unaffected by the door angle, and is also present for the isolated cylinder case. This phenomena is due to the interaction between the wake generated by the driving fan impinging on the guide vanes of the wind tunnel facility, which resonate to generate a strong tone only at this speed.

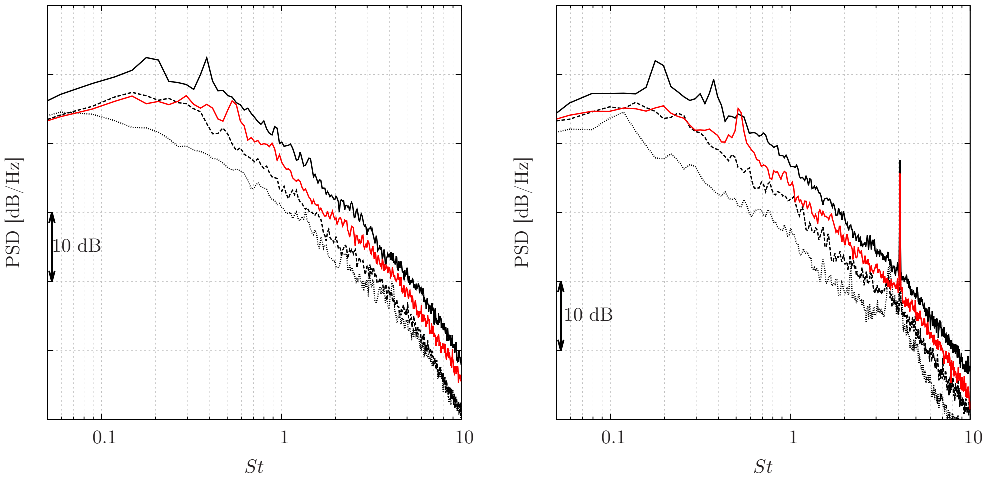

(a) $U_\infty = 20$

(b) $U_\infty = 30$

Figure 5.21: Surface pressure spectra at two free-stream speeds for an isolated cylinder: ——, $\alpha_D = 0^\circ$: ——, $\alpha_D = 5^\circ$: - - -, $\alpha_D = 10.7^\circ$: ······.

In Figure 5.22, the changes to the surface pressure spectra, compared to the isolated cylinder data, are given. These trends do not clearly identify changes in the tonal

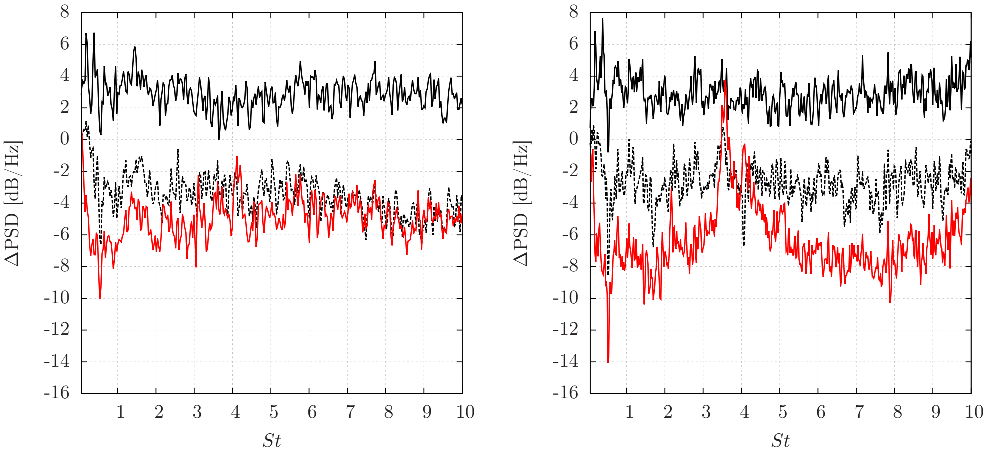

(a) $U_\infty = 20$

(b) $U_\infty = 30$

Figure 5.22: Differences in the surface pressure spectra compared to the isolated cylinder data. Data from $\alpha_D = 0°$: ——, $\alpha_D = 5°$: - - -, $\alpha_D = 10.7°$: ——.

behaviour, but they do clearly show how the overall energy levels shift in an almost uniform manner. These trends also show that the PSD levels for an interaction model at $\alpha_D = 0°$ are higher at all frequencies in comparison to an isolated cylinder. It also shows that as the door angle is increased from 0 to 5 degrees, the levels reduce by 8 dB. A further 1-2 dB reduction is observed as the door angle is increased from 5 to 10.7 degrees. The large peak difference for $\alpha_D = 10.7°$ at $U_\infty = 30$ in Figure 5.22 occurs at $St = 4$, which is partly discarded as this portion of the data may be influenced by the background tonal noise generated by the wind tunnel.

5.4 Summary

The flow behind an isolated door model at 0, 5 and 10.7 degrees AoA, was studied by oil flow and time-averaged load measurements. This data showed that at 0 and 5 degrees the loads are unaffected by the Reynolds number. However, at 10.7 degrees an end-plate interaction would occur in a narrow Reynolds number range modifying the lift coefficient by 16%. The key surface flow features for the isolated door consists of leading edge separation bubbles, induced by the adverse pressure gradients generated by the sharp edges from the door leading edge, as well as trailing edge flow separation induced by similar effects from the trailing edge profile.

When the cylinder is added to an isolated door model, the Reynolds number sensitivity is greatest for 0 and 5 degrees, and diminishes to at 10.7 degrees. The effects, as measured by the oil flow and mean loads data, are:

1. **Increased circulation**
   The mean lift and drag forces increase when a cylinder is added to an isolated door model. An increase of $\Delta C_L \approx 0.5$, $\Delta C_L \approx 0.7$, and $\Delta C_L \approx 0.35$ were measured for a model at 0, 5 and 10.7 degrees, respectively, due to the inclusion of a cylinder to an isolated door. The cylinder positioned along the lower section of the door induces a blockage that results in a net circulation that favours an increased lift force. The increase in the drag is due to the lift-induced component, as well as an increased frontal projected area.

2. **Additional surface flow features**
   The oil flow patterns for an isolated door model show the formation of additional flow features compared to those with a cylinder included. Firstly, along the mid chord of the lower surface of the door, a separation bubble may form due to the adverse pressure gradient induced by the stagnating flow on the cylinder. This feature is more likely to form at low door angles, where the pressure gradient along the lower surface of the door is less favourable, compared to higher door angles, and therefore more prone to the adverse pressure gradient induced by the cylinder. Secondly, flow separation occurs along the cylinder element, that was otherwise not present for an isolated door model. Finally, an additional feature forms along the upper surface of the door towards the trailing edge, at higher door angles. This forms as the jet flow is exhausted through the gap region between the cylinder and the door, and is skewed towards the low pressure formed along the upper surface of the door, and the flow rolls up along the door trailing edge.

The effects of increasing the door angle on a cylinder-door interaction model, as measured by the PIV and microphone data are:

1. **Widening of the wake region**
   As the door angle is increased, the projected frontal area increases, thereby inducing a wider wake. The PIV data shows that the mean velocity profile for $\alpha_D = 0^\circ$ in the wake is wider than for an isolated cylinder. The PIV data also shows that the velocity deficit widens beyond the frame of the PIV measurement window, at $\alpha_D = 10.7^\circ$. The surface pressure spectra show where tonal behaviour is observed, that it tends to lower frequencies with increasing door angle. This can be seen by the velocity magnitude profiles which tend less towards unity towards the lower and upper limits of the profile. Between 5 and 10.7 degrees, there is a significant change to the velocity profile at a y-position of $y/D > 0$. This shows that between the two configurations, the leg-door induces a much larger wake, and may suggest a fully separated flow along the upper section of the door.

2. **Asymmetry of the wake**
   The velocity profiles extracted form the PIV data show a reduction in the symmetry as the door angle increases, which may be due to the reduced geometric

symmetry with higher door angles. The streamline illustrations from the mean velocity field also show this asymmetry. As the door angle is increased, the peak velocity deficit of stream-wise mean velocity shifts to a lower transverse position (i.e., smaller y-coordinate).

3. **Changes to the 2-D TKE levels**
   Although the PIV data captures only two of the three components of the TKE equation, the trends show an overall reduction in the 2-D TKE levels in the immediate region behind the cylinder, as the door angle is increased. The production term for the TKE transport equation was simplified, and shows that the production at 0 degrees is, due to the detached shear layers formed along the sides of the cylinder, as expected. However, at $\alpha_D = 0°$, there is an asymmetry in the production term across the cylinder centreline axis, as well as in the 2-D TKE levels. The shear layer from the gap region seems to be weaker, and weakens as the door angle is increased from 0 to 5 degrees. As the door angle is increased from 5 to 10.7 degrees, the TKE production term from the gap flow increases significantly. This is likely due to the strong curvature of the fluid entrained through the gap region, towards the low pressure region formed along the upper surface of the door. This induces a strong velocity gradient, and increases the magnitude of the production term. Changes in the 2-D TKE levels are also observed along the upper surface of the door. At a door angle of 0 degrees, low levels of 2-D TKE are recorded at a high transverse position ($y/D > 0.5$), however at the non-zero door angles, the levels increase from TKE < 0.01, to TKE ≈ 0.04. Additionally, the decomposition of the 2-D TKE shows that the largest changes occur due to the reductions in the transverse TKE component. The microphone spectra, which records pressure energy spectra, shows that the energy levels decrease at higher door angles.

This experimental database may also serve as a validation case for CAA and CFD codes.

Chapter 6

High-order simulations

High-order numerical methods were used to study the sound generation and propagation of a cylinder and a leg-door in a side by side configuration. The proximity between the cylinder and leg-door was set to a constant gap width ratio of $G = 0.087$, which corresponds to the design of an A-340 MLG. The aeroacoustic effects of varying the door angle were investigated by modelling the flow around five interaction cases. Additional simulations of an isolated cylinder, and an isolated door at $\alpha_D = 10.7$ degrees were conducted in order to provide further insight into the effects of the aerodynamic interaction. These simulations were conducted with a free-stream Mach number of $M_\infty = 0.2$ and Reynolds number of $Re_D = 1.7 \times 10^6$, which is based on the cylinder diameter D.

The numerical solution to the fully compressible, three-dimensional Navier-Stokes equations is obtained by the Zonal Detached-Eddy Simulation (Z-DES) method. In blocks that do not contain wall regions Z-DES mode I is applied, otherwise mode II is applied. The effect of the aerodynamic interaction on the far-field acoustics is predicted by the FW-H method. Far-field noise calculations using both on-body, and off-body integration surfaces were conducted.

The cases studied with the high-order CAA solver are outlined in Table 6.1, which totals to eight simulations. The structure of this chapter is as follows. Firstly, the grid development strategy is outlined. In this section the domain edges, grid requirements, and boundary conditions are described. Then the validation of the numerical predictions is presented where the velocity field in the wake region is compared to the PIV data reviewed in Chapter 5.4. This is followed by a summary of the variations in the aerodynamic data between the eight simulations. Finally, the results from the FW-H calculations are presented. In the final results section, noise source maps along the cylinder and door surfaces are included, which aid in describing the spectral profile of the far-field noise signals.

The maximum time-step used in the simulations was equivalent to CFL < 20, based on the local sound speed. From the temporal scheme error analysis (outlined in Appendix

B), the ideal CFL for time-accurate solutions is CFL < 0.1. The areas of the grid that suffer from numerical dissipation errors, due to a large CFL, are confined to the boundary layer regions only. It should be noted that the grid spacing outside of the boundary layer mesh is at least 100 times larger than the smallest grid spacing. Therefore, the CFL in the majority of the grid is of the order of CFL $< O(10^{-3})$.

Case Name	Gap width ratio	Door angle (degree)	Cell count ($\times 10^6$)
Isolated cylinder	N/A	N/A	9.7
Isolated door	N/A	10.7	12.8
Case_0	0.087	0	14.4
Case_2.5	0.087	2.5	15.4
Case_5	0.087	5	15.4
Case_7.5	0.087	7.5	15.5
Case_10	0.087	10.7	15.5

Table 6.1: Case descriptions for the high-order numerical simulations.

6.1 Grid development

A fully structured mesh was designed in the software package Gridgen®. The grids from the preliminary 2-D URANS studies using FLUENT were enhanced by using the grid quality assessment tool that was outlined in Section 4.5. The use of the grid quality assessment tool ensures a high grid quality for all of the high-order simulations.

For the grid development the key design features were: (1) the domain size, (2) the local grid spacing in the near-field region, and (3) the boundary condition type. The domain size was based on previous high-order simulations conducted by Peers [95], and the local grid spacing in the near-field region averages to approximately $\Delta x \approx 0.01$ m. This grid resolution should allows waves of up to $f_{max} = 3400$ Hz assuming a 10 point per wavelength requirement, and a free-stream speed of sound of $c_\infty = 340$ m/s. However, according to Kim [100] the idealised maximal resolution requires only 3 points per wavelength. The overall frequency resolution of the spatial scheme may be lower than the idealised threshold due to the use of spatial filtering, and to the numerical dissipation from the implicit time stepping scheme.

The grid for the interaction cases is quite complex in the near-field region. To ensure that an ideal block edge topology is designed, the grids for the isolated configurations were developed first. Figures 6.1 and 6.2 illustrate the computational domain, and the regions of the mesh that contain some level of complexity. The boundary conditions between multi-block interfaces are specified either as a one-to-one interface, or by the characteristic interface boundary condition (CIC). In Figures 6.1 and 6.2, the multi-block edges are highlighted by the red lines, and the areas of grid with boundary conditions are highlighted by the black lines. Along the wall regions, a no-slip and iso-thermal condition is applied. Block interfaces that contain a discontinuity in the grid metrics are treated by the CIC. A boundary layer mesh is also specified near all wall surfaces to enable direct and local control of the boundary layer resolution. Initial estimates of the first-cell height were obtained using flat plate boundary layer theory, and additionally from the 2-D URANS studies. An overview of the URANS study is provided in the Appendix A.

An illustration of the grid for the interaction case at $\alpha_D = 10.7$ degrees is given in Figure 6.3. The block edge topology of the near-field mesh around the cylinder and door elements are based on the block edge topologies from the isolated cylinder and isolated door grids, which are shown in Figures 6.1 and 6.2, respectively. The span-wise extrusion of the 2-D grid is applied along the z-axis by a distance of $L_z = 3D$, and with a span-wise grid resolution of $\Delta z/D = 0.05$. Low-order 3-D simulations of an interaction case, provided in the Appendix A, were conducted with a denser grid to verify that a resolution of $\Delta z/D = 0.05$ is sufficient.

Once the primary features of the grid, such as the domain extent and the required grid resolution, were determined, the interior mesh was developed. By using the grid quality assessment tool, described in Section 4.5, the grids were refined for maximum grid quality. Due to the use of CIC along multiple block boundaries, the grid optimization strategy outlined in Section 4.5.4 is not applicable without further development of the grid optimization tool. A sample of the output from the grid quality assessment tool is provided in the Appendix D.

A Zonal-DES method [53] was applied whereby the turbulence modelling strategy is block specific. All blocks containing a wall region were treated by Mode II, and all other blocks were treated as Mode I. This strategy was employed to ensure that an accurate prediction of the boundary layer separation is obtained, and that a natural growth of non-linear instabilities along detached shear layers is possible in the regions away from the wall.

The numerical solutions of the velocity and acoustic fields are illustrated for two interaction cases in Figure 6.4. These figures illustrate the turbulent structures in the wake region by a surface plot of constant Q-criterion $Q = 0.1$, and they also illustrate the radiating sound field by the velocity divergence.

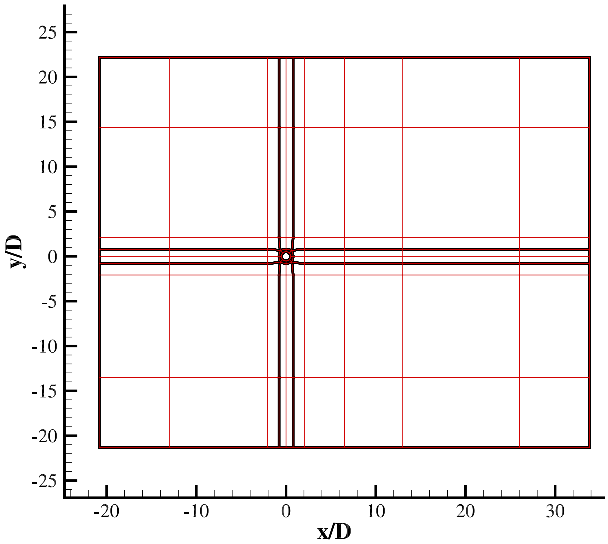

(a) Whole domain

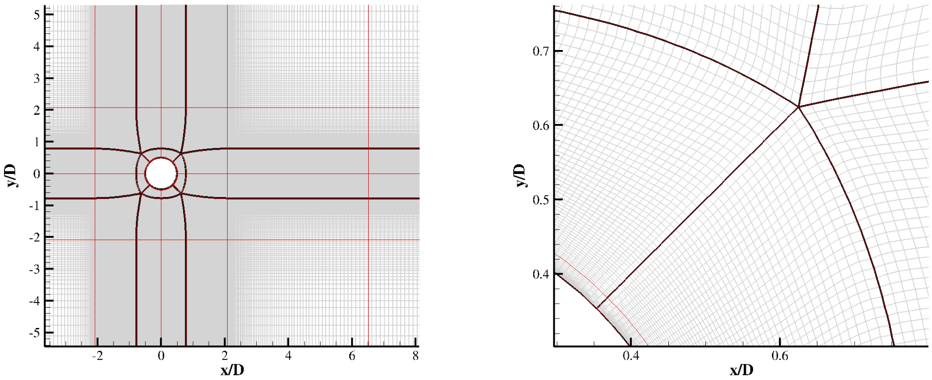

(b) Near field region

(c) Wake region

Figure 6.1: Computational grid for the isolated cylinder model. The block edges are highlighted in red, the boundary condition edges are highlighted in black, and the grid lines are highlighted in grey.

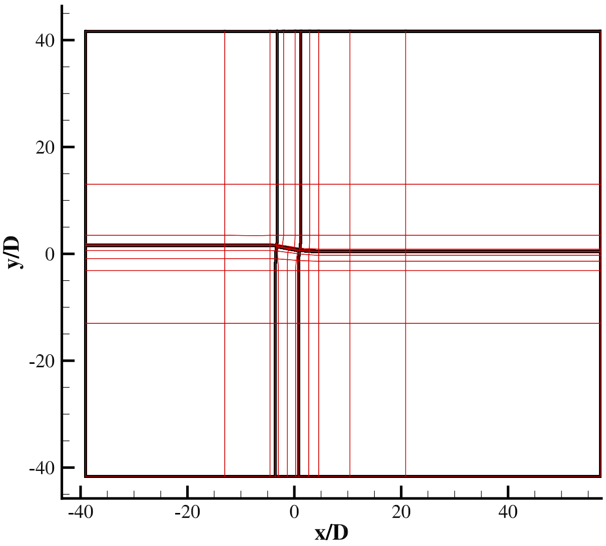

(a) Whole domain

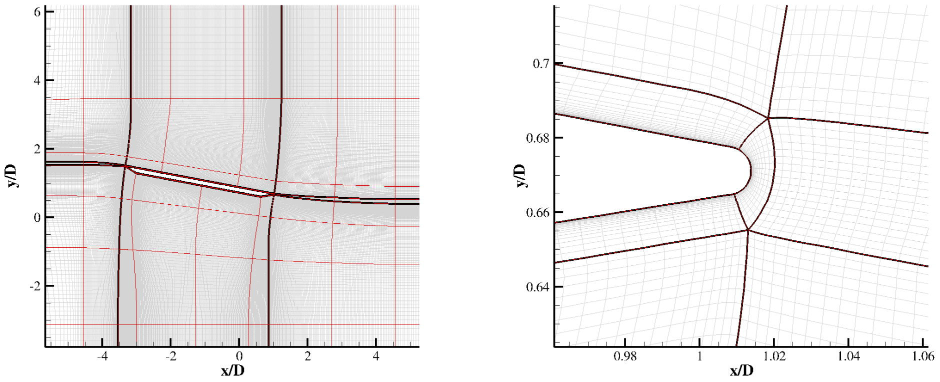

(b) Near field region

(c) Door trailing edge region

Figure 6.2: Computational grid for the isolated door model with an angle of attack. The block edges are highlighted in red, the boundary condition edges are highlighted in black, and the grid lines are highlighted in grey.

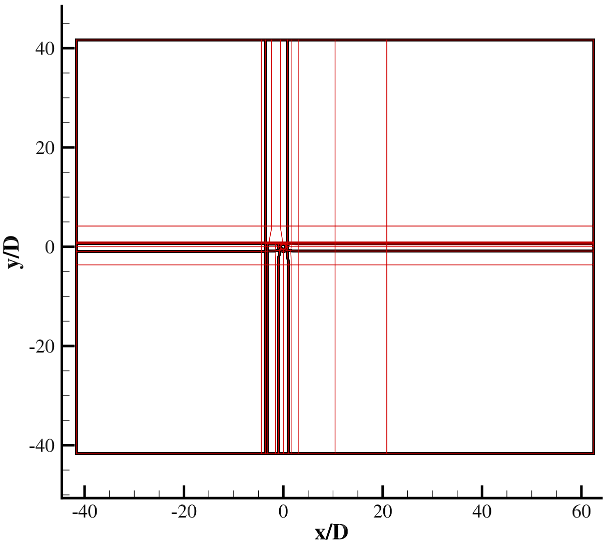

(a) Whole domain

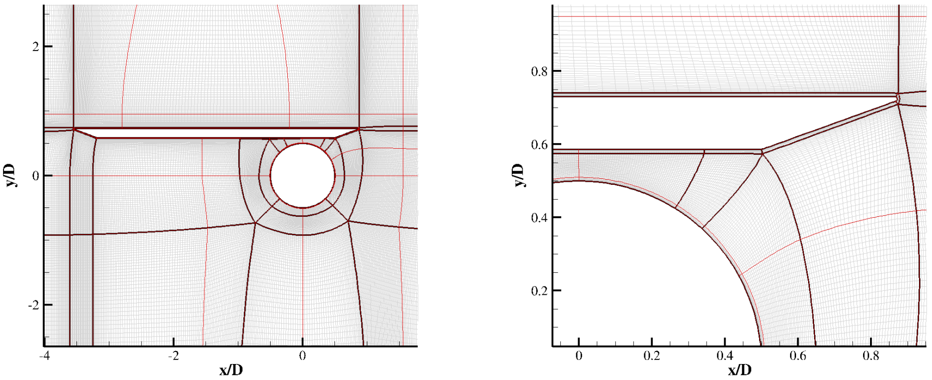

(b) Near field region

(c) Door trailing edge region

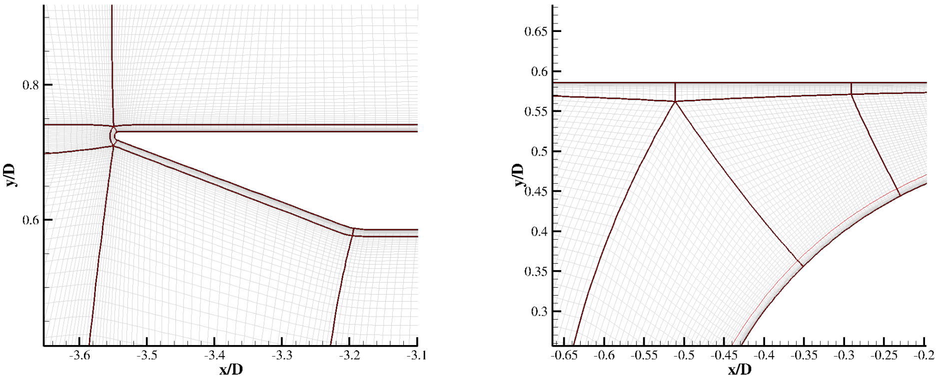

(d) Door leading edge region

(e) Gap region

Figure 6.3: Computational grid designed for the intercase case *Case_0*. Block edges are highlighted in red, boundary conditions are applied along the edges highlighted in black. Mesh lines are highlighted in grey.

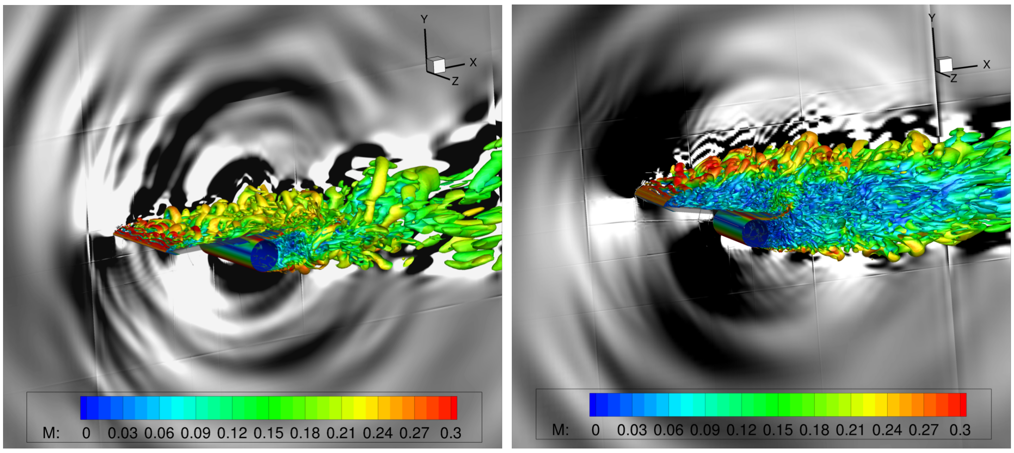

(a) $\alpha_D = 0°$ (b) $\alpha_D = 10.7°$

Figure 6.4: Instantaneous surface plot of constant Q-criterion $Q = 0.1$ coloured by the local Mach number and over set by the velocity divergence field in the range of $-0.01 < \nabla \cdot \vec{u} < 0.01$ in grey scale.

6.2 Validation of the numerical predictions

Figure 6.5 shows the mean surface pressure distribution along the cylinder surface from the numerical simulations, and it is compared to two experimental data sets that have been obtained at different Reynolds numbers. There is a good agreement between the numerical results and the experimental measurements obtained by Roshko [116], for the minimum pressure coefficient and the base pressure. Furthermore, the dominant vortex shedding mode of the circular cylinder, according to the FW-H far-field predictions, occurs at $St = 0.3$. This suggests that the flow is in the super-critical flow regime.

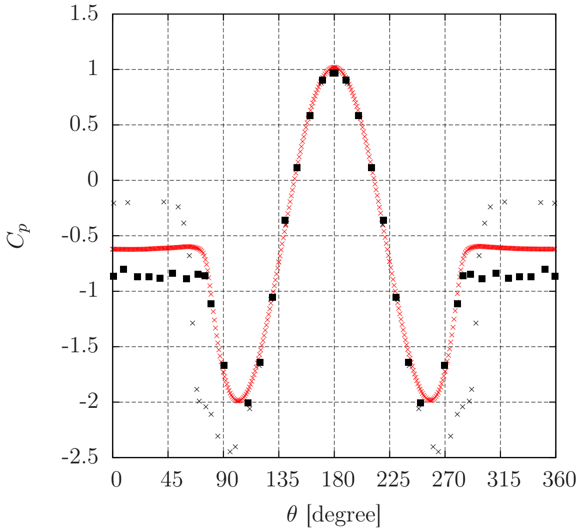

Figure 6.5: The mean pressure distribution along an isolated cylinder from the numerical simulation at $Re = 1.6 \times 10^6$ (red cross), and from experiments by Roshko [116] at $Re = 8.4 \times 10^6$ (black square) and by Flachsbart [116] at 6.7×10^5 (black cross).

The validity of the interaction cases is discussed next. The experimental PIV database measured for three interaction cases, with the door angled at 0, 5 and 10.7 degrees, was outlined in Section 5.4. Although the experimental data was acquired for a model with a lower Reynolds number and Mach number, it is still applicable as a validation case, as the flow regimes will be similar. Therefore, the experimental and numerical data can be compared in terms of normalised quantities.

The velocity magnitude predicted by the numerical methods is compared to the experimental measurements in Figure 6.6. This demonstrates an agreement for the mean flow field at a door angle of $\alpha_D = 0$ degrees. The asymmetry in the velocity profile and location of the maximum velocity deficit behind the cylinder element is predicted well by the simulations. Quantitative assessment for the validity of the numerical predictions is provided by comparing the mean and variance of the velocity field along two downstream locations that span across the wake region.

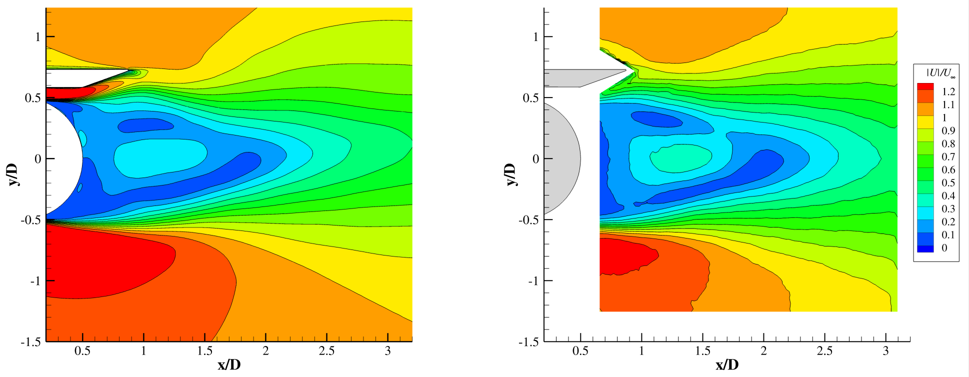

(a) Simulation

(b) Experiment at $U_\infty = 34$m/s

Figure 6.6: The mean velocity field behind an interaction model with $\alpha_D = 0°$, according to simulation and experiment.

Figure 6.7 shows the mean velocity profiles between the numerical predictions and the experimental measurements, for three door angles. A general agreement in the magnitude and the profile of the mean velocity distribution is demonstrated for all cases along the two down-stream positions. However, there are some slight differences between the simulation and experimental data. These differences are most likely due to the differences in the separation points along the cylinder surface. This difference would generate a disagreement in the deflection angle of the shear layers from both sides of the cylinder element. The best overall agreement in the velocity profile is obtained for the interaction case at $\alpha_D = 5°$, and the largest disagreement is found for the interaction case at $\alpha_D = 10.7°$. The differences for the latter configuration are largest towards the region of $(x/D, y/D) = (1.5, 0.65)$. This is associated with the accelerated flow through the gap region between the door and the cylinder.

Figure 6.8 shows the profiles of the 2-D TKE from the numerical simulations and the experimental database, for interaction cases configured to $\alpha_D = 0$, 5, and 10.7 degrees. Additionally, the stream-wise and transverse Reynolds stress profiles are illustrated in Figures 6.9 and 6.10. These additional Figures explain what the sources of the TKE profile disagreements may be. A general agreement of the 2-D TKE profiles is obtained for all door angles. However, the profiles from the numerical simulations tend to over-predict the experimental data. Over-estimations in the principle Reynolds stresses were also observed by Breuer *et al.* [54]. In their work, it was shown that the Reynolds stresses from DES calculations were larger than the LES predictions. They were also able to reduce the over-prediction by using a modified DES model. The over-estimation observed by the current work is therefore attributed to the turbulence model. Further differences in the profiles may be due to differences in the separation points along the cylinder. Finally, a comparison of the surface pressure spectra along a single position on the cylinder is also provided in Appendix E.

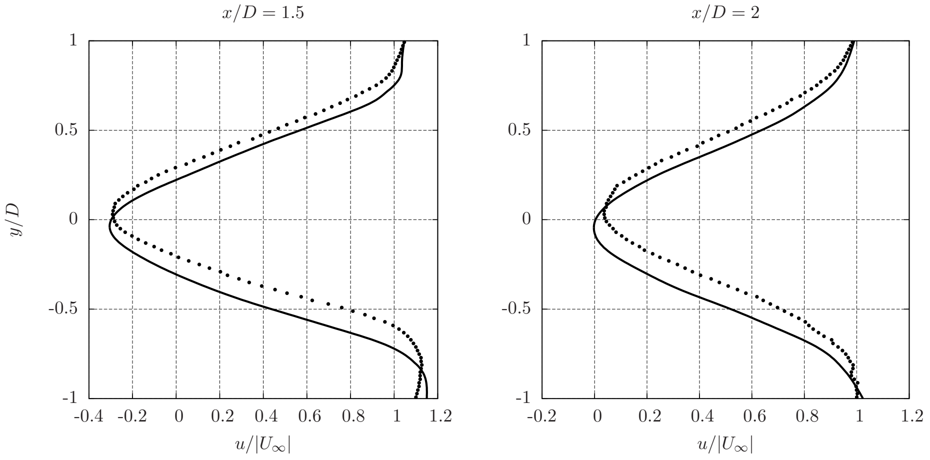

(a) $\alpha_D = 0°$

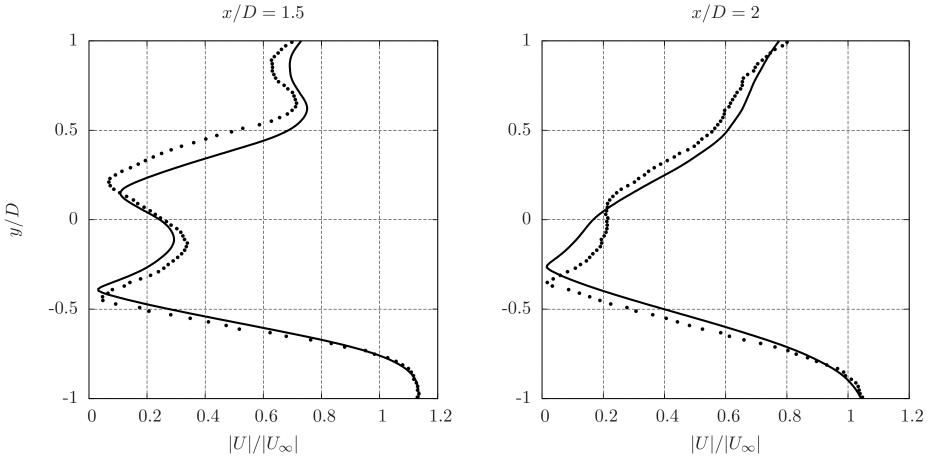

(b) $\alpha_D = 5°$

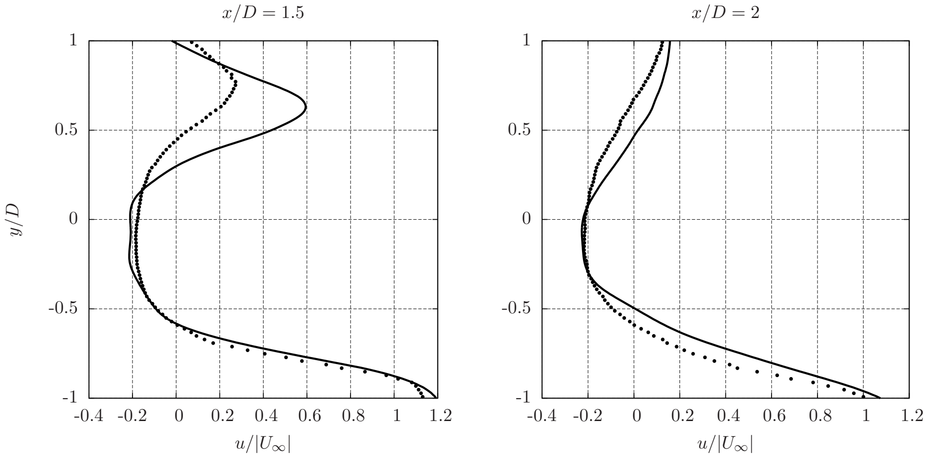

(c) $\alpha_D = 10.7°$

Figure 6.7: The mean velocity profiles across the wake region from the simulation (——) and experiments (•).

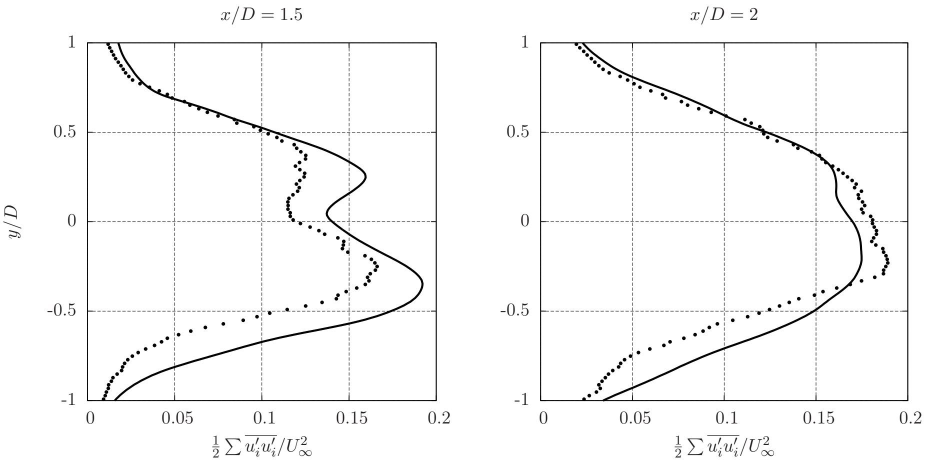

(a) $\alpha_D = 0°$

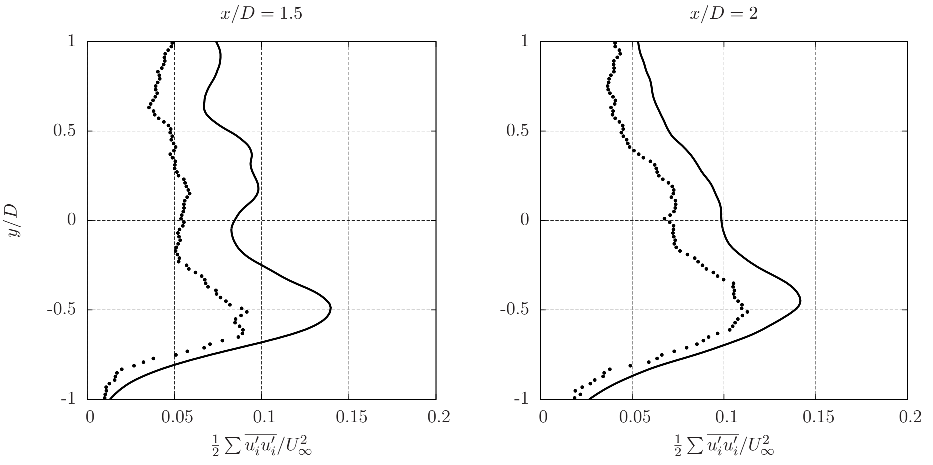

(b) $\alpha_D = 5°$

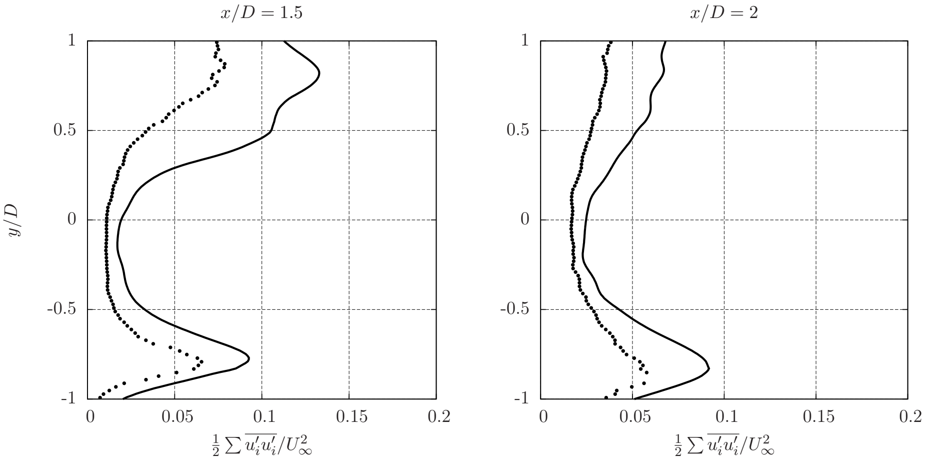

(c) $\alpha_D = 10.7°$

Figure 6.8: The 2-D TKE profiles across the wake region from the simulation (——) and experiments (•).

It is assumed that the validity of the velocity field in the wake region of the model implies the validity of the numerical predictions along upstream positions. Therefore, the simulation data can be applied to compute far-field noise predictions using a FW-H solver. This extension provides an insight to the effects of the aerodynamic interactions on the far-field noise.

6.3 Aerodynamic effects of the interaction

The distributions of the mean and the variance, of the surface pressures, are presented to illustrate the changes in the flow around the cylinder and door components due to the aerodynamic interactions, at various door angles.

Figure 6.11 shows the differences in the mean surface pressure distribution along the cylinder, at various interaction configurations, compared to a isolated cylinder flow. A cylinder under no interaction effects generates a symmetric pressure distribution. The aerodynamic interaction due to a leg-door at $\alpha_D = 0°$ induces two changes. Firstly, the stagnation point shifts towards the door side of the cylinder. This shift, together with the reduced symmetry of the model, results in the asymmetry of the pressure profile about $\theta = 180°$. The location of the suction peaks also shifts, due to similar effects that cause the stagnation point to move. However, the magnitude of the minimum pressure remains unchanged. As the door angle is increased, the stagnation position moves further away from $\theta = 180°$, and it shifts to $\theta = 160°$ when the door angle is $\alpha_D = 10.7°$.

Figure 6.12 shows the changes Sound Pressure Level (SPL) distribution along the cylinder element, from the interaction cases across various door angles. For an isolated cylinder flow, the surface SPL levels peak towards 90 and 270 degrees, and a minimum SPL is located near the stagnation region. The levels at the stagnation region are not zero, due the shifts in the stagnation point throughout the vortex shedding cycle. Finally, the portion of the profile associated with the wake behind the cylinder, contains a uniform and high SPL at approximately 85 dB.

The SPL distribution along a cylinder is increased by the addition of a leg-door at $\alpha_D = 0°$. The differences in the peak values of SPL, between an isolated cylinder, and an interacion model at $\alpha_D = 0°$, is 11 dB. The difference in the minimum value of SPL is much larger. This increase suggests that the shifts in the stagnation point throughout the vortex shedding cycle, become larger. As the door angle is increased from 0 to 5 degrees, there is a significant reduction in the SPL. The differences in the peak SPL between an isolated cylinder and an interaction model with $\alpha_D = 5°$, are within 3 dB. However, as the door angle is increased further to $\alpha_D = 10.7°$, the surface SPL increases to larger values.

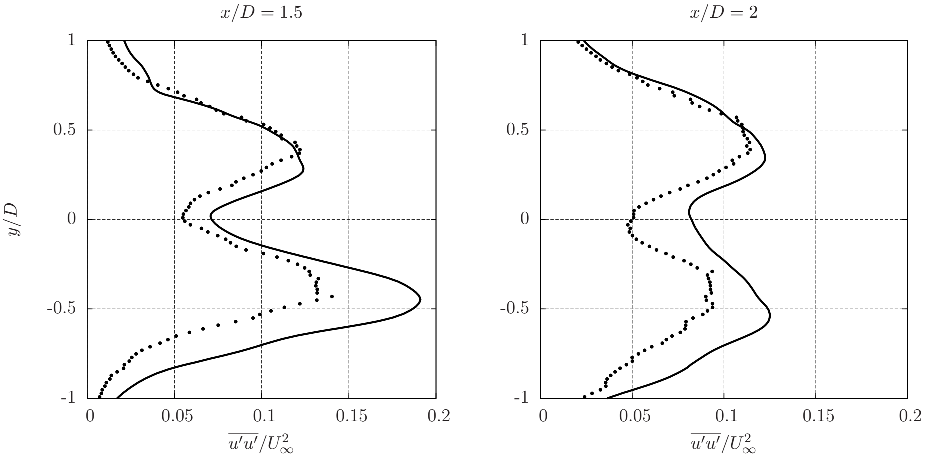

(a) $\alpha_D = 0°$

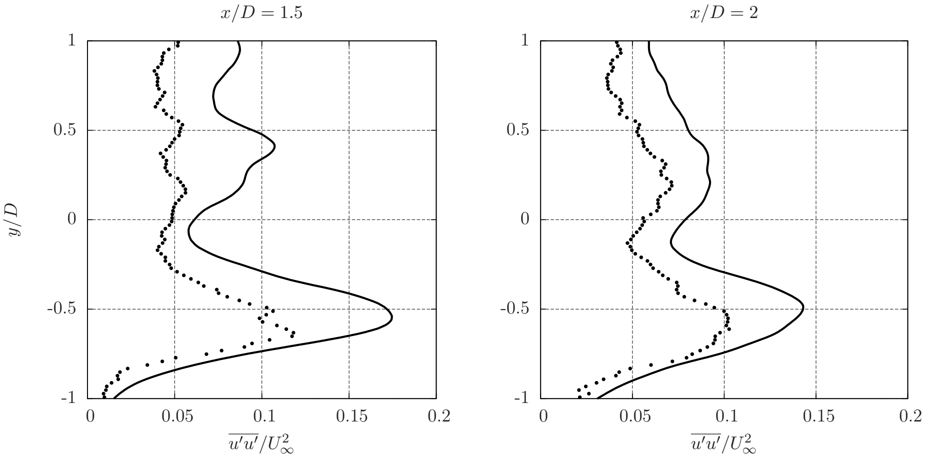

(b) $\alpha_D = 5°$

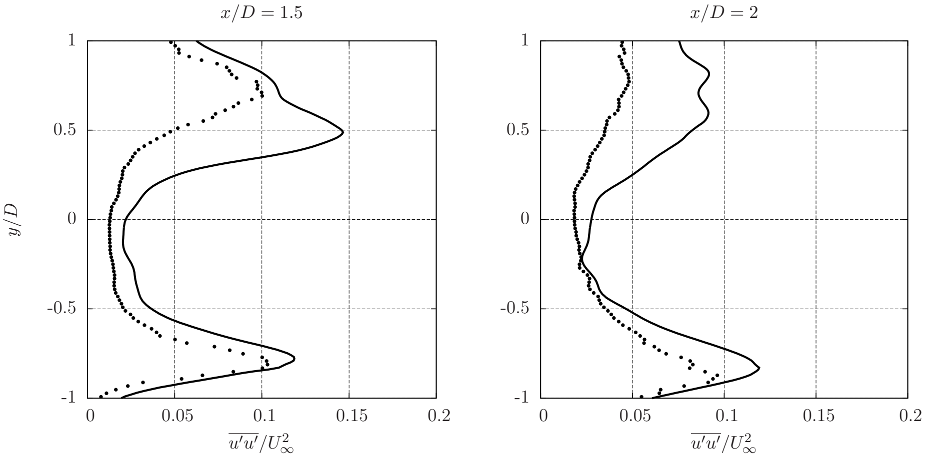

(c) $\alpha_D = 10.7°$

Figure 6.9: Comparison of the stream-wise velocity fluctuation profiles across the wake region between simulation (——) and experiments (•).

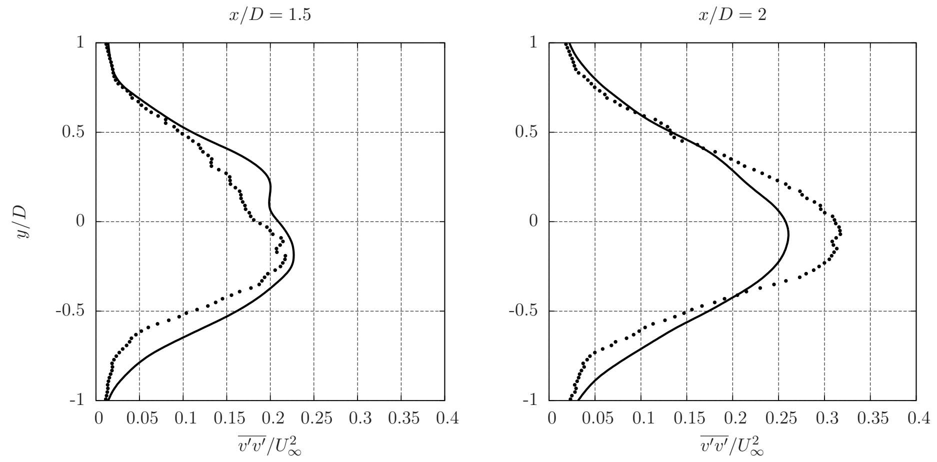

(a) $\alpha_D = 0°$

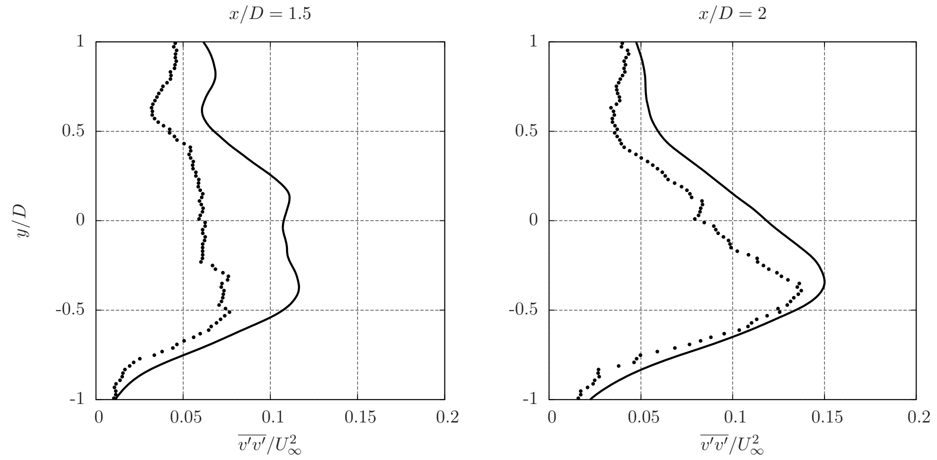

(b) $\alpha_D = 5°$

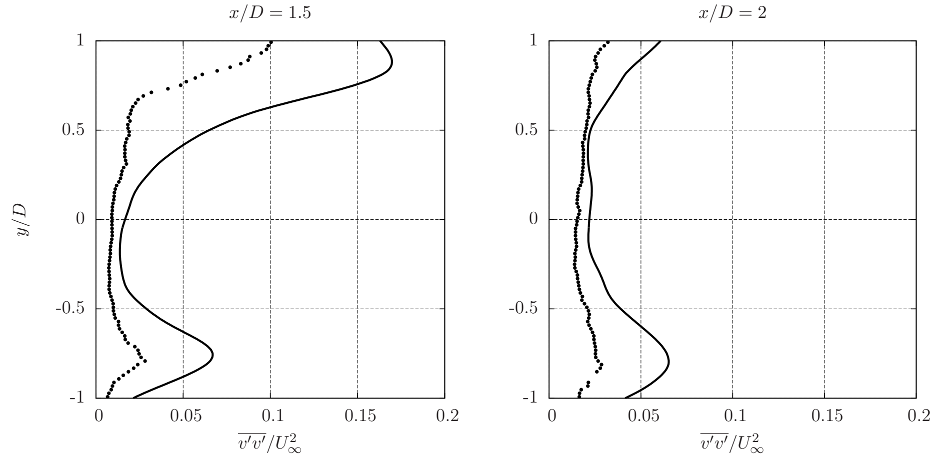

(c) $\alpha_D = 10.7°$

Figure 6.10: Comparison of the transverse velocity fluctuation profiles across the wake region between simulation (——) and experiments (•).

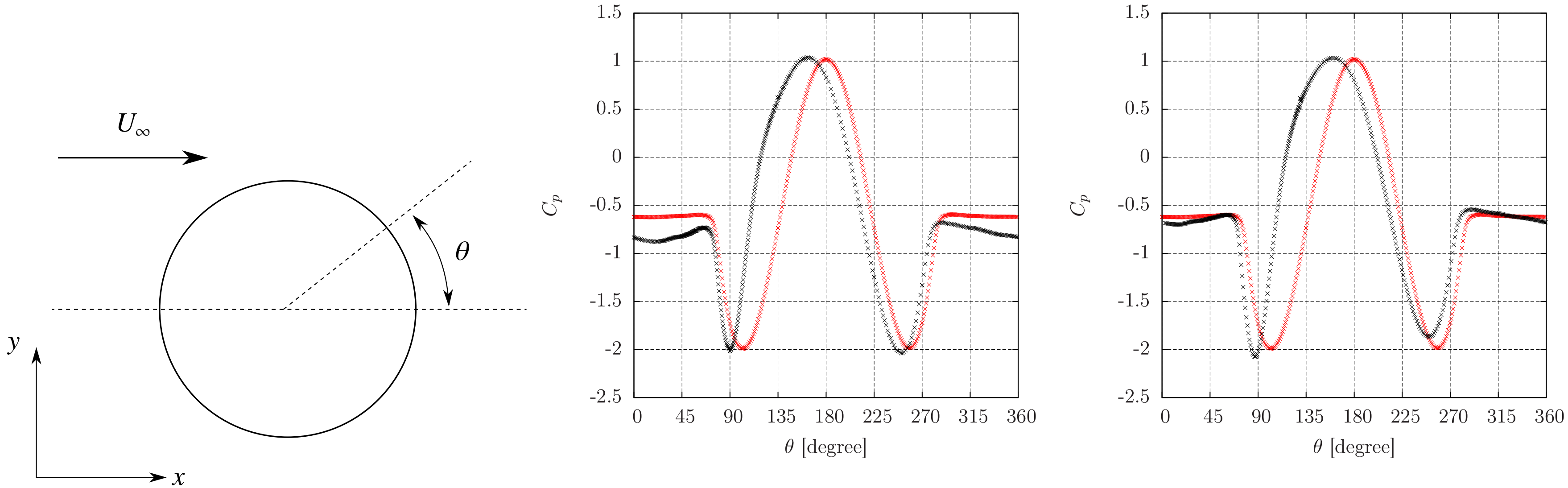

(a) Orientation

(b) $\alpha_D = 0°$

(c) $\alpha_D = 2.5°$

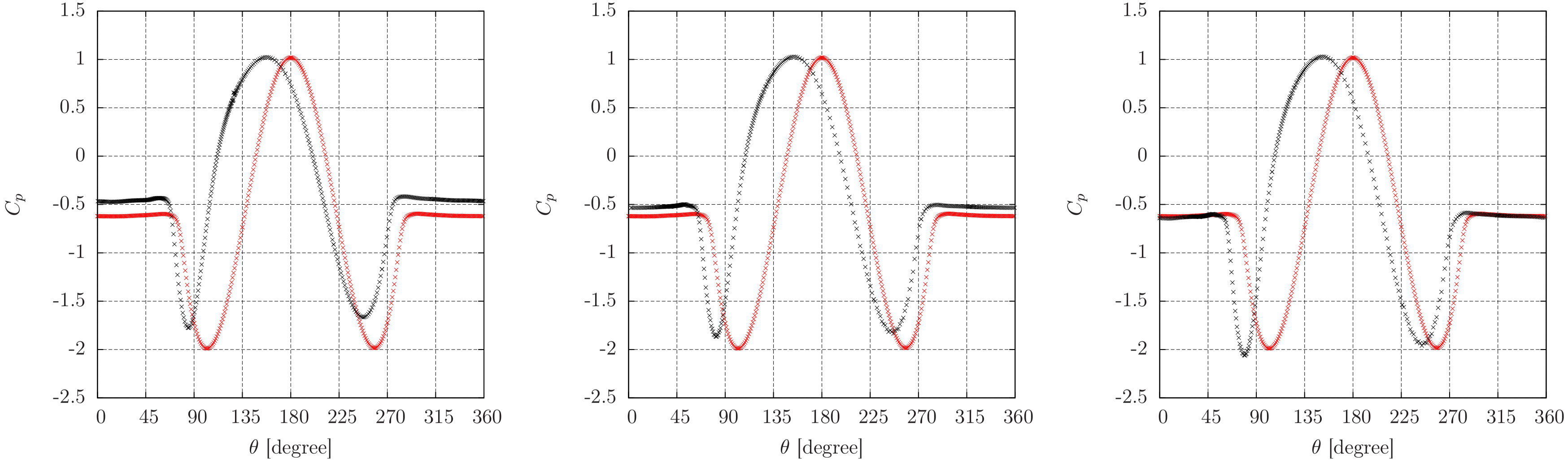

(d) $\alpha_D = 5°$

(e) $\alpha_D = 7.5°$

(f) $\alpha_D = 10.7°$

Figure 6.11: The distribution of mean pressure along the cylinder surface, from an interaction model with varying door angle. Data from the interaction case (black cross), and the isolated cylinder simulation (red cross).

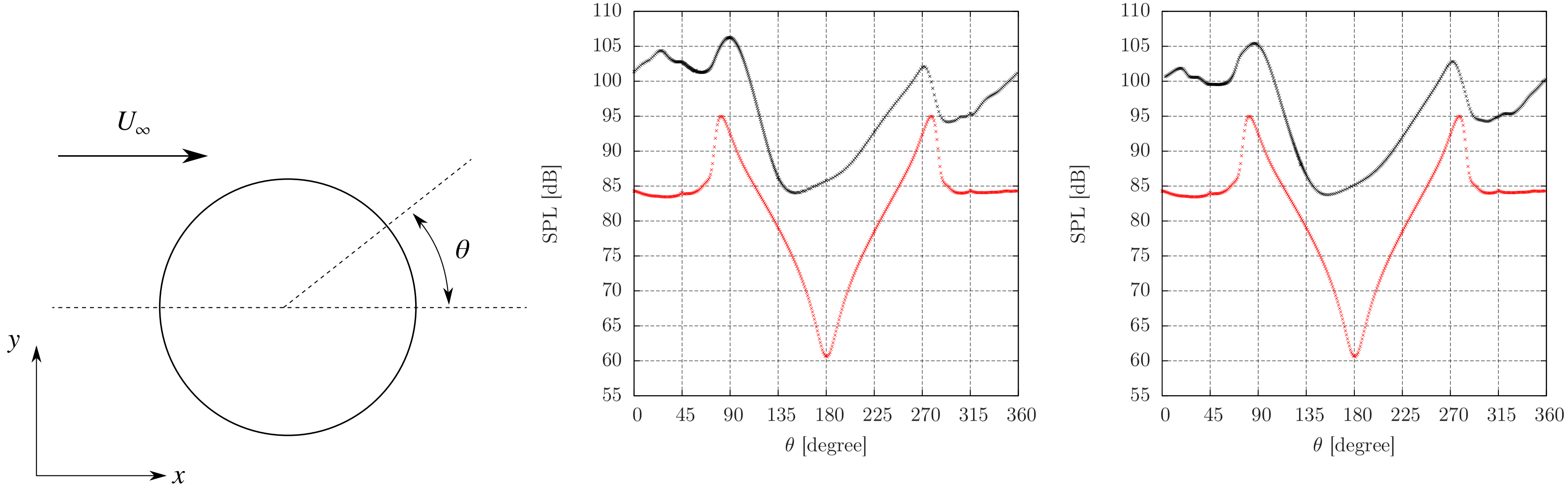

(a) Orientation (b) $\alpha_D = 0°$ (c) $\alpha_D = 2.5°$

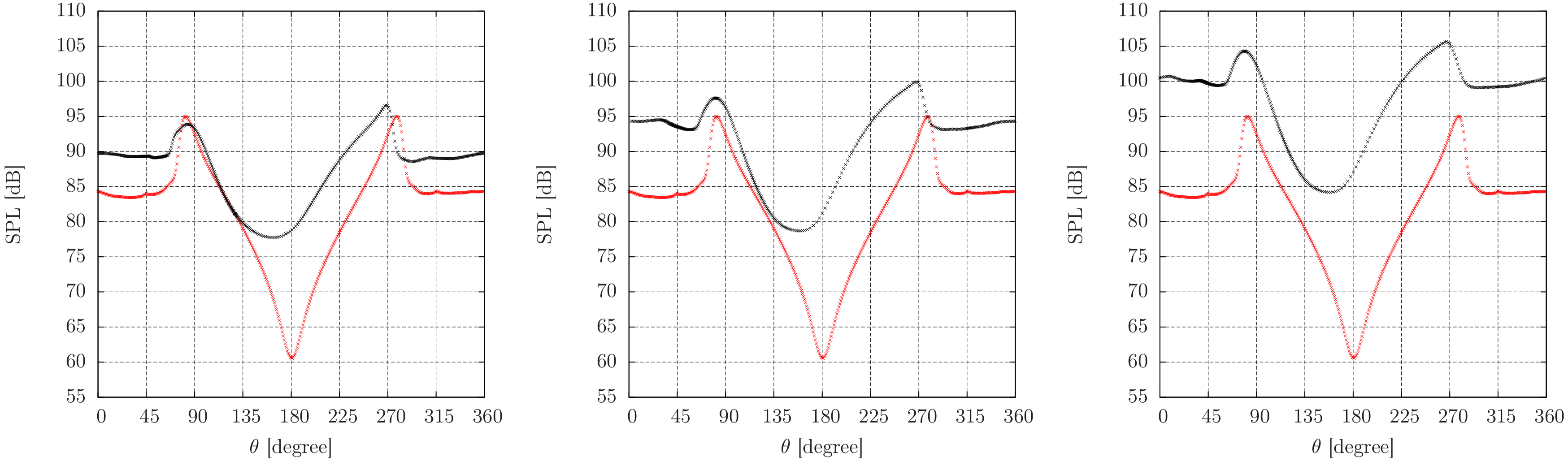

(d) $\alpha_D = 5°$ (e) $\alpha_D = 7.5°$ (f) $\alpha_D = 10.7°$

Figure 6.12: The distribution of SPL along the cylinder surface, from an interaction model with varying door angle. Data from the interaction case (black cross), and the isolated cylinder simulation (red cross).

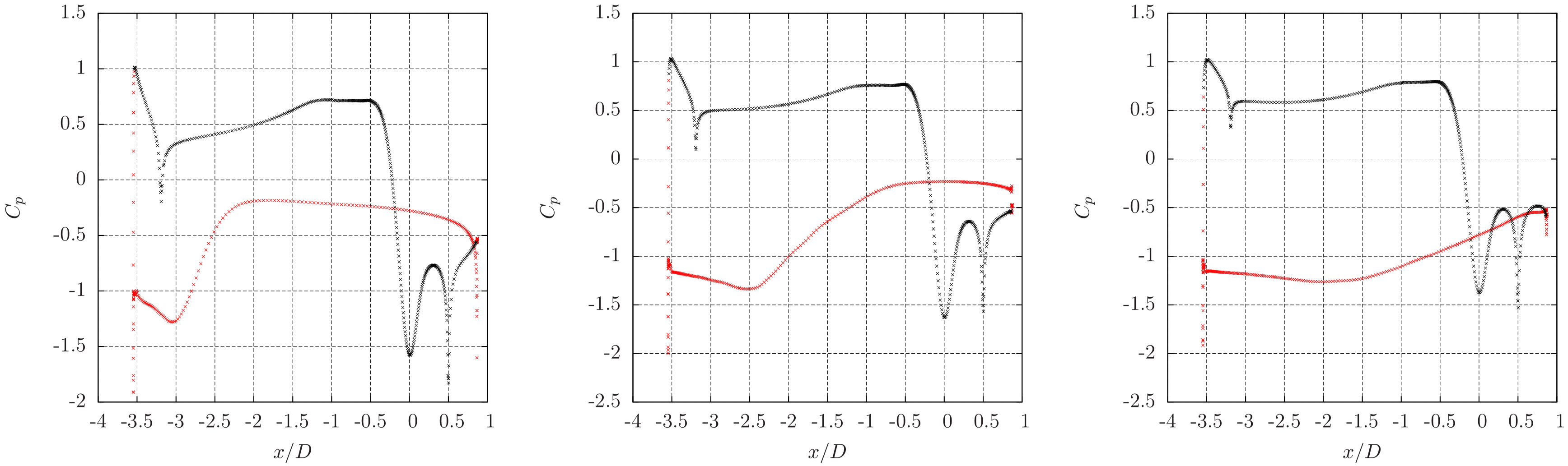

(a) $\alpha_D = 0°$ (b) $\alpha_D = 2.5°$ (c) $\alpha_D = 5°$

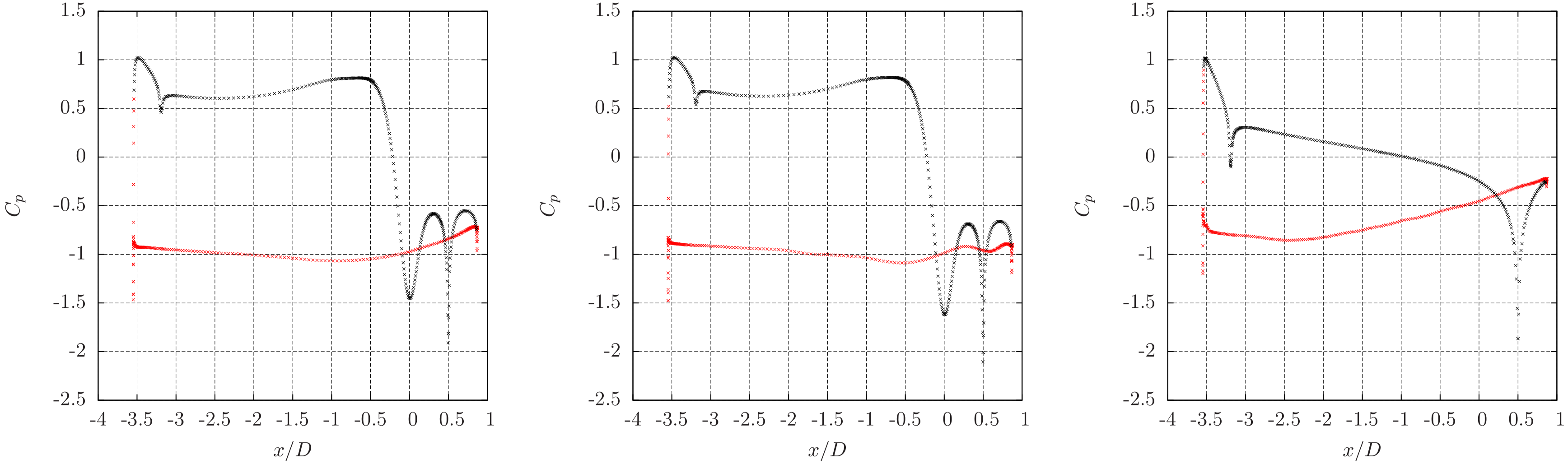

(d) $\alpha_D = 7.5°$ (e) $\alpha_D = 10.7°$ (f) Isolated door $\alpha_D = 10.7°$

Figure 6.13: The distribution of mean pressure along the leg-door surface, from an isolated, and interaction model with varying door angle. Data along the upper surface (red) and along the lower surface (black).

The changes in the aerodynamic behaviour around the door element, due to the interaction with a cylinder, and due the changes in the door angle, are explained with the aid of Figures 6.13 and 6.14. These figures illustrate the mean surface pressures, and SPL, recorded along the door. These plots illustrate the distribution along a stream-wise coordinate, x/D that represents the chord-wise position. The origin of this axis is set to be at the centre of the cylinder.

Case (f) in Figure 6.13 illustrates the pressure distribution for an isolated door at an angle of $\alpha_D = 10.7$ degrees. The stagnation position is located along the lower surface of the door towards the leading edge. The pressure distribution along the lower surface of the door contains two regions of sharp changes in the pressure gradient. These regions coincide with the location of the leading and trailing edge bevels, which are located at a stream-wise position of $x/D \approx -3.25$, and $x/D \approx 0.5$, respectively. At these locations, the geometry of the door turns away from the mean flow, and thereby induces an adverse pressure gradient. Towards the trailing edge bevel, there is a region of favourable pressure gradient that may be due to the low pressure region formed along the upper surface of the door. This feature draws the fluid from the lower surface and accelerates it towards the low pressure region. Along the upper surface of an isolated door, a continuous low pressure region is present with a low pressure gradient. Due to the high inclination angle, the upper surface flow is fully detached. Regions of largely separated flows generate a uniform and low pressure, similar to the wake region of a cylinder or a stalled aerofoil. Finally, towards the leading edge there is a sharp acceleration of the flow. This is caused by the stagnation point positioned along the lower surface, which forces the bifurcated flow to be displaced around the top side of the leading edge corner.

By comparing case (e) to case (f) in Figure 6.13, the changes in the mean pressure distribution along an isolated door at $\alpha_D = 10.7°$ by the aerodynamic interaction with a cylinder, can be summarised. It should be noted that the cylinder centre is positioned at $x/D = 0$, where D is the cylinder diameter. The cylinder interaction induces noticeable differences to the pressure distribution in the immediate vicinity of the door, along the lower surface. In this region, there are the following key effects are present:

- The stagnation of fluid on the cylinder generates a high pressure region. This induces an region of adverse pressure gradient along the lower surface of the door, and can be seen in case (e) of Figure 6.13 along $-2 < x/D < -0.75$. At higher door angles, the impact of the stagnation point along the cylinder is lower, as more of the free-stream flow impinges along the lower surface. However, at lower door angles, this adverse pressure gradient causes a separation of the boundary layer along the door.
- The gap region between the cylinder and the door forms a region of accelerated flow. Upstream of this gap, there is a region of favourable pressure gradient, as the

cylinder and door elements converge closer to the minimum gap distance. Downstream of this position, there is an adverse pressure gradient where the surfaces diverge away from each other.

- The effective AoA of the door element is increased. This is due to the blockage formed by the presence of the cylinder along the lower surface, which increases the net circulation around the entire model. This results in a more detached flow along the upper surface of the door, and this stalled region is illustrated in the pressure profile by the almost flat pressure profile.

Finally, the effect of varying the door angle on the mean pressure distribution along the door surface is shown by cases (a) - (e) in Figure 6.13. The key features can be summarised as follows:

- The distribution along the lower surface remains very similar. The adverse pressure gradient formed along the lower surface due to the stagnation of fluid on the cylinder is observed for all door angles. The adverse pressure gradient downstream of the cylinder centre is also consistent at all angles. The double dip profile in the pressure distribution on the lower surface towards the trailing edge, is due to the gap region jet flow being drawn towards the low pressure region along the upper surface of the door. This deflection is reduced at lower door angles. Therefore, this double dip feature is only observed for door angles of $\alpha_D > 5^\circ$.
- At all door angles, the stagnation point along the door surface is located along the lower surface. This induces a significant acceleration of the fluid since part of the bifurcated flow is displaced around the leading edge corner of the door. This causes the sharp reduction in the pressure coefficient, and forces the boundary layer to separate along the upper surface towards the leading edge. At low door angles, there is a reattachment of the flow, and this is clear due to the continual changes in the pressure profile in the chord-wise direction. As the door angle increases the pressure profile along the upper surface becomes invariant, which signifies a fully detached flow.

The distribution of the SPL along the door surface is given by Figure 6.14 for the interaction cases across various door angles, and additionally for the isolated door configuration. The isolated door at $\alpha_D = 10.7$ degrees consists of a largely separated flow along the upper surface. This induces the high SPL of 96 dB across the upper surface. It also peaks at a level of 98 dB towards the trailing edge. The minimum SPL is located near the stagnation point.

By comparing cases (e) to (f) in Figure 6.14, the effects of cylinder interaction is shown on a door at $\alpha_D = 10.7$ degrees. The SPL increases towards the door trailing edge by

10 dB, up to a peak SPL of 107 dB. This increase is associated with the TKE generated by the cylinder element, which occurs near the trailing edge and is associated with the enhanced upwards deflection of the gap flow. The latter deflection occurs as the fluid is drawn towards the low pressure region, which is generated along the upper surface of the door. At high door angles, this upwards deflection effect also generates a trailing edge recirculation bubble. This may also contribute to the high SPL observed towards the door trailing edge. Peaks in the SPL levels are formed along the lower surface of the door, near the cylinder region, at $x/D = 0$ and $x/D = 0.5$. These peaks corresponds to the detached shear layer along the cylinder surface, and its interaction with the trailing edge bevel. The remaining cases (a) - (d) in Figure 6.14 illustrate the effect of varying the door angle on the surface distribution of the SPL. The key effects can be summarised as follows:

- At low door angles ($\alpha_D < 5°$), the spatial variation of the surface SPL along the upper surface is greater. At $\alpha_D = 0°$, the leading edge separation bubble induces the broad peak in the SPL. The SPL along the upper surface decreases, downstream of the separation bubble and peaks in a secondary feature that is located towards the trailing edge of the door. This secondary feature is likely due to the interaction of the detached vortices from the cylinder interacting with the trailing edge of the door.

- As the door angle is increased from 0 degrees to 2.5, and 5 degrees, the average SPL along the upper surface increases. The aforementioned broad peak in SPL caused by the leading edge recirculation bubble, shifts further downstream as the door angle is increased. At larger door angles, the size of the recirculation bubble also increases.

- As the door angle is increased further from 5 degrees to 7.5 and 10.7 degrees, the peak SPL forms near the trailing edge on the upper surface of the door. Along the entire chord of the door surface, a larger SPL is present. The uniformity of the SPL distribution along the upper surface at high door angles, signifies the presence of a fully detached flow.

- At all door angles, there are two peaks in the SPL distribution that are due to the cylinder interaction. The first is an increased SPL towards $x/D = 0$, which is associated with the the shear layer of the cylinder along the gap region influencing the door surface. The secondary peak is located further downstream at $x/D = 0.5$, which is associated with the interaction of the cylinder wake interacting with the trailing edge bevel.

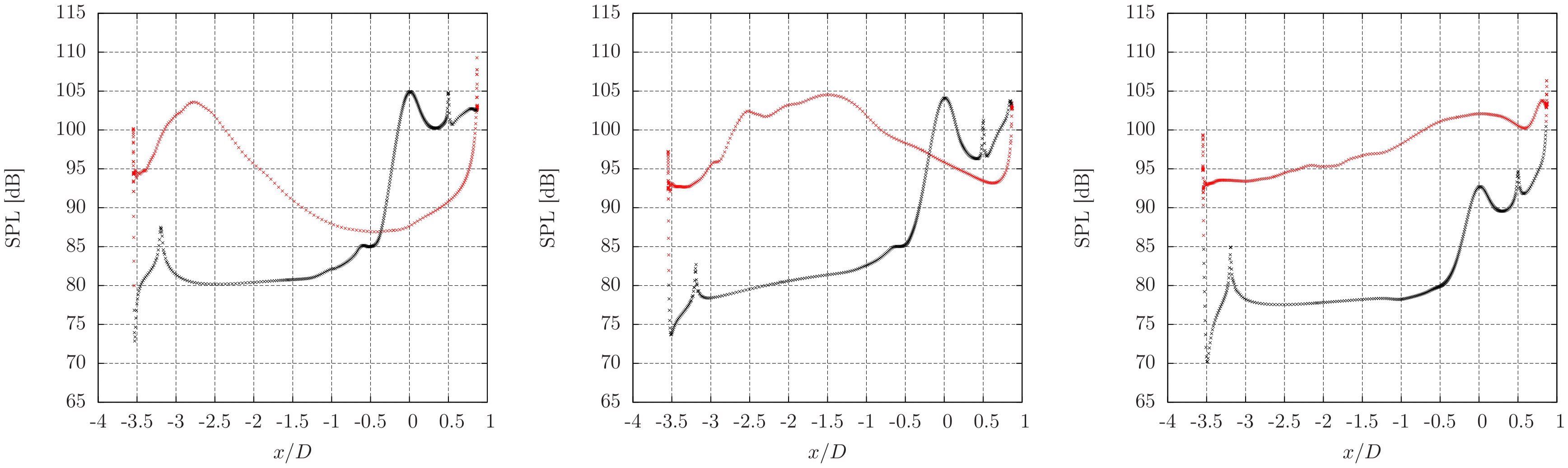

(a) $\alpha_D = 0°$

(b) $\alpha_D = 2.5°$

(c) $\alpha_D = 5°$

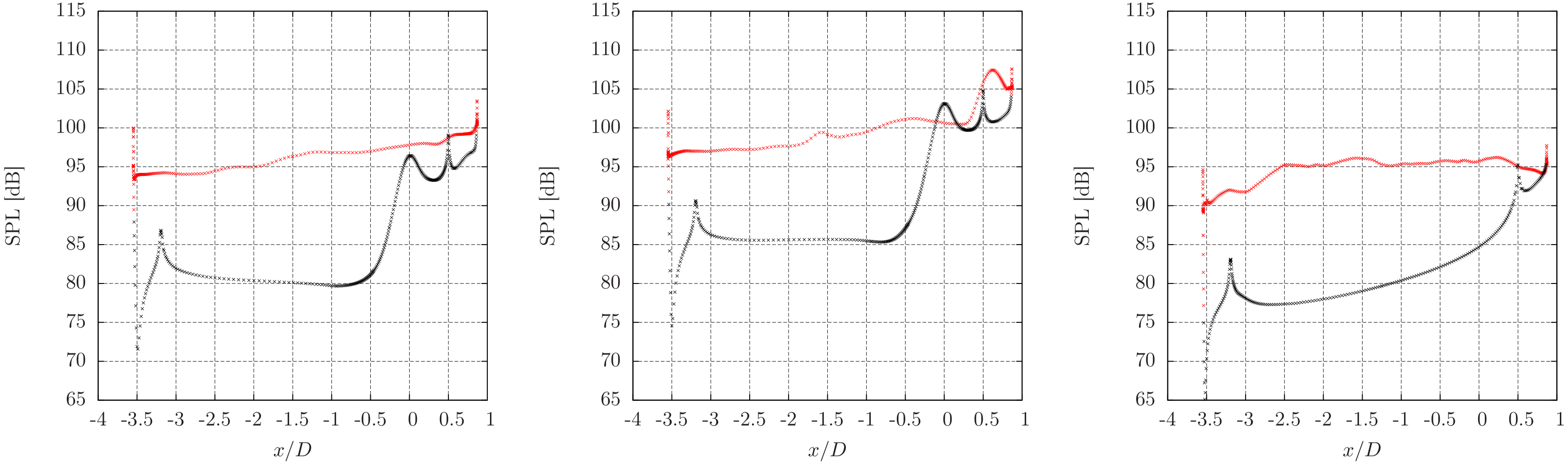

(d) $\alpha_D = 7.5°$

(e) $\alpha_D = 10.7°$

(f) Isolated door $\alpha_D = 10.7°$

Figure 6.14: Effect of door angle on the door surface distribution of the variance of pressure. Data along the upper surface (red) and along the lower surface (black).

6.4 Far-field noise calculations

The far-field acoustic signals were calculated for 360 observers placed at a radial distance of 120 m from the cylinder centre, and distributed around the source region by an azimuthal separation of one degree. The distant placement of the observer ensures that far-field signals are acquired. The placement of the integration regions is outlined first, and followed by the results.

The FW-H sources are defined from the recorded CFD data. The CFD data was recorded at various sample frequencies, for the various cases, in the range of $13600 < f < 33000$ Hz. In the rod-plate experimental study by Hutcheson and Brooks [8] the far-field microphone data shows that the major effects of the interaction occur in the range of $St < 0.4$. This limit is equivalent to a $f < 70$ Hz for the current simulations, and therefore the applied sampling rates are within a reasonable range. The high sampling frequency was applied to resolve any potential higher frequency sources, such as trailing edge noise. Examples of the far-field acoustic signals computed from the FW-H solver are shown in Figure 6.15. The typical signal length of the predicted far-field sound is of at least 0.3 seconds.

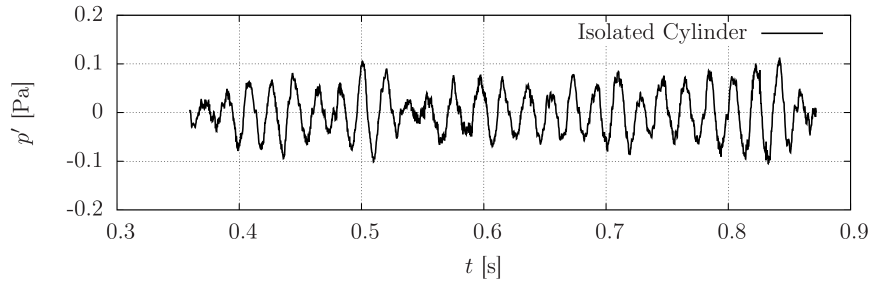

(a) Isolated cylinder

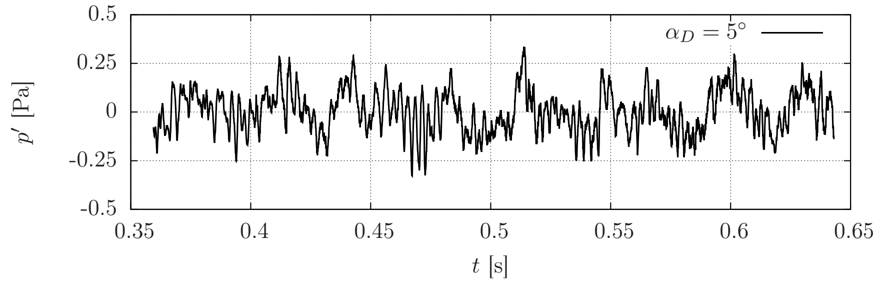

(b) Interaction case with $\alpha_D = 5°$

Figure 6.15: Far-field acoustic signal prediction at an observer angle of $\theta = 90°$.

6.4.1 FW-H surface placement

For each configuration, three off-body permeable FW-H surfaces were defined. Separate integration surfaces were additionally specified along the wall areas. The effect of the placement of off-body FW-H surfaces has been previously investigated [40, 43]. Based on the literature the following two guidelines are applied for the off-body FW-H surface placements. Firstly, the off-body FW-H surfaces should enclose the source region, and the surface should not intersect with the path of strong vortices. Secondly, a close placement of the surface to the source region is desirable to ensure that numerical discretisation errors affecting the acoustic propagation have a smaller effect.

To ensure a minimal influence of strong vortices passing through the integration surfaces, the lambda vector $\lambda = \vec{\omega} \times \vec{u}$ was computed from the mean flow solution. Figure 6.16 illustrates the placement of the off-body integration surfaces over a contour plot highlighting the areas that contain high levels in the magnitude of the lambda vector. The lambda vector $(\vec{\lambda})$ is defined as the cross product between the vorticity vector and the velocity vectors, and it is a key source term in Powell's acoustic analogy [20]. The off-body FW-H surfaces were chosen to enclose all relevant source regions, which are defined by $|\lambda| > 0.2$. Three off-body surface patches were defined for each simulation. These patches were combined to form two off-body integration surfaces that enclose the source region. The first combination is composed of the upstream zone (US) and the first of two downstream zones (DS1). The second combination applies an different downstream zone (DS2) that is placed further away from the source reigon, where weaker vortices are likely. Finally, on-body FW-H zones were composed of the wall zones covering the door (WZD) and cylinder (WZC).

6.4.2 Noise radiation from the isolated models

The far-field noise directivity patterns are illustrated in Figure 6.17, for an isolated cylinder and an isolated door at $\alpha_D = 10.7$ degrees. Three directivity patterns are given, from two off-body and one on-body surface calculation. The noise predictions from the solid FW-H surface data provide the most reliable data for the following reasons. Firstly, the scaling laws from the dimensional analysis of acoustic source terms suggests that quadrupole sources should be negligible at low Mach numbers. The differences in the SPL are up to 10 dB, which suggests that either the quadrupole sources are significant sources of noise, or that the off-body FW-H surfaces may be contaminated by strong and non-acoustic vortical modes.

The noise spectra of the far-field acoustic signals at observer angles of 90 and 270 degrees are shown in Figure 6.18 for an isolated cylinder and an isolated door at 10.7 degrees. As observed in the literature, an isolated cylinder flow at supercritical Re generates a dipole sound directivity. A tonal peak in the spectra occurs around $St = 0.3$, which verifies the delay in the separation along the cylinder surface, due to the turbulent state of the boundary layer. Convective amplification effects are also observed in the results, as the SPL is higher in the upstream positions.

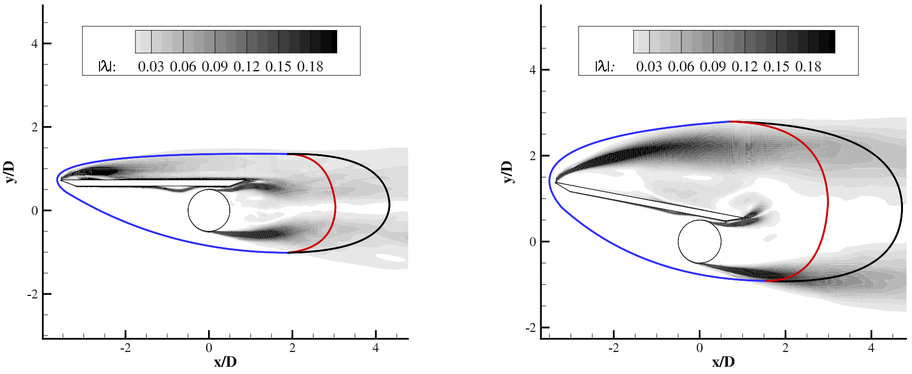

(a) Interaction case $\alpha_D = 0°$

(b) Interaction case $\alpha_D = 10.7°$

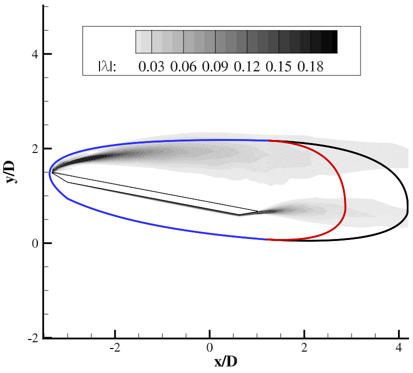

(c) Isolated door at $\alpha_D = 10.7°$

Figure 6.16: Integration surfaces for the FW-H calculations overset by contours of $|\lambda| = |\vec{\omega} \times \vec{u}|$. The surface zone names are US (blue), DS1 (red), DS2 (black), WZC (cylinder), and WZD (door) surface.

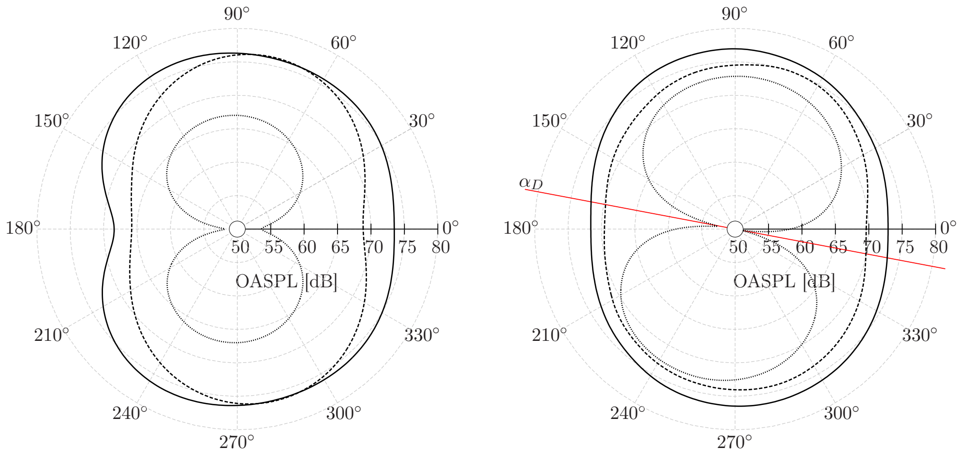

(a) Isolated cylinder

(b) Isolated door at $\alpha_D = 10.7°$

Figure 6.17: Far-field sound directivity plots from three FW-H calculations. Wall zone only (⋯⋯), US and DS1 zones (——), US and DS2 zones (- - -).

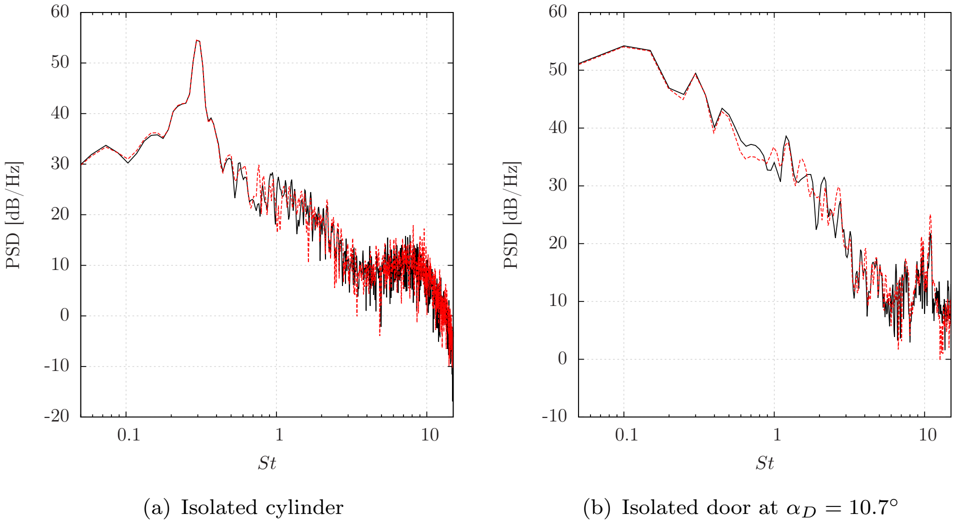

(a) Isolated cylinder (b) Isolated door at $\alpha_D = 10.7°$

Figure 6.18: Far-field noise spectra at observer angles of $\theta = 90°$ (——), and at $\theta = 270°$ (——).

The noise spectra from an isolated door is significantly louder than an isolated cylinder, by approximately 8 dB at an observer angle of 90 degrees. The dipole behaviour of the isolated door is symmetric about an angle of 10.7 degrees, which is due to the circulation induced by the inclination of the model that forces a downwash on the vortex shedding. The noise spectra of the far-field signal is mostly in the lower frequency range. Therefore, the dominant noise source is likely to be acoustically compact. The noise spectra at observers positioned at 90 and 270 degrees contain a dominant peak at a low Strouhal number of $St \approx 0.1$. However, there are two further peaks at $St = 0.3$, and $St = 1.1$. The sources of these peaks are identified by the surface source maps, which are discussed later in Section 6.4.4.

6.4.3 Noise radiation from interaction cases

Figure 6.19 illustrates the SPL directivity from interaction cases with various door angles, predicted by two off-body, and one on-body, FW-H surfaces. The on-body FW-H surface is composed of the two wall zones (WZD and WZC), and the two off-body permeable surfaces are composed of the upstream zone (US), and either one of the downstream zones (DS1 or DS2).

The SPL directivity predicted by the off-body surfaces are consistently larger, by differences exceeding 5 dB at an observer position of 90 degrees, for various α_D. This over-prediction is likely due to the convection of strong vortices across the integration surfaces. However, the differences between the off-body and on-body SPL levels are significantly less compared to the isolated model configurations. For the remainder of the following discussions, the acoustic data derived from only the on-body FW-H surfaces will be considered.

Figure 6.20 shows the changes in the SPL directivity patterns due to variations in the door angle. As the door angle is increased from 0 to 2.5 degrees, there is a reduction in the SPL by approximately 5 dB. Further increases of the door angle induce smaller changes in the SPL across all observer angles. The directivity profiles from each interaction case have a dipole pattern, and the angle of the dipole seems to be independent of the door angle.

The baseline spectra showed that most of the energy is contained towards the lower frequency range $St < 0.3$. The dimensions of the elements that compose the interaction model are much smaller than the acoustic wavelength associated to $St = 0.3$. Therefore, a compact source is likely. Additionally, Hutcheson and Brookes [8] suggested that a compact dipole characterises the noise generated by a cylinder and door in a side by side configuration. Since the majority of the noise sources in this model are compact, the acoustic scattering off the door surface is insignificant. Therefore, the shielding effects of the leg-door are not observed.

The noise spectra for observers at 90 and 270 degrees are given in Figure 6.21, for the interaction cases with a door angled at 0 and 10.7 degrees. These spectra contain two tonal features. The first peak at a Strouhal number of $St \approx 0.2$ is associated with the vortex shedding mode of the model. This is the dominant noise source at door angles lower than $\alpha_D < 5°$. The higher peak at $St \approx 1$ is likely due to the aerodynamic interactions, between the vortices from the cylinder shedding, and the trailing edge bevel of the door. These findings require further supporting evidence, which will be provided by the contour maps of surface pressure spectra.

6.4.4 Noise source maps

The noise source maps illustrate the SPL of the surface pressure for each panel of the FW-H surface, at various discrete frequencies. The time history of the surface pressure is applied to a Fast Fourier Transform (FFT). The spectra for each panel aligned in the span-wise direction are averaged to smooth the final result. This averaging assumes that the spectra is invariant to the span-wise position. Since the major noise sources are compact dipoles, the surface pressure fluctuations should be strongly correlated to the far-field sound. Therefore, this method can be used to identify the location of the major sources.

The noise maps illustrated in Figures 6.22, 6.23, and 6.24 correspond to the surface SPL at discrete frequencies along the cylinder surface, and to the upper and lower surfaces of the door, respectively. The general descriptions of the noise source maps have been

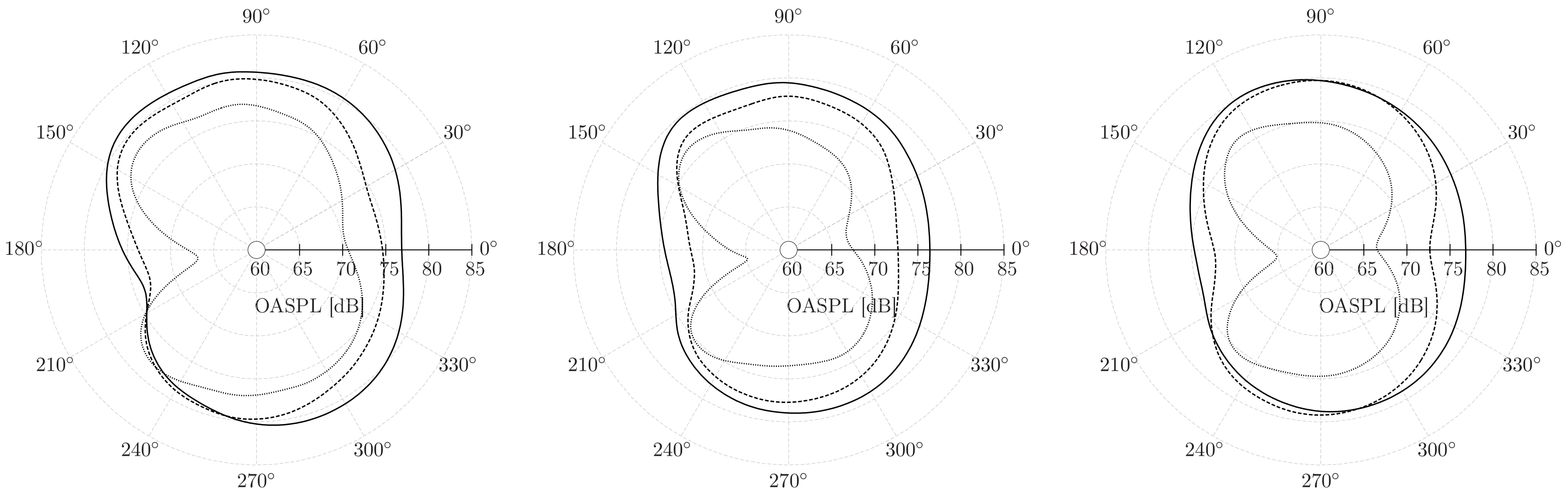

(a) $\alpha_D = 0°$ (b) $\alpha_D = 2.5°$ (c) $\alpha_D = 5°$

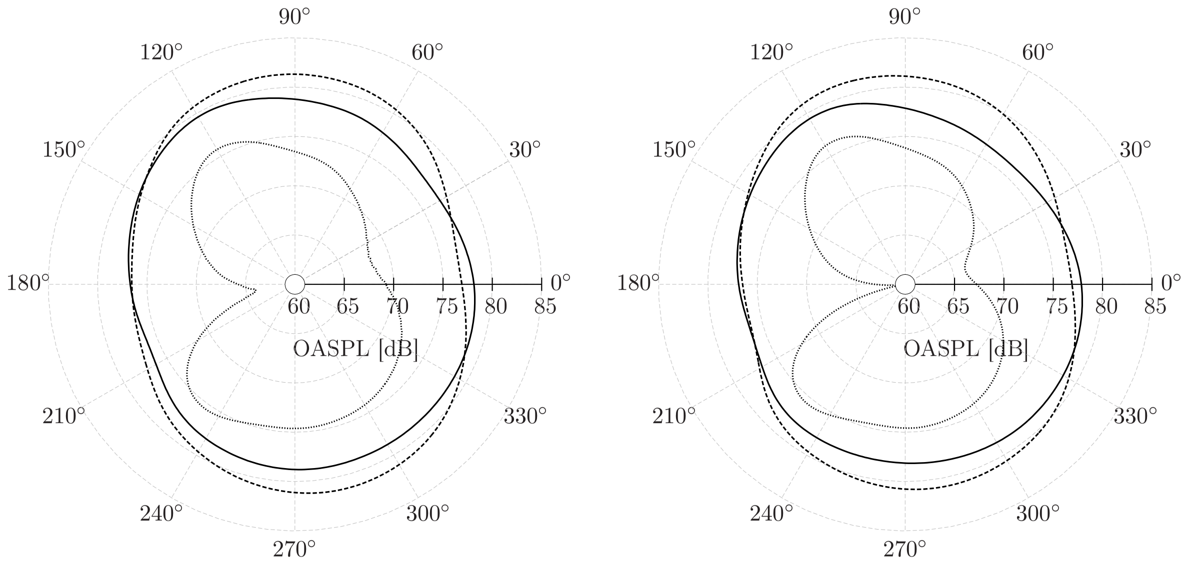

(d) $\alpha_D = 7.5°$ (e) $\alpha_D = 10.7°$

Figure 6.19: Far-field sound directivity plots for the interaction cases as predicted from three FW-H calculations. Wall zone only (⋯⋯), US and DS1 zones (——), US and DS2 zones (- - -).

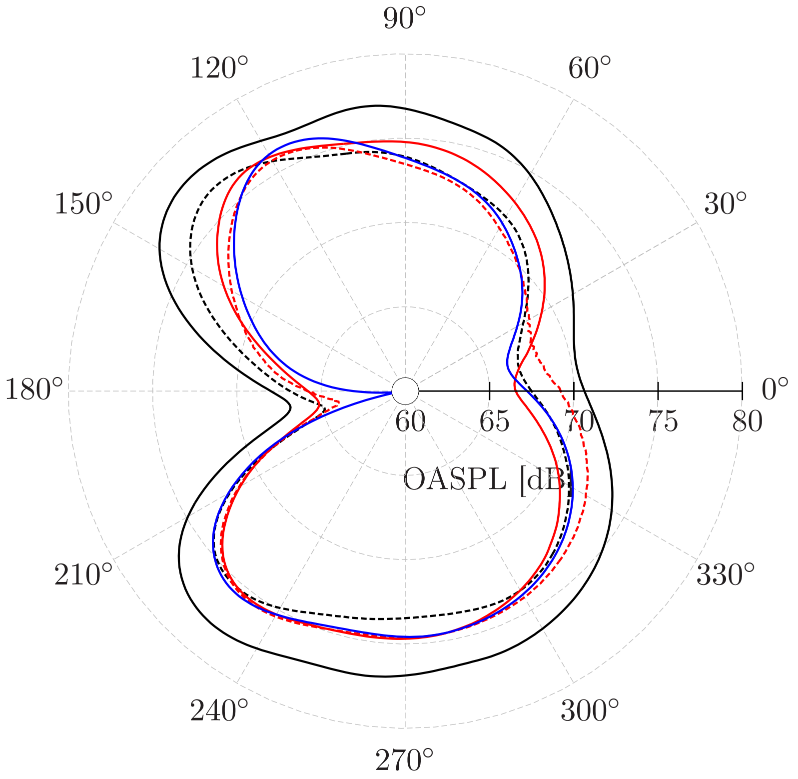

Figure 6.20: Far-field OASPL directivity computed from the on-surface FW-H integration surface (WZC and WZD zones) for the interaction cases at door angles of $\alpha_D = 0°$ (——), $\alpha_D = 2.5°$ (- - -), $\alpha_D = 5°$ (——), $\alpha_D = 7.5°$ (- - -), and $\alpha_D = 10.7°$ (——).

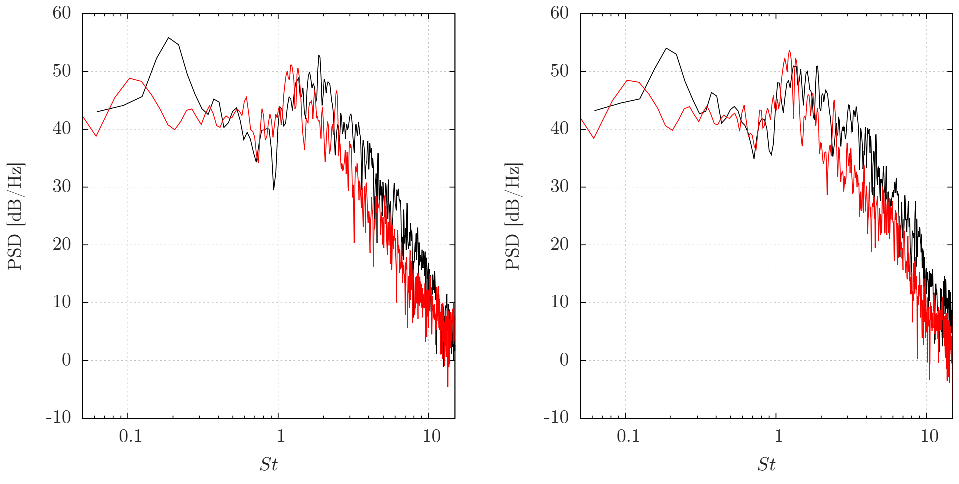

(a) $\theta = 90°$

(b) $\theta = 270°$

Figure 6.21: Far-field noise spectra computed from the on-body FW-H surfaces (WZC and WZD zones) for door angles of $\alpha_D = 0°$ (——), and $\alpha_D = 10.7°$ (——).

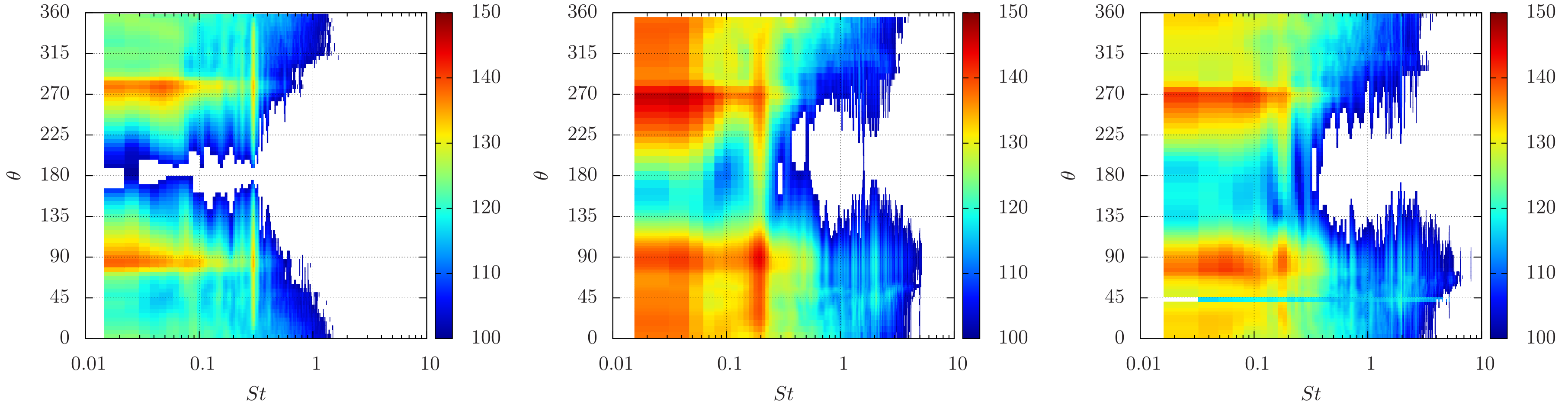

(a) Isolated cylinder

(b) $\alpha_D = 0°$

(c) $\alpha_D = 2.5°$

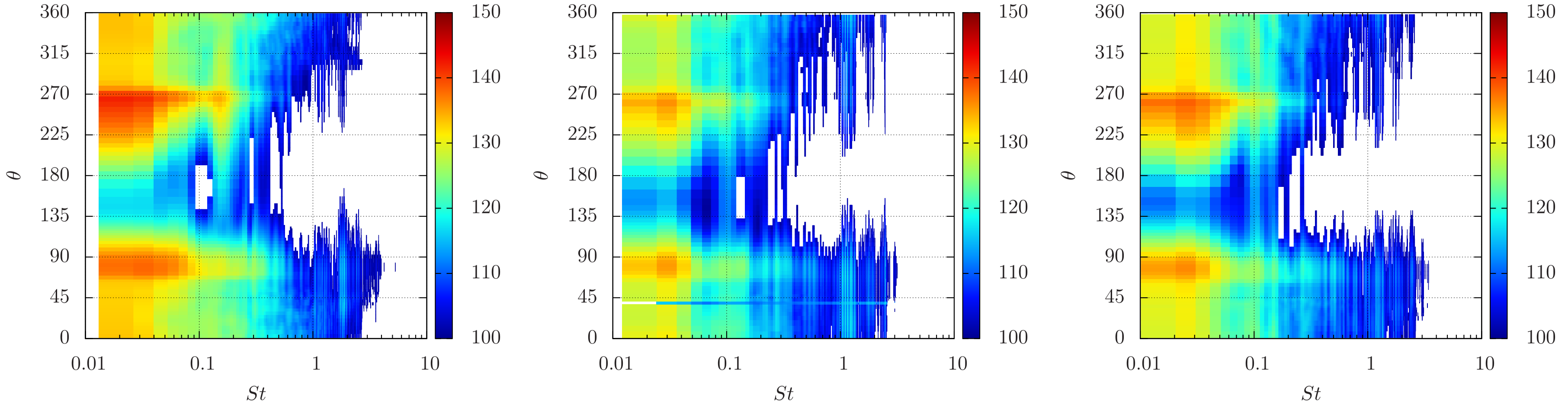

(d) $\alpha_D = 5°$

(e) $\alpha_D = 7.5°$

(f) $\alpha_D = 10.7°$

Figure 6.22: Cylinder surface SPL at varying Strouhal number and along varying azimuthal angles.

discussed in terms of the OASPL distributions, which were given by Figures 6.12, and 6.14. In this section, the source locations at specific frequencies will be discussed.

The cylinder source map, given by Figure 6.22, consists of concentrated regions of SPL at 90 and 270 degrees. At these azimuthal angles, the spectra peaks at $St = 0.3$ for an isolated cylinder. A similar peak at $St = 0.2$ occurs along the cylinder surface that is under an aerodynamic interaction with a door at 0 degrees. This shift of the spectral peaks to lower Strouhal numbers continues as the door angle is increased. Additionally, the intensity of this source also decreases with increasing door angle. This pattern is also observed in the far-field noise spectra in Figure 6.21. This St is likely associated with the vortex shedding mode of the cylinder, and the shift to lower levels indicates a reduced intensity of the cylinder vortex shedding.

The door source maps are given by Figures 6.23, and 6.24. An isolated door at 10.7 degrees AoA generates a large scale, low frequency, recirculation region along the upper surface, which generates a low frequency source at $St = 0.1$. This low frequency source is consistently observed along the upper surface of the door, and it is also present for the interaction case at door angles of $\alpha_D > 5°$. However, at lower door angles of $\alpha_D < 5°$, the source map pattern along the upper surface of the door changes. The chord-wise distribution of the source becomes focused to closed regions, which may signify the location of recirculation bubbles. As the door angle is reduced, the chord-wise position of maximum SPL shifts upstream towards the leading edge of the door.

Next, the noise map patterns derived for the lower surface of the door are discussed. By comparing cases (e) and (f) in Figure 6.24, two differences in the noise source maps are highlighted, as a result of the cylinder interaction on a door at $\alpha_D = 10.7°$. Firstly, the cylinder interaction induces two additional low frequency sources at $x/D = 0$ and $x/D = 0.5$. This is due to the vortex shedding behind the cylinder, and the unsteady features are echoed onto the door surface data due to the small gap distance. This source becomes more significant as the door angle is lowered. This suggests that the cylinder shedding becomes more intense at lower angles, and this behaviour correlates with the trends of the surface maps along the cylinder surface. Secondly, cases (e) and (f) show that an additional high frequency source at $St \approx 1$ is formed as a result of the cylinder interaction. This source is present across all interaction cases, at every door angle, and it is likely to be the source of the broadband and high frequency peak in the far-field noise spectra (Figure 6.21). This source is localised on the lower surface of the door, around the trailing edge bevel. The absence of this source for an isolated door suggests that this source is formed by the interactions between the vortex structures generated by the cylinder and the trailing edge bevel of the leg-door.

6.4.5 Summary

The primary noise source for the interaction model at low door angles is the vortex shedding behind the cylinder. The unsteady flow generated by the bluff body configuration predominantly consists of low frequencies, which result in a compact dipole. This reduces the impact of the door element as an effective acoustic shield, and the resulting far-field directivity is a fairly symmetric dipole. As the door angle is increased the vortex shedding intensity from the cylinder decreases, and the shedding mode shifts to lower frequencies. This results in an overall reduction of 2-5 dB in the far-field SPL, when the door angle is changed from 0 to 2.5 degrees. This reduction continues with increasing door angle until a secondary door-related source becomes significant. This limit occurs as the door angle approaches $\alpha_D = 5^\circ$. Therefore, further reductions in the overall SPL diminish with increasing door angle, as this limit is approached. A secondary limitation of the overall reduction in the SPL, at higher door angles, is due to the increased intensity of the angled door as a noise source. The scale of the detached flow along the upper surface of the door increases with higher angles, and consists of a low frequency mode, which also radiates as a dipole.

6.5 Summary

High-order simulations have been conducted to study the aerodynamic effects of varying the door angle on a cylinder and door model in a side by side configuration. Five interaction cases at a constant gap width ratio of $G = 0.087$, and varying door angles of $\alpha_D = \{0, 2.5, 5, 7.5, 10.7\}$ degrees were studied. Additionally, two further numerical simulations of an isolated circular cylinder, and an isolated angled door at $\alpha_D = 10.7$ degrees, were studied. The additional cases were conducted to determine the changes in the aerodynamic flow field due to the additional interactions between the door and the cylinder.

The velocity field in the wake region was compared to the experimental PIV database. This comparison was conducted for the interaction cases at $\alpha_D = \{0, 5, 10.7\}$ degrees. The mean and variance of the velocity field predicted by the numerical simulations are in good agreement with the experimental data, which validates the numerical predictions.

Far-field noise predictions were calculated using the FW-H method on three integration surfaces. Firstly, a non-permeable integration surface enclosing all solid bodies and neglecting all quadrupole sources was used. The other two surfaces enclose the source region by using two closed and permeable integration surfaces. The placement of the permeable surfaces was designed to contain the regions of strong vorticity-based acoustic sources, and minimise the impact of non-acoustic fluctuations recorded along the integration surfaces. However, the calculations based on the permeable surfaces show a

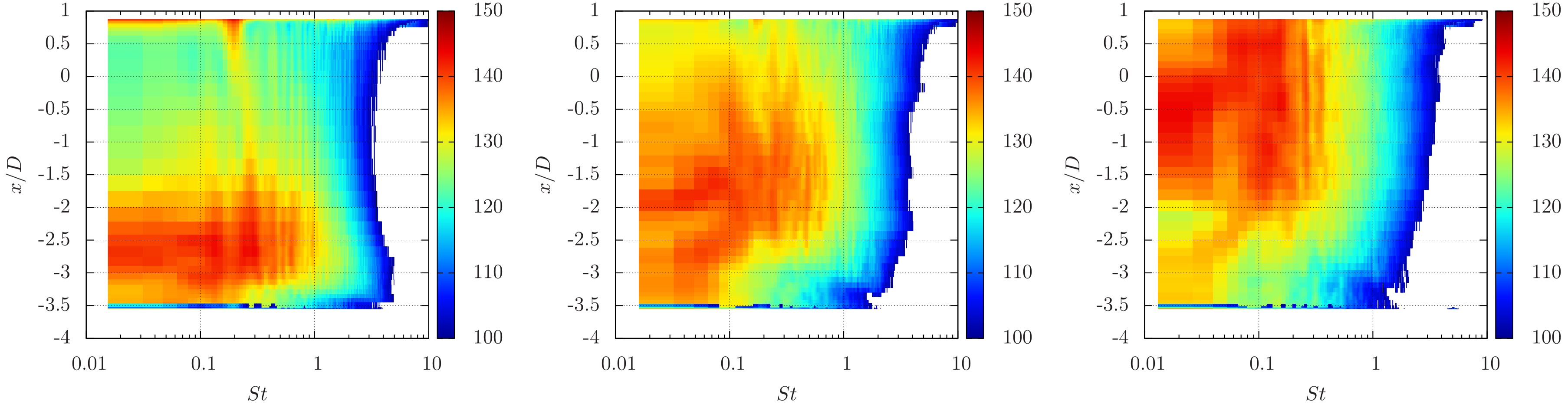

(a) $\alpha_D = 0°$

(b) $\alpha_D = 2.5°$

(c) $\alpha_D = 5°$

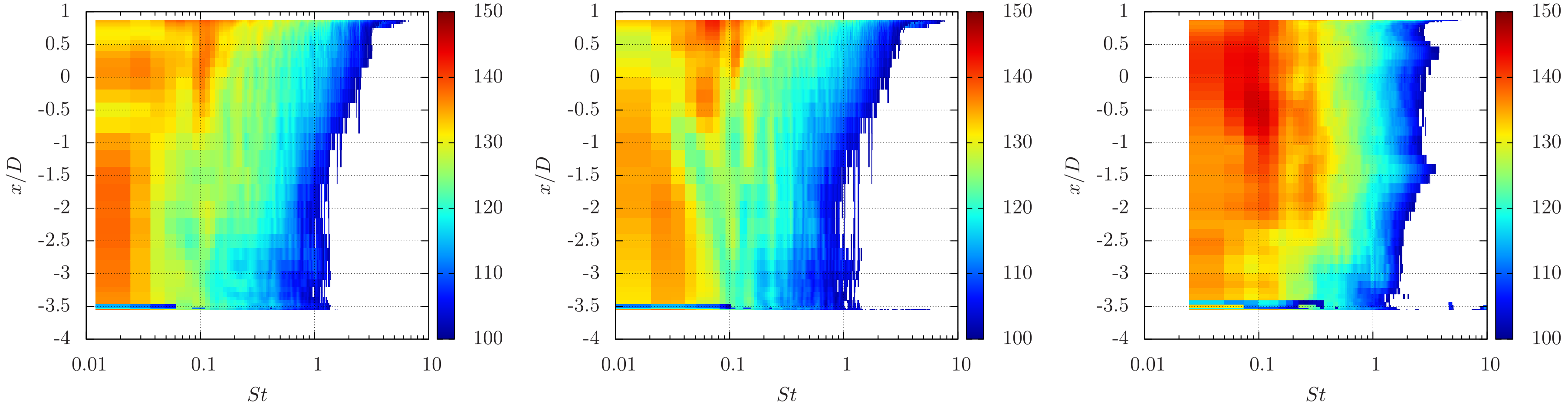

(d) $\alpha_D = 7.5°$

(e) $\alpha_D = 10.7°$

(f) Isolated door at $\alpha_D = 10.7°$

Figure 6.23: Door upper surface noise maps highlighted in SPL [dB].

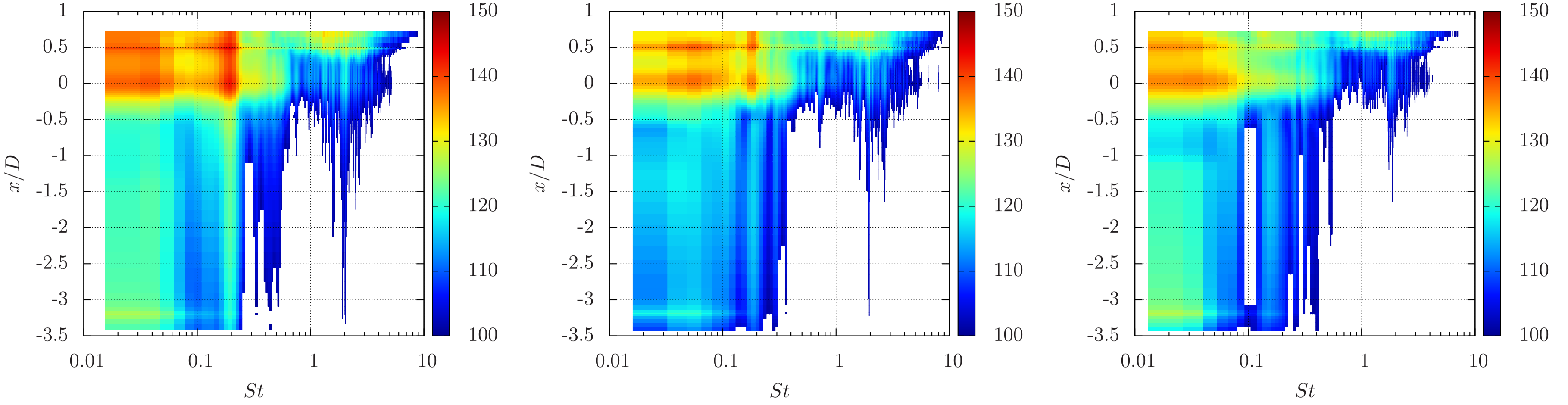

(a) $\alpha_D = 0°$

(b) $\alpha_D = 2.5°$

(c) $\alpha_D = 5°$

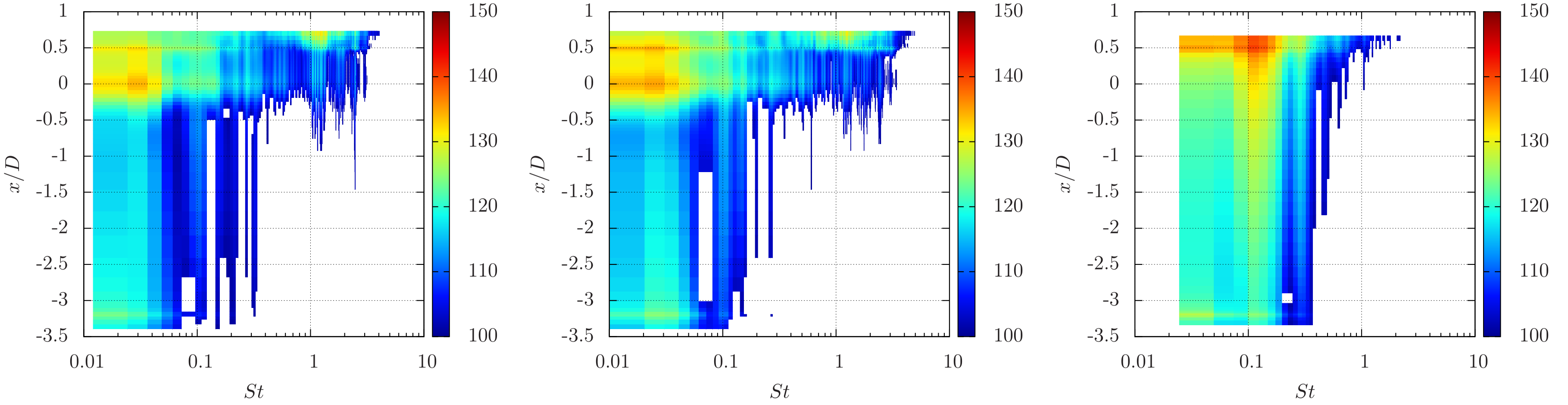

(d) $\alpha_D = 7.5°$

(e) $\alpha_D = 10.7°$

(f) Isolated door at $\alpha_D = 10.7°$

Figure 6.24: Door lower surface noise maps highlighted in SPL [dB].

significant increase in the far-field SPL when compared to the results obtained from the non-permeable surfaces.

The predominant aeroacoustic characteristic of bluff bodies at low Mach number is that of a compact dipole. Therefore, the additional quadrupole sources contained in the permeable FW-H surfaces should have a small contribution. The differences of 5-10 dB, depending on the case, suggests that strong vortical modes may be intersecting the integration surfaces. Therefore, the core of the far-field acoustic analysis was focused on the on-body FW-H surfaces only.

The major noise source of an isolated cylinder is the unsteady pressure distribution acting on the surface. The correlation between the surface pressure distribution and the far-field acoustic radiation is exploited to determine the origin of the dominant noise sources. The noise spectra distribution along the cylinder and door surfaces were plotted for the five interaction cases, and for the two isolated model cases. The dominant noise source at low door angles is the cylinder shedding mode at $St = 0.2$. As the door angle is increased, the cylinder shedding mode diminishes in intensity and shifts to lower frequency.

However, the overall noise level reduction is limited by two additional features. Firstly, the noise source intensity due to the separated flow along the upper surface of the door, increases with larger door angles. Secondly, a secondary high frequency mode at $St \approx 1$ becomes a significant source as the cylinder source diminishes. The origin of the high frequency source is the trailing edge bevel along the lower surface of the door. The absence of this high frequency source in isolated door simulations suggests that it is formed by the cylinder interaction.

The potential shielding effect of the door is not clearly observed in these studies as the dominant noise sources are compact dipoles. The presence of strong non-compact sources may present the effects of acoustic shielding more clearly. However, that study would either require a synthetic source, such as an monopole source at high frequency, or a model containing small scale features that would incite a high frequency acoustic response.

Throughout the aeroacoustic study, an FW-H method was applied using CFD data that was acquired by assuming a pseudo-infinite span, by the use of periodic boundary conditions. It should be noted that the simulations applied this boundary condition to minimise the computational cost. However, this simplification can lead to differences in terms of the absolute SPL for the far-field noise predictions, when compared against experimental data. This issue is not addressed in the present work.

Finally, the turbulence modelling strategy employed for the noise source modelling was set to the Z-DES strategy, based on the literature reviewed in Chapter 2. Therefore, the impact of different turbulence models has not been addressed in this work.

Chapter 7

Conclusions and recommendations

7.1 Summary of the work

Experimental and numerical studies have been conducted on a simplified bluff body configuration to understand the aerodynamic and aeroacoustic effects of a landing gear leg-door on the main strut. The simplified model is a span-wise extrusion of a two-dimensional geometry that consists of two components; the leg-door and the main strut. For this study there are many potential influential parameters.

Previous studies on cylinder and plane boundary interactions have identified the minimum gap distance along the cylinder, also referred to as the gap width ratio, to significantly affect the vortex shedding intensity [73, 74], and this effect is driven by the process of preventing the interaction of entrainment layers [28]. More recently Hutcheson and Brookes [8] measured the changes to the far-field noise radiation by a cylinder and door geometry with zero and finite gap width ratios. These studies effectively consider a leg-door interaction that is set to a zero degree angle of attack. However, it is clear from the Airbus (Figure 2.6) and Boeing CAD [36] models that the leg-door is not aligned with the free-stream flow. Horne *et al.* [13] state that a positively inclined door is implemented to aid in the MLG deployment under hydraulic failure. For these reasons, the leg-door angle was selected as the primary parameter to vary in this study, as it provides novel and practical insight.

Initial studies on the influence of the leg-door angle were conducted using the CFD software package FLUENT. A two-dimensional model of a cylinder and leg-door was derived from a planar cut of an A-340 MLG model (Figure 3.3). Two-dimensional URANS (using the $k-\omega$ SST turbulence model) computations were conducted on 20 cases, which varied the door angle between 0 and 10.7 degrees. Additionally, the gap width ratio, between the cylinder and the leg-door, was varied between $0.087 < G < 0.25$. The Airbus A-340 MLG is configured with a gap distance of $G = 0.087$, and a door angle of 10.7 degrees. The URANS computations predicted that the unsteady flow generated behind the bluff body could be reduced by increasing the door angle, as well as by reducing the gap distance.

One of the key drawbacks of URANS methods for bluff body aeroacoustic studies is their limited capacity to resolve the smaller scales in the generated turbulent field [44]. However, simulation strategies such as LES are currently infeasible due to the required computational resources [49]. Therefore, hybrid RANS/LES methods are favoured as a compromise between high fidelity and high cost. In this method, the unresolvable scales of turbulent motion are modelled by an eddy viscosity [48], similar to RANS methods. However, the bulk level of the eddy viscosity is significantly lower in the hybrid RANS/LES methods, which makes the numerical stability more sensitive to the numerical methods.

A high-order in-house CAA solver was used for further numerical simulations, to study the effect of the leg-door angle on a cylinder and door interaction with a fixed gap distance of $G = 0.087$. The CAA solver evaluates the three-dimensional Navier-Stokes equations in full-conservation form, using a high-order finite-differencing method. The solution was bounded along the edges of the computational domain by non-reflective boundary conditions. Along areas of solid walls, an iso-thermal no-slip boundary condition was applied. The free-stream Mach number was $M_\infty = 0.2$ and the Reynolds number, based on the cylinder diameter, was $Re_D = 1.66 \times 10^6$. The solution was advanced in time using a second-order fully implicit method [57]. Finally, the unresolvable scales of turbulence were modelled using the Zonal Detached-Eddy Simulation (Z-DES) method.

Finite differencing methods suffer from grid-induced errors in regions of the grid that contain discontinuities in the grid metrics. In these regions, a characteristic interface condition was applied. The performance of this interface condition is dependant on the accuracy of the boundary schemes. The penta-diagonal spatial schemes [51] were implemented to improve the accuracy of the boundary schemes. This change allowed for a reduction in the strength of the spatial filters, which enhanced the fidelity of the CAA solver.

The numerical stability can be enhanced by the use of stronger spatial filters [89], or additional artificial diffusion [50]. However, these counter measures will degrade the fidelity of the solution. A parameter that effects the numerical stability is the grid quality. A grid quality metric for curvilinear grids using high-order schemes was developed. The grid quality metric applies a modified spatial filter on the grid coordinates to identify areas of the mesh that are likely to contain large truncation errors in the grid metrics. It was also demonstrated that the grid quality metric can be used in a feedback-loop to optimise the grid and thus maximise the solution accuracy, by minimising the influence of grid-induced errors.

As part of the work on numerical methods development, an extension to the method of assessing numerical stability has also been achieved. Eigenvalue stability analysis of spatial schemes is limited to a single block case. This model is appropriate for explicit spatial schemes where the overall stability is unaffected by the number of sub-domains. For implicit spatial schemes, this is not the case, as sub-domain interfaces are treated by boundary schemes, which differ from the interior schemes. The development of a multi-block environment for the Eigenvalue analysis allows for more realistic configurations to be assessed. Therefore, the effects on the numerical stability due to characteristic interfaces, and different boundary schemes, can be assessed. This analysis showed that the prefactored schemes cannot be used with the penta-diagonal filters as this configuration is inherently unstable.

The implementation of newer spatial schemes into the high-order code has increased the fidelity of the solver. Comparisons of the flow field between the original and updated versions of the solver shows significant improvements in the resolution of small-scale turbulent structures, which has an impact on the high-frequency range of the far-field noise predictions.

The grid quality of the meshes used, in the set of URANS at $G = 0.087$, were improved with the aid of the grid quality assessment tool, and extruded in the span-wise direction to enable the use of the Z-DES.

Experimental measurements were taken in the wake region behind the cylinder element for an interaction model at 0, 5 and 10.7 degrees. This data was obtained using PIV, and it was used for validating the numerical predictions. Experiments were also conducted on an isolated door model at the three door angles. However, the isolated door model data was limited to oil flow and mean loads measurements. The numerical predictions of the flow were obtained for 5 interaction cases at various door angles, one isolated cylinder model, and another isolated door model at $\alpha_D = 10.7°$. The numerical predictions were found to be in good agreement with the experimental data.

7.2 Conclusions

The observations from the numerical and experimental studies are combined, and the following conclusions were drawn.

An isolated cylinder flow at high Re consists of a symmetric mean flow field. The interaction of the shear layers along the upper and lower surfaces generate a coherent vortex shedding mode, via mechanisms of fluid entrainment.

The cylinder flow is significantly altered by the aerodynamic interaction with a leg-door model at 0 degrees inclination. Firstly, the door interaction modifies the stagnation position along the cylinder towards the door side. This forms an asymmetry in the surface pressure profile along the cylinder, which results in greater differences in the shear layers that detach from the cylinder element. As the door angle is increased, the stagnation point shifts further towards the door side of the cylinder. Increasing the asymmetry of the cylinder pressure profile reduced TKE production by the cylinder, which results in a decreased intensity of the velocity fluctuations the wake region. The reduction of TKE production may be due to the reduced entrainment interaction between the shear layers formed along the cylinder element.

A secondary feature of the door interaction was the accelerated flow through the gap region between the cylinder and the door. This flow feature was enclosed by the shear layers along the door and cylinder surface, and this gap flow resembled a jet flow. This jet flow is sensitive to the door angle, and was found to be deflected towards the upper surface of the door at larger door angles. This deflection is due to the lower pressures generated along the upper surface of the door at higher door angles. The deflected jet flow also becomes a significant source of TKE production at higher door angles.

The effect of the door angle on the acoustic radiation was studied by calculating the far-field noise signals using the FW-H method. A far-field calculation was obtained by positioning observers at a distance of 120 m away from the source region. The results from the off-body surface integrations were shown, but are inconclusive as they are likely contaminated by the convection of strong vortical and non-acoustic modes. The results from the on-body FW-H integration surfaces show that the acoustic radiation of the bluff body is dipole. The energy of the far-field noise spectra is concentrated towards lower frequencies, and this suggest that the major noise is formed by a compact source.

The effect of increasing the door angle is a reduction in the SPL at all observer positions. This reduction is primarily due to the reduced intensity of the unsteady cylinder vortex shedding mode. The most significant noise reduction occurs when increasing the door angle from 0 to 2.5 degrees. Further increases of the door angle result in lower reductions in the far-field noise, due to the effects of a the door surface as a secondary noise source. The door source is composed of the detached flow along the upper surface, which contains low frequency disturbances, and towards the trailing edge bevel along the lower surface of the door, which is a higher frequency source. The absence of this high frequency source from the isolated door simulation suggests that it is a result of the cylinder interaction. Therefore, this mechanism is due to the interaction of the cylinder shear layer and the door trailing edge bevel.

7.3 Future work

The areas of future work are divided into three categories. Development of numerical methods, future experimental, and future numerical studies.

7.3.1 Future work on numerical methods

The areas of future work related to the development of numerical methods are summarised as follows:

- **Frequency resolution assessment of computational grids**
  This issue addresses the uncertainty of the frequency resolution limit of the numerical simulations. Traditionally, the frequency resolution of a computational grid is determined by the the local grid spacing, and the resolution capability of the spatial schemes employed. The latter is often referred to by the points-per-wavelength. However, the effective frequency resolution may be lower, due to the impact of artificial dissipation by the implicit time-stepping scheme, or by the filtering schemes. There is also uncertainty on the effects of aspect ratio and grid stretching on the noise propagation modelling. The group velocity of spatial schemes also depends on the grid resolution. Therefore high aspect ratio cells may predict an anisotropic and directional pattern from an omnidirectional monopole pulse.

  This uncertainty could be addressed by comparing solutions of the scattered acoustic field from a monopole source between CAA solver, and a Boundary Element Method (BEM) solver. As a simplification, a mean flow at rest would be considered. However, the scattered acoustic field from the CAA simulation would be obtained from the grid intended for DES or LES computations. Therefore, the accuracy of the acoustic propagation effects could be measured for increasing frequencies, until a frequency threshold is identified.

  By comparing BEM and CAA solutions of the scattered acoustic field, the frequency resolution of the near-field grid can be estimated. Additionally, the effects of grid stretching and cell aspect ratio, on the propagation behaviour of acoustic waves could be assessed.

  This exercise would also verify the frequency resolution of particular regions of the grid, and provide a measurable estimate on the frequency resolution of FW-H surface placements.

- **Grid quality assessment**
  The grid quality assessment tool has been demonstrated to improve the solution accuracy for a simple example. Further development of the grid quality tool to automatically modify more complicated, and possibly three-dimensional cases, would

be useful. The challenges with this task are on determining specific conditions to treat five-point grid singularities, and in treating wall regions without modifying the surface shape/profile.

- **Over-set and adaptive mesh refinement**

  Studies of more complex geometries using the high-order CAA solver are currently limited due to the need for a fully structured conformal grid. Local grid refinement of structured and conformal grids may result in significant increases in the total cell count. This effect may not be an issue on surface wrapped meshes that are self enclosing, such as boundary layer meshes.

  The application of over-set [117] grids and non-conformal patched interfaces [88] has been demonstrated in CAA studies. This extension of work would be useful for the proposed areas of further work related to more complex landing gear door models.

- **Correction methods for permeable FW-H methods**

  Off-body FW-H methods may suffer from strong non-acoustic vortical modes. Although correction methods [41, 118] have been proposed there is a lack of generic methods that are computationally efficient.

  Two methods of removing non-acoustic sources from an FW-H surface are suggested. The first is based on Gradient Term Filtering (GTF) [119]. This method assumes a linear decomposition the velocity field into vortical and acoustic components by defining additional variables for the acoustic and vorticity potential field. By obtaining the velocity potential of the vortical component, the acoustic variables can be isolated from the total field.

  The second method is based on characteristic decomposition. Characteristic methods are effective boundary conditions for CAA computations. These methods decompose the temporal derivative of the conserved variables into corresponding wave modes of entropy, vorticity and acoustic form. A modification of this method could be applied as a means of isolating the acoustic variables from the total field along FW-H integration surfaces.

  A simplified 2-D test case of an acoustic monopole immersed in a background of divergence free eddies, of varying intensity, could be used to determine the effectiveness of the proposed methods for off-body FW-H calculations.

- **Development of boundary closures for prefactored compact schemes**

  The primary advantages of prefactored compact schemes over other implicit schemes, is its small-stencil. Hixon's sixth order prefactored scheme [96] requires a 3 point stencil, which recovers the same accuracy as the standard sixth-order scheme [55] that requires seven points.

  The primary drawback of prefactored schemes is in their unique low-order boundary schemes that are complicated to derive. The development of high-order and stable boundary closures for prefactored schemes has not yet been achieved. Most prefactored schemes are bi-diagonal, which makes them simple to solve. A bi-diagonal system must be closed by an explicit scheme towards one of the boundary points. In Hixon's formulation, the type of scheme (explicit or implicit) is applied along both boundary regions. Therefore an implicit boundary scheme cannot be applied without changing the bi-diagonal matrix into a tri-diagonal form. This change will dramatically increase the computational cost.

A hybrid explicit and implicit boundary closure scheme could be explored. This alternative approach could improve the dispersion relation of boundary schemes, whilst maintaining the bi-diagonal form.

7.3.2 Future work on door cylinder interaction

Further works are also suggested to enhance the understanding of the aerodynamic and aeroacoustic effects of a landing gear door on landing gear noise.

The effects of the cylinder position along the chord-line of the door is an area that should be explored. This is a variable that is visually observed from Figures 2.6 on different aircraft MLG models. The Boeing 777 MLG model has a leg-door placement such that the main strut is positioned closer to the centre of the door, whereas Airbus models place the main strut closer to the trailing edge of the leg-door.

A more complex interaction study of the leg-door and cylinder could be achieved by considering the following effects of a finite leg-door model, or the interaction with other large-scale MLG components. The former would include the effects of the door tip vortex, and the latter would focus on the interactions with other large, and near-by components such as the MLG bogie, or the side-stay assembly.

More complex configurations may require further experimental studies for validation. Additionally, the more complicated configurations may be infeasible for the high-order CAA solver without further numerical development. Alternate means of numerical modelling using unstructured grids may be required. However, if the geometry remains fairly simple, the use of the high-order CAA solver may be possible, provided that it can be developed to work with over-set grids.

Appendix A

Low-order Simulations

Preliminary studies using two low-order CFD packages were conducted to establish initial flow diagnostics for a cylinder and door interaction model from 2-D URANS, and 3-D DDES simulations.

The incompressible Navier-Stokes equations were solved by a second-order accurate Finite Volume Method (FVM). The initialised flow, set to free-stream conditions of $U_\infty = 68$ m/s was advanced in time by a second-order accurate fully-implicit dual-time stepping method, with a Cournat-Friedrichs-Lewy (CFL) of $CFL < 20$. The solution field was bounded by a fixed velocity condition along the inlet section, a symmetry condition along the upper and lower bounds, and by a pressure-outlet along the outflow face. The domain edges were located at least 15 cylinder diameters (D) from the source region. The Reynolds number, based on the cylinder diameter, was $Re_D = 1.66 \times 10^6$.

The grids for the 2-D study consisted of approximately 2×10^5 cells. The initial grids were refined until a sufficiently fine boundary layer mesh ($y^+ < 1$) was obtained. The two-dimensional URANS computations were conducted using the CFD package FLUENT. The turbulence model of choice was the $k - \omega$ SST model of Menter [120], due to the study Cox *et al.* [66] on the use of various RANS models to predict 2-D bluff body flows.

The CFD package OpenFOAM was used for the three-dimensional DES calculations of a preliminary mesh for an interaction case configured at $G = 0.087$ and $\alpha_D = 10.7°$. The purpose of this exercise was to determine the effect of grid density on the unsteady flow field. The 3-D grid was developed by extruding the 2-D grids used in the FLUENT case studies along the span-wise direction to a length of three cylinder diameters $3D$. The grid spacing along the span-wise direction was between 20 and 35 points per cylinder diameter D. The boundary layer resolution from the DES calculations averaged around $\overline{y^+} = 1.5$ with a peak value of $y^+_{max} = 4$ across a small range of the entire wall region.

The lift load spectra along the door surface is compared between these two cases, at different span-wise grid resolution, in Figure A.2 and the small differences in the spectra

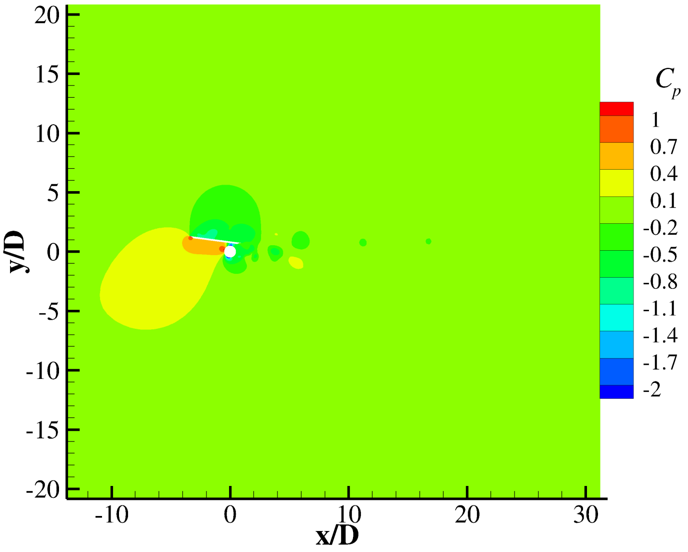

Figure A.1: Instantaneous field of pressure coefficient computed by 2-D URANS with the $k - \omega$ SST model, for an interaction model configured to $G = 0.087$ and $\alpha_D = 7.5°$.

are noted. These differences are within 5 dB across most of the spectra. The differences are attributed to the changes in the LED modelling of the detached flow, due to differences in the grid resolution.

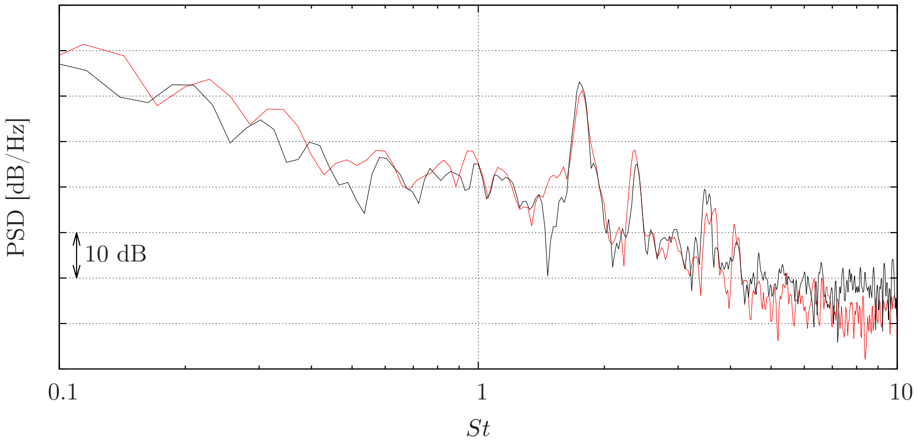

Figure A.2: Power spectral density of the lift force fluctuation recorded on the door surface for a grid with a span-wise grid resolution of 20 (red) and 35 (black) points per cylinder diameter.

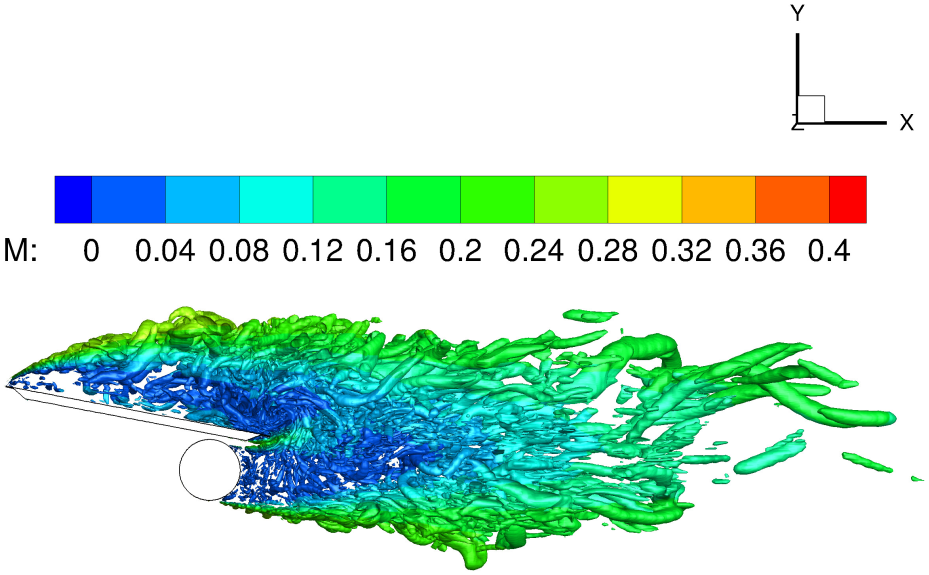

Figure A.3: Instantaneous iso-contour plot of constant Q-criterion at $Q = 100000\ \mathrm{s}^{-1}$ coloured by the local Mach number (assuming $c_\infty = 340$ m/s).

A.1 Input parameters for the OpenFOAM solver

The following Figures outline the numerical methods applied in the OpenFOAM solver.

```
/*---------------------------------*- C++ -*----------------------------------*\
| =========                 |                                                 |
| \\      /  F ield         | OpenFOAM: The Open Source CFD Toolbox           |
|  \\    /   O peration     | Version:  1.7.1                                 |
|   \\  /    A nd           | Web:      www.OpenFOAM.com                      |
|    \\/     M anipulation  |                                                 |
\*---------------------------------------------------------------------------*/
FoamFile
{
    version     2.0;
    format      ascii;
    class       dictionary;
    location    "system";
    object      fvSchemes;
}
// * * * * * * * * * * * * * * * * * * * * * * * * * * * * * * * * * * * * * //

ddtSchemes
{
    \\ STEADY SOLUTION MODE:  default         steadyState;
        default         backward;
}

gradSchemes
{
    default         Gauss linear;
    grad(p)         Gauss linear;
}

divSchemes
{
    default                             none;
    div(phi,U)                          Gauss limitedLinearV 1; // Gauss limitedLinearV 1; //
Gauss upwind; //
    div(phi,nuTilda)                    Gauss limitedLinear 1; // limitedLinear 1;
    div((nuEff*dev(T(grad(U)))))        Gauss linear;
}

laplacianSchemes
{
    default         Gauss linear corrected; //
}

interpolationSchemes
{
    default         linear;
}

snGradSchemes
{
    default         corrected;
}

fluxRequired
{
    default         no;
    p               ;
}


// ************************************************************************* //
```

Figure A.4: OpenFOAM system file for the finite volume schemes (part 1 of 4).

```
/*--------------------------------*- C++ -*----------------------------------*\
| =========                 |                                                 |
| \\      /  F ield         | OpenFOAM: The Open Source CFD Toolbox           |
|  \\    /   O peration     | Version:  1.7.1                                 |
|   \\  /    A nd           | Web:      www.OpenFOAM.com                      |
|    \\/     M anipulation  |                                                 |
\*---------------------------------------------------------------------------*/
FoamFile
{
    version     2.0;
    format      ascii;
    class       dictionary;
    location    "system";
    object      fvSolution;
}
// * * * * * * * * * * * * * * * * * * * * * * * * * * * * * * * * * * * * * //

solvers
{
    U
    {
        solver          GAMG;
        smoother        DILUGaussSeidel;
        tolerance       1e-07;
        relTol          0.01;
        cacheAgglomeration true;
        nCellsInCoarsestLevel 100;
        agglomerator    faceAreaPair;
        mergeLevels     1;
    }

    UFinal
    {
        solver          GAMG;
        smoother        DILUGaussSeidel;
        tolerance       1e-07;
        relTol          0;
        cacheAgglomeration true;
        nCellsInCoarsestLevel 100;
        agglomerator    faceAreaPair;
        mergeLevels     1;
    }

    p
    {
        solver          GAMG;
        smoother        DICGaussSeidel;
        tolerance       1e-07;
        relTol          0.01;
        cacheAgglomeration true;
        nCellsInCoarsestLevel 4000;
        agglomerator    faceAreaPair;
        mergeLevels     1;

    }

    pFinal
    {
        solver          GAMG;
        smoother        DICGaussSeidel;
        tolerance       1e-07;
        relTol          0.01;
        cacheAgglomeration true;
        nCellsInCoarsestLevel 4000;
        agglomerator    faceAreaPair;
        mergeLevels     1;
    }

    nuTilda
    {
        solver          GAMG;
        smoother        DILUGaussSeidel;
        tolerance       1e-08;
        relTol          0.01;
```

Figure A.5: OpenFOAM system file for the finite volume schemes (part 2 of 4).

```
        cacheAgglomeration true;
        nCellsInCoarsestLevel 100;
        agglomerator    faceAreaPair;
        mergeLevels     1;
    }


    nuTildaFinal
    {
        solver          GAMG;
        smoother        DILUGaussSeidel;
        tolerance       1e-08;
        relTol          0.01;
        cacheAgglomeration true;
        nCellsInCoarsestLevel 100;
        agglomerator    faceAreaPair;
        mergeLevels     1;
    }

    rho
    {
        solver          GAMG;
        smoother        DILUGaussSeidel;
        tolerance       1e-08;
        relTol          0.01;
        cacheAgglomeration true;
        nCellsInCoarsestLevel 100;
        agglomerator    faceAreaPair;
        mergeLevels     1;
    }

    rhoFinal
    {
        solver          GAMG;
        smoother        DILUGaussSeidel;
        tolerance       1e-08;
        relTol          0.01;
        cacheAgglomeration true;
        nCellsInCoarsestLevel 100;
        agglomerator    faceAreaPair;
        mergeLevels     1;
    }
}

PISO
{
    nCorrectors     3;
    nNonOrthogonalCorrectors 3;
    pRefCell        0;
    pRefValue       0;
}

SIMPLE
{
    nNonOrthogonalCorrectors 4;
    pRefCell        0;
    pRefValue       0;
}

PIMPLE
{
    nOuterCorrectors 3;
    nCorrectors     3;
    nNonOrthogonalCorrectors 1;
    pRefCell        0;
    pRefValue       0;
    momentumPredictor yes;

    // Residuals here (one per variable)
    // If one variable is not specified, zero is assumed as
    // desired residual (iterations will not stop)
    residualControl
    {
        "(U|k|epsilon|p)"
```

Figure A.6: OpenFOAM system file for the finite volume schemes (part 3 of 4).

```
        {
            relTol          0;
            tolerance       0.0001;
        }
    }
}

relaxationFactors
{
    fields
    {
        "p.*"           0.3;
    }
    equations
    {
        "(U|nuTilda).*" 0.7;
    }
}
// ************************************************************************* //
```

Figure A.7: OpenFOAM system file for the finite volume schemes (part 4 of 4).

Appendix B

Temporal Scheme Error Analysis

In this section a Fourier analysis of the second order implicit temporal scheme [57] is conducted. The methods applied in this section care based on the Von Newman, and Fourier stability analysis [93, 121]. We consider the one-dimensional scalar wave equation:

$$\frac{\partial f}{\partial t} + U\frac{\partial f}{\partial x} = 0, \tag{B.1}$$

where f is a scalar, t is the time, c_0 is the convection speed, and x is the spatial dimension. The solution to this may be expressed as:

$$f(x,t) = \mathrm{e}^{j(kx-\omega t)}, \tag{B.2}$$

where k is the wave number, and ω is the angular frequency, which is related to the wave number by $\omega = kc_0$. When applying a temporal scheme, the exact amplification factor is considered, which is defined by:

$$r = \frac{f(x,t+\Delta t)}{f(x,t)} = \mathrm{e}^{-j\omega\Delta t}. \tag{B.3}$$

By applying a temporal scheme, the numerical amplification factor $\tilde{r}$ can be expressed, which may differ due to dispersion and dissipation errors. Dissipation errors will affect the wave amplitude that may lead to an unstable solution, and dispersion errors may lead to phase errors. The second order backward differencing scheme is:

$$\frac{\partial f}{\partial t} = \frac{3f^{n+1} - 4f^{n} + f^{n-1}}{2\Delta t}, \tag{B.4}$$

where the time level is indicated by the superscript n. Using Fourier analysis, the semi-discrete form of Equation B.1 becomes:

$$\frac{\partial f}{\partial t} + jk^* c_0 f = 0, \tag{B.5}$$

where

$$k^* = \frac{-j}{\Delta x} \frac{\sum_{z=-n}^{m} \left(a_z e^{jk\Delta xz} \right)}{1 + \sum_{Z=-N}^{M} \left(\alpha_Z e^{jk\Delta xZ} \right)}. \tag{B.6}$$

The expression for the numerical amplification error using a second order implicit scheme is:

$$A\tilde{r}^2 + B\tilde{r} + 1 = 0, \tag{B.7}$$

$$A = 3 + 2\Delta t j c_0 k^*, B = -4, C = 1. \tag{B.8}$$

The total amplification error r^* is the ratio of the numerical to the exact, amplification errors:

$$\frac{\tilde{r}}{r} = |r^*| \mathrm{e}^{-j\phi}, \tag{B.9}$$

where $|r^*|$ represents the dissipation rate, and ϕ represents the phase error. The dissipation and phase errors from the time scheme are illustrated in Figure B.1. By defining a time-accurate criteria of $|1 - |r^*|| < 0.005$, and $|\phi| < 0.005$, the requirement of $c_0 k^* \Delta t < 0.253$ is obtained. Finally, the CourantFriedrichsLewy (CFL) number for time accurate solutions may be obtained by

$$\mathrm{CFL} < \frac{c_0 k^* \Delta t}{k^* \Delta x}. \tag{B.10}$$

The spatial resolution accuracy of the penta-diagonal spatial schemes is limited to $k_c \Delta x = 0.8\pi$ by the spatial filters. Therefore the time step requirement becomes CFL < 0.1. It should be noted that this analysis does not consider the numerical errors from the sub-iterative procedure. However, the solution error should converge to these errors with greater sub-iterations.

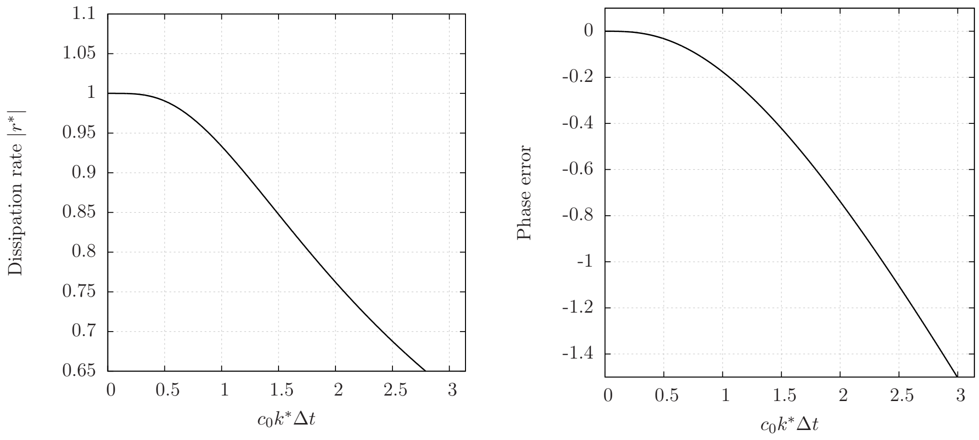

(a) Dissipation rate

(b) Phase error

Figure B.1: Numerical errors from a second order implicit time integration scheme on the one-dimensional wave equation.

Appendix C

High-order code validation and verification

The correct implementation of the governing equations and turbulence models is demonstrated in this section with a set of simplified test cases. The test cases are outlined to demonstrate the accuracy of the code in correctly modelling sound propagation effects, vortical convection, and wall bounded turbulent flows. The latter is outlined in the next section. The final section outlines validation cases conducted on the high-order CAA solver by other authors.

C.1 Boundary layer and SA model validation

The correct implementation of the Spalart-Allmaras (SA) RANS model was verified using the NASA 2-D zero pressure gradient flat plate boundary layer flow at a unit Reynolds number of $Re = 1 \times 10^6$, and a Mach number of $M_\infty = 0.2$. The grid and boundary conditions are specified in the benchmark description provided in the online repository [122]. The numerical predictions were obtained using the methods outlined in Section 3.2, where the time step size corresponded to a CFL of 10. The reference database for the verification exercise is the NASA CFD code CFL3D, and it consists of the velocity and the turbulent viscosity, profiles along the wall normal direction at a downstream position of $x = 0.97$ m, at which point, the Reynolds number is 1 million. The maximum height of the boundary layer thickness is approximately 0.03 m [122].

The close agreement between the flow field profiles in Figure C.1 verifies the correct implementation of the SA RANS model, and additionally verifies the correct implementation of the governing equations and boundary conditions.

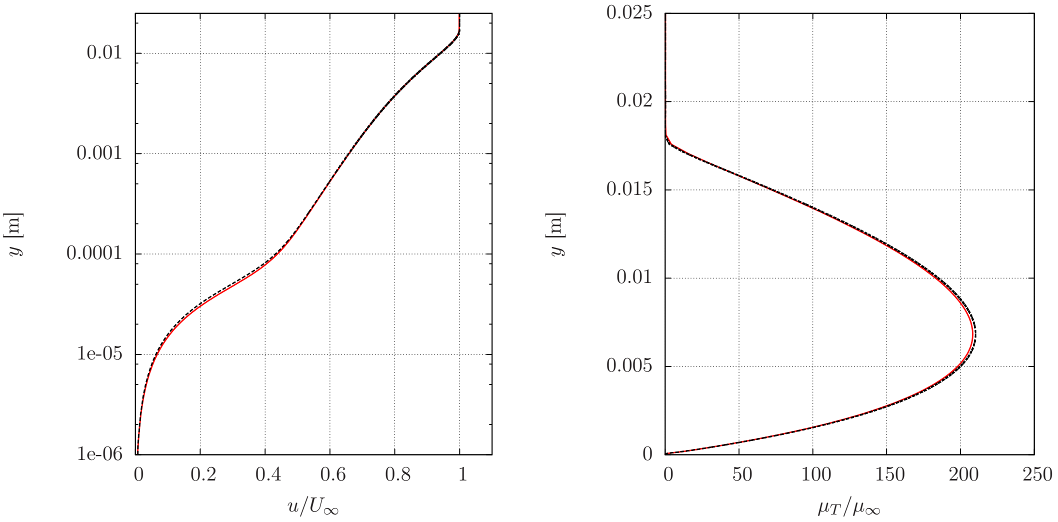

(a) velocity profile at $x = 0.97$m

(b) turbulent viscosity profile

Figure C.1: Comparison of the velocity and turbulent viscosity profiles between the high-order code (- - -) and CFL-3D (——).

C.2 Overview of validation cases for the high-order code

Table C.1 outlines the validation/verification cases conducted by other authors on the high-order CAA solver. Throughout the code development, various numerical methods have been implemented. The tests conducted with different numerical methods verify the governing equations are implemented correctly. Further tests conducted using the penta-diagonal schemes verify that it has been correctly implemented.

Author	Case	Equations	Spatial scheme	Temporal scheme	Validation/Verification
Richards [123]	acoustic scattering around a cylinder	2-D LEE	Prefactored 8-4	Explicit LDDRK	Analytical solution
Richards [123]	acoustic plane wave	2-D LEE	Prefactored 8-4	Explicit LDDRK	Analytical solution
Ma [124]	normal wave impedance tube	1-D LEE	Hixon 6th order	Explicit LDDRK	Analytical solution
Ma [124]	acoustic wave over impedance plane	1-D LEE	Hixon 6th order	Explicit LDDRK	Analytical solution
Ma [124]	vorticity wave propagation	2-D EE	Hixon 6th order	Implicit second order	Analytical solution
Peers [95]	acoustic pulse propagation	2-D EE	Prefactored 8-4	Explicit LDDRK	Analytical solution
Peers [95]	acoustic monopole radiation	FW-H	N/A	Second order	Analytical solution
Liu [125]	LAGOON	3-D NSE with DES	Prefactored 8-4	Implicit second order	Experiment
Current study	2-D Flat plate boundary layer	2-D NSE with S-A URANS	Penta-diagonal	Implicit second order	CFL 3D data [122]
Current study	3-D cylinder and door interaction	3-D NSE with S-A Z-DES	Penta-diagonal	Implicit second order	Experiment
Wang [14]	single cylinder	3-D NSE with S-A Z-DES	Penta-diagonal	Implicit second order	Travin data [67]
Wang [14]	tandem cylinders	3-D NSE with S-A Z-DES	Penta-diagonal	Implicit second order	Experiment [126]
Wang [14]	CADWIE wheel	3-D NSE with S-A Z-DES	Penta-diagonal	Implicit second order	Experiment

Table C.1: Validation and verification cases for the high-order CAA solver listed in chronological order.

Appendix D

Grid Quality Example

In this section the quality of two grids, developed for the interaction case with a door angle of $\alpha_D = 10.7°$, are shown. The grid quality assessment tool detailed in 4.5 was applied to two grids that are illustrated in Figure D.1.

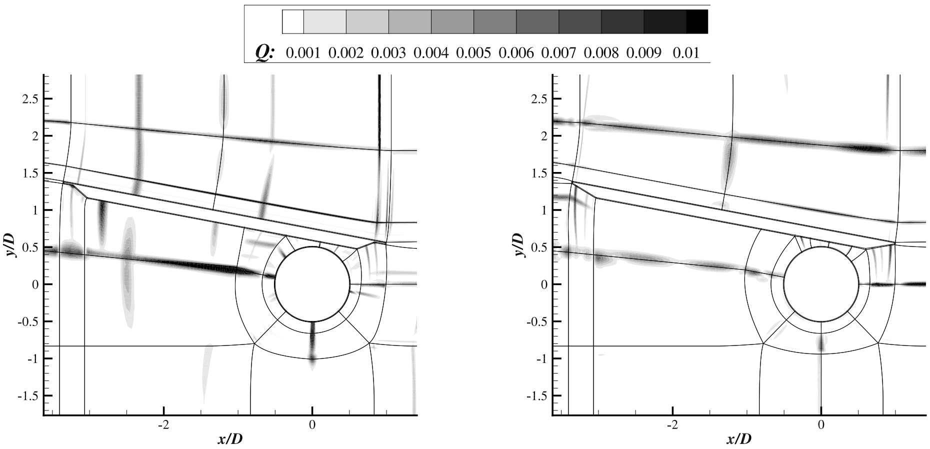

(a) Initial version

(b) Final grid

Figure D.1: The mesh quality for two grids developed for the interaction model with a door angle of $\alpha_D = 10.7°$.

Several grids were designed throughout the initial stages of the mesh development. In Figure D.1 the initial and final versions of the grid are shown. The grid quality is defined by a scalar field, Q. Areas of the mesh with a higher grid quality hold lower values of Q. In Figure D.1, the grid quality metric is illustrated in the area of greatest mesh complexity. The grid optimization tool outlined in Section 4.5.4 cannot be applied on grids that employ CIC along block interfaces, without further development. Therefore, the mesh refinements were conducted manually, with the aid of the grid quality metric output. Improvements to the grid were successfully applied, however a further improvement to the grid quality may require a change in the block topology.

Appendix E

Surface pressure spectra comparison

In this section the on surface pressure spectra obtained form the experiments in Section 5.4 are compared to the CFD data obtained form the simulations in Section 6.

The on surface microphone was located along the cylinder surface, at a position of $\theta = 0°$ based on the schematic illustrated in Figure 5.1. Using this microphone, the surface pressure spectra was obtained for an isolated cylinder configuration, and three leg-door and cylinder interaction cases. The door angles for the interaction cases were set to $alpha_D = 0, 5, 10.7$ degrees. The CFD data was obtained by high-order numerical simulation on the same geometry, but at a full scale Reynolds number.

In Figure E.1, the trends across the various cases seems to be captured well, in the range of $0.3 < St < 1$, as well as the decay rate at higher frequencies. Although the Reynolds number flow regime between experiment and simulations is similar, the differences in the scale and dimensions of the models makes the absolute levels incomparable to each other. It is also noted from the PIV data that the flow separation along the cylinder may be more sensitive to the flow conditions. Therefore, the differences in the model scale and dimension may attribute to some of the disagreements between the experimental measurements, and the numerical simulations.

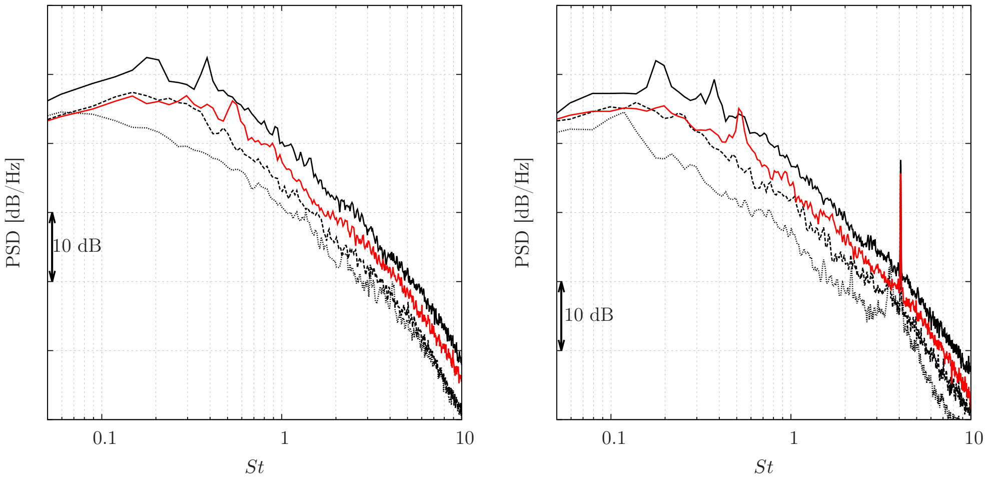

(a) Experiment $U_\infty = 20$ (b) Experiment $U_\infty = 30$

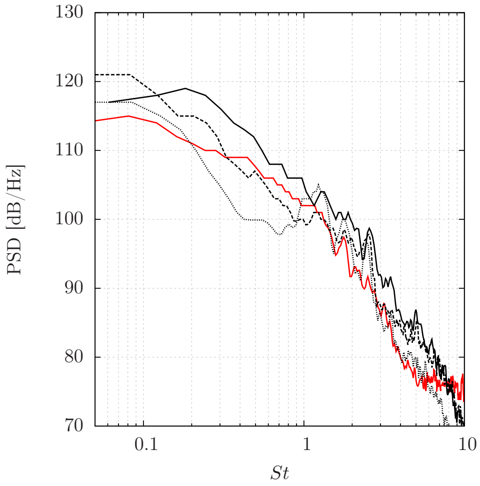

(c) Simulation

Figure E.1: Surface pressure spectra comparisons between experiments and simulation for an on-surface microphone located along the cylinder model at $\theta = 0°$. Data for an isolated cylinder: —, $\alpha_D = 0°$: —, $\alpha_D = 5°$: - - -, $\alpha_D = 10.7°$: ······.

References

[1] L. Butcher, "Aviation : noise pollution," *House of Commons Library, Buisness and Transport*, no. SN261, 2014.

[2] J. Lee, G. Cebrian, L. Edmonds, J. Patel, and E. Weston, "ERCD REPORT 1401 noise exposure contours for Heathrow airport 2013," Tech. Rep. October, 2014.

[3] C. Tullo, "Civil aviation act," *Her Majesty's Stationaery Office and Queen's Printer of Acts of Parliament*, pp. 1–53, 2006.

[4] L. C. Chow, K. Mau, and H. Remy, "Landing gears and high lift devices airframe noise research," in *8th AIAA/CEAS Aeroacoustics Conference*, no. AIAA 2002-2408, 2002.

[5] D. Casalino, F. Diozzi, R. Sannino, and A. Paonessa, "Aircraft noise reduction technologies: a bibliographic review," *Aerospace Science and Technology*, vol. 12, no. 1, pp. 1–17, Jan. 2008.

[6] B. S. Lazos, "Mean flow features around the inline wheels of four-wheel landing gear," *AIAA Journal*, vol. 40, no. 2, pp. 193–198, Feb. 2002.

[7] Y. Guo, "Effects of local flow variations on landing gear noise prediction and analysis," *Journal of Aircraft*, vol. 47, no. 2, pp. 383–391, 2010.

[8] F. V. Hutcheson and T. F. Brooks, "Noise radiation from single and multiple rod configurations," in *12th AIAA/CEAS Aeroacoustics Conference*, no. AIAA 2006-2629, Sep. 2006.

[9] W. M. Dobrzynski, B. Schöning, L. C. Chow, C. Wood, M. Smith, and C. Seror, "Design and testing of low noise landing gears," *International Journal of Aeroacoustics*, vol. 5, no. 3, pp. 233–262, Sep. 2006.

[10] W. Dobrzynski, L. C. Chow, M. Smith, A. Boillot, O. Dereure, and N. Molin, "Experimental assessment of low noise landing gear component design," in *AIAA/CEAS Aeroacoustics Conference*, no. AIAA 2009-3276, 2009.

[11] ——, "Experimental assessment of low noise landing gear component design," *International Journal of Aeroacoustics*, vol. 9, no. 6, pp. 763–786, Jul. 2010.

[12] W. M. Humphreys and T. F. Brooks, "Noise spectra and directivity for a scale-model landing gear," *International Journal of Aeroacoustics*, vol. 8, no. 5, pp. 409–444, 2009.

[13] W. C. Horne, N. J. Burnside, P. T. Soderman, S. M. Jaeger, B. R. Reinero, K. D. James, and T. K. Arledge, "Aeroacoustic study of a 26 % - scale semispan model of a Boeing 777 wing in the NASA Ames 40- by 80-foot wind tunnel," Washington, DC, Tech. Rep., 2004.

[14] M. Wang, R. Fattah, D. Angland, and X. Zhang, "High-order hybrid cell-centered method for computational aeroacoustics," in *21st AIAA/CEAS Aeroacoustics Conference*, no. AIAA 2015-3279, 2015.

[15] J. Gill, R. Fattah, and X. Zhang, "Evaluation and development of non-reflective boundary conditions for aeroacoustic simulations," in *21st AIAA/CEAS Aeroacoustics Conference*, no. AIAA 2015-2677, 2015.

[16] R. Fattah, Z. Hu, and D. Angland, "Aeroacoustics of a landing gear door," in *19th AIAA/CEAS Aeroacoustics Conference*, no. AIAA 2013-2259, 2013.

[17] R. Fattah, D. Angland, and X. Zhang, "A priori grid quality estimation for high-order finite differencing," *Journal of Computational Physics (Article under preparation)*, 2016.

[18] S. Uosukainen, *Foundations of acoustic analogies*, L. Ukskoski, Ed. Vuorimiehentie: Julkaisija - Utgivare, 2011.

[19] M. J. Lighthill, "On sound generated aerodynamically. i. general theory," *Proceedings of the Royal Society A: Mathematical, Physical and Engineering Sciences*, vol. 211, pp. 564–587, 1952.

[20] A. Powell, "Theory of vortex sound," *The Journal of the Acoustical Society of America*, vol. 36, no. 1, p. 177, 1964.

[21] N. Curle, "The influence of solid boundaries upon aerodynamic sound," *Proceedings of the Royal Society A: Mathematical, Physical and Engineering Sciences*, vol. 231, no. 1187, pp. 505–514, 1955.

[22] D. L. Ffowcs Williams, J. E., and Hawkings, "Sound generation by turbulence and surfaces in arbitrary motion," *Philosophical Transactions of the Royal Society of London. Series A, Mathematical and Physical Sciences*, vol. 264, no. 1151, pp. 321–342, 1969.

[23] M. S. Howe, *Theory of vortex sound.* Cambridge University Press, 2002.

[24] J. Delfs, "Grundlagen der aeroakustik (basics of aeroacoustics)," *Technische Universit Braunschweig*, no. October 2009, p. 116, 2009.

[25] A. E. Perry, M. S. Chong, and T. T. Lim, “The vortex-shedding process behind two-dimensional bluff bodies,” *Journal of Fluid Mechanics*, vol. 116, pp. 77–90, 1982.

[26] J. H. Gerrard, “The mechanics of the formation region of vortices behind bluff bodies,” *Journal of Fluid Mechanics*, vol. 25, no. part 2, pp. 401–413, 1966.

[27] M. Van Dyke, *Van Dyke Album of Fluid Motion.* Stanford: The Parabolic Press, 1982.

[28] M. Zdravkovich, “Review and classification of various aerodynamic and hydrodynamic means for suppressing vortex shedding,” *Journal of Wind Engineering and Industrial Aerodynamics*, vol. 7, no. 2, pp. 145–189, 1981.

[29] B. Sumer and J. Fredsoe, *Hydrodynamics around cyclindrical structures*, P. L.-F. Liu, Ed. Singapore: World Scientific Publishing Co. Pte. Ltd., 2006, vol. 26.

[30] G. Schewe, “Reynolds-number effects in flow around more-or-less bluff bodies,” *Journal of Wind Engineering and Industrial Aerodynamics*, vol. 89, no. 14-15, pp. 1267–1289, 2001.

[31] R. Elkoby, “Airframe noise results from the QTD II flight test program,” in *13th AIAA/CEAS Aeroacoustics Conference*, no. AIAA 2007-3457, 2007.

[32] L. V. Lopes, “Prediction of landing gear noise reduction and comparison to measurements,” in *16th AIAA/CEAS Aeroacoustics Conference*, no. AIAA 2010-3970, 2010.

[33] Y. Guo, K. J. Yamamoto, and R. W. Stoker, “Experimental study on aircraft landing gear noise,” *Journal of Aircraft*, vol. 43, no. 2, pp. 306–317, Mar. 2006.

[34] W. Dobrzynski, R. Ewert, M. Pott-Pollenske, M. Herr, and J. Delfs, “Research at DLR towards airframe noise prediction and reduction,” *Aerospace Science and Technology*, vol. 12, no. 1, pp. 80–90, Jan. 2008.

[35] M. R. Khorrami, “Towards establishing a realistic benchmark for airframe noise research: issues and challenges,” *IUTAM Symposium on Computational Aero-Acoustics for Aircraft Noise Prediction*, vol. 6, pp. 264–273, 2010.

[36] M. C. Remillieux, “Aeroacoustic study of a model-scale landing gear in a semi-anechoic wind-tunnel,” Ph.D. dissertation, Virginia Polytechnic Institute and State University, 2007.

[37] W. Dobrzynski, M. Pott-pollenske, D. Foot, and M. Goodwin, “Landing gears aerodynamic interaction noise,” in *European Congress on Computational Methods in Applied Sciences and Engineering*, 2004, p. 13.

[38] D. Casalino, “An advanced time approach for acoustic analogy predictions,” *Journal of Sound and Vibration*, vol. 261, no. 4, pp. 583–612, 2003.

[39] K. S. Brentner and F. Farassat, “An analytical comparison of the acoustic analogy and Kirchhoff formulation for moving surfaces,” *AIAA Journal*, vol. 36, no. 8, pp. 1379–1386, 1998.

[40] B. Singer, D. Lockard, and G. Lilley, “Hybrid acoustic predictions,” *Computers and Mathematics with Applications*, vol. 46, no. 3, pp. 647–669, 2003.

[41] D. P. Lockard and J. H. Casper, “Permeable surface corrections for Ffowcs-Williams and Hawkings integrals,” in *11th AIAA/CEAS Aeroacoustics Conference*, no. AIAA 2005-2995, 2005.

[42] P. R. Spalart, M. L. Shur, M. K. Strelets, and A. K. Travin, “Towards noise prediction for rudimentary landing gear,” *Procedia Engineering*, vol. 6, pp. 283–292, 2010.

[43] T. Imamura, T. Hirai, K. Amemiya, Y. Yokokawa, S. Enomoto, and K. Yamamoto, “Aerodynamic and aeroacoustic simulations of a two-wheel landing gear,” in *IUTAM Symposium on Computational Aero-Acoustics for Aircraft Noise Prediction*, no. 6, 2010, pp. 293–302.

[44] D. P. Lockard and M. R. Khorrami, “High resolution calculation of a simplified landing gear,” in *10th AIAA/CEAS Aeroacoustics Conference*, no. AIAA 2004-2887, 2004.

[45] D. P. Lockard, M. R. Khorrami, and F. Li, “Aeroacoustic analysis of a simplified landing gear,” in *10th AIAA/CEAS Aeroacoustics Conference*, no. AIAA 2004-2887, 2004.

[46] F. Farassat, *Derivation of formulations 1 and 1A of Farassat.* Washington, DC: National Aeronautics and Space Administration, Mar. 2007, no. March.

[47] B.-T. Chu and S. G. K. Leslie, “Non-linear interactions in a viscous heat-conducting compressible gas,” *Journal of Fluid Mechanics*, 1958.

[48] S. B. Pope, *Turbulent Flows.* Cambridge: Cambridge University Press, 2000, vol. 1.

[49] P. R. Spalart, “Strategies for turbulence modelling and simulations,” *International Journal of Heat and Fluid Flow*, vol. 21, no. 3, pp. 252–263, 2000.

[50] T. Colonius and S. K. Lele, “Computational aeroacoustics: progress on nonlinear problems of sound generation,” *Progress in Aerospace Sciences*, vol. 40, no. 6, pp. 345–416, Aug. 2004.

[51] J. W. Kim and R. D. Sandberg, "Efficient parallel computing with a compact finite difference scheme," *Computers & Fluids*, vol. 58, no. 15 April 2012, pp. 70–87, Apr. 2012.

[52] P. R. Spalart, S. Deck, M. L. Shur, K. D. Squires, M. K. Strelets, and A. Travin, "A new version of detached-eddy simulation, resistant to ambiguous grid densities," *Theoretical and Computational Fluid Dynamics*, vol. 20, no. 3, pp. 181–195, May 2006.

[53] S. Deck, "Recent improvements in the Zonal Detached Eddy Simulation (ZDES) formulation," *Theoretical and Computational Fluid Dynamics*, vol. 26, no. 6, pp. 523–550, Oct. 2011.

[54] M. Breuer, N. Jovičić, and K. Mazaev, "Comparison of DES, RANS and LES for the separated flow around a flat plate at high incidence," *International Journal for Numerical Methods in Fluids*, vol. 41, no. September 2002, pp. 357–388, 2003.

[55] S. K. Lele, "Compact finite difference schemes with spectral-like resolution," *Journal of Computational Physics*, vol. 103, no. 1, pp. 16–42, Nov. 1992.

[56] C. K. W. Tam and J. C. Webb, "Dispersion-relation-preserving finite difference schemes for computational acoustics," *Journal of Computational Physics*, vol. 107, no. 2, pp. 262–281, 1993.

[57] F. Li, M. R. Khorrami, and M. R. Malik, "Unsteady simulation of a landing-gear flow field," in *8th AIAA/CEAS Aeroacoustics Conference*, no. AIAA 2002-2411, 2002.

[58] L. S. Hedges, A. K. Travin, and P. R. Spalart, "Detached-eddy simulations over a simplified landing gear," *Journal of Fluids Engineering*, vol. 124, no. 2, p. 413, 2002.

[59] F. Souliez, L. Long, P. Morris, and A. Sharma, "Landing gear aerodynamic noise prediction using unstructured grids," *International Journal of Aeroacoustics*, vol. 1, no. 2, pp. 115–135, Aug. 2002.

[60] W. Liu, J. W. Kim, X. Zhang, D. Angland, and B. Caruelle, "Landing-gear noise prediction using high-order finite difference schemes," *Journal of Sound and Vibration*, vol. 332, no. 14, pp. 3517–3534, 2013.

[61] S. Windiate, "An experimental and numerical study of bluff body," Ph.D. dissertation, University of Southampton, 2014.

[62] K. van Mierlo, K. Takeda, and E. Peers, "Computational analysis of the effect of bogie inclination angle on landing gear noise," in *16th AIAA/CEAS Aeroacoustics Conference*, no. AIAA 2010-3971, 2010.

[63] M. Aubert, O. Stanlov, D. Angland, and X. Zhang, "Numerical investigation of active flow control using steady blowing for landing gear noise reduction," in *20th AIAA/CEAS Aeroacoustics Conference*, no. AIAA 2014-2893, 2014.

[64] G. Lilley, "The prediction of airframe noise and comparison with experiment," *Journal of Sound and Vibration*, vol. 239, no. 4, pp. 849–859, Jan. 2001.

[65] R. Orselli, J. Meneghini, and F. Saltara, "Two-dimensional computation of sound generated by flow around a circular cylinder," in *12th Brazilian Congress of Thermal Engineering and Sciences*, 2008.

[66] J. S. Cox, K. S. Brentner, and C. L. Rumsey, "Computation of vortex shedding and radiated sound for a circular cylinder: subcritical to transcritical Reynolds numbers," *Theoretical and Computational Fluid Dynamics*, vol. 12, no. 4, pp. 233–253, 1998.

[67] A. Travin, M. Shur, and M. Strelets, "Detached-eddy simulations past a circular cylinder," *Flow, Turbulence and Combustion*, vol. 63, no. 1, pp. 293–313, 1999.

[68] P. R. Spalart and S. R. Allmaras, "A one-equation turbulence model for aerodynamic flows," *La Recherche Aerospatiale*, vol. 1, pp. 5–21, 1994.

[69] K. D. Squires, V. Krishnan, and J. R. Forsythe, "Prediction of the flow over a circular cylinder at high Reynolds number using detached-eddy simulation," *Journal of Wind Engineering and Industrial Aerodynamics*, vol. 96, no. 10-11, pp. 1528–1536, Oct. 2008.

[70] A. Stokes and M. Welsh, "Flow-resonant sound interaction in a duct containing a plate, II: Square leading edge," *Journal of Sound and Vibration*, vol. 104, no. 1, pp. 55–73, 1986.

[71] Y. Nakamura, Y. Ohya, and H. Tsuruta, "Experiments on vortex shedding from flat plates with square leading and trailing edges," *Journal of Fluid Mechanics*, vol. 222, pp. 437–447, 1991.

[72] J. M. Chen and Y.-C. Fang, "Strouhal numbers of inclined flat plates," *Journal of Wind Engineering and Industrial Aerodynamics*, vol. 61, no. 2-3, pp. 99–112, Jul. 1996.

[73] S. Price, J. Smith, K. Leong, and M. Paidoussis, "Flow visualization around a circular cylinder near to a plane wall," *Journal of Fluids and Structures*, vol. 16, no. 2, pp. 175–191, 2002.

[74] P. W. Bearman and M. M. Zdravkovich, "Flow around a circular cylinder near a plane boundary," *Journal of Fluid Mechanics*, vol. 89, no. 01, pp. 33–47, Apr. 1978.

[75] T. Nishino, G. T. Roberts, and X. Zhang, “Vortex shedding from a circular cylinder near a moving ground,” *Physics of Fluids*, vol. 19, no. 2, pp. 025 103–12, 2007.

[76] T. Nishino, G. Roberts, and X. Zhang, “Unsteady RANS and detached-eddy simulations of flow around a circular cylinder in ground effect,” *Journal of Fluids and Structures*, vol. 24, no. 1, pp. 18–33, Jan. 2008.

[77] F. H. Post and T. van Walsum, “Focus on scientific visualization,” in *Computer Graphics: Systems and Applications*, H. Hagen, H. Mueller, and G. M. Nielson, Eds. Springer Berlin Heidelberg, 1993, ch. Fluid Flow, pp. 1–40.

[78] R. D. Keane and R. J. Adrian, “Theory of cross-correlation analysis of PIV images,” *Applied Scientific Research*, vol. 49, no. 3, pp. 191–215, 1992.

[79] W. Sutherland, “The viscosity of gases and molecular force,” *Philosophical Magazine*, vol. 5, no. 36, pp. 507–531, 1893.

[80] X. Deng, M. Mao, G. Tu, H. Liu, and H. Zhang, “Geometric conservation law and applications to high-order finite difference schemes with stationary grids,” *Journal of Computational Physics*, vol. 230, no. 4, pp. 1100–1115, Feb. 2011.

[81] D. C. Wilcox, *Turbulence Modeling for CFD*, 3rd ed. DCW Industries, 2006.

[82] C. Rumsey, “The Spalart-Allmaras Turbulence Model,” 2015. [Online]. Available: http://turbmodels.larc.nasa.gov/spalart.html#sa

[83] P. R. Spalart, “Detached-eddy simulation,” *Annual Review of Fluid Mechanics*, vol. 41, no. 1, pp. 181–202, Jan. 2009.

[84] J. Anderson, *Computational Fluid Dynamics: The Basics with Applications. 1995*, 6th ed. McGraw-Hill Higher Education, 1995.

[85] S. L. Kirst, R. T. Biedron, and C. L. Rumsey, *CFL3D Users Manual (Version 5.0)*, 2nd ed. Hampton, VA: The NASA Langley Research Center, 1997, no. September.

[86] J. W. Kim and D. J. Lee, “Generalized characteristic boundary conditions for computational aeroacoustics,” *AIAA Journal*, vol. 38, no. 11, pp. 2040–2049, 2000.

[87] ——, “Characteristic interface conditions for multiblock high-order computation on singular structured grid,” *AIAA Journal*, vol. 41, no. 12, pp. 2341–2348, 2003.

[88] E. Peers, X. Zhang, and J. W. Kim, “Patched characteristic interface condition for high-order multiblock aeroacoustic computation,” *AIAA Journal*, vol. 48, no. 11, pp. 2512–2522, Nov. 2010.

[89] M. R. Visbal and D. V. Gaitonde, “On the use of higher-order finite-difference schemes on curvilinear and deforming meshes,” *Journal of Computational Physics*, vol. 181, no. 1, pp. 155–185, Sep. 2002.

[90] Y. Du and P. J. Morris, “A new block interface condition for aeroacoustic applications,” in *19th AIAA/CEAS Aeroacoustics Conference*, no. AIAA 2013-2210, Reston, Virginia, May 2013.

[91] S. Richards, X. Zhang, X. Chen, and P. Nelson, “The evaluation of non-reflecting boundary conditions for duct acoustic computation,” *Journal of Sound and Vibration*, vol. 270, no. 3, pp. 539–557, Feb. 2004.

[92] R. D. Sandberg and N. D. Sandham, “Nonreflecting zonal characteristic boundary condition for direct numerical simulation of aerodynamic sound,” *AIAA Journal*, vol. 44, no. 2, pp. 402–405, 2006.

[93] F. Hu, M. Hussaini, and J. Manthey, “Low-dissipation and low-dispersion RungeKutta schemes for computational acoustics,” *Journal of Computational Physics*, vol. 124, no. 1, pp. 177–191, 1996.

[94] J. Li, F. Li, and E. Qin, “A fully implicit method for steady and unsteady viscous ow simulations,” *International Journal for Numerical Methods in Fluids*, vol. 43, no. 2, pp. 147–163, 2003.

[95] E. Peers, “Physics-Based Aeroacoustic Modelling of Bluff-Bodies,” Ph.D. dissertation, University of Southampton, 2009.

[96] R. Hixon, “Prefactored small-stencil compact schemes,” *Journal of Computational Physics*, vol. 165, no. 2, pp. 522–541, Dec. 2000.

[97] R. Hixon and E. Turkel, “Compact implicit MacCormack-type schemes with high accuracy,” *Journal of Computational Physics*, vol. 158, no. 1, pp. 51–70, Feb. 1999.

[98] G. Ashcroft and X. Zhang, “Optimized prefactored compact schemes,” *Journal of Computational Physics*, vol. 190, no. 2, pp. 459–477, Sep. 2003.

[99] R. Vichnevetsky and J. Bowles, “Fourier analysis of numerical approximations of hyperbolic equations,” *Society for Industrial and Applied Mathematics*, vol. 26, no. 3, 1984.

[100] J. W. Kim, “Optimised boundary compact finite difference schemes for computational aeroacoustics,” *Journal of Computational Physics*, vol. 225, no. 1, pp. 995–1019, Jul. 2007.

[101] ——, “High-order compact filters with variable cut-off wavenumber and stable boundary treatment,” *Computers & Fluids*, vol. 39, no. 7, pp. 1168–1182, Aug. 2010.

[102] X.-L. Zhao and T.-Z. Huang, “On the inverse of a general pentadiagonal matrix,” *Applied Mathematics and Computation*, vol. 202, no. 2, pp. 639–646, Aug. 2008.

[103] M. H. Carpenter, D. Gottlieb, and S. Abarbanel, “The stability of numerical boundary treatments for compact high-order finite-difference schemes,” *Journal of Computational Physics*, vol. 108, no. 2, pp. 272–295, 1993.

[104] M. Vinokur, “On one-dimensional stretching functions for finite-difference calculations,” *Journal of Computational Physics*, vol. 50, no. 2, pp. 215–234, 1983.

[105] C. W. Mastin, “Error induced by coordinate systems,” *Applied Mathematics and Computation*, vol. 10-11, pp. 31–40, 1982.

[106] D. Lee and M. Tsuei, “A formula for estimation of truncation errors of convection terms in a curvilinear coordinate system,” *Journal of Computational Physics*, vol. 98, no. 1, pp. 90–100, 1992.

[107] S. Sankaranarayanan and M. L. Spaulding, “A study of the effects of grid non-orthogonality on the solution of shallow water equations in boundary-fitted coordinate systems,” *Journal of Computational Physics*, vol. 184, no. 1, pp. 299–320, 2003.

[108] J. F. Thompson, Z. U. A. Warsi, and C. W. Mastin, “Chapter 5,” in *Numerical grid generation: foundations and applications.* New York: North-Holland, 1982, ch. 5, p. 483.

[109] S. J. Alter, “A structured-grid quality measure for simulated hypersonic flows,” in *42nd AIAA Aerospace Sciences Meeting and Exhibit, 5-8 January, Reno, Nevada*, no. AIAA 2004-0612, 2004.

[110] J. F. Dannenhoffer, “Correlation of grid quality metrics and solution accuracy for supersonic flows,” in *50th AIAA Aerospace Sciences Meeting, Nashville, Tennessee*, no. AIAA 2012-0610, 2012.

[111] P. M. Knupp, “Elliptic grid generation,” *Society for Industrial and Applied Mathematics*, vol. 17, no. 6, pp. 1475–1490, 1996.

[112] ——, “Remarks on mesh quality,” in *46th AIAA Aerospace Sciences Meeting*, no. AIAA 2008-933, 2008.

[113] O. V. Vasilyev, T. S. Lund, and P. Moin, “A general class of commutative filters for LES in complex geometries,” *Journal of Computational Physics*, vol. 146, no. 1, pp. 82–104, Oct. 1998.

[114] H. C. Yee, N. D. Sandham, and M. J. Djomehri, “Low-dissipative high-order shock-capturing methods using characteristic-based filters,” *Journal of Computational Physics*, vol. 150, no. 1, pp. 199–238, 1999.

[115] S. Prince, “University of Southampton 7 x 5 Low Speed Wind Tunnel,” p. 1, 2014.

[116] A. Roshko, “Experiments on the flow past a circular cylinder at very high Reynolds number,” *Journal of Fluid Mechanics*, vol. 10, no. 3, pp. 345–356, 1961.

[117] P. Spalart and K. Mejia, “Analysis of experimental and numerical studies of the rudimentary landing gear,” in *49th AIAA Aerospace Sciences Meeting*, no. AIAA 2011-355, 2011.

[118] M. L. Shur, P. R. Spalart, M. K. Strelets, and a. K. Travin, “Towards the prediction of noise from jet engines,” *International Journal of Heat and Fluid Flow*, vol. 24, no. 4, pp. 551–561, 2003.

[119] X. Zhang, X. Chen, J. Gill, and X. Huang, “Gradient term filtering for stable sound propagation with linearized Euler equations,” in *20th AIAA/CEAS Aeroacoustics Conference*, no. AIAA 2014-3306, 2014.

[120] F. R. Menter, “Zonal Two Equation k-w Turbulence Models for Aerodynamic Flows,” in *AIAA Paper 93-2906, 24th Fluid Dynamics Conference, July 6-9, Orlando, Florida, USA*, no. AIAA 1993-2906, 1993.

[121] C. Hirsch, *Numerical Computation of Internal and External Flows*, 2nd ed. Oxford: John Wiley & Sons, Ltd, 2007.

[122] C. L. Rumsey, “Turbulence Modeling Resource,” 2015. [Online]. Available: http://turbmodels.larc.nasa.gov/flatplate.html

[123] K. Richards, “Aeroacoustic computation of sound radiation from ducts,” Ph.D. dissertation, University of Southampton, 2004.

[124] Z. Ma, “Numerical investigation of slat noise attenuation using acoustic liners,” Ph.D. dissertation, University of Southampton, 2008.

[125] W. Liu, “Numerical Investigation of Landing Gear Noise,” Ph.D. dissertation, University of Southampton, 2011.

[126] “Third Computational Aeroacoustics (CAA) Workshop on Benchmark Problems,” vol. NASA/CP-20, p. 470, 2000.

Todo list